Simulation of plastic strain localization by Discrete Dislocation Dynamics and crystal plasticity

Baptiste Joste

PSL UNIVERSITÉ PARIS

THÈSE DE DOCTORAT

DE L'UNIVERSITÉ PSL

Préparée à MINES Paris

Simulation of plastic strain localization by Discrete Dislocation Dynamics and crystal plasticity

~

Simulation de la localisation de la déformation plastique par Dynamique des Dislocations Discrètes et plasticité cristalline

Soutenance par

Baptiste JOSTE

Soutenue le 11 décembre 2023

École doctorale n°621

Ingénierie des Systèmes, Matériaux, Mécanique, Energétique

Spécialité

Mécanique

Composition du jury :

Sandrine BROCHARD Professeure, Université de Poitiers	*Présidente*
Marc FIVEL DR CNRS, Grenoble INP - UGA	*Rapporteur*
Marc LEGROS DR CNRS, Université Toulouse 3	*Rapporteur*
Amine BENZERGA Professor, Texas A&M University	*Examinateur*
Lionel GELEBART Ingénieur de recherche, CEA	*Examinateur*
Henry PROUDHON DR CNRS, Mines Paris	*Directeur de thèse*
Benoit DEVINCRE DR CNRS, LEM CNRS-ONERA	*Examinateur*
Riccardo GATTI CR CNRS, LEM CNRS-ONERA	*Examinateur*

MINES PARIS | PSL

Remerciements

Mes premiers remerciements se tournent tout naturellement vers les membres de mon jury de thèse. Je remercie en premier lieu, Sandrine BROCHARD pour avoir accepté de présider ce jury ainsi que pour ses remarques et questionnements sur mes travaux. Je remercie ensuite Marc FIVEL qui a accepté de rapporter mes travaux et avec qui les échanges au sujet des simulations DDD ont été très constructifs. Je remercie Marc LEGROS pour avoir lui aussi accepté de rapporter mes travaux même si son domaine d'expertise semble éloigné des modèles de simulations, les échanges que nous avons eus lors de ma soutenance ont été particulièrement enrichissants. Je tiens à remercier les autres membres de jury, Lionel GELEBART et Amine BENZERGA qui ont tous deux soulevé des points intéressants lors de la soutenance.

Ce manuscrit de thèse n'aurait pu voir le jour sans le soutien de mon encadrement de thèse. Dans un premier temps, je tiens à remercier mon directeur de thèse Henry PROUDHON qui a toujours su être là dans les moments où j'en avais besoin et qui m'a permis de travailler comme je le souhaitais, « en sous-marin ». Merci pour tous, depuis la diffraction des rayons X en stage DMS jusqu'à cette soutenance de thèse sur la plasticité cristalline, que de chemin parcouru depuis ces quatre années. Je garderai en mémoire les BBQ organisés avec toute l'équipe et les longs moments passés au synchrotron à Grenoble.

Dans un second temps, je tiens à remercier tout particulièrement Benoit DEVINCRE qui m'a toujours apporté son soutien et a toujours su trouver les mots pour me remotiver et me relancer dans la course aux simulations. Nos discussions bien que par ZOOM ont toujours été pour moi une source d'apprentissage considérable. Avant ces travaux, ma connaissance des dislocations était « lacunaire » mais je pense maintenant en connaître un peu plus grâce à toi. Merci d'avoir pris le temps de m'expliquer précisément les choses quand il le fallait et surtout avec une formidable pédagogie.

Pour en terminer avec mes encadrants, je tiens à remercier chaleureusement Riccardo GATTI pour sa gentillesse et sa bonne humeur permanente. Ton soutien technique mais aussi nos discussions sur la physique des dislocations m'ont permis de tenir sur ces trois longues années de thèse. Merci aussi de m'avoir accompagné sur chacune de mes conférences, je me rappellerai toujours avoir fait une bonne trentaine de kilomètres dans New-York en une seule journée et sous la pluie, un grand souvenir dont certains en ont peut-être encore des courbatures. Merci pour ton avis aiguisé sur les présentations et sur la qualité de présentation des résultats, grâce à toi je pense maintenant pouvoir faire de « jolies » figures.

J'ai une pensée pour tous mes compagnons de travail, au LEM ou au Centre des Matériaux. Je tiens tout particulièrement à remercier mes camarades de promotion avec qui nous avons partagé de bons moments autours de bières bon marché et de débats parfois enflammés. Merci à vous d'avoir aussi été des bons compagnons de dépression sur la terrasse du centre où les années nous paraissaient être si longues et les résultats si mauvais.

Pour finir, je tiens à remercier tous mes proches, ceux présents à la soutenance mais aussi ceux qui n'ont pas pu venir. Sans votre soutien depuis le début de ces longues années d'étude, rien n'aurait été possible. Sans avoir à citer personne, je sais qu'ils se reconnaitront.

Acronyms, Notation and Symbols

Acronyms

FEM	Finite Element Method
DDD	Discrete Dislocation Dynamics
CPFEM	Crystal Plasticity Finite Element Method
FCC	Face-Centered Cubic
GB	Grain Boundary
DCM	Discrete Continuous Model
GND	Geometrically Necessary Dislocation
SSD	Statistically Stored Dislocation
TT	Topo-Tomography
TEM	Transmission Electron Microscopy
DCT	Diffraction Contrast Tomography
EBSD	Electron Backscatter Diffraction
AFM	Atomic Force Microscopy

Notation

x	scalar (order 0)
$\underline{x}$	vector (order 1)
$\underset{\sim}{\boldsymbol{X}}$	tensor (order 2)
$\underset{\approx}{\boldsymbol{X}}$	tensor (order 4)
$\dot{x}$, $\underline{\dot{x}}$, $\underset{\sim}{\dot{\boldsymbol{X}}}$	time derivatives
$\underline{x}.\underline{y}$	scalar product
$\underset{\sim}{\boldsymbol{X}}.\underset{\sim}{\boldsymbol{Y}}$	simple contraction
$\underset{\sim}{\boldsymbol{X}} : \underset{\sim}{\boldsymbol{Y}}$	double contraction
$\underline{x} \otimes \underline{y}$	dyadic product on vectors
$\underset{\sim}{\boldsymbol{I}}$	Second order identity tensor

Symbols

$\underset{\sim}{\boldsymbol{F}}$	Deformation gradient tensor
$\underset{\sim}{\boldsymbol{E}}$	Elastic part of $\underset{\sim}{\boldsymbol{F}}$
$\underset{\sim}{\boldsymbol{P}}$	Plastic part of $\underset{\sim}{\boldsymbol{F}}$
$\underset{\approx}{\boldsymbol{C}}$	Fourth order elastic tensor
$\underset{\sim}{\boldsymbol{\sigma}}$	Cauchy stress tensor
$\underset{\sim}{\boldsymbol{\varepsilon}}$	Strain tensor (small perturbation)
$\underset{\sim}{\boldsymbol{\omega}}$	Rotation tensor (small perturbation)
$\underset{\sim}{\boldsymbol{m}}^s$	Schmid tensor
m^s	Unidirectional Schmid factor
$\underline{n}^s$	Normal to the slip plane for slip system s
$\underline{l}^s$	Slip direction for slip system s
τ^s	Resolved shear stress on slip system s
γ^s	Plastic slip on slip system s
γ^s_{vox}	Plastic slip on slip system s in one voxel
ρ^s	Dislocation density on slip system s

Contents

Introduction

The objective of the present thesis is to acquire an improved comprehension of the deformation mechanisms in polycrystalline materials, ultimately resulting in failure. Despite all the progress in experimental characterization techniques and computational methods, phenomena like intragranular plastic strain localization into intense slip bands and the transmission of these bands to other grains is still not fully understood [Spearot and Sangid, 2014; Bayerschen et al., 2016]. This is particularly the case for pure metals, for which there are no obvious mechanisms to explain the presence of localization bands. Under other conditions and for different types of materials, localization phenomena are closely linked to reactions between dislocations and other defects present in the crystalline structure. One of the main difficulties in understanding the physics of the phenomena associated with plastic deformation of crystals is its multi-scale nature. To get a precise description of these phenomena, understanding both behaviours taking place at the mesoscopic and macroscopic scales is essential. In particular, through the formation of intragranular dislocation patterns during the deformation or even by complex multi-axial stress distribution dictated by the arrangement of the microstructure.

In this context, a collaborative project was set up using pure nickel as the study material. Ni polycrystal is a model crystallographic system for elementary plastic deformation processes. This project is titled "3DiPolyplast" and was financially supported by the French National Research Agency (ANR). In the 3DiPolyplast project, we combine electron and synchrotron-based characterization techniques (characterization at the surface (EBSD) and in the bulk (DCT/TT)) with multi-scale crystal plasticity simulations (DDD/FEM).

My thesis is part of the ANR 3DiPolyplast project and was devoted to the simulation part. The other parts of the project refer to two other doctoral theses carried out by my colleagues Zheheng LIU (MATEIS) and Muhammad Fakhry HATTA (Institut Pprime). In order to model crystal plasticity on a multi-scale basis, two types of modelling have been used. On one hand, the Finite Element Method (FEM) and on the other, the Discrete Dislocation Dynamics (DDD) simulation. In brief, the FEM is used to describe crystal plasticity at the macroscopic scale while DDD simulations are used to describe crystal plasticity at the mesoscopic scale. Jointly, these two modelling frameworks are known to be complementary. On one hand, FEM provides a good description of the complex boundary conditions in-

volved in polycrystalline computations and allows computing the polycrystalline behaviour of representative aggregates (with numerous grains) [Lim et al., 2014; Choi et al., 2014; Pokharel et al., 2014]. On the other hand, DDD simulation offers a more physically justified description of deformation mechanisms by modelling the mobility and interactions between dislocations during plastic deformation considering both individual and collective dislocation behaviour.

Most of the numerical research carried out during the thesis was made with a coupling between FEM and DDD simulations. This coupling is considered weak, as opposed to other strong couplings such as the discrete-continuous model (DCM), which has much higher numerical costs for routine calculations. The main aim of the simulations carried out is to understand the physical mechanisms that control the localization of intragranular plastic deformation in pure nickel into intense slip bands. Such a numerical study is challenging because direct comparisons with experiments are not obvious, and the formation of slip bands in pure FCC metals can potentially be associated with several elementary dislocation mechanisms.

The following thesis report is organized as follows. Chapter I is devoted to a detailed review of the literature and the state of the art on the subject of plastic strain localization in polycrystalline metals. In this review, we briefly present the main experimental observations and simulation models that have, in one way or another, addressed the thesis problem. Particular attention is paid to the description of plastic strain localization mechanisms that have already been identified, for example, in alloys or irradiated materials. The models presented in this chapter are mainly related to FEM, CPFEM and DDD, a brief description of which is given.

Chapter II focuses mainly on the systematic study of intragranular elastic loading and, more specifically, its level of heterogeneity, using FEM simulations. In agreement with recent experimental results, it is shown that the microstructure of the aggregate can play a dominant role in the appearance of an intense, localized plastic slip. Several series of simulations are carried out, demonstrating the role of elastic deformation incompatibility between grains in the aggregate. These are the origin of the presence of stress concentration zones that increase the heterogeneity of intragranular loading and give rise to intense, localized plastic slip events, as shown by the first DDD simulations, which initially considered the cross-slip mechanism to be inactive.

Chapter III focuses more specifically on the mechanisms linked to the dislocation microstructure that explain the appearance (initiation) and maintenance (persistence) of a slip band within a grain. In this chapter, particular attention is paid to two mechanisms: cross-slip and collinear annihilation. Observations of the dislocation dynamics and the calculations carried out in the course of the chapter demonstrate the key role of these two mechanisms

in the initiation of intense localized plastic deformation. However, these two elementary mechanisms do not provide an explanation for the persistence of plastic deformation in a region of the grain like a slip band. In fact, neither of these mechanisms allows for a local reduction in kinematic strain hardening, the backstress.

In Chapter IV we explore the additional hypothesis that reactions between dislocations and grain boundaries play an important role in the localization of plastic deformation. Contact reactions between dislocations and grain boundaries are known to exist experimentally and to contribute to a reduction in the elastic energy of the system and thus potentially modify the grain's internal stress. Prior to this work, as these mechanisms were not integrated into the DDD code at the beginning of my work, it was necessary to develop and implement a local rule to model dislocations/grain boundaries contact reaction on a mesoscopic scale. The simulations carried out in this chapter show the role played by these mechanisms on the strain localization properties.

In conclusion, Chapter V explores the potential of strong coupling between FEM and DDD through DCM to study the thesis problem. DCM simulations are conducted in model cases and clearly demonstrate the significant advantage of this type of modelling. In particular, the simulation of diffraction spots during a topo-tomography acquisition is carried out based on simulation results. Thanks to these simulations, the presence of a diffraction contrast on a virtual detector can simply be demonstrated. In the coming months, these results could be used to consolidate and refine experiments already underway. In addition, the first simulations of a grain embedded in a plastic matrix of grains part of a periodic aggregate are performed. These simulations reveal significant changes in behaviour when either plastic-elastic or plastic-plastic interactions between grains are considered in the simulations. We demonstrate that plastic deformation in the vicinity of a grain can strongly modify the plastic deformation process within that grain, and interact with the internal grain mechanisms controlling the localization of plastic deformation in bands.

Introduction en français

L'objectif de ce sujet de thèse est d'acquérir une meilleure compréhension des mécanismes de déformation dans les matériaux polycristallins, qui aboutissent finalement à la rupture de ces derniers. Malgré tous les progrès réalisés dans les techniques de caractérisation expérimentale et les méthodes de calcul, des phénomènes tels que la localisation de la déformation plastique intragranulaire en bandes de glissement intenses et la transmission de ces bandes à d'autres grains ne sont toujours pas entièrement compris [Spearot and Sangid, 2014; Bayerschen et al., 2016]. C'est particulièrement le cas pour les métaux purs, pour lesquels il n'existe pas de mécanismes évidents pour expliquer la présence de bandes de localisation.

Dans d'autres conditions et pour différents types de matériaux, les phénomènes de localisation sont étroitement liés aux réactions entre dislocations et autres défauts présents dans la structure cristalline. L'une des principales difficultés pour comprendre la physique des phénomènes associés à la déformation plastique des cristaux est leur nature multi-échelle. Pour obtenir une description précise de ces phénomènes, il est essentiel de comprendre les comportements qui se produisent à l'échelle mésoscopique et macroscopique, en particulier, par la formation d'arrangement de dislocations intragranulaires au cours de la déformation ou même par une distribution complexe des contraintes mutli-axiales dictée par la microstructure polycristalline.

Dans ce contexte, un projet de collaboration a été mis en place, sélectionnant le nickel pur comme matériau d'étude, le nickel étant un système cristallographique modèle pour les processus élémentaires de déformation plastique. Ce projet, intitulé "3DiPolyplast", a été soutenu financièrement par l'Agence nationale de la recherche (ANR). Dans le projet 3DiPolyplast, nous combinons des techniques de caractérisation basées sur les électrons et le synchroton (caractérisation à en surface (EBSD) et dans le volume (DCT/TT)) avec des simulations de plasticité cristalline multi-échelles (DDD/FEM).

Ma thèse fait partie du projet ANR 3DiPolyplast et a été consacrée à la partie simulation. Les autres parties du projet font référence à deux autres thèses de doctorat réalisées par mes collègues Zheheng LIU (MATEIS) et Muhammad Fakhry HATTA (Institut Pprime). Afin de modéliser la plasticité cristalline sur une base multi-échelle, deux types de modélisation ont été utilisés. D'une part, la méthode des éléments finis (FEM) et d'autre part, la dynamique des dislocations discrètes (DDD). En bref, la méthode des éléments finis est utilisée pour décrire la plasticité cristalline à l'échelle macroscopique, tandis que les simulations DDD sont utilisées pour décrire la plasticité cristalline à l'échelle mésoscopique. Ces deux cadres de modélisation sont connus pour leur complémentarité. D'une part, la FEM fournit une bonne description des conditions aux limites complexes impliquées dans les calculs polycristallins et permet de calculer le comportement d'agrégats polycristallins représentatifs (avec de nombreux grains) [Lim et al., 2014; Choi et al., 2014; Pokharel et al., 2014]. D'autre part, la DDD offre une description plus physiquement justifiée des mécanismes de déformation en modélisant la mobilité et les interactions entre les dislocations pendant la déformation plastique et en tenant compte du comportement individuel et collectif des dislocations.

La plupart des recherches numériques effectuées au cours de cette thèse ont été réalisées avec un couplage entre les simulations FEM et DDD. Ce couplage est considéré comme faible, par opposition à d'autres couplages forts tels que le modèle continu discret (DCM), qui ont des coûts numériques beaucoup plus élevés pour les calculs de routine. L'objectif principal des simulations effectuées est de comprendre les mécanismes physiques qui contrôlent la localisation de la déformation plastique intragranulaire dans le nickel pur en bandes de glissement intenses. Une telle étude numérique est difficile car les comparaisons directes

avec les expériences ne sont pas évidentes, et la formation de bandes de glissement dans les métaux FCC purs peut potentiellement être associée à plusieurs mécanismes de dislocation élémentaires.

Ce manuscrit est organisé comme suit. Le Chapitre I est consacré à une revue détaillée de la littérature et de l'état de l'art sur le sujet de la localisation des déformations plastiques dans les métaux polycristallins. Dans cette revue, nous présentons brièvement les principales observations expérimentales et les modèles de simulation qui ont, d'une manière ou d'une autre, abordé la problématique décrite plus haut. Une attention particulière est accordée à la description des mécanismes de localisation de la déformation plastique qui ont déjà été identifiés, par exemple, dans les alliages ou les matériaux irradiés. Les modèles présentés dans ce chapitre sont principalement liés à FEM, CPFEM et DDD, dont une brève description est donnée.

Le Chapitre II se concentre principalement sur l'étude systématique du chargement élastique intragranulaire et, plus particulièrement, de son niveau d'hétérogénéité, à l'aide de simulations FEM. En accord avec les résultats expérimentaux récents, il est montré que la microstructure de l'agrégat peut jouer un rôle dominant dans l'apparition d'un glissement plastique intense et localisé. Plusieurs séries de simulations sont réalisées, démontrant le rôle des incompatibilités de déformation élastique entre les grains de l'agrégat. Celles-ci sont à l'origine de la présence de zones de concentration de contraintes qui augmentent l'hétérogénéité du chargement intragranulaire et donnent lieu à des glissements plastiques intenses et localisés, comme le montrent les premières simulations DDD, qui considéraient initialement que le mécanisme de cross-slip était inactif.

Le Chapitre III se concentre plus spécifiquement sur les mécanismes liés à la microstructure des dislocations qui expliquent l'apparition (initiation) et le maintien (persistance) d'une bande de glissement à l'intérieur d'un grain. Dans ce chapitre, une attention particulière est accordée à deux mécanismes : le cross-slip et l'annihilation colinéaire. Les observations de la dynamique des dislocations et les calculs effectués au cours du chapitre démontrent le rôle clé de ces deux mécanismes dans l'initiation d'une déformation plastique localisée intense. Cependant, ces deux mécanismes élémentaires ne permettent pas d'expliquer la persistance de la déformation plastique dans une région du grain comme une bande de glissement. En effet, aucun de ces mécanismes ne permet une réduction locale de l'écrouissage cinématique, le backstress.

Dans le Chapitre IV, nous explorons l'hypothèse supplémentaire selon laquelle les réactions entre les dislocations et les joints de grains jouent un rôle important dans la localisation de la déformation plastique. Les réactions de contact entre les dislocations et les joints de grains sont connues pour exister expérimentalement et pour contribuer à une réduction de l'énergie élastique du système et donc potentiellement à une modification de la contrainte

interne du grain. Avant ce travail, comme ces mécanismes n'étaient pas intégrés dans le code DDD, il a été nécessaire de développer et d'implémenter une règle locale pour modéliser la réaction de contact dislocations/joints de grains à une échelle mésoscopique. Les simulations réalisées dans ce chapitre montrent le rôle joué par ces mécanismes sur les propriétés de localisation de la déformation plastique.

En conclusion, le Chapitre V explore le potentiel d'un couplage fort entre FEM et DDD à travers le modèle discret-continu (DCM). Les simulations DCM sont effectuées dans des cas modèles et démontrent clairement l'avantage significatif de ce type de modélisation. En particulier, la simulation des taches de diffraction lors d'une acquisition topo-tomographique est réalisée à partir de résultats de simulation. Grâce à ces simulations, la présence d'un contraste de diffraction sur un détecteur virtuel peut être simplement démontrée. Dans les mois à venir, ces résultats pourront être utilisés pour consolider et affiner les expériences déjà en cours. Par ailleurs, les premières simulations d'un grain noyé dans une matrice plastique de grains faisant partie d'un agrégat périodique sont réalisées. Ces simulations révèlent des changements significatifs de comportement lorsque les interactions plastiques-élastiques ou plastiques-plastiques entre les grains sont prises en compte dans les simulations. Nous démontrons que la déformation plastique au voisinage d'un grain peut fortement modifier le processus de déformation plastique à l'intérieur de ce grain, et interagir avec les mécanismes internes du grain qui contrôlent la localisation de la déformation plastique dans les bandes.

Chapter I

State of the art

Résumé :

Dans ce chapitre est présenté l'état de l'art des connaissances autour de la localisation de la déformation plastique intragranulaire au sein d'agrégats polycristallins en se focalisant sur les métaux purs. En effet, la localisation de la déformation plastique dans ce type de matériau et dans le cadre d'un chargement uniaxial et monotone est à ce jour un phénomène dont les origines physiques sont peu connues. Certains mécanismes permettant d'expliquer la présence d'un comportement plastique localisé sont cependant observés sous d'autres conditions et pour d'autres type de matériaux, comme les métaux irradiés. Comme cela est discuté au cours de ce chapitre, ces phénomènes sont intrinsèquement liés à des réductions de l'écrouissage local permettant de rendre certaines régions favorables au glissement plastique. Au cours de ce chapitre, des observations expérimentales ainsi que des résultats de simulations sont présentés afin de donner une bonne vision d'ensemble de l'état de l'art des connaissances physiques mais aussi des capacités de modélisation.

Contents

1.1 The plastic deformation of crystalline materials

Plastic deformation, in contrast to elastic deformation, is an irreversible phenomenon. This deformation takes place without any change in volume (for crystalline materials) and has been observed very early on by metallurgists in the form of slip traces on the surface of samples. They soon realised that this was actually the shearing of one part of the crystal from another along particular directions. However, before the 1930s the theory of plastic deformation was not consistent with experimental observations, in particular with respect to the yield stress. Theoretically, an analytical model was used to describe the stress required to shear one part of the crystal from another over the smallest distance, the interatomic distance. This theoretical model predicted extremely high stress values compared to experimentally observed stress levels. It was not until 1930 through the work of Orowan, Polanyi and Taylor [Taylor, 1934] that the concept of shearing by the motion of dislocations appeared. The concept of dislocation in a continuous elastic medium has been known since the work of Volterra [Volterra, 1907].

It was around that time that several authors independently predicted that plastic deformation was possible due to the movement of these defects (dislocations) within the crystalline structure. Indeed, the defects would move by destruction and formation of interatomic bonds thus requiring a much lower flow stress and allowing consistency with experimental observations. These dislocations glide along particular directions and on particular crystalline planes, the densest atomic planes. Indeed, it is on these planes that the movements of the atoms are the weakest, which is therefore energetically favourable.

When a dislocation reaches the end of the crystal structure, i.e. the surface of the sample, it leaves a residual displacement equal to the closure defect imposed by the presence of the dislocation, defined as the Burgers vector. Slip traces observed experimentally (see Fig. 1.1) are the result of the passage of numerous dislocations at the sample surface.

Another mechanism is also well known to produce plastic deformation, twinning [Mahajan and Williams, 1973]. Twinning, which consists of the tilting of one part of the crystal with respect to another, takes place mainly in hexagonal crystal structures, having fewer slip systems and is not in the scope of this manuscript. However, observation of face-centred cubic (FCC) structures such as copper, nickel or aluminium shows the systematic presence of annealing twins within the polycrystalline microstructure. These annealing twins, whose particular shape is easily observed by EBSD orientation mapping (see for example [Jin et al., 2015]), are not linked to plastic deformation but constitute obstacles to the movement of dislocations within the microstructure, in the same way as grain boundaries. The appearance of these twins is directly linked to heat treatment processes such as cold working. Annealing twins boundaries in the polycrystalline microstructure are thus considered as particular

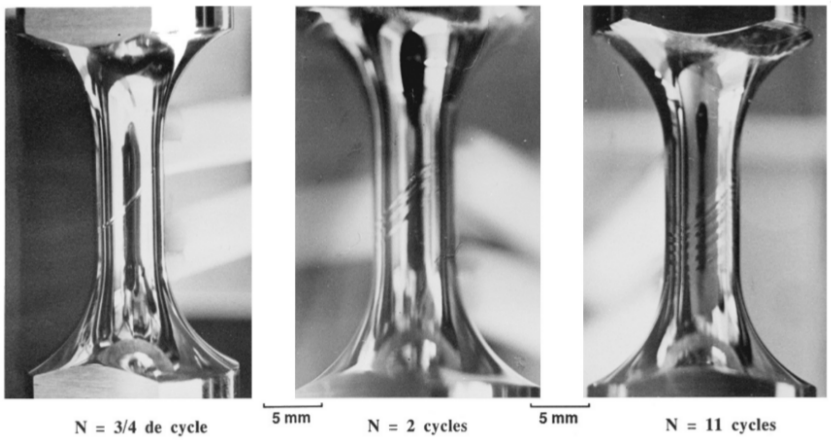

Figure 1.1: *Illustration of steps appearing at the surface of a single crystal Nickel-based superalloy sample [Hanriot et al., 1991] due to the arrival of a large number of dislocations at the surface.*

grain boundaries of a given energy [Hasson and Goux, 1971; Holm et al., 2010; Bulatov et al., 2014]. For FCC structures, the most usual deformation is thus glide, motion provided by the dislocations and will be the one studied in this manuscript.

Considering therefore that plastic deformation is produced by the movement of dislocations within the crystalline structure, it is in fact discrete because it depends on the presence or absence of these defects on particular planes. For each of the crystallographic structures, it is possible to define the set of slip systems that may be involved in the plastic deformation. A slip system is defined by a slip direction and a slip plane. Pure nickel, with a face-centred cubic structure, has twelve independent slip systems, four planes and three different directions as illustrated in Fig. 1.2. In this manuscript, each slip system will be referred to using the Schmid and Boas notation [Schmid et al., 1935], as illustrated later in Tab. 2.2.

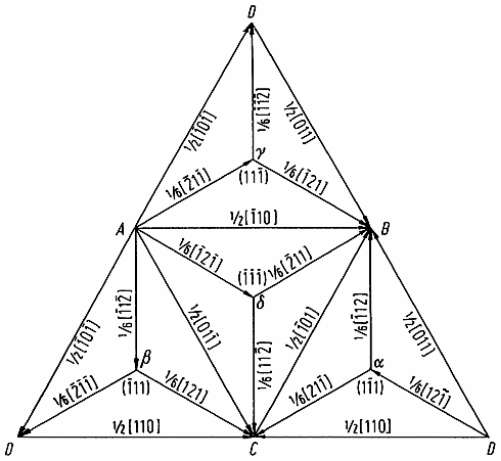

Figure 1.2: *Thompson tetrahedra illustrating slip planes and slip directions for the FCC crystalline structure.*

Each slip system can produce a different amount of plasticity as it depends on the external loading but also on the orientation of the crystal following the so-called Schmid law (presented later in the manuscript, see Eq. 2.1).

1.2 Intragranular plastic strain localization phenomena in polycrystals

1.2.1 Strain localization modes

Plastic strain localization phenomena can be observed at different scales, from the nanoscopic to the macroscopic scale. The appearance of localization is directly linked to physical mechanisms that modify the organisation of the material's internal microstructure as it will be described in § 1.2.2, thus understanding these mechanisms and the way dislocations interact with each other or with other defects is therefore necessary.

As previously stated in the introduction of this manuscript, we are interested here in the intragranular localization modes that arise in polycrystalline materials. The localization of plastic deformation is defined as an instability in the sense of mechanics caused by softening mechanisms, the modes of appearance of which can be predicted by Asaro and Rice's bifurcation criterion [Asaro and Rice, 1977] by the appearance of slip bands and kink bands in single crystal deformation as an example. In the context of this manuscript, we will only be interested in slip band localization modes, as kink bands appear predominantly in metals with a hexagonal structure and a high anisotropy coefficient. Slip bands are regions of intense plastic deformation where deformation occurs under the effect of loading or according to certain microstructural reactions. As will be discussed in the remainder of this manuscript, slip bands can represent regions of deformation that are more or less thick depending on the material or loading conditions. The kinematics of plastic deformation proposed by [Korbel and Martin, 1986] in the case of a polycrystalline aggregate clearly shows the major importance of these localization events, which are initially confined to certain grains and then gradually extend to the aggregate as a whole.

The appearance of these slip bands is a complex mechanism that depends on many factors such as the crystalline structure, the type of loading and the loading conditions such as temperature or irradiation. Understanding these phenomena is of major importance as the presence of these localization bands subsequently leads to the appearance of fracture sites, reducing the service life of the materials.

1.2.2 Mechanisms favoring plastic localization

The role of this part of the manuscript is to describe the mechanisms identified in the literature for different types of material and under different types of loading that allow plastic deformation to localize. Particular interest is taken to dislocation reactions and microstructure evolution during loading, leading to the apparition of localization. As a matter of fact, depending on certain conditions, polycrystals can exhibit a more or less localized plastic behaviour at the grains scale. The work presented in this part of the manuscript deals with the problem of slip band localization for irradiated materials, in the presence of cyclic loading or in alloys.

1.2.2.1 The role of irradiation

The emission of fast neutrons produced by nuclear fission is known to strongly interact with the atoms composing the crystalline structures of metals and alloys, introducing for example numerous defects in it, like dislocation loops. The effects of irradiation on the mechanical behaviour of these materials are numerous, such as plastic strain localization as is well represented in Fig. 1.3. This figure shows the apparition of intense localized slip bands in the irradiated region whereas localization patterns are much less pronounced in the non-irradiated region. In fact, slip bands appear to be less intense and clearly more numerous at the grain surface. Reasons for such localization have been extensively studied over the past years: authors reveal the systematic presence of clear channels [Sharp, 1974; Luppo et al., 2000; Onimus et al., 2013], bands of very low density of defects. These bands are found to be parallel with crystallographic planes and are highly strained regions as reported by [Nishioka et al., 2008; Miura et al., 2009]. The presence of these free channels has been well understood

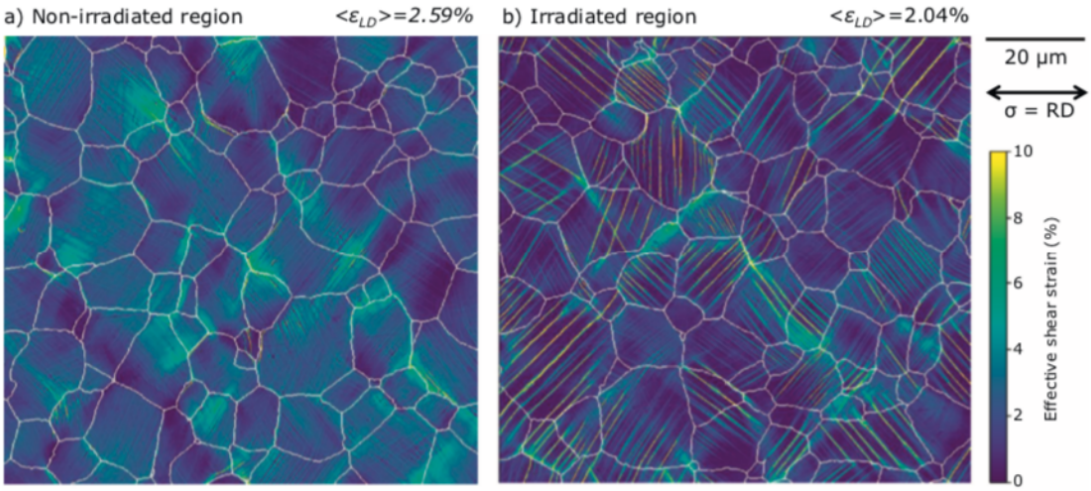

Figure 1.3: *Strain maps reported for a proton irradiated Zr alloy [Thomas et al., 2019] in a non irradiated region (a) and irradiated region (b).*

from a microstructural point of view, resulting in a dislocation channelling process. As a matter of fact, irradiation defects are successively annihilated or dragged by dislocation glide. A synthesis of the various mechanisms involved in the annihilation of dislocation loop defects is given by [Wechsler, 1972; Hirsch, 1977]. As an example, the drag of defects by dislocations glide provides a region of slip with fewer defects for the next dislocations thus promoting plastic slip in this area. During the drag of irradiation defects by the dislocations, the defect can be annihilated by another defect of the opposite sign promoting again the formation of clear channels. Nevertheless, these junctions are not always glissile as reported by [Onimus et al., 2004] in the case of prismatic planes of Zr alloys thus allowing localization only on predicted planes.

1.2.2.2 The formation of Persistent Slip Bands (PSB)

Some of the very first observations of the deformation events at the surface of a metallic material [Ewing and Humfrey, 1903] during cyclic loading reveal the presence of strong damage induced by the formation of slip bands. Some of these slip bands are called Persistent Slip Bands (PSB) and are considered as characteristic features of FCC material deformation at the early stage of fatigue. Over the years, many investigations have been performed on the will to better understand such a mechanism, a very detailed description is given by [Suresh, 1998]. Various aspects of the formation of PSB have been studied, like the dislocation microstructure involved in PSB [Mughrabi, 1978; Brown, 2006] formation and evolution. The formation of PSB has been shown to be influenced by core dislocation properties, like the stacking fault energy and the probability of cross-slip [Lukas, 1996], but are still not fully understood. From a microstructural point of view, it is now very clear that PSB contributes to the formation of a particular microstructure arrangement inside the material. Each band appear to be delimited by walls of edge dislocations that cannot move due to the formation of dipoles (see Fig. 1.4), induced by the reversal of the loading and stabilised by interactions with dislocations on the deviated slip system [Li and Laird, 1994]. The dislocation mobility in between the walls is known to be mainly produced by the motion of screw dislocations.

In the work of [Déprés et al., 2004, 2006], the authors show the discrepancy between two kinds of dislocation density, one which is not reversible and the other which is reversible. The irreversible density is attributed to dislocations composing PSB walls and the reversible density to the one that allows to accommodate plastic deformation. Once the loading is reversed, many dislocations are thus annihilated promoting localization. By this whole process, at the early stage of fatigue strong localization pattern appears in single and polycrystals. It should also be noted that the formation of PSB is always experimentally observed to be accompanied by a saturation regime in the PSB volume fraction and position as evidenced by DDD simulations performed by [Meng et al., 2021].

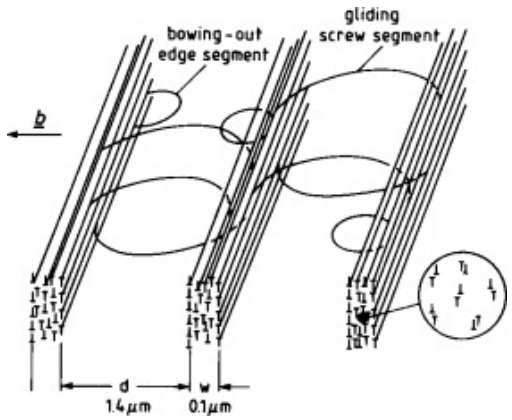

Figure 1.4: *The schematic representation of PSB walls, composed of edge dislocation dipoles [Differt and Essmann, 1993].*

1.2.2.3 Slip localization in alloys

Alloys are generally considered to have several sources of plastic strain localization during loading, such as precipitate shear mechanisms or short-range order destruction. The book by [Martin, 1980] lists the various possible interactions and their role in the appearance of intense slip bands. Depending on the type of precipitate, its size and whether or not it is coherent with the matrix, different mechanisms may appear to enable dislocations to bypass this obstacle [Reppich, 1992]. In general, small coherent precipitates can be sheared by dislocations. This phenomenon reduces the radius of the precipitate as the dislocations successively pass through it, reducing its capability to block dislocations and thus favouring plastic slip and therefore localization. When the precipitate is too resistant or too large, the dislocations can bypass it following the process described in [Gerold, 1979] named as Orowan looping. However, this does not reduce the strength of the precipitate; on the contrary, a residual dislocation loop surrounds the precipitate, resulting in excess stress for the following dislocations. Authors like [Lütjering and Weissmann, 1970] have shown, for example, studying titanium-based alloys, that different heat treatment methods can produce different deformation structures. In fact, the production of small coherent precipitates favours the appearance of intense slip bands of fairly low density. Conversely, the production of semi-coherent precipitates by heat treatment leads to the appearance of much more homogeneous deformation events at the surface, with less intense, thinner and more dense slip bands overall.

PFZs (Precipitate Free Zones) are also found in some alloys, as described in [Arani et al., 2022], allowing plastic deformation to be localized in the form of intense slip bands. Indeed, regions where the density of precipitates is reduced allow easier dislocation mobility.

1.2.3 The particular case of pure metals under monotonic loading

As discussed in the previous sections, there are special cases where significant plastic deformation can be localized in polycrystalline materials, in the form of slip bands of varying thickness and intensity. However, in the case of pure metals and monotonic tensile stress, these mechanisms do not apply. To date, as already stated in the introduction, little is known about the mechanisms that allow plastic deformation to be localized in this type of condition. Because they are of no real industrial interest, metals in their purest configuration and in the context of monotonic loading have not been the subject of as much research as applications linked to fatigue or mechanisms linked to the irradiation of metals in nuclear reactors. However, this literature review will examine some of the research conducted in order to gain greater insight into the microstructures of localization under specific conditions.

The localization of plastic deformation in pure metals has been the subject of particular interest since the end of the first half of the twentieth century, notably through research focused on the plastic deformation of single and polycrystals of copper and aluminium. This early work showed the presence of very specific localization events on the surface or in the volume of samples, known as slip bands. The book by [Jaoul, 2008] on the plastic deformation of metals brings together most of the research work and the phenomena observed during the appearance of localization in the form of slip bands. From this book, we learn that some authors, such as [Heidenreich and Shockley, 1947; Brown, 1952], have been interested in defining the notion of slip bands as the grouping of a set of slip lines that can give rise to regions of intense plastic deformation. Others, such as [Crussard, 1945; Chen and Pond, 1952], have focused on the kinematic aspect of the formation of slip bands in single crystals and have shown that the formation of slip bands occurs successively on the surface of deformed samples. In fact, the first slip events appear in particular regions, initially in a fairly sporadic manner, and then spread to the whole of the single crystal, giving a more or less homogeneous structure to the deformation. A good observation of this kinematic is provided by [Kahloun et al., 2016] through AFM observations in copper and iron single crystals. Especially for copper samples, plastic deformation first appear in a given region of the surface and thus spreads out over the whole surface, as an homogenization process.

These observations initially limited to the study of single crystals, were then extended to polycrystals [Ikeno et al., 1990; Kitajima and Ono, 1995; Konuma, 1964; Lindholm and Yeakley, 1965; Yoshida and Nagata, 1966] for which the mechanisms leading to the appearance of slip bands may vary. In fact, the study of plastic deformation in polycrystalline aggregates requires each of the grains constituting the aggregate to be considered individually, as each participates in its own way in accommodating plastic deformation. In a polycrystalline aggregate, each of the grains has its own crystallographic orientation, giving it a greater or lesser degree of rigidity and a plastic accommodation level that can vary according to the

activity of the slip systems given by Schmid's law. As a result, it is common to observe in polycrystals that some grains remain undeformed or only slightly plastically deformed even after significant levels of macroscopic deformation, while others already show strong localization in the form of slip bands. This type of observation is particularly visible in Fig. 1.5 taken from [Goulmy et al., 2022]. In this figure, we can clearly see the microstructure of the slip bands forming on the surface of the sample and for a large number of grains. However, as can be seen, some of these grains, even at high deformation levels, greater than 10 %, do not show any apparent slip bands. Another factor that must be taken into account when considering the plastic deformation of polycrystals is the interaction between neighbouring grains. These interactions can give rise to strong incompatibilities, as we shall see in the next section, modifying the local stress state and making it highly multi-axial. As a result, it is common to see several slip systems activated in these grains, giving rise to slip lines or bands in several directions. Grain boundaries are also a source of significant blockage of dislocations, leading to a significant change in the stress state associated with the presence of dislocations and giving rise to the well-known backstress effect whose definition is given in § 1.3.2.

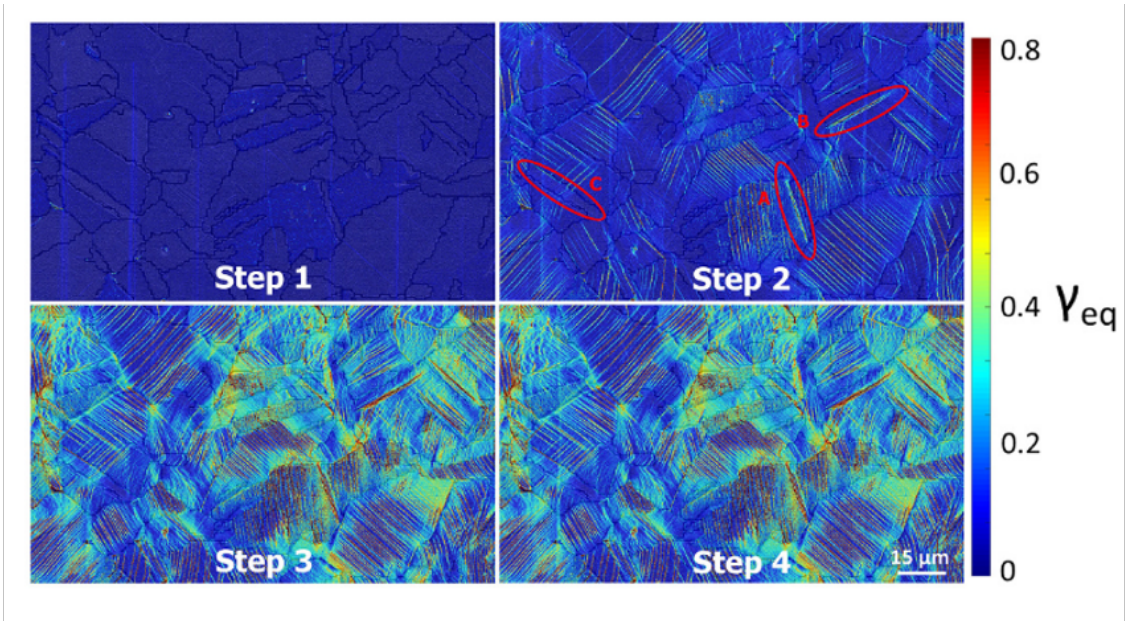

Figure 1.5: *Illustration of plastic strain mapping for various loading steps in pure polycrystalline copper, step 1 : 0.39-0.41 %, step 2 : 4.35-4.39 %, step 3 : 14.34-14.38 % and step 4 : 14.09 % [Goulmy et al., 2022].*

Over the years, other observations have shown the dependence of the formation of these microstructures on temperature or on the strain rate in single crystals [Brown, 1949; Rosi and Mathewson, 1950] and polycrystals [Yoshida and Nagata, 1966; Raza, 1982]. More recent studies [Xiong et al., 2018; Gruber et al., 2020; Dimanov et al., 2021] have shown that temperature has the effect of reducing the number of slip bands observed in grains during plastic deformation, but that the plastic slip per band is greater, giving rise to more

localized behaviour. A direct observation of this phenomenon is clearly visible in Fig. 1.6 showing the state of the localization and slip bands for two aluminium polycrystals deformed at 2 and 5% for temperatures ranging from ambient to 300°. In fact, in this representation, we can clearly see a strong difference in plastic localization between the temperature levels, particularly for deformation of 5 %. At moderate temperatures, plastic deformation is more or less homogeneous, with the appearance of slip bands of the same intensity and thickness. As the temperature increases, very intense and thicker slip bands appear. It should be noted that temperature also leads to high levels of plastic deformation at the grain boundaries, as shown in the figure. The bands thickened, and the plastic deformation became more localized due to increased cross-slip activity and other recovery processes, such as dislocation climb, which are thermally activated mechanisms.

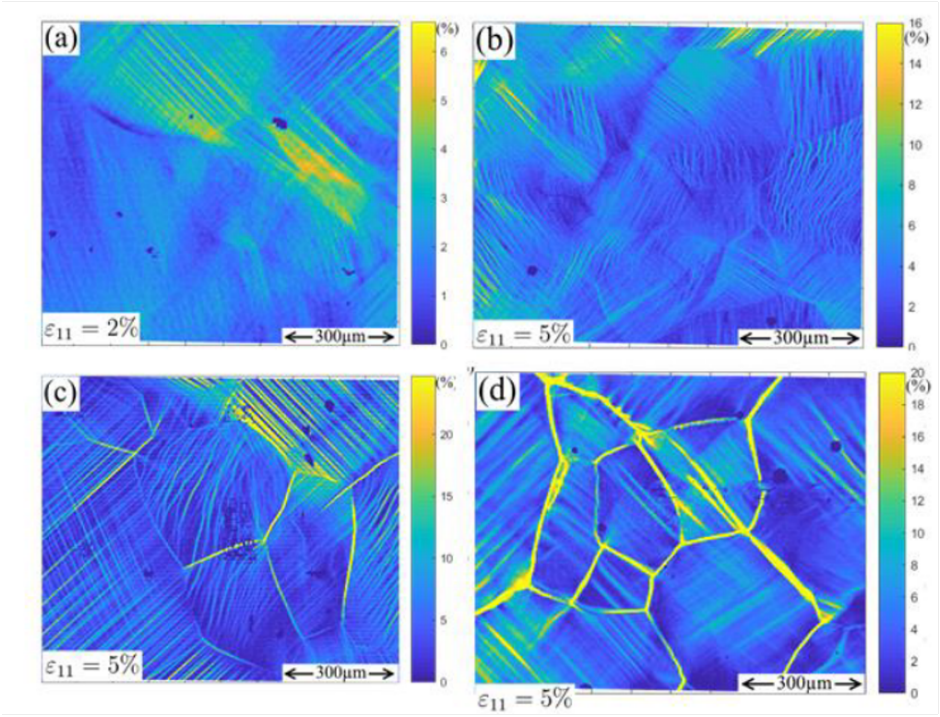

Figure 1.6: *Illustration of strain maps measured in polycrystalline aluminium [Dimanov et al., 2021] at ambient temperature and 2 % of strain (a),* $110°C$ *and 5 % of strain (b),* $200°C$ *and 5 % of strain (c) and* $300°C$ *and 5 % of strain (d).*

In line with what is observed at high temperatures, the opposite conclusions can be drawn through dynamic loading effects, as shown in particular by the results of [Yoshida and Nagata, 1966]. It is well known that increasing the temperature increases the ductility of metals, as can be seen from the tensile curves of metallic materials but in contrast, increasing the loading speed makes the material's behaviour stiffer and plastic deformation less intense. What the work of [Yoshida and Nagata, 1966] shows is that this has an impact on the formation and appearance of slip bands. In fact, in the case of dynamic loading, slip bands appear to be more numerous and less intense than in the case of quasi-static loading.

In general, slip bands seem to appear homogeneously in pure metals under monotonic tensile loading at ambient temperature. This is supported by the observations of [Boas and Ogilvie, 1954; Kitajima and Ono, 1995; Delaire et al., 2000; Goulmy et al., 2022]. The slip bands appear thin, narrow and without a strong intensity gradient, as can be seen in particular in alloys or irradiated materials [Polák et al., 1990; Di Gioacchino and da Fonseca, 2015; Thomas et al., 2019; Sangid et al., 2020]. It will be interesting to see how the dislocation microstructure evolves and how plastic deformation occurs within a grain during our DDD simulations.

1.2.4 On the role of the microstructure

Recent developments in experimental observations allow to precisely measure the bulk grain behaviour in 3D during plastic deformation [Pokharel et al., 2015; Stinville et al., 2022a; Sangid et al., 2020; Han et al., 2018]. The main challenges of these experiments lie in the ability to perform in-situ bulk measurements, from the atomic scale to capture the features associated with dislocations, to the macroscopic scale to capture the microstructural effects. In the literature, most of the studies focused on the fatigue crack nucleation sites in polycrystalline nickel-based superalloy [Miao et al., 2012; Llanes and Laird, 1992; Stinville et al., 2015, 2016] or in other materials [Kobayashi et al., 2005, 2008] lead to the idea that the microstructure play a key role on highly intragranular localized slip events. As an example, in [Charpagne et al., 2021] authors provide a statistical analysis of the slip localization behaviour related to the microstructure. This statistical analysis performed over five hundred slip bands reveal the strong correlation between their location and microstructure configuration. As illustrated in Fig. 1.7, more than half of the intense slip bands emanate from a triple junction showing the strong impact of the microstructure on the intragranular behaviour. Authors identified these regions as potentially stress concentration regions thus providing the necessary driving force to initiate a slip band. Many times, these bands are found parallel to the twin boundaries planes thus providing a region of slip with fewer obstacles. The statistical observation also reveals the presence of intense slip bands produced by transmission events.

Triple junctions are intersection lines between grains in a polycrystalline aggregate. In general terms, three kinds of intersections are encountered in polycrystalline aggregate :

- Grain boundaries: Intersection surface between two grains
- Triple junctions: Intersection line between three grains, which is also the intersection of two grain boundaries

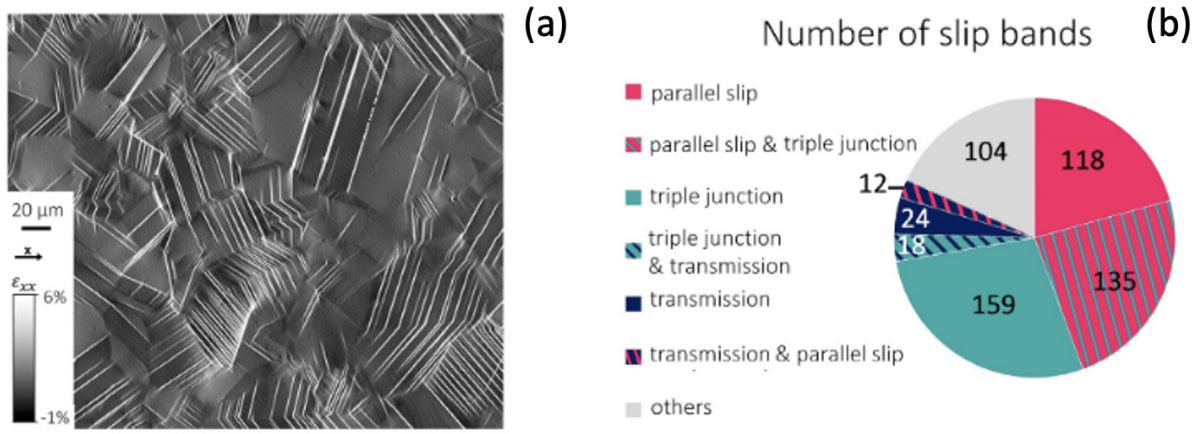

Figure 1.7: *Illustration of slip bands structure by DIC in the Inconel 718 polycrystal [Charpagne et al., 2021] at 0.2 % of plastic strain (a) and statistic on the intense slip bands location over the whole aggregate (b).*

- Quadruple nodes: Intersection point between four grains, which is also the intersection of two triple lines

Let us consider these topological elements as regions of high elastic strain incompatibilities due to the anisotropic elasticity of the crystal which, depending on the grain orientation, will change the local stiffness significantly. The role of these regions on the elastic strain and stress fields have been well described by [Yeratapally et al., 2016; Stein et al., 2014] and [Latypov et al., 2021]. Elastic strain incompatibilities lead to strong dispersion of the mechanical fields providing the apparition of high or low stress concentration in the intersection regions. In doing so, the intragranular mechanical behaviour also becomes more heterogeneous and is a possible explanation for intense slip band localization. An illustration of strain field dispersion is given in Fig. 1.8 from FEM computations with various coefficients of anisotropy. As a reminder, the coefficient of anisotropy A is computed following the given equation for a cubic symmetry with C_{11}, C_{12} and C_{44} the elastic constants:

$$A = \frac{2C_{44}}{(C_{11} - C_{12})} \tag{1.1}$$

From these results, it is clear that the elastic strain field dispersion, computed by the ratio $\frac{\epsilon_{11}}{\bar{\epsilon}}$ with $\bar{\epsilon}$ the strain field computed for isotropic consideration of the material is maximized near intersection regions. The higher the coefficient of anisotropy, the more intense the dispersion will be. In addition, looking at the Young's modulus map in Fig. 1.8-(a) we can see that this dispersion appears where the Young's modulus difference is maximized.

All these considerations let us think that microstructure should play an important role in the apparition of slip localization into intense slip bands for the model material, pure

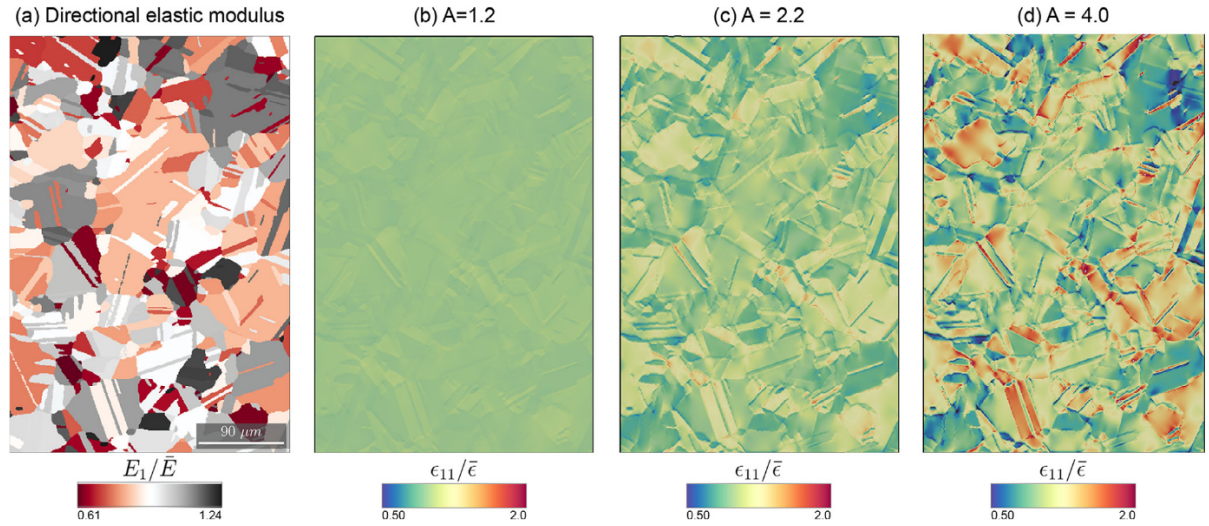

Figure 1.8: *Elastic anisotropy in a Rene 88DT nickel-based superalloy microstructure. Young's modulus (a) and elastic strain field ratios for various anisotropy coefficients (b)-(d) [Latypov et al., 2021].*

polycrystalline nickel. This will be discussed in detail in Chapter II of the manuscript.

1.3 Strain hardening in polycrystals

In order to determine the origins of plastic strain localization, it is important to clearly define the different strain-hardening mechanisms encountered in polycrystalline materials. Indeed, localization is necessarily associated with a local reduction in strain-hardening, which favours plastic deformation. Two types of hardening behaviour are observed in polycrystalline materials, isotropic and kinematic hardening. Both hardening behaviours come from different contributions from a microstructural point of view and do not exhibit the same contribution on the total hardening experienced by the material [Daveau, 2012; Jiang et al., 2019]. Isotropic hardening is generally found to be of lower intensity in comparison with kinematic hardening for polycrystalline materials. Nowadays, it is common to divide dislocations present in the crystal into two families, the so-called SSD and GND dislocations with :

$$\rho_{SSD} = \rho_{tot} - \rho_{GND} \tag{1.2}$$

In the next paragraphs § 1.3.1 and § 1.3.2 a brief description of these two mechanisms is given from a microstructural point of view. More detailed information regarding this point can be found for example in [Madec et al., 2002] for the isotropic hardening and [Mughrabi, 1983] for the kinematic hardening.

1.3.1 Isotropic hardening

Prior to any mechanical loading, the dislocations present in a metallic crystal are considered to be in equilibrium and form a network of dislocations, the so-called Frank network [Cottrell, 1957]. The density of dislocations present at this stage is typical of the order of 10^{10} to 10^{12} m^{-2} [Hull and Bacon, 2001]. During deformation, some of these dislocations are said to be mobile and others that are non-coplanar with previous ones are said to be immobile or quasi immobile. These dislocations thus obstruct the passage of the mobile dislocations during plastic deformation, producing junctions at the intersections between dislocations that may be more or less strong [Devincre et al., 2008]. In Fig. 1.9 a good observation of the pinning of mobile dislocations by immobile dislocations is illustrated. It is this type of hardening that is defined as isotropic hardening better known as forest hardening. The immobile dislocations are called forest dislocations, various junctions are possible from the interactions in between dislocations and are listed in § 1.5.2.1. During plastic deformation, dislocation density increases and more and more junctions can be created, thus leading to more hardening.

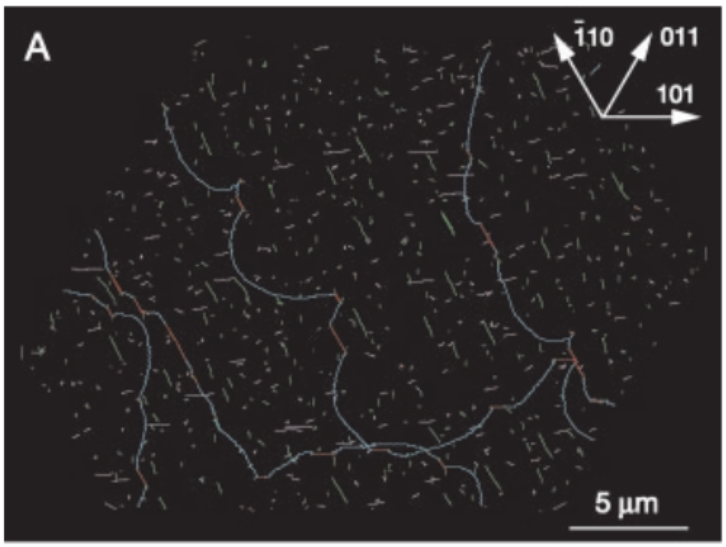

Figure 1.9: *Illustration of the mobility of a dislocation through forest dislocations crossing the slip plane of the mobile dislocation [Madec et al., 2003].*

The stress required to move a dislocation taking into consideration a forest dislocations density follows the given relationship

$$\tau_c^i = \alpha \mu b \sqrt{\rho_f} \tag{1.3}$$

With ρ_f the density of forest dislocations, μ the shear modulus, b the Burgers vector and α a coefficient called forest coefficient. It is important to note that the forest density can be composed of SSD and GND dislocations. Mobility of the dislocations in such mechanisms

is highly controlled by the line tension as it will be the force opposed to the motion of dislocation segments pinned at both ends. This type of hardening does not depend on the loading path and thus corresponds to isotropic hardening.

1.3.2 Kinematic hardening

Kinematic hardening is defined by a translation of the yield surface as opposed to the isotropic hardening leading to an increase of the yield surface [Chaboche, 2008]. Such mechanism depends on the loading path and is the result of dislocation accumulation for instance at the grain boundaries. One of the best-known consequences of this type of strain hardening is the Bauschinger effect. In tensile-compression tests, a different yield stress in compression is measured in comparison with the yield stress in tension after an initial tensile load [Proudhon et al., 2008]. This yield stress anisotropy is the direct effect of the change in the sign of dislocations while passing from tensile to compression loading within the microstructure, leading to a push-back motion of some of the accumulated dislocations at grain boundaries and to annihilations. This results in the diminution of the backstress reducing the yield stress in compression.

Grain boundaries are well well-known obstacles to dislocation motion thus leading, during the plastic deformation, to dislocation pileups. Dislocations piling up at grain boundaries are polarized, meaning that they have the same sign and thus exhibit a backstress on the emitting source of dislocations preventing it from emitting new dislocation loops. This backstress is thus the result of the summation of all the dislocations internal stress present in the pileup. These polarized dislocations are denoted as GND [Ashby, 1970]. The backstress is a long-range internal stress and it has been proved to strongly affect the mechanical behaviour of the material [Mughrabi, 1983; Kassner et al., 2013; Jiang et al., 2020; Jiang and Devincre, 2022]. Other sources of GND can be for example twin boundaries, precipitates or simply a heterogeneous internal stress distribution.

1.4 Intergranular plastic strain phenomena

1.4.1 Dislocation-grain boundaries interactions

Plastic deformation is not confined to the grains in which it occurs. During loading, it propagates from one grain to the next and thus has an intergranular component. With this in mind, it becomes important to discuss the various phenomena associated with this propagation, such as dislocations-grain boundaries interactions. Since the work of [Hall, 1951; Petch, 1953], it is well established that grain boundaries play an important role in the mechanical

properties of materials such as strengthening. It is generally admitted that grain boundaries represent a barrier to dislocation motion thus providing stronger resistance to plastic deformation than single crystals. To consider only this statement would be very limited as grain boundaries and dislocations are strongly interacting during plastic deformation as evidenced by experimental observations [Delaire et al., 2000; Miller, 2009; Abuzaid et al., 2012]. Grain boundaries are defects necessary to accommodate misorientation between crystals of a given thickness, two or three atomic layers. The dislocation-grain boundaries reactions are generally decomposed into three different mechanisms [Shen et al., 1988; Priester, 2020]: dislocation reaction with intrinsic grain boundary dislocation, dislocation dissociation in the grain boundary into a glissile and a sessile part and dislocation transmission to the other grain (see Fig 1.10). In the case of dislocation transmission, one should consider direct and

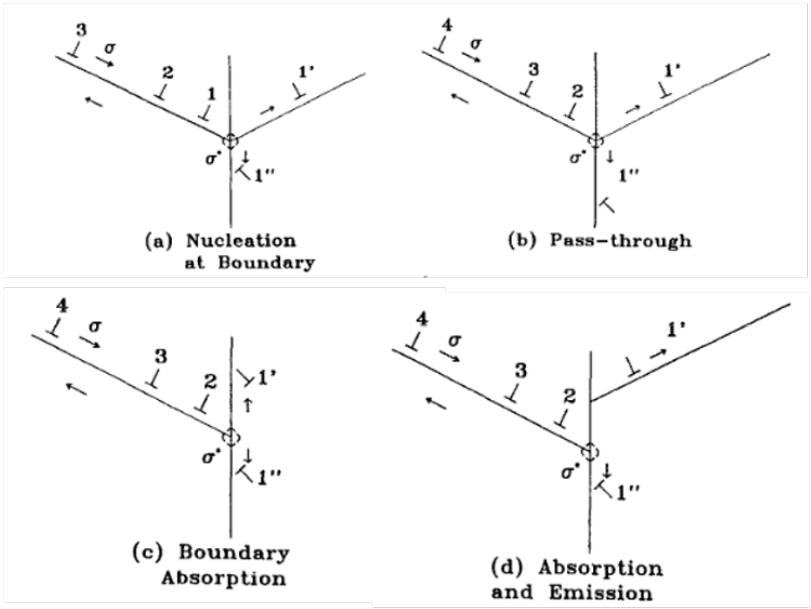

Figure 1.10: *Dislocation-grain boundary interactions models [Shen et al., 1988].*

indirect transmission. Direct transmission refers to very restrictive events that are rarely encountered in the deformation of polycrystalline materials [Lee et al., 1989] as they are only possible for low-angle grain boundaries. Main observed events refer to indirect transmission giving rise to dislocation pileup at the grain boundary and to the rise of a stress concentration at the head of the pileup [Eshelby et al., 1951; Hall, 1951; Petch, 1953; Hirth et al., 1983] but also to very localized rotations of the crystal lattice. These transmission events can be observed in the neighbouring grain (transmission) or in the same grain of the incoming dislocation (reflection) [Kacher and Robertson, 2012]. It is important to note that the image force linked to the presence of a grain boundary on a dislocation can be both repulsive and attractive.

1.4.2 The prediction of slip transmission events

Interactions between a dislocation and a grain boundary are only possible if they allow a reduction of the total energy of the system and are dependent on many factors like the misorientation, the stress, the dislocation type, the energy barrier and the stacking fault energy [Pan et al., 2021]. Over the years, many researchers have proposed criteria to predict slip transmission based on transmission electron microscopy (TEM) experiments through several approaches. In the pioneering work of [Livingston and Chalmers, 1957], a geometrical criterion is proposed, the N criterion. This criterion allows to define, knowing slip systems directions and normals, which slip system will be activated by transmission in the neighbouring grains. One of the limitations of this criterion is that it does not take into account the grain boundary plane orientation. Other authors like [Shen et al., 1986, 1988] work on the development of a new criterion taking into consideration the orientation of the grain boundary plane, well-known as the M factor. Both of these criteria are found to well predict slip transmission in selected configurations but are not fully predictive. The notion of the residual burgers vector that is known to have a strong impact on slip transmission is initially suggested by [Lim and Raj, 1985] and formalized by [Lee et al., 1989]. Such criterion is found to be consistent with molecular dynamic simulations [Koning et al., 2002; De Koning et al., 2003; Dewald and Curtin, 2006, 2007, 2011]. Other criteria offer geometrical and stress approach to the development of transmission criteria like [Seal et al., 2012; Bieler et al., 2014]. These criteria are numerous and generally refer to only one or two of the previously listed factors, and thus cannot be fully predictive. Many simulations in molecular dynamics studied interactions between one dislocation and a particular grain boundary. All these studies revealed the strong multi-factorial dependence of the dislocation and grain boundary interactions. An intensive review of such simulations is given in [Spearot and Sangid, 2014]. As expressed by the authors, there is still a lot to understand as most of the previous simulations were mainly focused on a small number of particular grain boundary structures.

In recent years, many authors have been interested in quantifying the critical stress values that define the resistance of a grain boundary in relation to its penetrability by dislocations. Numerous atomic-scale (MD) [Jin et al., 2006; Zhu et al., 2007; Chen et al., 2007; Jin et al., 2008; Chassagne et al., 2011; Zhu and Gao, 2012] and mesoscopic-scale (DDD) [Liu et al., 2012] simulations have shown that this depends strongly on the character of the dislocation and the orientation of the grain boundary. As stated in the review presented in [Hunter et al., 2018] and [Pan et al., 2021], the critical stress at which dislocations and grain boundaries interact ranges approximately from 400 MPa to 1 GPa.

1.4.3 Simulation of dislocation-grain boundaries interactions in DDD

Modelling the interaction phenomena between dislocations and grain boundaries at the mesoscopic scale through the DDD framework is not an easy task as mechanisms clearly depend on atomic scale consideration. Nevertheless, numerous attempts have been listed in the literature and more or less complex integration has been provided to incorporate slip transmission mechanisms in DDD simulations. Some work has been reported to model grain boundary as an array of dislocations [Lim et al., 2009, 2012; Liu et al., 2012], a dislocation wall based on theoretical works of [Read and Shockley, 1950; Sutton, 1995]. This type of integration provides good results and does not require explicit integration by a local rule implementation. Those studies are however limited to a low-angle grain boundary, and thus cannot address realistic polycrystalline materials. Other researchers like [Ahmed and Hartmaier, 2011; Quek et al., 2014] limited their study to 2D DD simulations to model grain boundary sliding, absorption, emission and transmission. In [Quek et al., 2014] the study offers the opportunity to see how dislocation can react with grain boundary and how it can change the surrounding stress field. As an example, dislocation activation in the neighbouring grain is able to relieve some part of the stress in the emitted grain. Exporting this model to the simulation of 3D polycrystalline aggregate with random orientation grain boundary looks very complex as the number of reactions is amplified and complexified. Other well-known models are the line tension model [Koning et al., 2002] used for example in [Zhou and LeSar, 2012] or the Resultant Dislocation Loop method [Tran et al., 2015; Tummala, 2016]. These models are also limited by physical implementation like in the line tension model where the Frank-Read source to trigger transmission needs to be placed beforehand. Most advanced simulations of the dislocation and grain boundary reactions are found to be for nodal DDD code [Cho et al., 2020; Bamney et al., 2022], where complex integration of some key mechanisms are realised.

1.5 The continuous description of crystal plasticity

1.5.1 Kinematic of crystal deformation

The kinematics of crystal deformation have been formalised by Mandel [Mandel, 1973] by the multiplicative decomposition of the strain gradient tensor $\underset{\sim}{\boldsymbol{F}}$. Following Mandel, the strain gradient tensor should be decomposed into two parts as illustrated in Fig. 1.11, a plastic transformation $\underset{\sim}{\boldsymbol{P}}$ and an elastic deformation $\underset{\sim}{\boldsymbol{E}}$. The plastic transformation refers to the motion of dislocations inside the materials thus leading to the shearing of one part of the crystal from another and the elastic deformation is the sum of a pure deformation

and rotation of the material lines. From this decomposition, an intermediate configuration is introduced, defining the material state after plastic deformation with a crystalline orientation identical to the initial one. We can write this decomposition as:

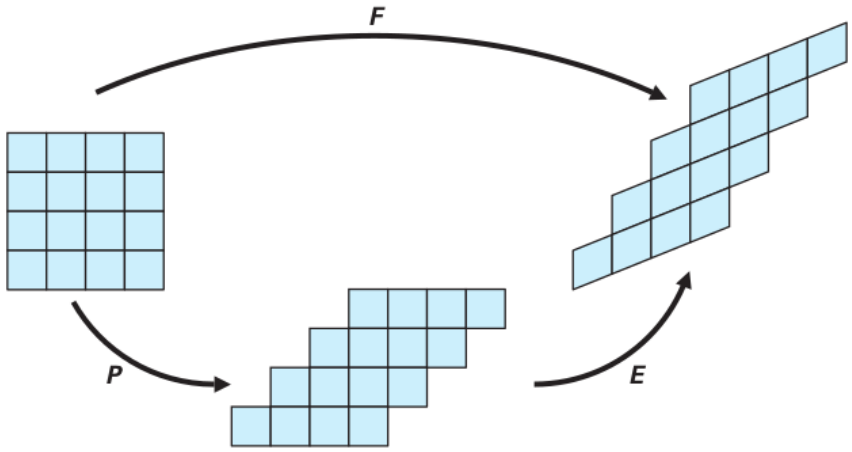

Figure 1.11: *The multiplicative decomposition of the deformation gradient* $\underset{\sim}{\boldsymbol{F}}$ *[Fivel, 2004].*

$$\underset{\sim}{\boldsymbol{F}} = \underset{\sim}{\boldsymbol{E}}.\underset{\sim}{\boldsymbol{P}} \tag{1.4}$$

From the polar decomposition of the elastic deformation gradient, one can have access to the elastic distortion $\underset{\sim}{\boldsymbol{V}}$ and rotation $\underset{\sim}{\boldsymbol{R}}$:

$$\underset{\sim}{\boldsymbol{F}} = \underset{\sim}{\boldsymbol{V}}.\underset{\sim}{\boldsymbol{R}}.\underset{\sim}{\boldsymbol{P}} \tag{1.5}$$

Under the hypothesis of small perturbation, one can rewrite the deformation $\underset{\sim}{\boldsymbol{F}}$ as:

$$\underset{\sim}{\boldsymbol{F}} \approx (\underset{\sim}{\boldsymbol{I}} + \underset{\sim}{\varepsilon}^e).(\underset{\sim}{\boldsymbol{I}} + \underset{\sim}{\omega}^e).(\underset{\sim}{\boldsymbol{I}} + \underset{\sim}{\varepsilon}^p + \underset{\sim}{\omega}^p) \tag{1.6}$$

With,

$$\underset{\sim}{\boldsymbol{R}} \approx (\underset{\sim}{\boldsymbol{I}} + \underset{\sim}{\omega}^e) \tag{1.7}$$

$$\underset{\sim}{\boldsymbol{V}} \approx (\underset{\sim}{\boldsymbol{I}} + \underset{\sim}{\varepsilon}^e) \tag{1.8}$$

And the additive decomposition of the total strain and rotation field :

$$\underset{\sim}{\varepsilon}^{tot} = \underset{\sim}{\varepsilon}^e + \underset{\sim}{\varepsilon}^p \tag{1.9}$$

$$\underset{\sim}{\omega}^{tot} = \underset{\sim}{\omega}^e + \underset{\sim}{\omega}^p \tag{1.10}$$

1.5.2 Single crystals models

The crystal plasticity models are an extension of the classical 3D plasticity models allowing to take into account the plastic deformation on each slip systems. Classical 3D plasticity models are based on the assumption of a homogeneous material and are generally based on phenomenological and experimental study of the macroscopic deformation. Crystal plasticity models allow to take into consideration crystal orientation dependencies and heterogeneities of the plastic deformation. They are thus well suited for describing the behaviour of polycrystalline aggregates composed of grains with various orientations. Such models suppose that each grain acts as a single crystalline material and that plastic behaviour is fully described by taking into account these three considerations [Besson et al., 2009], as in classical 3D plasticity models :

- A yield function : $f(\underset{\sim}{\boldsymbol{\sigma}}, ...)$
- A plastic flow rule : $\dot{\varepsilon}^p = ...$
- A hardening law : $\sigma_y = ...$

In the next paragraphs § 1.5.2.1 and § 1.5.2.2, a non-exhaustive description of phenomenological and physics-based crystal plasticity models is given, more detailed description of these models is given by [Tabourot, 1992; Roters et al., 2010].

1.5.2.1 Phenomenological models

Since the 70s, numerous authors have proposed various formulations for the constitutive equations of phenomenological crystal plasticity models. As an example, [Rice, 1971; Hutchinson, 1976; Peirce et al., 1982, 1983; Teodosiu et al., 1975] propose to describe the flow rule as classical power law depending on the resolved shear stress on the slip system τ^s and the critical resolved shear stress of the slip system τ_c^s defining the activation or not of the plastic flow. This relation is still very much used nowadays :

$$\dot{\gamma^s} = \dot{\gamma}_0 \left| \frac{\tau^s}{\tau_c^s} \right|^{\frac{1}{m}} \text{sign}(\tau^s) \tag{1.11}$$

with $\dot{\gamma}_0$ and m scaling parameters to fit the plastic strain evolution to target data. This relation is obtained thanks to the Orowan equation [Rauch, 1993], allowing to link $\dot{\gamma^s}$ with the mobile dislocation density ρ_m^s and dislocation mean velocity v:

$$\dot{\gamma^s} = \rho_m^s b v \tag{1.12}$$

Other formulations can be listed from the literature as for example [Cailletaud, 1992], introducing a kinematic hardening variable or [Cuitino and Ortiz, 1993]. As for the flow rule, other authors proposed a definition for the hardening law. The first development of such equations can be attributed to [Taylor, 1934] and [Mandel, 1965] that introduced the notion of the so-called interaction matrix (h_{su}) defined as follows:

$$\dot{\tau}^s = \sum_{u=1}^{n} h_{su} |\dot{\gamma}^u| \tag{1.13}$$

With this formulation, Mandel introduces the discrepancy between self ($s = u$) and latent ($s \neq u$) hardening for the first time in continuum mechanics. Under the scope of FCC metals, [Franciosi, 1985] propose a generalization of Mandel's interaction matrix in order to describe all the existing dislocation interactions. A list of these interactions is given below:

- a_1, self-hardening
- a_2, coplanar interaction
- a_3, Hirth lock
- a_4, collinear interaction
- a_5, glissile junctions
- a_6, Lomer lock

Identification of these coefficients values is not an easy task, in the past [Chang and Asaro, 1981] proposed an analytical expression to describe each coefficient under the scope of aluminium and copper single crystals. Nevertheless, since the development of DDD simulations, it has been possible to access more easily these values and to define them in a justified way [Devincre et al., 2008] revealing for example the unknown high contribution of collinear interactions on the hardening behaviour of single crystals.

1.5.2.2 Physics-based models

Physically based models include variables that allow to account for the phenomena related to the movement of dislocations during plastic deformation. These models involve the density of dislocations in the strain hardening laws and therefore require the addition of a relation allowing to vary this density system by system during the deformation. Many authors have worked on the development of physical strain hardening laws such as [Mecking and Kocks, 1981] who proposed the following relation :

$$\tau_\mu^s = \alpha \mu b \sqrt{\rho} \tag{1.14}$$

With τ_μ^s the critical resolved shear stress here defined as the isotropic hardening. This relation was further generalised by [Franciosi, 1985; Tabourot, 1992; Delaire et al., 2000] using the interaction matrix (a^{su}):

$$\tau_\mu^s = \mu b \sqrt{\sum_u a^{su} \rho^u} \tag{1.15}$$

Describing the density evolution can be done in many ways, nevertheless, one very common expression is the one provided by [Mecking and Kocks, 1981] allowing to describe density evolution with a multiplication and an annihilation term as expressed:

$$\dot{\rho}^s = \frac{1}{b}\left(\frac{1}{L^s} - g_c \rho^s\right)|\dot{\gamma}^s| \tag{1.16}$$

This expression uses the difference between a multiplication $(\frac{1}{L^s})$ and an annihilation term $(g_c\rho^s)$ to define the evolution of the dislocation density (ρ^s). The dislocations mean free path L^s which is expressed as follows with κ being proportional to the number of obstacles crossed by a dislocation before it is stopped :

$$L^s = \frac{\kappa}{\sqrt{\sum_{u=1}^{12} b^{su}\rho^u}} \tag{1.17}$$

In this equation, b^{su} refers to a second interaction matrix of the same form as a^{su} to describe dislocation density evolution. The annihilation term provided by g_c is material dependent and is physically linked to the average annihilation distance between two dislocations of opposite sign.

1.5.3 On the consideration of polycrystalline aggregates

The constitutive equations presented in previous paragraphs § 1.5.2.1 and § 1.5.2.2 are well suited to describe the behaviour of single crystals as they take into consideration the main source of strain hardening, forest interactions. Considering the behaviour of polycrystalline aggregate needs the addition of other contributions to the strain hardening, the kinematic hardening due to GND dislocations, as discussed in § 1.3.2. Consideration of GND dislocations and the properties of grain boundaries needs the introduction of length scales that are not intrinsically part of the classical FE models. Over the years, strong attention has been deployed to model the polycrystalline behaviour of materials across various considerations including for example Field Dislocation Dynamics, Continuum Dislocation Dynamics or higher order crystal plasticity model. As an example, strain gradient crystal plasticity models naturally introduce the consideration of GND dislocations through the Nye

tensor $\underset{\sim}{\boldsymbol{\alpha}}$ [Forest, 2008; Bargmann et al., 2010; Ma et al., 2006]:

$$\underset{\sim}{\boldsymbol{\alpha}} = -\text{curl}(\underset{\sim}{\boldsymbol{E}}^{-1}) = \text{curl}(\underset{\sim}{\boldsymbol{H}}^{e}) \tag{1.18}$$

With $\underset{\sim}{\boldsymbol{H}}^{e}$, the elastic part of the displacement gradient tensor. Such consideration can thus be used in the hardening law, adding a kinematic hardening contribution depending on $\underset{\sim}{\boldsymbol{\alpha}}$ as in the work of [Marano et al., 2021] leading to a modification of the flow rule:

$$\dot{\gamma}^{s} = \text{sign}(\tau^{s} - \chi^{s}) \left\langle \frac{|\tau^{s} - \chi^{s}| - \tau_{c}^{s}}{K} \right\rangle^{n} \tag{1.19}$$

with χ^{s} the kinematic hardening expressed as:

$$\chi^{s} = -B(\text{curl}(\text{curl}(\underset{\sim}{\boldsymbol{H}}^{p})) : \underset{\sim}{\boldsymbol{m}}^{s}) \tag{1.20}$$

with B containing the length scale associated with the GND density storage, $\underset{\sim}{\boldsymbol{H}}^{p}$ the plastic part of the displacement gradient and $\underset{\sim}{\boldsymbol{m}}^{s}$ the orientation tensor as defined in Eq 2.2.

Other contributions are reported in the literature about the model of the polycrystalline behaviour and in particular the role of grain boundaries across modification of the existing crystal plasticity constitutive equations. As an example in the PhD work of [Daveau, 2012], a modification of the classical Kocks-Mecking crystal plasticity equations is proposed by the introduction of a kinematic hardening contribution in the hardening rule. The expression of the kinematic hardening is based on DDD simulations for the evolution of the GND dislocation density law and is an extension of the unidimensional pileup model [Hirth et al., 1983] :

$$\chi^{s} = \beta cos(\theta)\mu b\sqrt{\rho_{GND}^{s}(x)\sqrt{x}} \tag{1.21}$$

with θ, the angle to the grain boundary plane with the slip plane and x the distance to the grain boundary. Values of x are tabulated at the beginning of the simulation and it is thus necessary to define for each integration point its distance to grain boundaries. Such a model shows good agreement in comparison with DDD simulations and is able to well reproduce the GND density storage close to grain boundaries regions. Another notable work is presented in [Haouala et al., 2020] where a different modification of the dislocation storage rule is proposed to consider GND storage depending on the distance to grain boundaries.

1.5.4 Intragranular plastic strain localization simulation

Crystal plasticity and FE simulations have been shown over the years to well reproduce the macroscopic quantities of a large variety of materials. When dealing with more local behaviour like the one of a grain embedded in an aggregate, these models show more difficulties

in reproducing local fields obtained experimentally for example in the case of plastic strain localization into slip bands. The simulation of plastic deformation localization phenomena is not an easy task using existing continuous modelling methods. In order to allow the transition from a homogeneous state to a heterogeneous state of deformation in bands, these models generally use softening laws to favour plastic slip in certain regions of the material. This type of softening law makes it possible to model the mechanical instability at the origin of the plastic deformation location and thus to allow a reduction in stress in these regions while allowing the plastic deformation to be persistent. Softening laws can be classically modelled by exponential functions with saturation as in [Marano et al., 2019]:

$$\tau_c^s = \tau_{ci}^s - \Delta\tau^s \left(1 - \exp\left(-\frac{\gamma_{cum}^s}{\gamma_0^s}\right)\right) \tag{1.22}$$

with, τ_{ci}^s the initial critical resolved shear stress and $\Delta\tau^s$ the maximum softening that can be reached on one slip system and γ_{cum}^s the cumulated plastic slip on slip system s.

In recent years, a great deal of work has focused on modelling such deformation microstructures in the context of irradiated material [Barton et al., 2013; Patra and McDowell, 2016]. Other work has also been carried out on the modelling of deformation in titanium alloys [Zhang et al., 2007, 2010] and HCP materials [Ahmadikia et al., 2021]. In some of these works, particularly those on irradiated metals, we can clearly see that it is possible to localize intragranular plastic deformation into slip bands using more or less sophisticated models. However, the vast majority of this work concerns idealised microstructures or 2D cases. Furthermore, with regard to the physical validity of these results, it is difficult to draw conclusions, as plastic deformation seems to be localized in a single slip band, which then propagates to the other grains.

Some authors, in order to model the formation of slip band structure, predefine the regions where plastic deformation takes place in a favourable manner, as in [Zhang et al., 2010] where a microstructure of bands is initially introduced. In this way, each of the bands has the same thickness and the inter-band distance is constant. Such modelling seems unfeasible from the point of view of realistic modelling of polycrystal behaviour and without explicit intervention in plastic deformation. The computation illustrated in Fig. 1.12 only provides a qualitative description of the plastic deformation into slip band in comparison with experimental data.

To the best of the author knowledge, the most advanced work is the one of [Marano et al., 2019, 2021] where the band microstructures formed inside the grains seem qualitatively consistent with what can be observed experimentally and does not require any explicit definition of the plasticity domain. However to date, this type of model has few intrinsically physical variables to describe mesoscopic scale effects such as interactions between dislocations, and as a result, no comparison with experimental data has been carried out yet, or

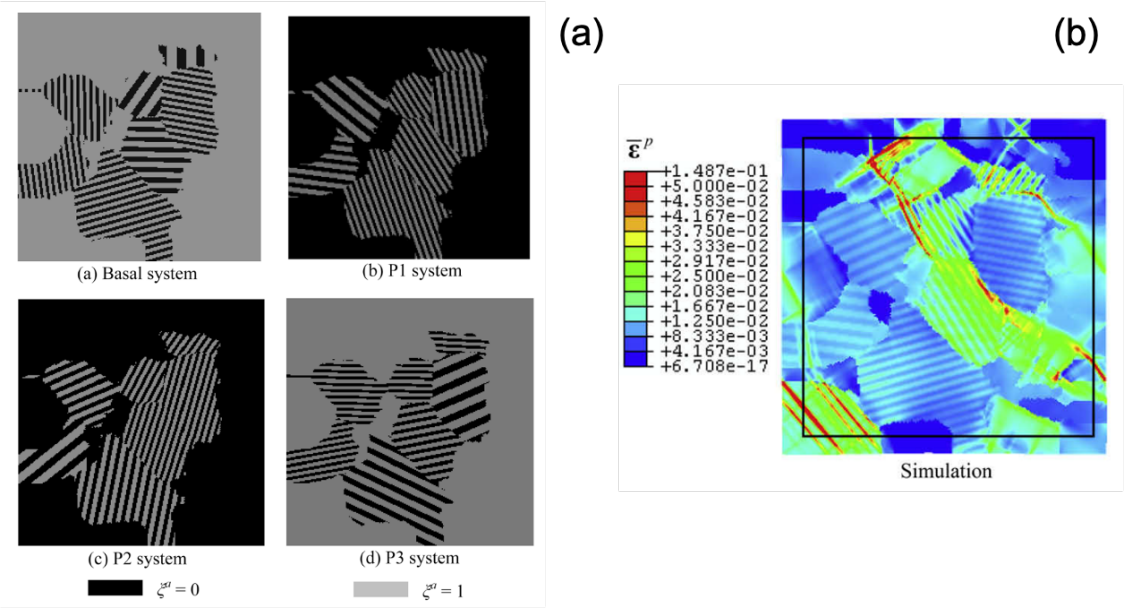

Figure 1.12: *Explicit definition of slip band plastic domain (a) for $\xi^a = 1$ on the basal and prismatic slip systems of the hexagonal structure as illustrated in [Zhang et al., 2010], result of the simulation at 2 % total strain (b).*

even sensitivity studies with respect to microstructure or material type. In addition, no discussions about the kinetics of slip bands formation is given in these articles. As illustrated in Fig. 1.13, plastic strain localization into slip bands is well reproduced and in comparison with results in other articles, slip bands can be numerous inside one grain as it is generally observed experimentally.

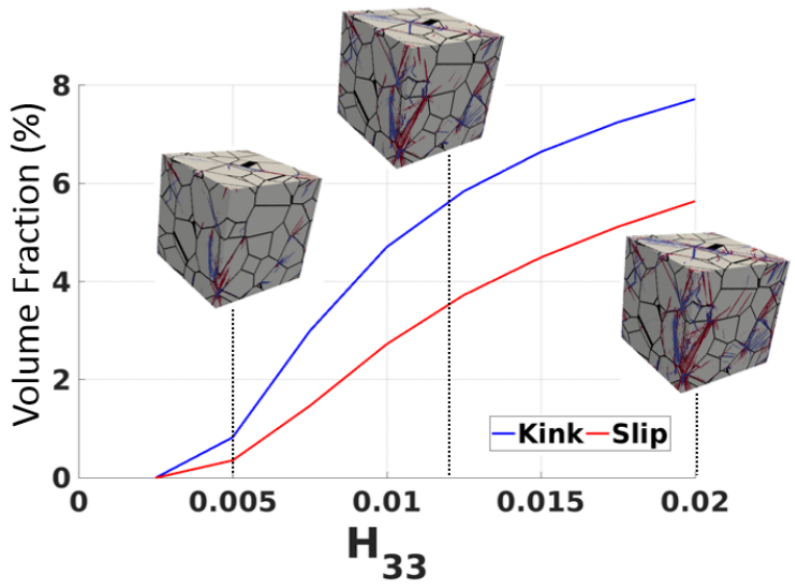

Figure 1.13: *Evolution of slip and kink band volume fraction as a function of the distortion component H_{33} for the simulation of a FCC 3D polycrystal with classical crystal plasticity model [Marano et al., 2019].*

The development of this type of modelling is therefore still an open subject on which many contributions need to be made. The results are encouraging and suggest potential for future developments in the coming years. The comparison of this type of model with DDD models could also lead to a better understanding of the physical mechanisms inherent to the localization of plastic deformation.

1.6 The discrete description of crystal plasticity

1.6.1 The Discrete Dislocation Dynamics (DDD)

Since the early 90s and the improvement of computational capacities, DDD has become an essential method for the study of physical mechanisms at the mesoscopic scale [Kubin, 2013]. In 1987, the very first 2D computation was launched by [Lepinoux and Kubin, 1987] allowing an intensive study of the collective properties of dislocations. Since then, various codes rapidly emerged like *'microMegas'* [Devincre et al., 2011], the code developed at the LEM, as well as 3D computations. Over the years, DDD has offered key information about physical mechanisms linked to the dislocation microstructure able to enrich continuous model [Madec et al., 2003; Daveau, 2012; Jiang, 2019; Marian et al., 2020]. In the following paragraphs, a non-exhaustive description of the DDD simulation method is presented, only the information necessary to understand this manuscript are listed. For more details about the DDD framework, the reader is referred to [Devincre et al., 2011; Kubin, 2013].

1.6.1.1 Line description of dislocations

In *'microMegas'*, the physical space is described as an elastic continuum where the dynamic is solved at integration points based on a homothetic lattice, this type of code is called lattice-based. Dislocation segments are allowed to move on predicted slip planes separated by a given distance. Such distance is not the real interplanar distance as it would lead to many potential configurations for segment position. Various types of line descriptions exist for the description of dislocation loops in DDD codes. The first DDD codes used the edge-screw model, a dislocation line is only represented thanks to a pure edge and pure screw set of segments [Devincre and Condat, 1992]. Generalization of this concept leads to the mixed model, a segment of mixed character is added to better model line curvature and mobility [Devincre et al., 2001]. The elementary vectors used for dislocation description are schematically given in Fig. 1.14, this kind of configuration is the one used in *'microMegas'*.

Other DDD codes used nodal-based discretization [Weygand et al., 2002; Arsenlis et al., 2007] allowing a better description of line curvature and some physical mechanisms like glissile and multi-junctions.

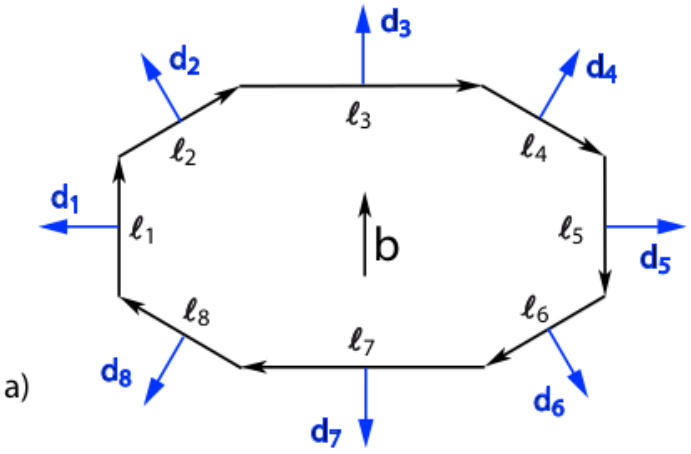

Figure 1.14: *Representation of the elementary vectors used per slip system to discretize dislocation lines [Devincre et al., 2011]. The screw, mixed and edge components are represented.*

1.6.1.2 Dislocation mobility

Dislocation mobility is ensured by the computation of the effective stress applied on each segment, the stress is computed on the centre of segments used for the discretization of the dislocation loops. Stress computation is the main algorithmic step, the most computational consuming in DDD codes and thus needs to be parallelized [Devincre, 2005]. The origin of the stresses on a dislocation segment can be two-fold:

- The external loading : $\underset{\sim}{\boldsymbol{\sigma}}_{app}$
- The internal loading : $\underset{\sim}{\boldsymbol{\sigma}}_{int}$

In DDD codes, without any coupling with a FEM computation, either by the Superposition Principle or by the Discrete Continuous Model, the external loading is homogeneously defined in the simulation volume and evolves following phenomenological laws. The internal loading is due to the effect of the presence of the dislocations in the volume leading to attractive or repulsive force in between dislocations. Solutions for such loading are well known under the hypothesis of infinite and isotropic medium [De Wit, 1967]. Such relations have been modified by [Devincre, 1995] to be numerically more efficient. Other stresses are added to this balance of stresses, the image stress (τ_i), the line-tension stress (τ_{TL}) and the lattice friction stress (τ_f). The force exerted on a dislocation segment is thus defined by the Peach-Koehler force :

$$\underline{f}^{PK} = (\underset{\sim}{\boldsymbol{\sigma}}).\underline{b} \wedge \underline{l} \tag{1.23}$$

with $\underline{l}$ the tangent vector the dislocation line. The mobility is generally defined as follows for FCC structures [Philibert, 1979]:

$$v^i = \frac{\tau_{eff} \times b^i}{B} \tag{1.24}$$

with B a material dependant parameter known as the viscous drag coefficient and τ_{eff} the effective resolved shear stress from the previous balance :

$$\tau_{eff} = \tau^{PK} + \tau_{TL} + \tau_i + \tau_f \tag{1.25}$$

The line-tension stress is analytically defined by [Gomez-Garcia et al., 1999] and depends on the angular description of the dislocation line.

1.6.1.3 Local rules

In DDD codes, local rules are used to model via analytical relationships, dislocations behaviour at the atomistic scale, like core properties. Near core regions, linear elasticity is no longer valid and thus specific computations should be made to take these effects into account. Main local rules are used to model the cross-slip, the dislocations mobility or the dislocations reactions. A description of such rules is given in [Devincre, 2005] for the DDD code *'microMegas'*. In this part, we will only be focused on the description of the cross-slip mechanisms in DDD as it will be of major interest for the rest of the manuscript.

The cross-slip is the mechanism by which screw dislocations can move from an initial slip system, the primary slip system to a new slip system of identical Burgers vector, the deviate slip system. These deviated dislocations can also come back to their initial slip system, the double cross-slip as illustrated in Fig. 1.15.

A theoretical description of the cross-slip is given by [Friedel, 1957; Escaig, 1968b], allowing implementation in DDD codes. Following these results, local rules have been introduced to model the effect of the cross-slip at the mesoscopic scale [Kubin et al., 1992; Devincre, 1996]. Modelling cross-slip can be based on the computation of a probability defined by an Arrhenius law :

$$P(l) = \beta \frac{l}{l_0} \frac{\Delta t}{\Delta t_0} \exp\left(\frac{-W}{\kappa_B T}\right) \tag{1.26}$$

where $l_0 \approx 1 \mu m$ and $\Delta t_0 \approx 1$ ns, are scaling factors, κ_B the Boltzmann constant, T the temperature, β a parameter adjusted to experiment and W defines the activation energy variously expressed for a mobile and immobile dislocation segment [Kubin et al., 1992; Sansal, 2007] :

$$W = V(|\tau^g_{int}| - \tau_{III}) \tag{1.27}$$

$$W = V(|\tau^{cs}_{eff}| - \tau_{III}) \tag{1.28}$$

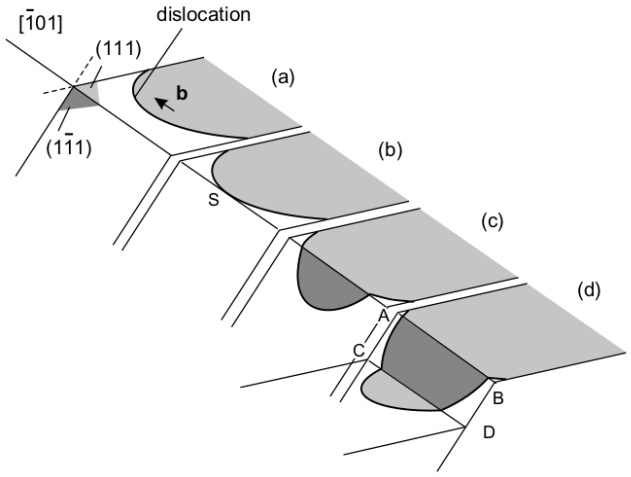

Figure 1.15: *Schematic representation of the cross-slip and double cross-slip mechanism of screw dislocations character [Hull and Bacon, 2001].*

where τ_{III} defines the activation stress for cross-slip in three stages of single crystal tensile curves, $\tau^{(g)}$ the resolved shear stress on the glide plane and $\tau^{(cs)}$ the resolved shear stress on the cross-slip plane. In addition to the probability computation, other conditions should be verified in order to activate cross-slip in DDD simulations :

- The screw segment should be part of a dislocation line whose angle is with the Burgers vector is smaller than a fixed value (classically fixed to $\pm$ 5°);
- The ratio noted α, between the resolved shear stress on the deviated and on the primary slip system, should be higher than a fixed value;
- The computed probability should be higher than a randomly generated number.

Following these rules, cross-slip is modelled as a stochastic event.

1.6.1.4 Local computation of plastic slip increment

In the scope of identification of plastic strain localization phenomena, it is necessary to locally define the plastic slip during the whole loading on each of the slip systems. Such computation can be performed following the relationship:

$$\partial\gamma^i = \frac{b_i \times \partial S^i}{V} \tag{1.29}$$

The plastic slip increment $\partial\gamma^i$ due to one segment i is defined as the swept area ∂S^i divided by the volume of the domain V. A particular post-processing is applied in our DDD simulations to compute plastic slip in every point of the 3D space, by a voxel tessellation as represented

in Fig. 1.16 for one voxel. Following this consideration, V is the volume of the voxel and in the manuscript plastic slip values computed on each voxel are denoted γ^s_{vox}. Defining the size and position of each voxel, it is then possible to access to more or less local description of the material point plastic state. In this manuscript, voxels are parallelepipedic of size 1.38 µm ×1.32 µm ×1.5 µm.

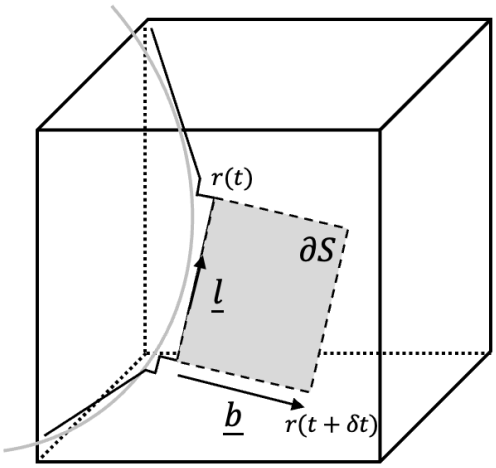

Figure 1.16: *Schematic representation of the motion of one dislocation segment use for the discretization of the dislocation line (grey curve) inside a voxel element. Initial $r(t)$ and final $r(t+\delta t)$ positions of the dislocation segment are computed from the balance of forces expressed on the dislocation segment. The plastic slip increment is then calculated from the swept area ∂S and the volume of the voxel V.*

1.6.2 Intragranular plastic strain localization simulation

Localization into slip bands has been widely studied through DDD simulations in the case of metals under irradiation, cyclic loading and in the particular case of alloys and precipitate shearing as these conditions are known to favour localization. In this subsection, a non-exhaustive list of these simulations is given to show the ability of DDD simulations to reproduce key physical mechanisms and dislocation reactions involved in plastic strain localization mechanisms.

As described in § 1.2.2.1, irradiation is known to produce strong localization patterns by the formation of clear bands and dislocation channelling. DDD simulations have been used to better understand the formation of clear bands by studying the interactions between dislocations and crystalline defects induced by irradiation. These studies allow to well represent these mechanisms for various materials as reported for example in [Ghoniem et al., 2001, 2002] as results are in close agreement with experimental observations. DDD simulations allow to better understand and represent the physical mechanisms involved in clear band formation but also to study a variety of interactions that can bring more knowledge about

these interactions as in [Onimus et al., 2021]. From this article, authors listed interactions between a dislocation of various characters and a loop and show that reaction processes can either lead to pinning, partial clearing or total clearing of the defect as illustrated in Fig. 1.17.

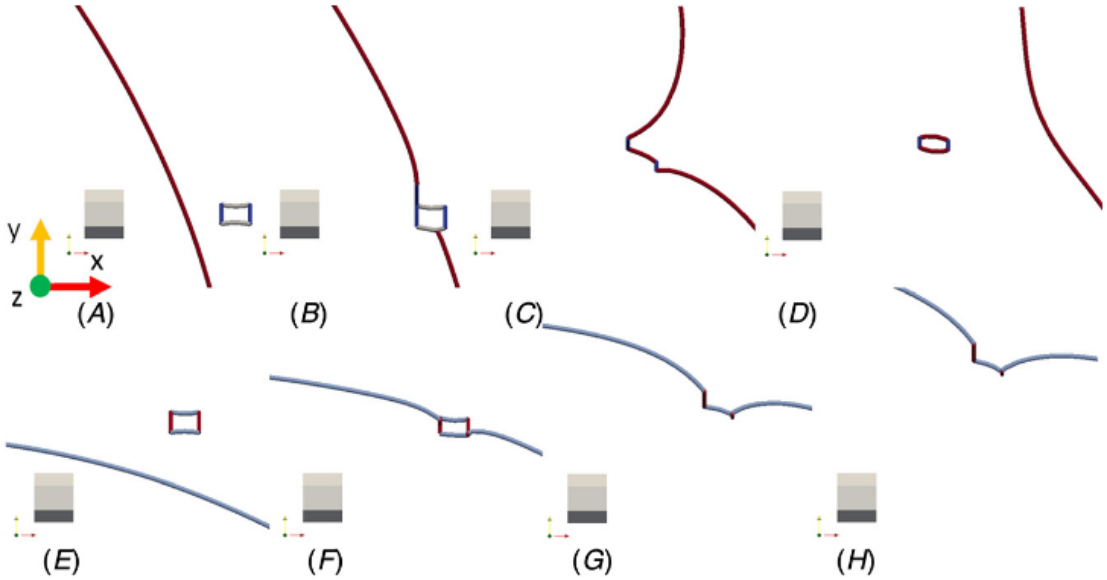

Figure 1.17: *Sequence showing the interaction between a mixed dislocation and a loop for various angular configuration [Onimus et al., 2021]. Sequence (A)-(D) shows a strong pinning and no clearing process while sequence (E)-(H) highlights no pinning and a clearing of the crystalline defect by the dislocation glide.*

Other authors work on more massive simulations as in [Arsenlis et al., 2012] where interest is taken on the density of defect and its effect on slip localization or in [Cui et al., 2018a] where they demonstrate the preponderant role of the cross-slip on the formation of clear bands and localization bands. As a logical extension of these results, DDD simulations have also been utilized to study the suppression of localized plastic flow [Cui et al., 2018b] in the scope of reliable service of irradiated materials by the deep comprehension of microstructural mechanisms.

Extensive research about the simulation and comprehension of PSB formation under cyclic loading have been reported through the years [Déprés et al., 2015; Hussein and El-Awady, 2016; Erel et al., 2017; Meng et al., 2021]. In these studies, DDD has been proven to well reproduce that kind of localization and for various materials. As reported in [Meng et al., 2021] DDD simulations well represent the saturation process associated with the formation of PSB under cyclic loading as illustrated in Fig. 1.18. In this illustration the saturation process is well reproduced as since the 26^{th} cycle, all the plastic deformation is produced through the same bands, positions and thicknesses of the PSB are almost invariant.

In this work, the role of the cross-slip has also been discussed through a comparison

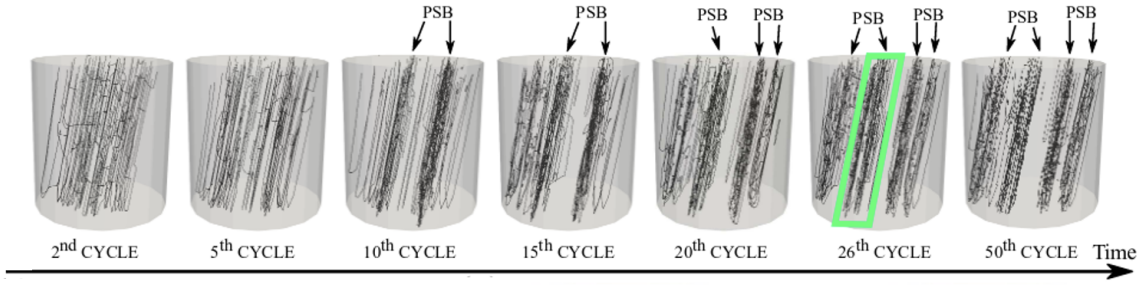

Figure 1.18: *Evolution of the dislocation microstructure for copper single crystal simulation [Meng et al., 2021]. Sequence of the loading cycle are taken at maximal deformation amplitude.*

between AISI 316L stainless steel and copper single crystals. Both materials do not have the same probability of cross-slip due to the difference in their stacking fault energy thus leading to different localization patterns. In the case of copper, more slip bands are formed with also relatively larger thicknesses. In the work of [Déprés et al., 2015; Erel et al., 2017] more attention is paid to the microstructure evolution inside the PSB during deformation through the formation of dislocations dipoles, tangles or prismatic loops. A precise description of this evolution is also provided in the thesis of C. Depres [Déprés, 2004].

These researches show the potential of DDD simulations for understanding localization mechanisms on a mesoscopic scale which, unlike a continuous model such as the CPFEM, naturally reproduces a large proportion of the interactions that take place during plastic deformation, as well as localization in the form of slip bands.

1.7 Solving the Boundary Value Problem (BVP)

As previously discussed, the stress field associated with the presence of a dislocation segment in an elastic media is analytically defined and only valid under the assumption of isotropic elasticity and for an infinite continuum. Thus precisely defining the boundary conditions associated with internal boundaries such as grain boundaries is not possible only considering a DDD framework. Over the years, solutions were formalised and developed to solve the so-called Boundary Value Problem (BVP) imposed by the definition of the DDD problem. Such solutions are based on a coupling between DDD and a Finite Element solver for example in order to solve the mechanical equilibrium and to access a precise description of the boundary conditions. Two main coupling methods are generally used to address this issue, the Superposition Principle (SP) and the Discrete-Continuous Model (DCM).

1.7.1 The Superposition Principle (SP)

One way to solve the BVP is to consider that the solution of the problem can be decomposed into two sub-problems, better known as the Superposition Principle [Van der Giessen and Needleman, 1995]. According to it, the problem is able to be decomposed into an infinite domain sub-problem composed of dislocations and external boundary conditions and a finite domain with corrected boundary conditions. Thus, the SP problem can be written like :

$$\mathcal{P} = \mathcal{P}^{FE} + \mathcal{P}^{S} \tag{1.30}$$

With $\mathcal{P}^{FE}$ the finite domain problem and $\mathcal{P}^{S}$ the infinite domain problem. It should be noted that with this approach, the strain and displacement fields are known at the boundaries only. A schematic representation of the SP model is given in Fig. 1.19 showing the decomposition into two sub-problems. The first sub-problem gives the solution $(\tilde{\mathbf{u}}, \sigma^{\infty})$ of the infinite domain containing dislocations and the second sub-problem the solution $(\hat{\mathbf{u}}, \hat{\sigma})$ of the finite domain without dislocation. This second sub-problem is solved by a FE code and is used to correct boundary conditions taking into consideration the solutions of the first one.

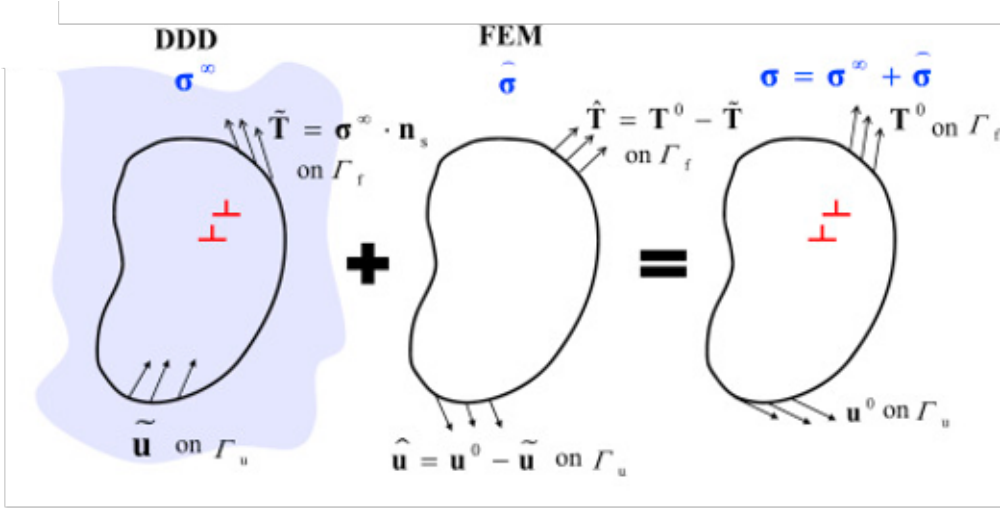

Figure 1.19: *Illustration of the Superposition Principle for a coupling DDD/FEM [Zhuang et al., 2019].*

1.7.2 The Discrete-Continuous Model (DCM)

The other generally used model to solve the BVP is the Discrete-Continuous Model (DCM) first proposed by [Lemarchand et al., 2001] based on the work of [Mura and Mura, 1987]. This later article states that dislocations can be seen as inclusions generating a uniform plastic strain field, the eigenstrains. Eigenstrains are generally used to introduce residual strains inside a given material with no external loading necessary. The theory of

eigenstrains generally relies on linear elasticity under the hypothesis of small perturbation leading to the additive decomposition of the total strain field :

$$\underset{\sim}{\boldsymbol{\varepsilon}} = \underset{\sim}{\boldsymbol{\varepsilon}}^{e} + \underset{\sim}{\boldsymbol{\varepsilon}}^{p} \tag{1.31}$$

With ε^p being the eigenstrain field leading to the following stress inside the material :

$$\underset{\sim}{\boldsymbol{\sigma}} = \underset{\approx}{\boldsymbol{C}} : (\underset{\sim}{\boldsymbol{\varepsilon}} - \underset{\sim}{\boldsymbol{\varepsilon}}^{p}) \tag{1.32}$$

With $\underset{\approx}{\boldsymbol{C}}$ the fourth-order elastic tensor. Using this kind of coupling method does not need any correction as in the SP model as the eigenstrains generate eigenstresses that directly interact with all the boundaries of the FE problem. A precise description of the latest formalism used for the DCM is given in [Jamond et al., 2016] introducing a new method to better deal with the short-range interactions. In a general way, a DCM model is composed of two main procedures, the regularisation procedure and the interpolation procedure. On one hand, the regularisation allows to transmit the discrete information of plastic slip computed from the DDD simulation to a continuous information usable for FE simulation and is the most difficult task. On the other hand, the interpolation allows to define the total stress σ that should be applied in the DDD part of the code to compute dislocations mobility. A detailed description of these procedures can be found in [Vattré et al., 2014; Jamond et al., 2016; Korzeczek, 2017].

The DCM can be seen as an extension of the superposition method by the addition of two sub-problems to solve the BVP without introducing extra computational costs. In addition, strain and displacement fields are defined in the whole volume which is not the case for the superposition method and for a large number of segments, computations appear to be faster with the DCM. Nevertheless, the DCM is more difficult to implement than the superposition method.

Chapter II

The effect of the polycrystalline microstructure

Résumé :

Dans ce chapitre, nous présentons les résultats obtenus à propos de l'étude du rôle de la microstructure polycristalline sur le comportement plastique intragranulaire. Conformément à ce qui est présenté dans le chapitre précédent, l'influence de la microstructure polycristalline et notamment les incompatibilités de déformation élastique semblent jouer un rôle prépondérant sur les premiers événements de localisation. Ainsi, nous nous proposons d'étudier dans un premier temps et de manière statistique l'évolution du comportement élastique intragranulaire par le biais de simulations FEM et pour un grain de référence sélectionné aléatoirement dans un agrégat polycristallin complet. Au cours de ces différentes études statistiques, les conditions de simulations sont modifiées afin de mieux comprendre le rôle joué par les interactions avec les grains voisins, à travers notamment la modification des orientations cristallines ou encore la forme et la taille des grains. Les résultats obtenus permettent notamment de quantifier les niveaux d'hétérogénéités intragranulaires et de les lier à la présence de régions de concentrations et de déplétions de contraintes. Un critère est proposé sur la base de ces résultats et permet de classifier les grains ou configurations les uns par rapport aux autres. Ce critère dont l'objet est de sélectionner le grain plastifiant en premier au sein de l'agrégat et dont le niveau d'hétérogénéité intragranulaire est élevé permet notamment les premières simulations d'un comportement plastique localisé via des simulations de DDD sans le mécanisme de cross-slip. Nous montrons au cours de ce chapitre que la région de concentration de contrainte, bien que localisée dans des régions confinées du grain permet l'apparition d'une activité plastique intragranulaire intense et localisée.

Contents

2.1 Introduction

In this chapter, we look at the mechanisms by which intragranular plastic strain is localized in relation to the polycrystalline microstructure. In the literature review given in § 1.2.4, it was shown that interaction zones (grain boundaries, triple junctions and quadruple nodes) could play a major role in the appearance of intense plastic deformation events in the form of slip bands. These particular regions are the site of significant variations in the intragranular mechanical behaviour and favour the appearance of a heterogeneous state of stress and strain. According to the hypothesis of the first grain that plastifies within an aggregate, we can study the role of these incompatibilities on the intragranular plastic behaviour. Following this hypothesis, we only consider elastic strain incompatibilities due to differences in stiffness between grains with various crystalline orientations. The role of plastic strain incompatibilities on the intragranular plastic behaviour will be discussed in Chapter V.

Mechanisms promoting incipient plastic strain localization in intense slip bands at the grain scale during monotonic tensile deformation are investigated. First, the two computational methods used, i.e. the Finite Element Method (FEM) and the Discrete Dislocation Dynamics (DDD) simulation, are briefly presented in § 2.2. Then, the behaviour of a reference grain, part of a periodic polycrystal, is studied in a linear elastic framework using FEM in a systematic way according to the aggregate microstructure (crystalline orientations and shapes of grains) in § 2.3.1. With this we will highlight the effect of elastic strain incompatibility, trying to better understand the origin of the heterogeneity of intragranular stress and strain fields. In addition, a criterion to identify within an aggregate the most favourable grain for plastic strain localization is proposed in § 2.3.3. This criterion is proposed on the basis of FEM calculations, which means that statistical trends can be obtained with much shorter calculation times than with the DDD. Lastly, DDD simulations are performed to elucidate the role of elastic strain incompatibilities on dislocation microstructure evolution in § 2.4. The outcome of these simulations highlights more intense slip activity, even at low plastic strain levels, in the regions with larger stress concentrations.

2.2 Computational methods

As stated in the introduction section, we propose to study the problem of intragranular plastic strain localization through two simulation methods, FEM and DDD. It is commonly accepted that these two simulation methods are complementary since FEM provides a good description of the complex boundary conditions of a polycrystalline aggregate and DDD offers a more justified description of plastic mechanisms. In addition, FEM allows computing the

polycrystalline behaviour of representative aggregates (with several grains) [Lim et al., 2014; Choi et al., 2014; Pokharel et al., 2014] whereas DDD simulations are more limited to the modelling of one or few grains due to limits in computational capacities. In this work, to take advantage of both methods, a weak coupling between FEM and DDD is proposed. FEM computations will be used to model the behaviour of all grains in the aggregate during the elastic part of the loading, thus providing necessary boundary conditions for the DDD computation. One grain of the aggregate is then selected to run DDD simulations to model its plastic behaviour. A detailed description of simulation parameters and main characteristics is given in § 2.2.1 and § 2.2.2.

2.2.1 FEM simulations

Finite Element simulations were run using the *Z-set* software package jointly developed by Ecole des Mines de Paris and Onera [Zset, 2022]. Polycrystalline aggregates have been generated and meshed with c3d10 elements by the open source software *Neper* [Quey, 2019], well suited for building up Voronoi and Laguerrre tessellations. In order to explore the intragranular elastic behaviour in a systematic way, three distinct series of simulations of polycrystalline aggregates were performed. The first series of simulations (series 1) considers a change in the crystalline orientation of neighbouring grains relative to a reference grain chosen in the aggregate. For this reference grain, the crystalline orientation remains unchanged for all simulations. Referring to the notations in Fig. 2.1, this means changing the neighbouring grains' matrices $\underset{\sim}{\boldsymbol{P}}_j$ while the grain orientation matrix $\underset{\sim}{\boldsymbol{P}}_i$ is fixed. The second series of simulations (series 2) considers the modification of the reference grain crystalline orientation while orientations of its neighbouring grains are fixed. Again referring to Fig 2.1, this means changing the grain orientation matrix $\underset{\sim}{\boldsymbol{P}}_i$ while the other orientation matrices $\underset{\sim}{\boldsymbol{P}}_j$ are fixed. Finally, the third series of simulations (series 3) is used to study the role of the morphology (grain size, aspect ratio) while the reference grain crystalline orientation is fixed. Series 1 and 2 contain two hundred draws, while series 3 contains only one hundred draws. In each series, quantities of interest like heterogeneity, stresses, and strains are computed.

Simulation parameters are also listed in Tab. 2.1 and are identical for all five hundred simulations. Elastic constants for pure nickel can be found in [Shuvalov et al., 1988]. The aggregates constructed are elementary periodic units that can be repeated ad infinitum, so the boundary conditions used are periodic boundary conditions, allowing us to avoid boundary effects. At each Gauss point, the resolved shear stress is computed for each slip system s thanks to the Schmid law :

$$\tau^s = \underset{\sim}{\boldsymbol{\sigma}} : \underset{\sim}{\boldsymbol{m}}^s \tag{2.1}$$

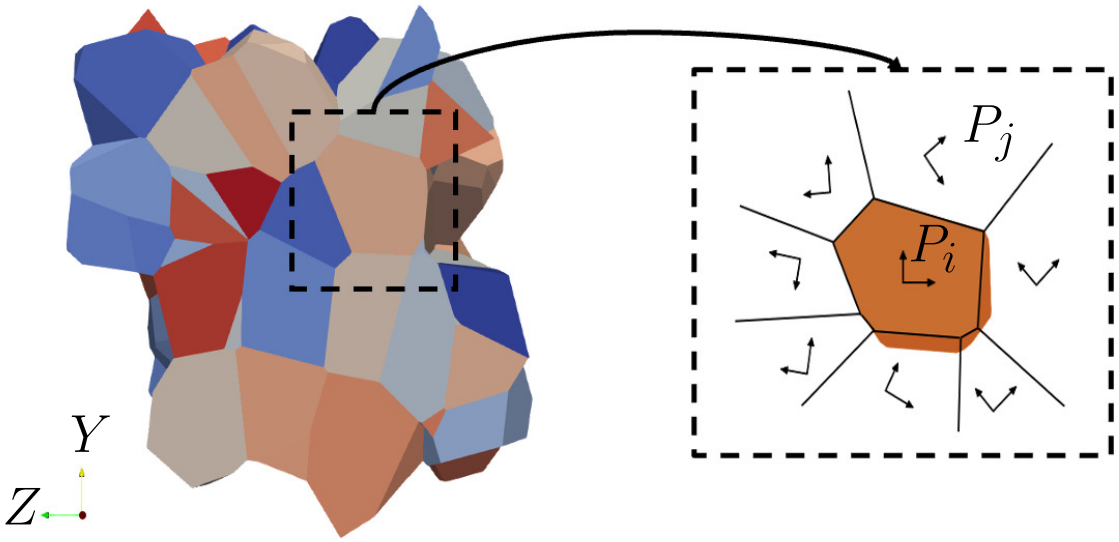

Figure 2.1: *Schematic of the simulations associated with series 1 and 2 used in the present work. On the left side is the reference periodic aggregate used in series 1 and 2. On the right side, the definition of* $\underset{\sim}{\boldsymbol{P}}_i$ *and* $\underset{\sim}{\boldsymbol{P}}_j$*, the orientation matrix of the reference grain (in orange) and the orientation matrices of the neighbouring grains, respectively. In the first simulations series, the orientations of* $\underset{\sim}{\boldsymbol{P}}_j$ *while keeping* $\underset{\sim}{\boldsymbol{P}}_i$ *constant are randomly changed. In the second simulations series, the orientation of* $\underset{\sim}{\boldsymbol{P}}_i$ *while keeping* $\underset{\sim}{\boldsymbol{P}}_j$ *constant is randomly changed. Lastly, in the third simulations series, one hundred aggregates with different grain morphologies are randomly defined while keeping the reference grain orientation constant.*

With $\underset{\sim}{\boldsymbol{\sigma}}$ the Cauchy stress tensor and $\underset{\sim}{\boldsymbol{m}}^s$ the orientation tensor defined as :

$$\underset{\sim}{\boldsymbol{m}}^s = \frac{1}{2}(\underline{n}^s \otimes \underline{l}^s + \underline{l}^s \otimes \underline{n}^s) \tag{2.2}$$

let us note $\underline{n}^s$ the normal to the slip plane and $\underline{l}^s$ the slip direction.

To the best of the author's knowledge, a systematic analysis of the role of the microstructure on the intragranular elastic loading has never been reported, especially considering local values. Few authors have studied the polycrystalline elastic behaviour statistically but focused on average stress values variation and not with the scope of plastic strain localization phenomena [Bretin et al., 2019; Pilvin et al., 2017; Pourian et al., 2014].

2.2.2 DDD simulations

DDD simulations were run with the 'microMegas' code [Devincre et al., 2011] and using a kind-like superposition principle [Van der Giessen and Needleman, 1995; Fivel et al., 1996] as already discussed. This solution is preferred to other methods like the discrete-continuous model [Vattré et al., 2014; Jamond et al., 2016] for reasons of simplicity. The heterogeneous stress applied inside the simulated grains ($\underset{\sim}{\boldsymbol{\sigma}}_{FEM}$) is the sum of a mechanical loading cor-

Aggregate size (µm)	**Anisotropy coef.**	**Mean grain size (µm)**
95 × 95 × 95	2.51	24
$\boldsymbol{C_{11}}$ **(GPa)**	$\boldsymbol{C_{12}}$ **(GPa)**	$\boldsymbol{C_{44}}$ **(GPa)**
246.5	147.3	124.7
Burgers vector (m)	**Loading**	**Series 1†**
2.489×10^{-10}	$\langle \varepsilon_{zz} \rangle = 0.1$ %	$\dot{\underset{\sim}{\boldsymbol{P}}}_i = 0$, $\dot{\underset{\sim}{\boldsymbol{P}}}_j \neq 0$
Series 2†	**Series 3***	**Draws per series**
$\dot{\underset{\sim}{\boldsymbol{P}}}_i \neq 0$, $\dot{\underset{\sim}{\boldsymbol{P}}}_j = 0$	Morphology	200(†)/100(*)

Table 2.1: *Simulation parameters for the FEM computations presented in this chapter.*

responding to the tensile test in the Z direction (see Tab. 2.1) and the stress field induced by the incompatibility of elastic deformation between the grains, part of the polycrystalline aggregate. The stress field $\underset{\sim}{\boldsymbol{\sigma}}_{app}$ is calculated directly with the FEM simulations presented in § 2.2.1. The simulated grain in DDD is supposed to be surrounded by fully linear elastic grains, this hypothesis allows for faster computations as the initial $\underset{\sim}{\boldsymbol{\sigma}}_{FEM}$ can be updated by applying a pre-factor. This process is further described later in this section. Such a hypothesis is supposed to be valid as the total plastic deformation calculated during DDD simulations is small (less than 0.001). In addition, the simulated grain is supposed to be the first one to trigger plasticity in the aggregate, this point is better detailed in § 2.3.3.

The initial microstructure is made of a random distribution of Frank-Read sources. That kind of initial microstructure is known to describe well the plastic behaviour of large grains in DDD simulations [Jiang et al., 2021]. The reason the use of Frank-Read sources is preferred in this work is motivated by the desire to consider low dislocation density in the initial configurations. Indeed, the dislocation density is increasing very fast in such simulations, and for numerical reasons, it is useful to start the computations with a low number of dislocation sources. With low dislocation density, if one uses configurations made of relaxed loops, the number of junctions anchoring the dislocation network is low and may not be sufficient to stabilize the few dislocation sources in the volume of the grain. This well-known problem is even amplified in this work focusing on the plasticity of polycrystals. In such types of materials, the flow stress is high enough to result in the destruction of all the formed junctions during the relaxation process. Frank-Read sources are described by their length, their character, and the fact that they are pinned at both ends by infinitely rigid pinning points [Foreman, 1967]. For our simulations, we impose initial dislocation segments of length 5 µm, the initial dislocation density is $\rho^s_{ini} = 1 \times 10^{11}$ m^{-2}, which correspond to a set of 30 Franck-Read sources per slip systems and the grain boundaries facets are impenetrable

barriers for dislocations. All simulations are made at a constant plastic strain rate $\dot{\varepsilon}^p_{zz}$ equal to 200 s^{-1}.

To impose a constant plastic strain rate, a proportionality coefficient, $0 < \alpha < 1$, is applied to the elastic stress field solution calculated with the FEM simulations of the § 2.2.1 at 0.001 total deformation. Such a solution has already been used in [Roy et al., 2019] to model size effects in nanoparticles. Thus, let's note :

$$\underset{\sim}{\boldsymbol{\sigma}}_{app} = \alpha \times \underset{\sim}{\boldsymbol{\sigma}}_{FEM} \tag{2.3}$$

with the proportionality coefficient α computed at any time step t from the relationship :

$$\alpha_{t+\Delta t} = \alpha_t + \Delta\alpha \tag{2.4}$$

and,

$$\Delta\alpha = \frac{(\dot{\varepsilon}^p - \dot{\varepsilon}^p_m) \times \delta t}{\zeta} \tag{2.5}$$

where $\dot{\varepsilon}^p$ is the desired plastic strain rate, $\dot{\varepsilon}^p_m$ is the measured plastic strain rate at the time δt and in a given direction, ζ is a scaling factor.

To calculate the local intragranular plastic strain field, specific post-processing is used as described in § 1.6.1.4. This provides a precise measure of slip system activity inside the grain at the scale of a few slip plane spacing. One example is illustrated in Fig. 2.2-(b) where the activity of $(\overline{1}11)$ slip planes can easily be identified. Applying various visualization thresholds allows us to only visualize the most intense slip events and then quantify slip localization events during the simulations. On the other hand, Fig. 2.2-(a) offers a more global description of the slip system activities, following the evolution of the plastic slip as a function of the average applied stress inside a grain.

2.3 Investigation of the intragranular elastic behaviour

As observed in the literature, the intragranular elastic loading is supposed to play an important role in plastic strain localization, as most intense slip bands look to be influenced by the so-called intersection zones [Charpagne et al., 2021]. Therefore, the detection of elastic strain incompatibility between the grains is important as it is the source of the strain and stress field heterogeneity inside the grains. In this section, FEM calculations are used to investigate this effect. The reference grain is randomly selected from the microstructure used in series 1 and 2, then reused for series 3. Fig. 2.3 shows the dispersion of the local

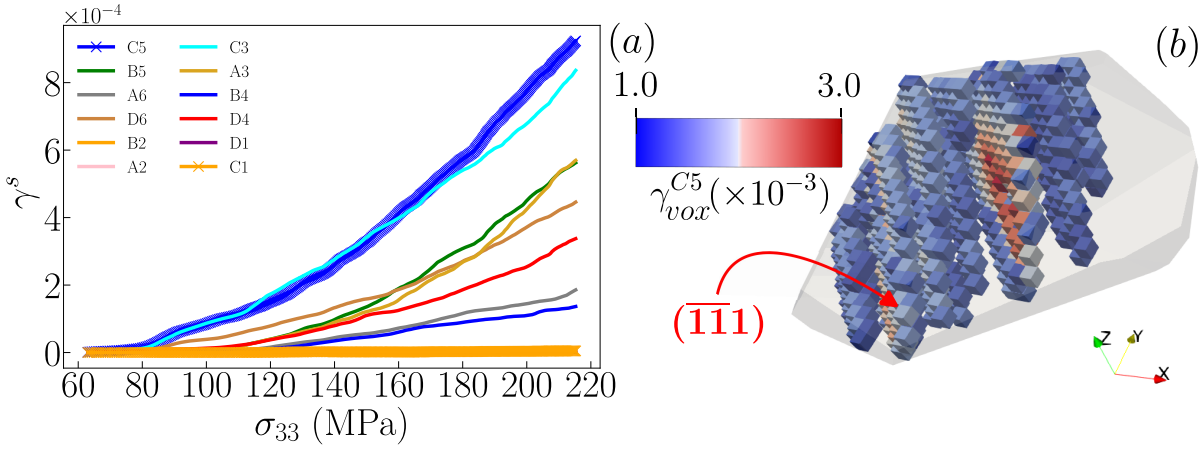

Figure 2.2: *Heterogeneity of the plastic deformation inside the grain. (a) Illustration of the slip system activity on the whole grain as a function of the increasing applied stress. (b) Visualization of slip system activity of slip system C5 for* $\gamma^{C5}_{vox} \in [1. \times 10^{-3}; 1.7 \times 10^{-3}]$ *whose mesoscopic value is* $\gamma^{C5} = 0.6 \times 10^{-3}$.

resolved shear stress inside the reference grain for a given set of orientations.

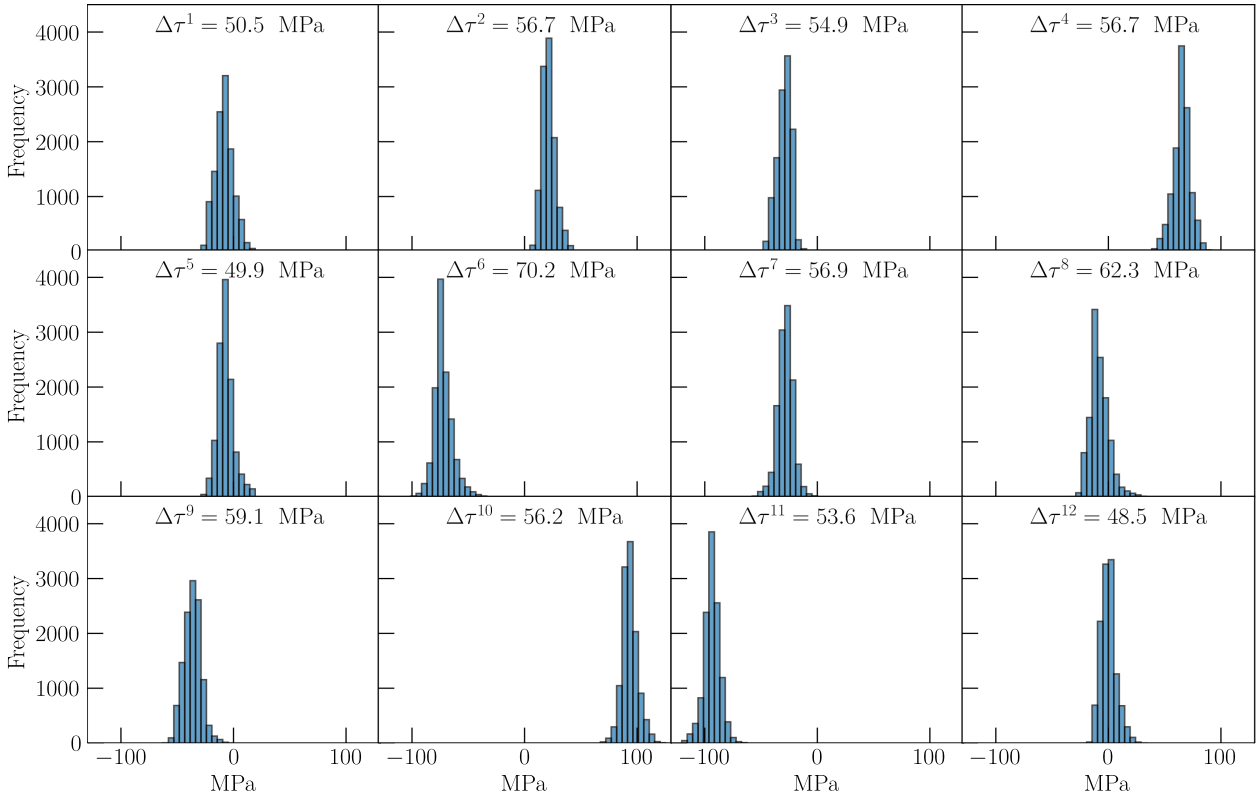

Figure 2.3: *Distributions of the resolved shear stress* τ^s *computed at each Gauss point inside the reference grain for one of series 1 simulations on the twelve FCC slip systems (from 1 to 12).*

Histograms show values computed at each Gauss point of the defined mesh (the whole mesh contains 1843230 Gauss points and the reference grain contains 11890 Gauss points).

Significant dispersion of resolved shear stress values can be observed by the amplitude $\Delta\tau^s = |\tau^s_{max} - \tau^s_{min}|$ as the average dispersion of all slip systems is approximately ±30 MPa from the mean resolved shear stress value computed over the total grain volume. This behaviour is very different from that of single crystals, as dispersion is the direct result of incompatibility in elastic deformation. Looking at $\Delta\tau^s$ values, not many differences are reported from the comparison between slip systems, although Schmid factors are very different (see Tab. 2.2). This first result therefore shows that the calculated stress dispersion is influenced more by interactions with neighbouring grains than by the grain's own orientation, once again highlighting the predominant role of elastic deformation incompatibility.

A complementary observation of the resolved shear stress field dispersion is provided by Fig. 2.4 showing a mapping of the resolved shear stress at the surface of the reference grain with two different visualization viewpoints (a) and (b). Computation of the resolved shear stress is made on the most active slip system C5. The field is strongly heterogeneous at the surface of the grain and zones of lower or higher intensity are mainly located near intersection zones. These dispersion regions are quite thick (∼10 µm) and can be amplified by increasing the stiffness differences between the grains in contact. Similar results are given in [Latypov et al., 2021] where strain field dispersion is found to be mostly influenced by the anisotropy ratio A.

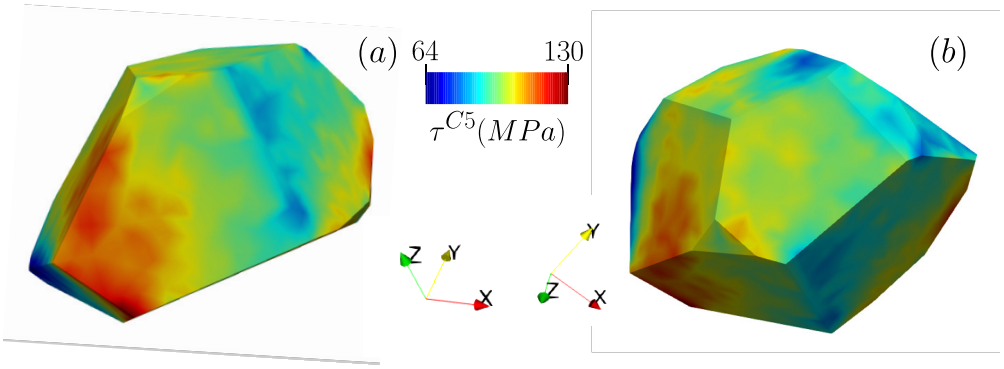

Figure 2.4: *Resolved shear stress mapping at 0.1 % strain, (a) the reference view of the DDD-simulated grain that will be used in the following, and (b) an alternative view. Stress values are extrapolated to the nodes.*

This first set of calculations shows the importance of statistically analyzing the elastic interactions between grains. More details and an analysis of the role of the aggregate microstructure on intragranular elastic loading are given in the next subsection.

2.3.1 Statistical analysis of the aggregate microstructure effect

Following the protocol described in § 2.2.1, a total of five hundred different aggregate configurations are created. We first analyze the results of series 1 (configurations where the

orientation of a reference grain is constant while the orientations of all the other grains are modified at each run), which will be compared with series 2 and 3 later. Analysis of the Schmid factor values reveals two predominant slip systems, C5 and C3, which are coplanar, and two other slip systems with relatively high factors, D4 and D6.

Slip System	**1-B4**	**2-B2**	**3-B5**	**4-D4**
Schmid factor	0.02	0.05	0.03	0.325
Slip System	**5-D1**	**6-D6**	**7-A2**	**8-A6**
Schmid factor	0.03	0.362	0.122	0.05
Slip System	**9-A3**	**10-C5**	**11-C3**	**12-C1**
Schmid factor	0.07	**0.447**	0.417	0.03

Table 2.2: *Solution of the calculation of the theoretical unidirectional Schmid factors with a theoretical tension along the Z-axis and for the 12 FCC slip systems in the reference grain 'i' of the series 1. The latter orientation is given according to the Euler angle convention* (ϕ_1, Φ, ϕ_2) = (27.790, 48.067, 167.920)*, in degrees. Schmid-Boas notation is used to index slip systems.*

As shown in Fig. 2.3, elastic strain incompatibility appears to play a major role in the stress distribution within the grain. Since the shear stress deviations resolved on each slip system do not vary much from one slip system to another, it should also be noted that the Schmid factor has little or no influence on the amplitude of the stress heterogeneity.

To study the role of the neighbouring grains on the average intragranular resolved shear stress, the orientation of all other grains is now randomly modified for each computation. Fig. 2.5 shows for two hundred draws, the distribution of the average intragranular resolved shear stress on each slip system in the reference grain with 11890 Gauss points. We first notice from this figure that the slip system hierarchy as planned by the Schmid factors is globally respected for all the orientation sets. Slip systems C5 and C3 have the most intense resolved shear stress followed by D4 and D6. Nevertheless, the aggregate microstructure strongly influences the average resolved shear stress intensity as highlighted by the comparison with the Schmid factors prediction (dotted vertical lines). Those values are computed considering the grain as a single crystal, thus not taking into account elastic strain incompatibility. In some cases, the effect of the surrounding microstructure on the reference grain leads to an increase (slip system 3) or a decrease (slip system 10) in the average resolved shear stress with respect to considering the grain as a single crystal. These variations can be important, an average standard deviation of 5 MPa is computed on every slip system. Thus, without changing the orientation of the reference grain, the intragranular elastic load depends on interactions with neighbouring grains, but the hierarchy of the slip system's activity remains

unchanged.

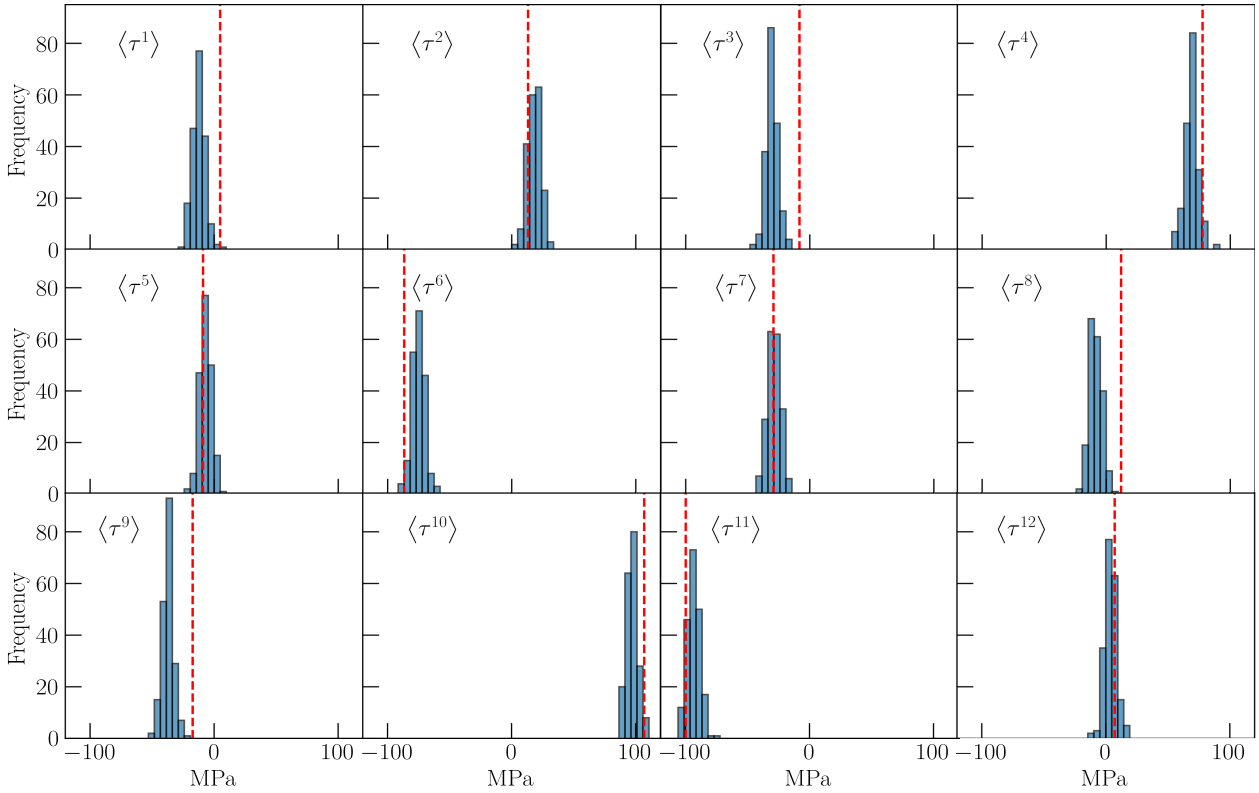

Figure 2.5: *Histograms of the mean resolved shear stress $\langle\tau^s\rangle$ for all slip systems (from 1 to 12) on the reference grain 'i' for the 200 configurations randomly drawn of series 1. The dotted lines represent the single crystal prediction for the homogeneous stress solution.*

Keeping in mind the fact that anisotropy clearly influences the stress and strain field dispersion, it is of major interest to quantify the intragranular heterogeneity for all the configurations. There, we propose to describe the heterogeneity of a mechanical field by its standard deviation following the relation: $\sqrt{V_a^s} = \sqrt{\frac{1}{n}\sum_{i=1}^{n}(\tau_i^s - \overline{\tau_i^s})^2}$. This is computed for all the configurations and for all slip systems and reported in Fig. 2.6. The use of the amplitude as in Fig. 2.3 to quantify heterogeneity is not advised, as in elasticity no convergence from the mesh size can be obtained on the maximum or minimum resolved shear stress values near grain boundaries. Standard deviation is well more suited to give a justified quantification of heterogeneity and in our computations, a convergence is quickly reached when increasing the mesh density.

Once again, and in accordance with the results of Fig. 2.6, the Schmid factor seems to play a minor role as the shape of the histograms is more or less the same for all the slip systems. In addition, the mean standard deviation calculated for each slip system shows very similar values. The dominant factor seems to be the interaction between the grains because from one configuration to another, on a particular slip system, the standard deviation can vary greatly. For example, heterogeneity can vary from 5 MPa to 13 MPa in the same grain for two different configurations.

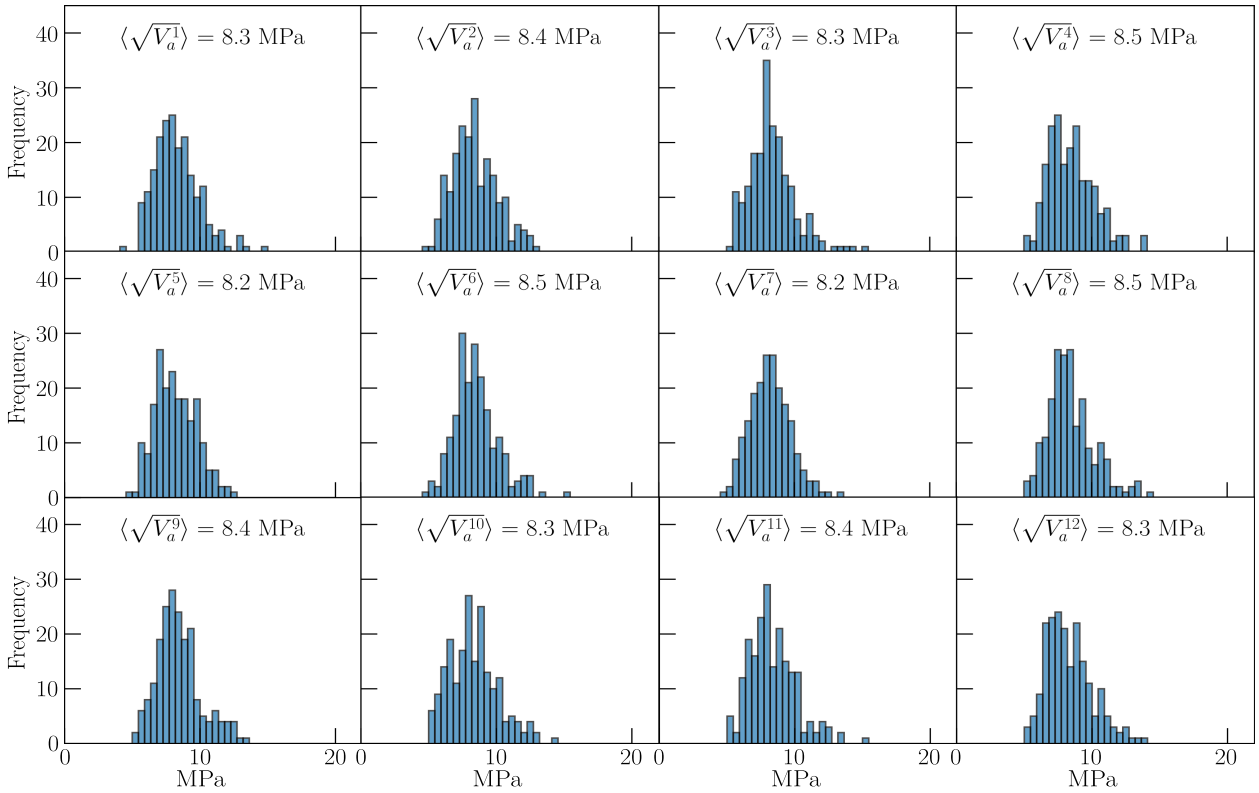

Figure 2.6: *Standard deviation calculated on each slip system (from 1 to 12) on the reference grain and for each configuration of the series 1 simulations.*

Fig. 2.7 illustrates this difference in the case of a low or high standard deviation. Here, we see that the highest resolved shear stress in the grain is increased by 50 MPa from one configuration to another. However, the average resolved shear stress in both configurations remains the same, meaning that the increases between the lower and upper stress areas balance out.

The above results demonstrate the important role of elastic interaction between neighbouring grains leading to elastic strain incompatibilities that modify the intragranular elastic loading of the reference grain. On the one hand, the orientation of the reference grain well defines the hierarchy of the slip systems that will be mainly active, on the other hand, the orientation of the neighbouring grains seems to be the most important parameter to determine the amplitudes and heterogeneity of the intragranular loading stress controlling the dislocation dynamics.

Equivalent observations are made for series 2, where the orientation of the reference grain is modified while other orientations are kept constant. From the results of series 2, changing the reference grain orientation also leads to important modification of the intragranular elastic loading. As the orientation is modified for every configuration, one should refer to the standard deviation computation to better interpret the effect on the intragranular elastic loading. In Fig. 2.8, series 1 and 2 are compared highlighting some differences. On this figure,

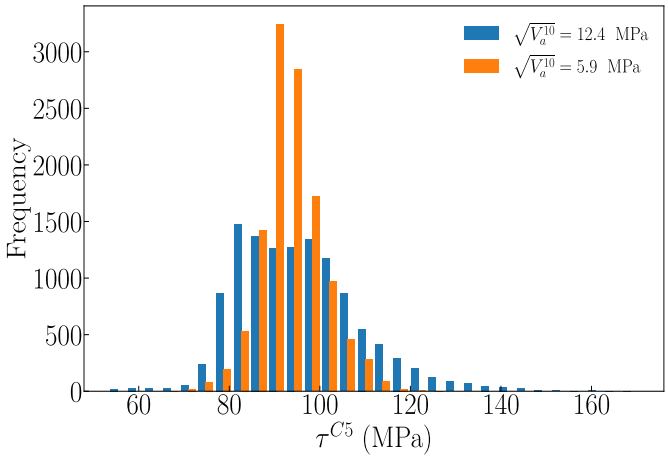

Figure 2.7: *Illustration of the resolved shear stresses for two different configurations of neighbours grain orientations which correspond to the case of a low or high standard deviation. Slip system C5 distribution is represented.*

the cumulative frequency ($f_n^{cum} = \sum_{i=1}^{n} f_i$) is computed to highlight differences between both series. It is observed that a quasi-systematic shift in the standard deviation values appears between the two series. Indeed, every slip system, except for slip system 5, shows in the reference grain a more intense standard deviation (more heterogeneous patterns) in the case of the series 1 simulations.

From the second set of simulations (series 2), we can conclude that the exploration of heterogeneity within grains is simpler using the simulation protocol of series 1 simulations, which allows the modelling of larger amplitudes of heterogeneity. Changing the orientation of the grains surrounding a reference volume fixed within an aggregate is therefore the simplest approach to a systematic numerical exploration with DDD simulations.

The last series of simulations (series 3) we tested to better understand and control elastic heterogeneity in a periodic aggregate is now briefly presented. This series of simulations is based on a variation of the morphology of the grains such as their diameter and aspect ratio. In these simulations, a reference grain is selected and the size of neighbouring grains varies randomly, but the set of grains must always form a periodic aggregate and the total volume of the simulation must be the same.

This series 3 leads to the same results as those observed in series 1 and 2, but with smaller heterogeneity amplitudes as illustrated in Fig. 2.9-(a) in comparison with “Series 1”, “Series 1, set 2” and “Series 1, set 4” curves. The “Series 1, set 2” curve and “Series 1, set 4” curve (green and purple curves in the figure) represent the evolution of the average standard deviation on all slip systems for two other crystalline orientations of the same reference grain:

- $(\phi_1, \Phi, \phi_2) = (287.801, 101.222, 16.740)$

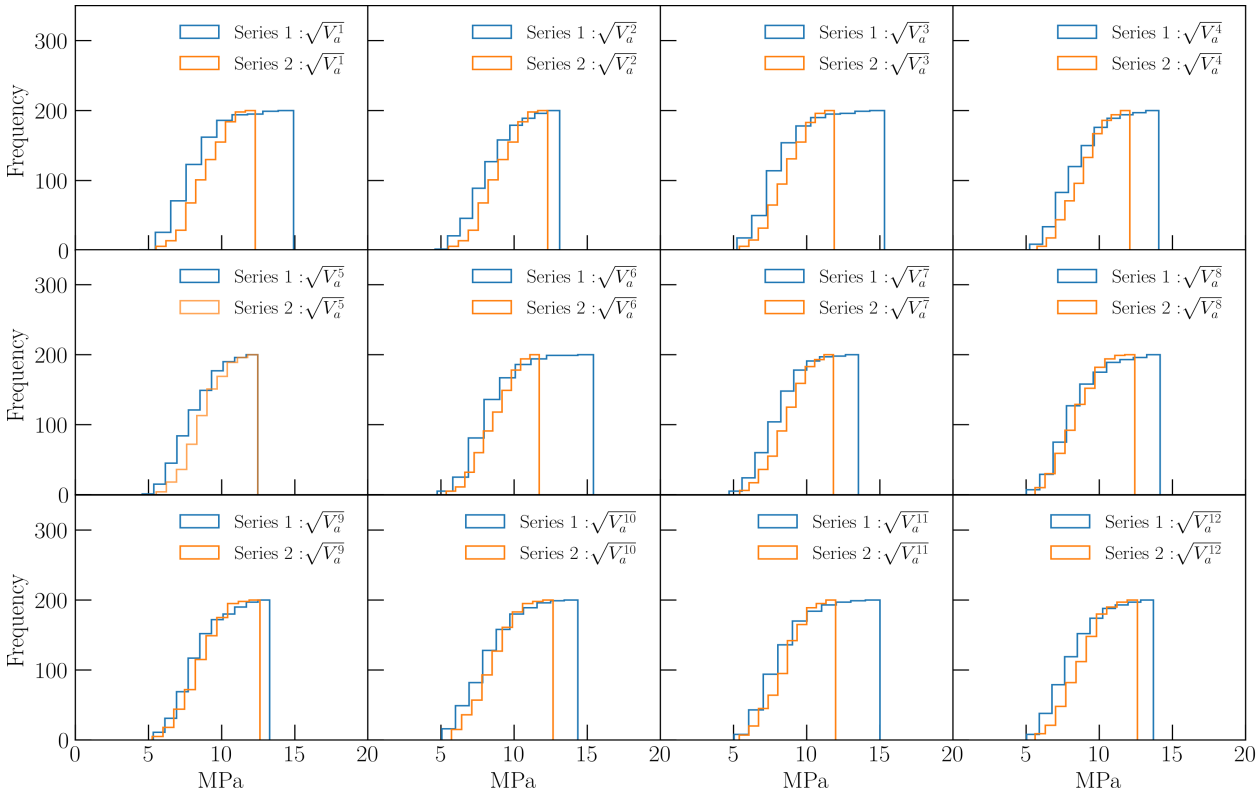

Figure 2.8: *Comparison of the calculated standard deviation of the intragranular stress for both simulations series 1 and 2, values are represented as a function of the cumulative frequency for all the slip systems (from 1 to 12).*

- $(\phi_1, \Phi, \phi_2) = (16.797, 75.154, 271.874)$

The curves of "Series 1", "Series 1, set 2" and "Series 1, set 4" show close evolution highlighting a weak dependency from the crystalline orientation. In comparison, in series 3 simulations, the number of grains in contact with a reference grain is often modified and generally reduced as seen in Fig. 2.9-(b). For the hundred build configurations, only 8 % of them have a number of neighbours equivalent to or higher than the one in series 1 and 2. This result strongly suggests that there is a correlation between the number of neighbours and heterogeneity. Close attention to the "Series 1, set 3" curve consolidates this assumption. Indeed, this set of calculations is realized considering a reference grain with a lower number of neighbours, 12 in total (against 23 for "Series 1", "Series 1, set 2" and "Series 1, set 4"), but with the same crystalline orientation as for the "Series 1" curve. The average standard deviation calculated for this series of simulations is lower due to the smaller number of neighbours. What these results demonstrate is that intragranular elastic loading heterogeneity is statistically amplified with a high number of neighbours. Indeed, the larger this number, the larger the probability of being in contact with much "harder" or much "softer" grains.

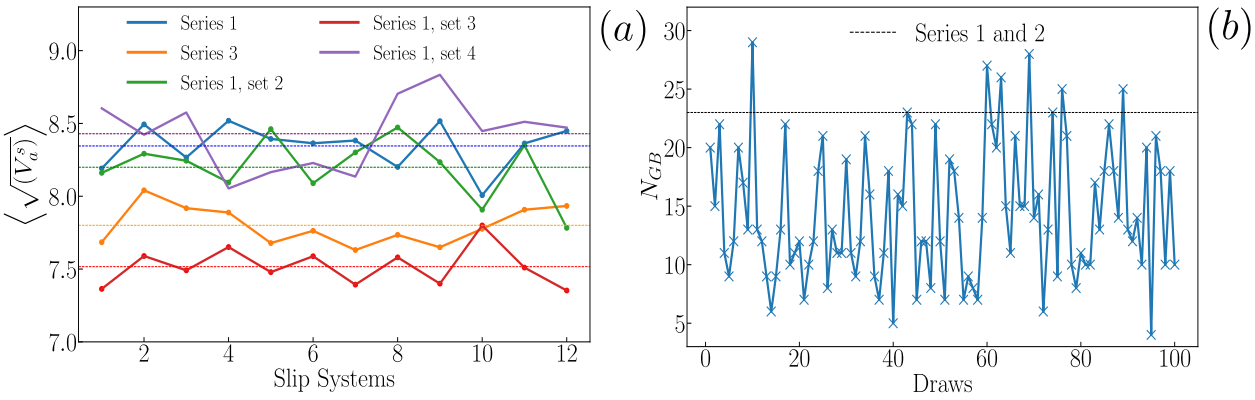

Figure 2.9: *Comparison of the average standard deviation per slip system between series 3 and various sets of series 1 (a). Sets 2 and 4 correspond to the series 1 statistical analysis with two other crystalline orientations of the reference grain while set 3 corresponds to the series 1 statistical analysis with a reduced number of neighbours. The number of neighbours is represented by the number of grain boundaries N_{GB} for the reference grain and for every configuration in series 3 (b). As a comparison, the dashed line represents the number of neighbours for series 1 and 2 simulations (23 neighbours).*

2.3.2 Stress concentration analysis

The numerous observations from the three series studied in § 2.3.1 (see for instance the results in Fig. 2.4) and from the literature show that the heterogeneity of the stress field is not constrained to isolated points, but refers to more mesoscopic regions with length comparable with the grain size. These regions are located near intersections in between grains as grain boundaries, triple junctions, and quadruple nodes. One way to validate these observations from our statistical analysis is to plot the evolution of the resolved shear stress on a particular slip system as a function of the distance to the quadruple node (see Fig. 2.10). In our simulations, quadruple nodes are supposed to be the most critical intersection for the emergence of stress concentration leading to heterogeneity as it represents the intersection among the largest number of grains.

Fig. 2.10-(a) shows the evolution of the resolved shear stress in the reference grain volume as a function of distance to the N quadruple node existing on the surface of the grain (in series 1). The calculation is performed as follows: for each configuration, the stress concentration regions are identified by calculating the maximum resolved shear stress on the mesh. Then, from these regions, the distance to all N quadruple nodes is calculated and the smallest one is selected. As a result of all these computations, an average curve is plotted as in Fig. 2.10-(a) representing the average evolution obtained from all the configurations. It should be noted that quadruple nodes are also the regions where low stresses can be concentrated depending on the neighbouring grains' configuration. Fig. 2.10-(a) confirms that stress concentration regions are systematically observed in the vicinity of quadruple nodes and the way the stress decreases from the quadruple nodes, progressively, shows that the stress concentration is

more or less distributed in the vicinity of the quadruple nodes.

Another interesting observation is that the calculated stress in those specific regions decreases at the centre of the grain to values close to the grain mean value. Hence maximum and minimum stress regions are more expected close to the grain boundaries. Fig. 2.10-(b) shows an example of one specific configuration with a stress concentration near one quadruple node and three triple junctions, this region is spread at the grain surface (about 10 µm long). It is hard to quantify if stress concentration regions are systematically of this importance (in terms of stress intensity and spatial distribution) but it has been observed in many configurations tested in the present work.

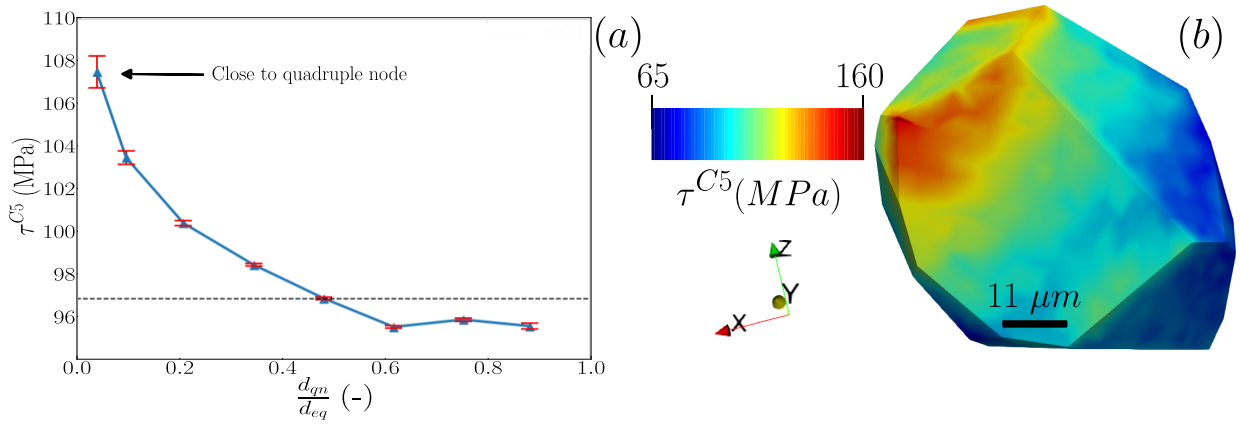

Figure 2.10: *Illustration of the existence of stress concentration near quadruple nodes. (a) Variation of the resolved shear stress τ^{C5} as a function of distance from the quadruple nodes d_{qn} divided by grain diameter d_{eq}. This curve is computed from all configurations of the simulations series 1. The dashed line represents the mean resolved shear stress computed in the full grain volume $\langle\tau^{C5}\rangle$. (b) Visualization of the stress gradient for one particular configuration where stress concentration zone is observed close to one quadruple node.*

Besides reported computations, many attempts have been made to identify a simple mathematical model to predict the emergence of stress concentration within grain from its own configuration and the one of its neighbours. Such research appeared to be difficult as the number of neighbours can be large (see Fig. 2.9-(b)) for a given grain, resulting in many possible configurations. The simulation results strongly suggest that the primary parameter explaining the presence of stress concentration and heterogeneity in an aggregate is the disorientation between neighbouring grains. Nevertheless, no simple relationship has been found based on a direct calculation of the disorientation between grains in contact. Alternatively, we explored other possibilities like focusing our study on grain triplets. We define grain triplets as three grains in contact with each other and with the reference grain, thus defining a quadruple node intersection. In this case, we focused on computing the strain dispersion in the triplets, also leading to very low correlation coefficients. What these attempts suggest is that the problem of stress fluctuation within a grain is a very local problem depending on every interaction and cannot be assimilated to a less local variable

that would suppose interactions to be averaged.

2.3.3 Identification of the most favourable grains for a localization of the plastic deformation

On the basis of the previous results and observations, we have proposed a simplistic criterion based on elasticity, which makes it possible to select, within a simulated aggregate, the grains that are expected to plastically deform first and that exhibit a high degree of stress heterogeneity, i.e., the grains most favourable to the observation of strong localization of the early stages of plastic deformation.

This criterion is based on the correlation between two quantities, the intensity of the resolved shear stress and the level of heterogeneity, as shown in Fig. 2.11. The use of quantities projected onto slip systems as resolved shear stresses instead of stress tensor components or invariants is justified by our will to study plastic strain localization at the scale of dislocations. The first grain to plastify is expected to be the one with the most intense resolved shear stresses and the most heterogeneous field. As a matter of fact, in Eq. 2.6 we define an average over all the slip systems of the resolved shear stress maximum values calculated at Gauss points, and in Eq. 2.7 an average on slip systems of the standard deviation value ($\sqrt{V_a^s}$). To give more weight to the most active slip systems in this criterion, we add to the computation of the standard deviation a correction by the Schmid factors (m^s). In addition, the calculation result is weighted by the average Schmid factor ($\langle m^s \rangle$), which represents the expected average plastic activity for the given crystalline orientation. This normalizes the results and makes them independent of the number of active slip systems.

$$\langle \max(\tau^s) \rangle = \frac{\sum_{s=1}^{12} \max(\tau^s)}{12} \tag{2.6}$$

$$\Lambda = \frac{\sum_{s=1}^{12} \sqrt{V_a^s} \times m^s}{12} \times \frac{1}{\langle m^s \rangle} \tag{2.7}$$

Fig. 2.11 presents the evolution the corrected standard deviation Λ as a function of maximum resolved shear stress $\langle \max(\tau^s) \rangle$ for three distinct following simulation cases:

- a test performed on one aggregate containing a hundred grains;
- a test performed on a grain for which we modify the orientation a hundred times;
- a test performed on two grains of different orientations for which neighbour's orientations are changed a hundred times.

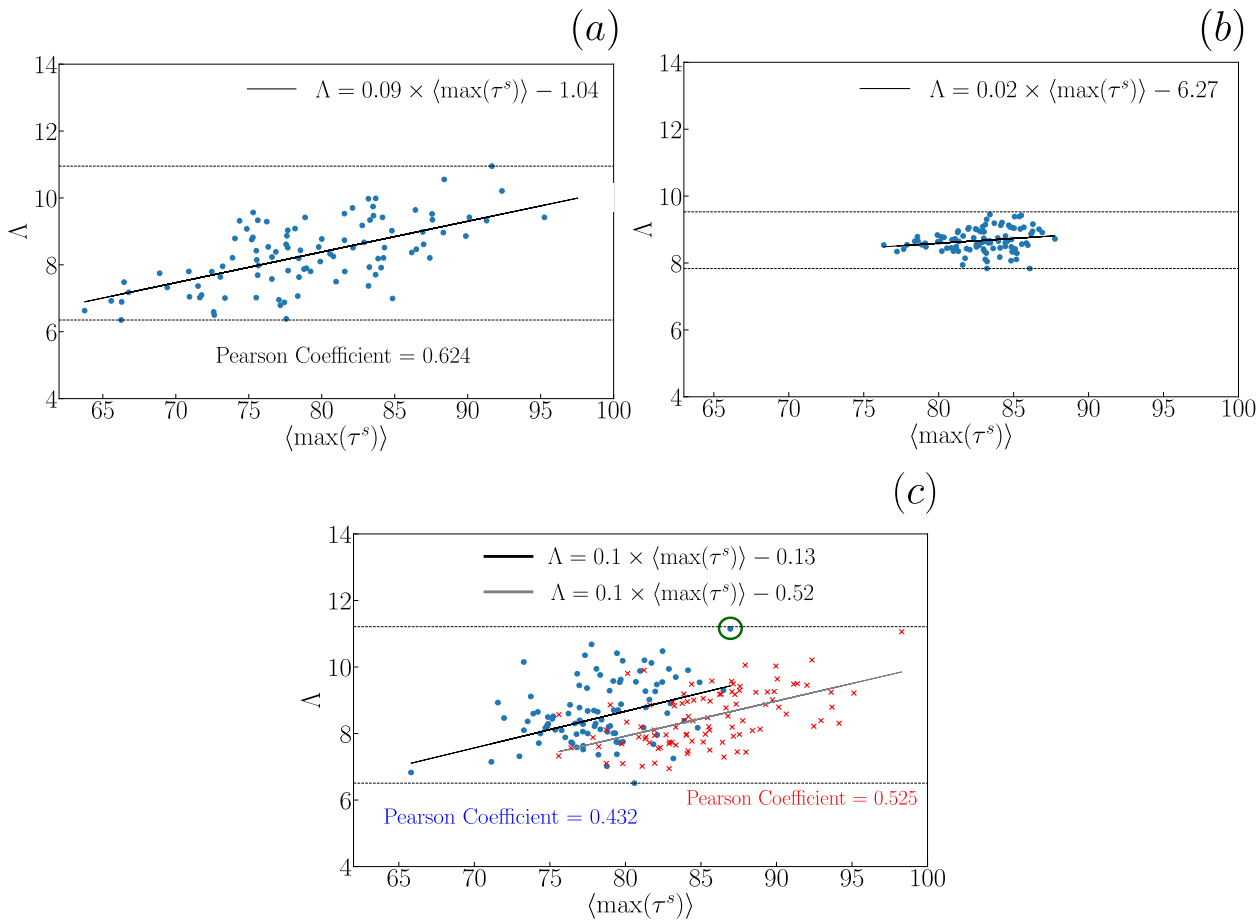

Figure 2.11: *Corrected standard deviation* Λ *evolution as a function of maximum resolved shear stress* $\langle max(\tau^s) \rangle$ *for three different cases explained in the text. Horizontal lines represent the maximum and minimum values of the interval. The criterion is applied to a random aggregate (a), to a grain whose orientation varies (b) and to two grains of different orientations for which neighbour's orientations are changed (c). The green dot shows the configuration used in § 5.3.2.*

By applying the formulations presented in Eq. 2.6 and Eq. 2.7, it is possible to classify the configurations (grains or orientations) from the most favourable to the appearance of localized plastic deformation to the least favourable. For each of the examples, a linear regression is calculated from the point clouds derived from the statistical data. In graphs (a) and (c), the slopes calculated are almost identical, showing that the criterion is consistent. The Pearson coefficients [Pearson, 1895] calculated on these two graphs indicate a good correlation and justify the link between the presence of stress concentration and the presence of intragranular heterogeneity. The two trends presented in graph (c) show an equivalent slope, the two linear regression curves are parallel but have a slightly different Pearson coefficient certainly linked to the number of points used for the statistics. If we look a little more closely at the evolution shown in graph (b), we can see that the slope calculated is weaker. Furthermore, the correlation coefficient calculated for this case study is very low and does not allow us to conclude on the presence of a correlation. In addition, we can

see that for this particular case, the corrected standard deviation and maximum resolved stress value intervals are small. This last statement reflects the greater difficulty in obtaining heterogeneous configurations within the framework of series 2 simulations, as illustrated in Fig. 2.8, and demonstrates once again the importance of the neighbourhood in comparison with reference grain crystalline orientation.

This simple relationship between heterogeneity and resolved shear stress concentration was developed for the present study in order to identify the most important grains in simulated aggregates on which data analysis with DDD simulations can be focused. We note in passing that this criterion can also be used to help identify the grains to be monitored as a priority during in situ experiments.

2.4 Investigation of the plastic behaviour

2.4.1 Plasticity and elastic strain incompatibilities

It is now clear that elastic strain incompatibilities between grains play a major role in intragranular elastic loading. To see how plastic deformation is affected by stress heterogeneity within the grain, DDD simulations are performed on a configuration of interest selected from the simulations series 1 (see Fig. 2.11-(c)).

DDD simulation conditions are the following: Plastic slip is considered on the twelve slip systems of the FCC structure. We first decided to run simulations without considering the possibility of dislocation to cross-slip. The resolved shear stress dispersion associated with the simulated configuration is reported in Fig. 2.7. To avoid biases coming from initial conditions, the plastic strain is averaged in every voxel with the results of 5 simulations started with different random dislocation source configurations :

$$(\gamma_{vox}^{C5})_{av} = \frac{1}{5} \times \sum_{k=1}^{5} (\gamma_{vox}^{C5})_k \tag{2.8}$$

All the other important simulation parameters are described in § 2.2.2.

Fig. 2.12 shows the results of the most intense slip traces observed during the simulations (a) and the intragranular elastic loading associated with the chosen configuration (b). We can compare the location of the simulated slip traces with the applied stress field and see that the most intense slip trace develops near a region of stress concentration.

Note that this result is obtained without cross-slip. Hence, in order to obtain this simulation result, the density of dislocation sources in the grain must be large, or at least one dislocation source must be located close enough to the stress concentration region. Intense plastic slip is then observed due to successive emission of dislocation loops on the slip plane

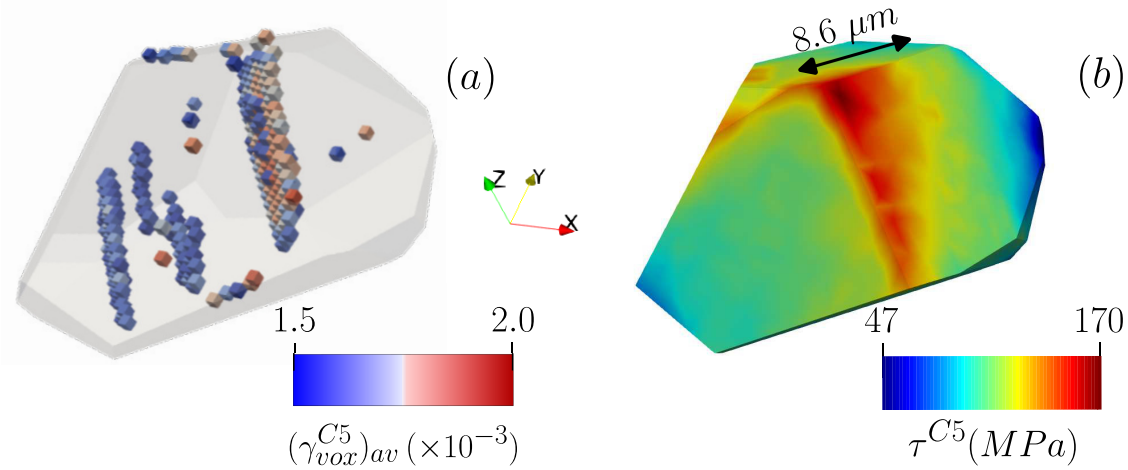

Figure 2.12: *Local slip system activity on slip system C5 for a reduce interval* $(\gamma_{vox}^{C5})_{av} \in [1.5 \times 10^{-3}; 2. \times 10^{-3}]$ *at the loading level of* $\gamma^{C5} = 0.6 \times 10^{-3}$. *The most intense slip traces are shown in the grain (a) and compared with the applied stress field obtained by FEM calculation (b).*

piling up at the grain boundary. Based on these preliminary results, we show for the first time that DDD simulations are capable of systematically reproducing and studying the elementary dislocation mechanism controlling the formation of slip bands in a polycrystal during the first stages of monotonous loading.

2.5 Conclusion

The mechanisms involved in the localization of intragranular plastic strain were studied using two simulation methods, FEM and DDD. These two types of simulations were used to gain a better understanding of the phenomena of stress heterogeneity in a grain included in a polycrystalline aggregate, both on a macroscopic scale via transgranular elastic behaviour and on a mesoscopic scale via intragranular plastic behaviour.

In this chapter, we have shown how the polycrystalline microstructure can affect the behaviour of a grain from an aggregate. Indeed, depending on the configuration of its surroundings, a grain can develop a very different state of intragranular elastic loading. In some configurations, the loading state is relatively homogeneous compared with other configurations where the loading state is actually very heterogeneous. The effects of heterogeneity are amplified by the type of interactions (e.g. crystalline orientation) with neighbouring grains in direct contact with the grain in question, as well as by the number of interactions, i.e. the number of neighbours. From the results obtained on numerous configurations, it appears that the crystalline orientation of the reference grain plays a minor role in the levels of intragranular heterogeneity.

Understanding the precise reasons for the appearance of this heterogeneity is not an

easy task, as the number of neighbours can be large. However, we have shown in this chapter that the regions of stress concentration that favour the appearance of heterogeneous elastic loading are systematically observed close to quadruple nodes. These observations are consistent with the literature and justify the dominant role of interaction regions on intragranular behaviour. The stresses calculated at quadruple nodes decrease rapidly away from them and the loading becomes more homogenized towards the centre of the grain.

A criterion based on these calculations and the conclusions we have drawn from them has been proposed to list in order of importance the configurations (grains and crystalline orientations) with a probability of developing localized plastic behaviour in the form of intense slip bands. The most favourable grain or crystalline orientation is defined as the one with a heterogeneous and intense state of stress. This criterion, which is clearly of interest for the selection of configurations of interest for DDD simulations, also has the ultimate aim of serving as a tool for experimental observations, and in particular for volume observations using X-ray topo-tomography. Indeed, by means of calculations carried out on digital twins, it is possible to use this criterion to select the grain of interest to be visualized in topo-tomography.

Finally, a configuration of interest was selected from the database linked to the series 1 simulations and used as a loading to solve the DDD. The results of these simulations, carried out with the cross-slip inactive, showed the dominant role of the stress concentration region on the appearance of intense and localized plastic slip. Indeed, the calculation of the average plastic slip carried out on a series of five dislocation microstructures shows the presence of a slip trace where the intensity of the plastic slip is intense and close to the region of stress concentration.

Chapter III

On the investigation of slip band initiation and persistence mechanisms

Résumé :

Dans ce chapitre, nous nous intéressons à donner une description plus précise des réactions entre dislocations et mécanismes physiques prenant place au cours de la déformation plastique. A travers plusieurs séries de simulations DDD, nous cherchons à déterminer des mécanismes permettant d'expliquer l'initiation d'une bande glissement ainsi que sa persistance au cours de la déformation plastique. Dans un premier temps, une modification des conditions de simulations du chapitre précédent, par l'ajout du cross-slip permet une description plus justifiée de la plasticité cristalline et démontre à quel point ce mécanisme est capable d'influencer le glissement plastique intragranulaire et notamment sa répartition. Par l'activation du cross-slip, la déformation plastique s'homogénéise au sein du grain rendant ainsi nulle la dépendance par rapport à la microstructure initiale pouvant être initialement introduite par les conditions de simulations. Nous montrons au cours de ce chapitre, que deux mécanismes sont la cause évidente de l'initiation d'une déformation plastique locale et donc d'une bande de glissement, par le cross-slip et les annihilations colinéaires. Par ailleurs, à ce stade des recherches, aucune réduction de l'écrouissage locale n'est calculée au cours de nos simulations et ne permet ainsi pas de conclure quant à la présence de mécanismes liés à la persistance d'une bande de glissement. Pour finir, sont présentées dans ce chapitre des observations de réactions microstructurales originales à travers notamment les annihilations colinéaires ou encore dans les mécanismes de recombinaison de lignes de dislocations à l'origine d'une forte activité du cross-slip proche de joints de grains non orientés dans la direction vis.

Contents

3.1 Introduction

This part of the manuscript investigates the mechanisms involved in the initiation and persistence of a slip band during plastic deformation. The evolution of the dislocation microstructure is studied in detail using DDD simulations, focusing on a single grain, with the aim of highlighting the underlying physical mechanisms, such as dislocation reactions and dislocation microstructure organisation. As will be further discussed in the next sections from the results of the DDD simulations, two mechanisms appear to play a predominant role in the initiation of a slip band. These two mechanisms, cross-slip and collinear annihilation are associated with important microstructural changes during plastic deformation and thus affect the local plastic behaviour of the grain. The role of these mechanisms in the persistence of a slip band is also discussed in detail using model simulations.

The calculations carried out in this chapter take as initial loading conditions the stress field presented in Fig 2.12, the selection of which is based on the calculation of our criterion in elasticity as discussed in § 2.3.3 from the results of series 1 statistical study. For a more local and precise study, the grain is split into three distinct regions, these regions are delimited by $(\overline{1}11)$ planes, let's define :

- Zone I, the region at the left of the stress concentration region;
- Zone II, the stress concentration region;
- Zone III, the region at the right of the stress concentration region.

An illustration of this grain region definition is given in Fig 3.1. By doing so, physical quantities like the plastic slip, dislocations density or even the stress state can be studied separately, in each zone of the grain.

In the following, computational methods and simulation parameters are first summarized (§ 3.2). Then, the contribution of the cross-slip on the intragranular plastic behaviour is discussed through comparisons between configurations with and without cross-slip being activated (§ 3.3). This discussion is of major interest as results obtained in Chapter II considered the cross-slip as being inactive. In the next parts, results of the research of slip band initiation and persistence mechanisms are presented by separating the contribution of the cross-slip and of the collinear annihilation mechanism (§ 3.4 and § 3.5). Finally, a qualitative description of some original microstructural reactions is given (§ 3.6). From these studies and results, we gain a better understanding of how the dislocation microstructure can reorganise during the loading to allow plastic deformation to initiate and persist on a particular slip plane.

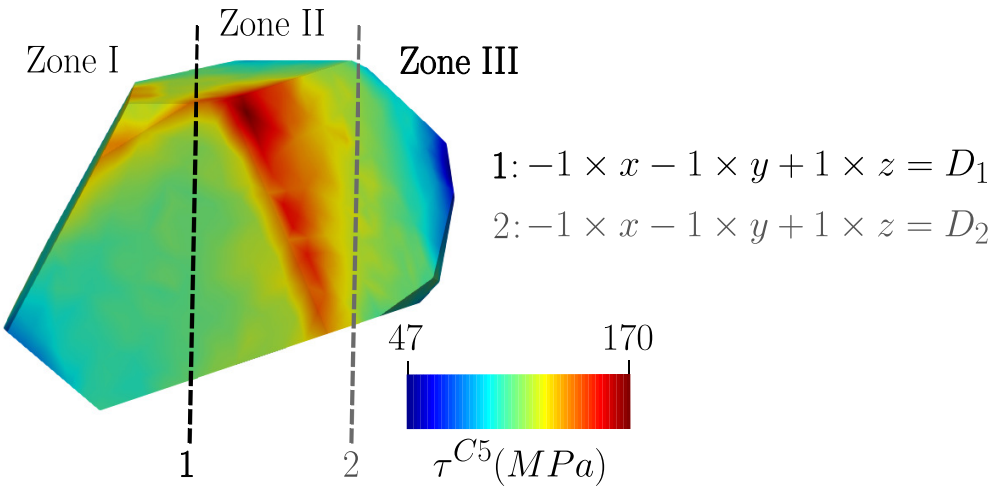

Figure 3.1: *Illustration of the grain separation in three regions delimited by* $(\overline{1}11)$ *planes given by their Cartesian equations.* D_1 *and* D_2 *are set so that the grain is separated into three regions of approximately equivalent volume. The grain equivalent diameter is 30 µm. The applied stress field here represented by the resolved shear stress on the C5 slip system is identical to the one selected and studied in Fig 2.12.*

3.2 Computational methods

Two types of simulation series are used in this chapter: the so-called global simulations, which describe the overall behaviour of the grain during plastic deformation without making major hypotheses, and the so-called model simulations, with the aim of providing a better description of certain physical mechanisms occurring during plastic deformation. These model simulations are also used to verify certain observations and hypotheses made on the basis of the global simulations.

3.2.1 The "global" simulations

This type of simulation makes use of the simulation conditions depicted in Chapter II. Nevertheless, it should be noted that two kinds of global simulations are run. The first type of simulation considers the plastic deformation on the twelve slip systems of the FCC structure, named "set 1". When the second type of simulation only considers the plastic deformation on the most active slip system C5 and its collinear slip system B5 (see Tab. 2.2 for the Schmid factor definition), thus reducing the plastic deformation to only two slip systems, named "set 2". The "set 1" simulation parameters are used in § 3.3.1 only for the discussion about the role of the cross-slip on the intragranular plastic behaviour and the impact on the initial source distribution. For the "set 2" simulations, it is assumed that the most important mechanisms are well represented by these two slip systems (C5 and B5). Thereby, simulations can reach higher deformation levels as the total number of dislocation

segments is highly reduced. A brief summary of the simulation parameters is given in Tab. 3.1 for "set 1" and "set 2" simulations.

Global simulation	$\boldsymbol{\rho^s}$ $\boldsymbol{(m^{-2})}$	$\boldsymbol{\rho_{ini}^{tot}}$ $\boldsymbol{(m^{-2})}$	$\boldsymbol{\dot{\varepsilon}^p}$ (s^{-1})	**Slip system**
Set 1	8×10^9	1×10^{11}	200	12
Set 2	8×10^9	1.6×10^{10}	50	2 (C5/B5)

Table 3.1: *Main simulation parameters for global simulations "set 1" and "set 2".*

Cross-slip mechanism is considered in the simulations when reported in the text. Parameters for the cross-slip rule are extrapolated from previous studies [Bonneville et al., 1988] in the case of pure crystalline copper. To the author's knowledge, no similar work was performed on pure nickel, thus, a scaling factor (H) is applied to the τ_{III} values to account for the differences in elastic constants between Copper and Nickel :

$$H = \frac{1}{3} \times \left(\frac{C_{11}^C}{C_{11}^N} + \frac{C_{12}^C}{C_{12}^N} + \frac{C_{44}^C}{C_{44}^N} \right) = 1.44 \tag{3.1}$$

with C_{ij}^C and C_{ij}^N the elastic constant of copper and nickel respectively [Shuvalov et al., 1988]. Applying this scaling factor to τ_{III} for copper leads to :

$$\tau_{III}^N = H \times \tau_{III}^C \approx 45\ MPa \tag{3.2}$$

The two material dependant parameters for cross-slip used in the simulations for the cross-slip activation rule are thus :

- $\tau_{III} = 45$ MPa
- $\alpha = \dfrac{\tau^{(g)}}{\tau^{(dev)}} = 0.6$

with α set to the value identified for pure copper as detailed in [Kubin et al., 1992].

3.2.2 The "Model" simulations

Model simulations differ from other simulations since their goal is to represent in the most simple way key physical mechanisms. Two types of particular model simulations are described in this section. These simulations will be used to investigate the slip band persistence mechanisms in section § 3.5 through the role of cross-slip and collinear annihilation on isotropic and kinematic hardening. For simplicity, these simulations are carried out according to the hypothesis of a homogeneous external loading.

The first set of simulations ("set a") to study the role of cross-slip and collinear annihilations on kinematic hardening consists of limiting the plastic deformation to one or two Frank-Read sources. These sources are arranged on different slip planes separated by a distance d. As a result, there are no forest interactions and the only remaining hardening is due to the accumulation of dislocations at the grain boundaries. For these simulations, grain boundaries are considered impenetrable to dislocations, grain geometry and crystalline orientations are identical to the one in Chapter II and for the "global" simulations.

The second set of model simulations ("set b") was designed to precisely measure the effect of the cross-slip and collinear annihilations on isotropic hardening. In this case, periodic boundary conditions (PBC) are used to avoid GND accumulation and kinematic hardening. Such simulation conditions have been previously used in numerous studies like [Madec, 2001; Devincre et al., 2008; Jiang et al., 2019] to study the role of dislocations interaction on forest hardening. For this set of simulations, the forest density is considered to be constant and a constant density of immobile dislocations is introduced to model a forest density (ρ_f). A $[\bar{1}35]$ single slip orientation is considered, with A6 $[110](\bar{1}11)$ forest dislocations producing Lomer lock with B4 $[\bar{1}01](111)$ mobile dislocations, following the given reaction :

$$\underline{b}_3 = \underline{b}_1 + \underline{b}_2 = \underline{b}_{Lomer} \tag{3.3}$$

$$\underline{b}_{Lomer} = \frac{1}{2}[110] + \frac{1}{2}[\bar{1}01] = \frac{1}{2}[011] \tag{3.4}$$

Following this reaction, the plane that both contains the junction dislocation line and the resulting Burgers vector is (100), as this slip plane is not a close-packed slip plane the junction is sessile. Lomer junctions are known to be of great importance on forest hardening [Devincre and Kubin, 2010], producing strong lock to dislocations motion.

As it will be described in this chapter, cross-slip events enable plastic deformation to be distributed over new, previously unoccupied slip planes, while collinear annihilations increase the density of mobile dislocations on a given slip plane. In order to better understand the effect of these two mechanisms on both kinematic and isotropic hardening, several simulations were carried out. By varying the distance between the slip planes for both types of simulation as in § 3.5.1, we can model in a simple way the role played by cross-slip and, in particular, double cross-slip on kinematic and isotropic strain hardening. Similarly, by varying the mobile density on a slip plane as in § 3.5.2, we can study the role of collinear annihilations on kinematic and isotropic strain hardening. The main simulation parameters for both sets of simulations are summarized in Table. 3.2 with N the number of Frank-Read sources initially introduced in the simulations and d the distance in between slip planes containing dislocations. The simulations are numbered without star exponents in the case of cross-slip model simulations and with star exponents in the case of collinear annihilation model simulations.

Model simulation	Simulation	$d\ (m)$	N (FR source)	$\rho_f\ (m^{-2})$	Set
Cross-Slip § 3.5.1,	1	-	1	-	"a"
	2	50b	2	-	"a"
	3	100b	2	-	"a"
	4	500b	2	-	"a"
	5	1000b	2	-	"a"
	6	2000b	2	-	"a"
	7	-	1	$0,6 \times 10^{11}$	"b"
	8	50b	2	$0,6 \times 10^{11}$	"b"
	9	50b	3	$0,6 \times 10^{11}$	"b"
	10	50b	4	$0,6 \times 10^{11}$	"b"
Collinear Annihilation § 3.5.2	1*	-	1	-	"a"
	2*	-	2	-	"a"
	3*	-	3	-	"a"
	4*	-	1	$0,6 \times 10^{11}$	"b"
	5*	-	2	$0,6 \times 10^{11}$	"b"
	6*	-	3	$0,6 \times 10^{11}$	"b"
	7*	-	8	$0,6 \times 10^{11}$	"b"

Table 3.2: *List of the initial conditions for various simulations series, "set a" and "set b" in order to model the role of the cross-slip and collinear annihilations on the kinematic and isotropic hardening.*

Illustration of these two series of simulation is given by Fig. 3.2, for the kinematic hardening (a) in the case where $N = 2$ and isotropic hardening (b) in the case where $N = 1$. For visualization purposes, the interplanar distance in (a) is deliberately magnified.

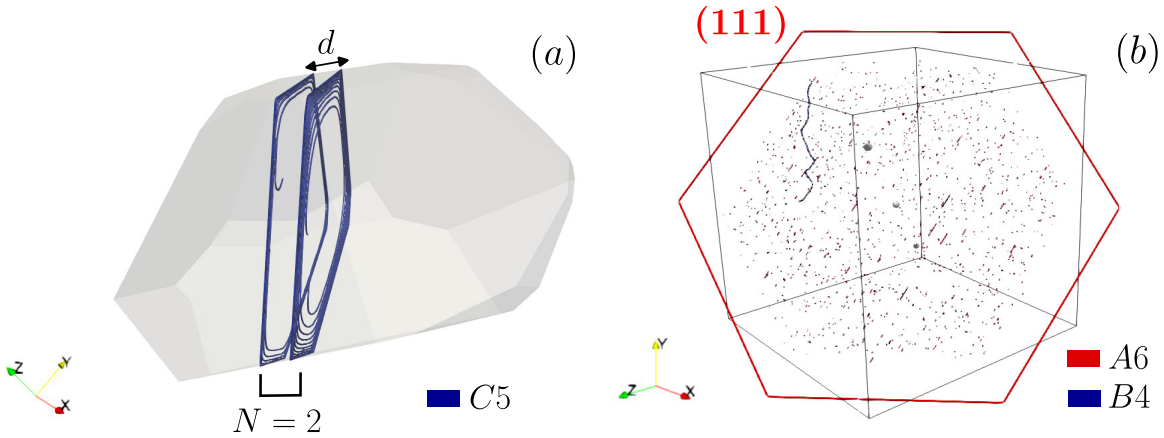

Figure 3.2: *Illustration of the two sets of model simulations performed to study the role of cross-slip and collinear annihilation: (a) kinematic hardening, i.e "set a" and (b) isotropic hardening, i.e "set b".*

3.3 The contribution of the cross-slip to local slip system activity

The results presented in Chapter II have shown the importance of mechanical loading on the development of regions of intense plastic activity. Indeed, Our first simulations have shown, in the case of a particular Voronoi single grain, that if the dislocation microstructure allows it, an intense plastic slip will be localized near the stress concentration regions. These first observations were obtained by preventing dislocation cross-slip, which is not representative of the real material behaviour.

The role of cross-slip on local and average slip system activity is discussed through the results of simulations comparing the plastic behaviour with and without cross-slip being activated. First of all, the cross-slip activity is discussed from simulation results following the "global" scheme and "set 1" simulation conditions in § 3.2.1. As for that kind of simulation, plastic deformation is considered on all the slip systems, the deformation level reached at the end of the simulations on each slip system is quite low but sufficient to observe important trends. In a second time, simulations following the "set 2" conditions are used as they allow reaching larger deformation levels per system and to discuss the contribution of cross-slip on the intragranular plastic deformation. In addition, the role of elastic strain incompatibilities, i.e. the presence of stress concentration on plasticity, is investigated again when considering the cross-slip mechanism (following "set 2" conditions).

3.3.1 Impact on the initial dislocation source distribution

Dislocation cross-slip is a well-known mechanism by which screw dislocations can move from their initial slip plane to a deviated plane, injecting a dislocation segment into a collinear slip system with the same Burgers vector, and possibly forming new dislocation sources. Fig. 3.3 shows the results of two identical simulations, but one where the dislocation dynamics is solved without any contribution from the cross-slip mechanism (a) and one with the cross-slip mechanism active (b). For such simulations, the initial dislocation configuration was deliberately taken without favourable dislocation sources close to the stress concentration region. As a result, in the simulation without cross-slip illustrated in Fig. 3.3-(a) the most intense slip trace is not located near the stress concentration region but in a region where dislocation sources are available. Examining the cross-slip simulation shown in Fig. 3.3-(b), with the same initial dislocation microstructure, we observe the emergence of a second intense slip trace formed near the stress concentration region. In the last simulation, the two intense slip traces have approximately the same intensity, of the order of half the plastic deformation concentrated in the single slip trace of the first simulation without cross-slip.

This model numerical experiment illustrates that cross-slip is an essential mechanism for the spreading of plastic deformation within a grain. This propagation, associated with the apparition of new dislocation slip planes in the grain, occurs preferentially in regions of stress intensity where the formation of dislocation sources is made possible by cross-slip.

Illustration of the role of the cross-slip and double cross-slip mechanisms is well represented in Fig. 3.3 where dislocation dynamics is followed for one particular slip plane near the stress concentration region. In Fig. 3.3-(c), we show the existence of double cross-slip events associated with a stress relaxation mechanism. More precisely, dislocations of the primary slip system C5 are piling up at grain boundaries thus leading to the rise of a back-stress on the emitting source. Screw dislocations at equilibrium, blocked, in this pileup can eventually cross-slip [Devincre et al., 2011; Brown, 2002; Bonneville et al., 1988], allowing plastic deformation to be accommodated. Therefore, in the small red square in Fig. 3.3-(c), cross-slip events are monitored. Segments of dislocation after a cross-slip event begin to slip on the collinear slip system B5. After a small displacement, the stress outside the pile-up configuration becomes stronger again on the primary slip system (see Tab. 2.2) and the screw sections of these bowing dislocation segments return to their original slip system C5, following the so-called double cross-slip mechanism. Examples of such events are illustrated in Fig. 3.3-(c). Here it must be noted that such double cross-slip mechanism events do not necessarily lead to the creation of a new source and new active slip traces. Indeed, many of those dislocation segments that cross-slip close to a grain boundary are blocked and can hardly evolve to become a dislocation source. Nevertheless, it was observed during the simulation that relaxation of dislocation pile-up with double-cross-slip can sometimes lead to the creation of a new source emitting many dislocations in a region of high stress.

Another dislocation source formation mechanism that we have observed is illustrated in Fig. 3.3-(d). In this second capture, the creation of a new source is monitored close to an existing slip plane C5 and through cross-slip in the central region of the grain. This cross-slip event originates from a B5 dislocation gliding in from another region of the grain and interacting elastically with the numerous dislocations of the C5 slip system accumulated in the initial slip plane C5. At the end of the process, a new C5 slip plane parallel to the pre-existing one has formed. It is important to note that for the deformation levels achieved in this type of simulation with the cross-slip, a precise comparison of the influence of the level of resolved shear stress heterogeneity on intragranular plastic slip does not reveal any major differences. For both configurations (high and low heterogeneity), it is possible to obtain more intense plastic slip in certain regions of the grain whose position varies with the applied stress field. However, the slip traces obtained in this type of comparison do not show strong differences in the intensity of plastic slip. Thus, reaching higher levels of plastic deformation is a major challenge for studying the effect of the level of heterogeneity on plastic slip.

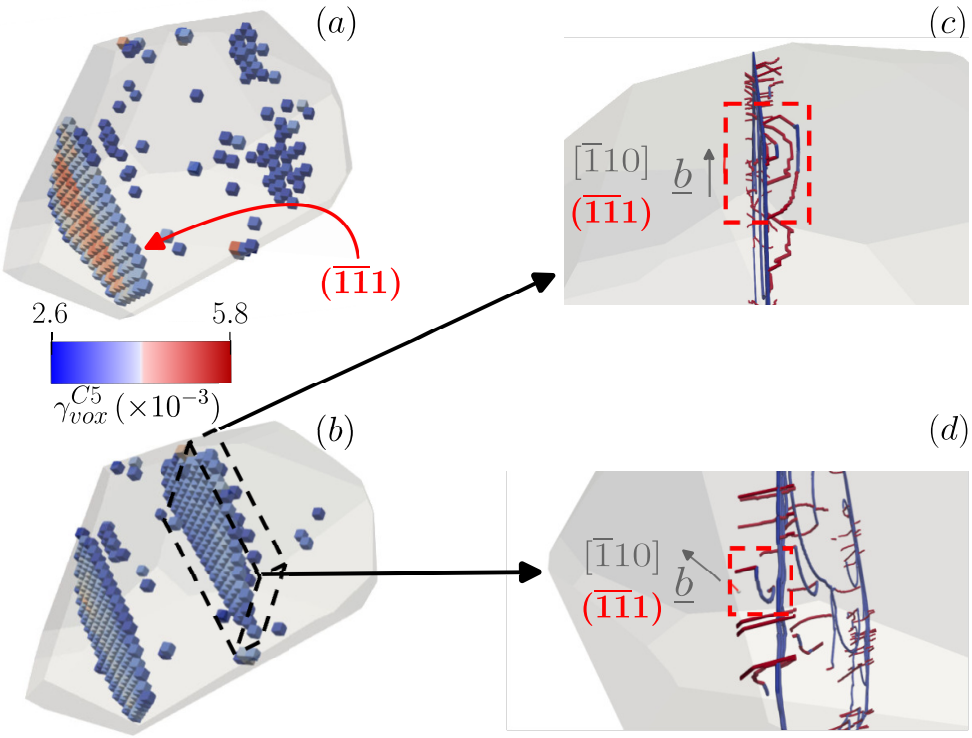

Figure 3.3: *Illustration of the most intense regions of slip system activity associated with slip system C5 calculated over a local deformation interval at the end of the simulation ($\gamma_{vox}^{C5} \in [2.6 \times 10^{-3}; 5.8 \times 10^{-3}]$). Comparison between two simulations starting from the same initial dislocation configuration without cross-slip activity in (a) and with the active cross-slip mechanism in (b). (c) and (d) are further illustrations of the cross-slip activity associated with deformation near the stress concentration zone. Double cross-slip on dislocations accumulating at the grain boundary near the stress concentration zone (c). Cross-slip from other parts of the grain leading to the formation of pinning points (d). These last two observations are given by two independent slices that are not necessarily observed at the same loading level and dislocation segments outside the defined box in (b) have been hidden for clarity.*

This initial analysis of the simulation highlights the dominant role of cross-slip. These results show, that dislocations cross-slip is a key mechanism that we should take into consideration for further investigation into the localization of intragranular plastic deformation.

3.3.2 Ductility and homogenization of the plastic deformation

On the basis of the results presented in § 3.3.1 for simulations following "set 1" conditions, cross-slip appears to be a key mechanism when studying phenomena associated with intragranular plastic deformation and microstructure organisations. As those observations have been obtained at a relatively low deformation level we now extend this investigation with the "set 2" simulation conditions allowing the role of the cross-slip to be further discussed at larger strains. In Fig. 3.4 we provide two graphs highlighting cross-slip activity in the

grain during plastic deformation. The activity of the cross-slip can be seen by plotting the stress-plastic slip curves for two series of simulations and for slip systems C5 and B5. Similar to the previous section, we compare here the evolution of these quantities in the context of a resolution with and without cross-slip. Results are illustrated in Fig. 3.4-(a). What can be said from these first results is that cross-slip activation provides a gain in ductility. In comparison with calculations without cross-slip, simulation with cross-slip allows for greater plastic deformation at the same stress level on both slip systems. This result can be explained by the ability of the cross-slip or double cross-slip to bring deformation to new, previously unoccupied slip planes [Koehler et al., 1954; Gilman and Johnston, 1957], reducing the flow stress necessary for dislocation mobility. At equivalent applied stress, (σ_{33} = 212 MPa), plastic strain gain due to cross-slip activation on B5 is about 0.000375 (+75 %) whereas it is of 0.00025 (+16 %) on C5. Cross-slip therefore has a major influence on the collinear slip system.

In a different way, cross-slip activity can be quantified by counting the number of slip planes with non-zero dislocation density for a particular slip system. Results of such computation are illustrated in Fig. 3.4-(b). Due to the initial simulation conditions, namely the position of initial Frank-Read sources, at the beginning of the loading, for $\gamma^s \in [0.0; 0.0005]$ the number of slip planes is constant and equal to 32. This number does not vary until cross-slip activation, triggered after reaching a given stress level in the grain. It can be seen in the figure that this stress level is reached at γ^s value around 0.0005. Beyond this γ^s value the number of slip planes with a non-zero dislocation density on the primary slip system significantly increases.

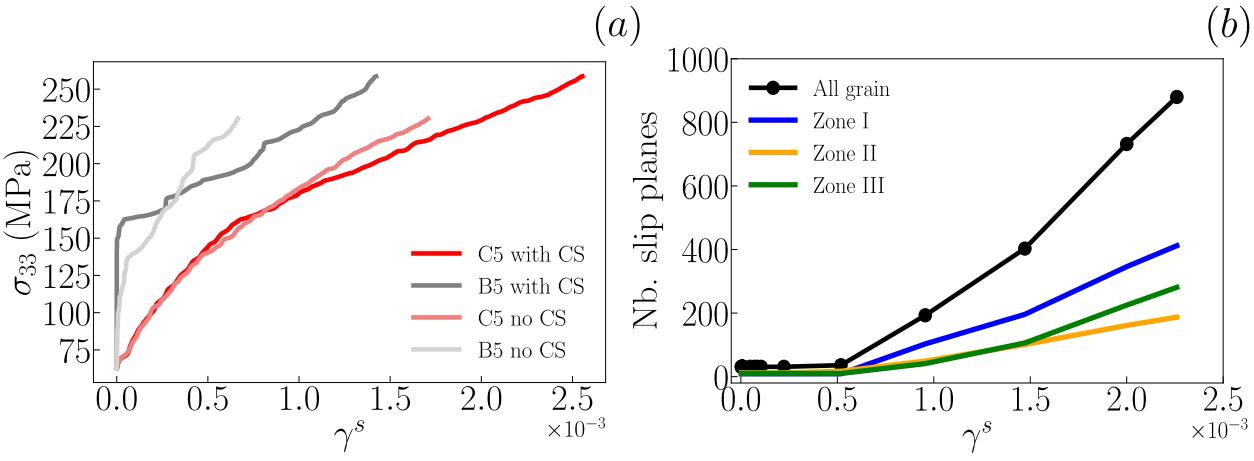

Figure 3.4: *Stress-plastic slip curves (a) for the primary (C5) and collinear (B5) slip system. Initial dislocation density for the simulation with cross-slip is* $\rho^{C5} = 0.1 \times 10^{11}\ m^{-2}$*, all density reported on the collinear slip system C5 is coming from cross-slip events as* $\rho^{B5}_{ini} = 0$*. In the simulation without cross-slip, the same initial dislocation density is introduced following the relation* $\rho^{B5} = 0.2 \times \rho^{C5}$*. Evolution of the number of slip planes seeing non-zero density in the C5 slip system during plastic deformation (b).*

It should be noted that the cross-slip activity varies with position in the grain. Zone I displays the highest cross-slip activity. In comparison, Zones II and III exhibit a lower activity. Within the grain, cross-slip activity has increased the number of slip planes by over 25 with respect to the initial dislocation microstructure, highlighting a significant role of cross-slip in the homogenization of plastic deformation within the grain. All the new dislocation segments made by cross-slip, even if they are not necessarily mobile at the level of deformation investigated with the simulation, may end up playing a role in further plastic deformation.

3.3.3 On the role of elastic strain incompatibilities

For the same simulations as in § 3.3.2, it is possible to verify the impact of the cross-slip activity on the intragranular plastic deformation and in particular the apparition or not of intense plastic slip events. Results for the simulation with cross-slip are illustrated in Fig. 3.5-(a) and without cross-slip in Fig. 3.5-(b). In this figure, we show the intragranular plastic deformation state for various intervals of plastic slip values on slip system C5. For each representation, only plastic slip events whose value falls within the interval illustrated by the colormap are displayed. For both simulations, those calculations are made at equivalent plastic slip value ($\gamma^{C5} = 0.0017$, see Fig. 3.4-(a)).

Firstly, the intragranular plastic deformation state is relatively different between the simulation with and without cross-slip. There is no doubt that the simulation with cross-slip shows less localized plastic behaviour. The intensity gradient between slip traces is small, as demonstrated by the uniformity of colour across the entire panel (a). This is quite different in the case without cross-slip, where gradients are perfectly observable on panel (b). In addition, the majority of the slip traces represented in panel (a) are of a lower intensity than in panel (b). This is particularly noticeable for $\gamma^s_{vox} \in [0.0027; 0.006]$ and $\gamma^s_{vox} \in [0.0037; 0.006]$ intervals. Furthermore, for the third interval ($\gamma^s_{vox} \in [0.0045; 0.006]$), the one with the highest strain values, the results of the simulation with cross-slip show that none of the slip events reached this level of deformation. In comparison, the simulation without cross-slip shows the presence of few events in the form of well-defined slip traces.

Secondly, as we can see, the position of the most intense slip events is located in a different region for the two simulations. In the case where cross-slip is not active, most intense slip events are clearly localized in zone II close to the stress concentration region. In comparison in the simulation with cross-slip, it is more difficult to define where these events are localized as there is no obvious plastic slip gradient.

Monitoring plastic slip activity during time intervals of the loading may be one approach to investigate more precisely the simulations. This allows a better identification of the areas in which plastic slip activity is most pronounced over a given period of time. Let's define

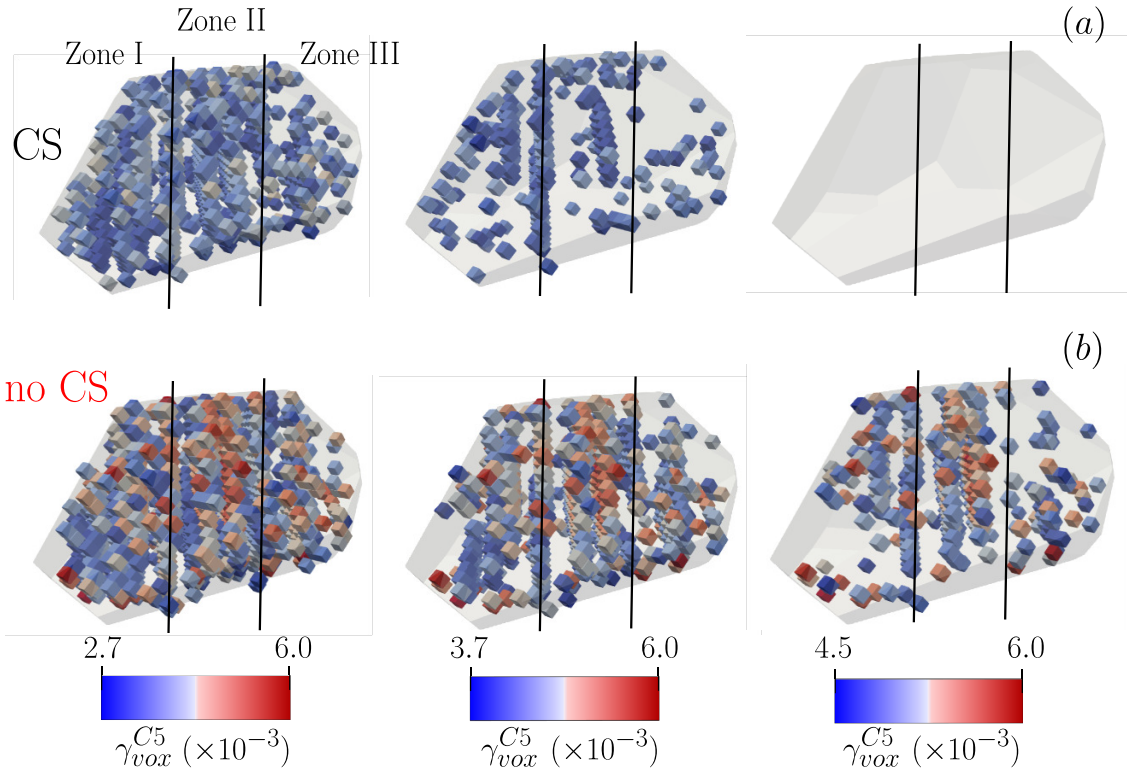

Figure 3.5: *Local plastic state described with the most intense slip traces computed in the grain for a simulation with and without the cross-slip (a) and (b).*

slip system activity for a given interval $[t,t+\delta t]$ as:

$$\Delta\gamma^s_{vox} = \gamma^s_{vox}(t+\delta t) - \gamma^s_{vox}(t) \tag{3.5}$$

This calculation is done for three time intervals and illustrated in Fig. 3.6-(a) for the simulation with cross-slip. These intervals have been selected to represent plastic activity during particular stages of plastic deformation:

- Interval 1-: This interval is used to describe plastic activity in the grain before cross-slip activation;
- Interval 2- and 3-: These intervals are used to describe plastic activity in the grain after cross-slip activation. Plastic activity is calculated for two various intervals to see if there is any change in the space distribution or intensity of the plastic activity.

For the first interval, it is clear that plastic activity is preferentially localized in zone II, close to the stress concentration region. As no cross-slip events are monitored during this interval it is expected to see that kind of trend as discussed in Chapter II. Thanks to this result, we understand that one or more dislocation sources are favourably positioned in relation to the stress concentration and allow the production of plastic slip in zone II.

For the second interval, the most intense plastic activity region has moved to zone I. As cross-slip is now active and more favourably active in zone I as illustrated in Fig. 3.5-(b) it is not surprising to observe such behaviour. As a consequence, plastic activity decreases sharply in Zone II because kinematic strain hardening due to previous slip events is stronger there than in Zone I. The cross-slip also allows sources to be deposited on new slip planes, which makes it easier for dislocations to move. The question is whether this is temporary or whether it has a lasting effect on the plastic behaviour of the grain.

By analysing the plastic activity during the third interval, we can provide some answers. During this last interval, intense plastic activity is monitored in Zone II supporting the idea that the intense activity in Zone I was temporary due to cross-slip activation. This idea is also supported by the results illustrated in Fig. 3.6-(b) showing the stress versus sum of plastic slip evolution for the three regions of the grain (zone I, II and III). As is clearly visible, zone III shows a more rigid plastic behaviour, which is corroborated by the fact that we did not monitor any intense slip events in this region. It is preferable to concentrate on the curves for zones I and II. Differences emerge during plastic deformation between these two curves. After the cross-slip activation, the blue curve experiences a change in slope, thus, a decrease in the strain-hardening rate. This impact is specifically related to the preferred cross-slip activation in this particular region. Throughout interval 2, the blue curve's slope is systematically lower than that of the orange curve. In other words, plastic behaviour is more ductile in Zone I than in Zone II. Conversely, during interval 3, the blue curve experiences a notable increase in slope, while the orange curve shows a relatively constant slope, thus, strain-hardening rate. Hence, in this interval, plastic behaviour becomes more ductile in zone II than in zone III, in agreement with the observations made in Fig. 3.6-(a).

In summary, we show that cross-slip modifies the local plastic activity. This is particularly visible in zone I where no stress concentration is applied but where the cross-slip is very active. Nevertheless, this preferential plastic activity in zone I seems to be transient as shown by Fig. 3.6. From these results, we can conclude that intense plastic deformation will rather be located in the region close to the stress concentration for higher levels of deformation. Hence, the local slip system activity and the role of the stress concentration are not being questioned by the cross-slip effect, which confirms the findings of the simulations presented in Chapter I, where the cross-slip mechanism was not considered.

3.4 Mechanisms involved in slip band initiation

To understand the physical mechanisms at the origin of intragranular plastic strain localization, it is essential to distinguish between the process of slip band initiation and persistence of the deformation in a slip band. In this section, using DDD simulations together with

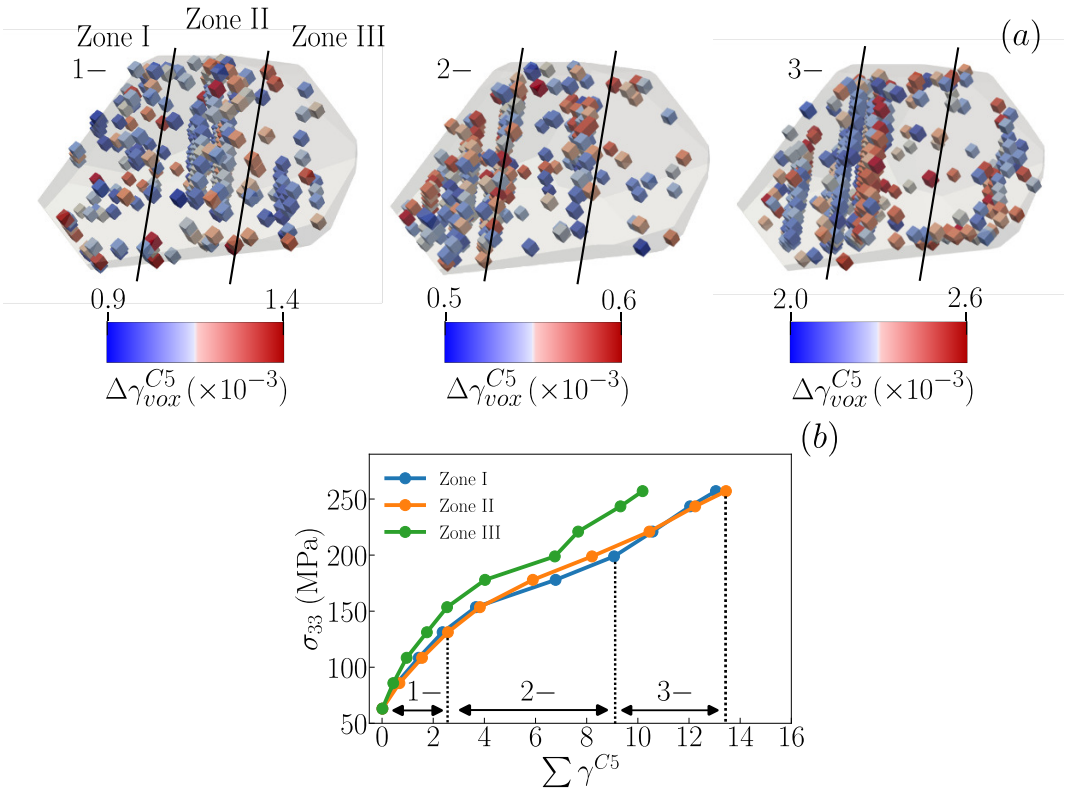

Figure 3.6: *C5 Slip system activity for several time intervals (a). Stress-sum of plastic slips ($\sum\gamma^{C5}$) curve (b). The sum of plastic slips is calculated for each voxel and for the three grain zones.*

detailed dislocation microstructure and reaction analysis, we investigate two mechanisms involved in the initiation of slip bands. By slip band initiation, we mean a mechanism that allows plastic deformation to be promoted in a finite region that contains a large number of parallel active slip planes, in a given grain. The simulations carried out in this section show the key contributions of these two mechanisms, namely the cross-slip (3.4.1) and the collinear annihilation (3.4.2).

3.4.1 Cross-slip contribution

In § 3.3, we presented the various ways that cross-slip can contribute to intragranular plastic deformation and the development of dislocation microstructure. On one hand, cross-slip facilitates a uniform distribution of dislocation sources within the grain volume, resulting in new dislocation segments that can serve as potential sources of plastic slip. On the other hand, slip bands are regions of extremely high plastic deformation with varying thicknesses that can reach micron-scale values. A slip band refers to a thick region where dislocations are numerous and deposited on a large number of slip planes. As a consequence, double cross-slip might be a mechanism that contributes to the thickening of areas with intense plastic deformation by introducing sources of dislocations in specific grain regions. Finally,

the results obtained and depicted in previous sections inspire confidence in the role of stress concentration in highly localized and intense plastic slip promotion. From the results illustrated in Fig. 3.4-(b), we understand that most of the cross-slip activity is localized in zone I. Nevertheless, cross-slip activity in Zone II is not negligible as the deformation in this zone is distributed at the end of the simulation in more than 200 slip planes. This represents an increase of 625 % with respect to the initial configuration.

To better understand the contribution of cross-slip in Zone II, let us focus on a thin band-like region of 1.6 µm as illustrated in Fig. 3.7 and located close to the stress concentration. As depicted in Fig. 3.7-(a) it is possible to calculate the evolution of the average interplanar distance in-between slip planes of this particular thin band-like region. Initially, interplanar distance is constant and equal to 1.6 µm, the thickness of the initial band-like region which is bounded by two active slip planes. Once the cross-slip is active, the average interplanar distance drops rapidly. At the end of the simulation, the average interplanar distance was decreased to 0.2 µm. Hence, the slip band spacing has been divided by eight with respect to the initial one. As a consequence, the effect of the cross-slip in this "band" is particularly visible and illustrates how a slip band-like region is progressively formed with the help of cross-slip. This thickening process is particularly visible in Fig. 3.7-(b), illustrating the dislocation microstructure in the thin band-like region before and after cross-slip events. At step 1, plastic deformation on slip system C5 (blue) is ensured by two slip planes while at step 2, it is ensured by seven slip planes. In this figure, the plastic activity of the collinear slip system (red) is also shown to be important as dislocations piling up at grain boundaries are numerous. This is partly due to the effect of the elastic strain incompatibilities, which allow an increase, locally, of the resolved shear stress on the system, but also to an effect linked to the interactions between dislocations of the primary and collinear system (collinear annihilations), which will be discussed in § 3.6.

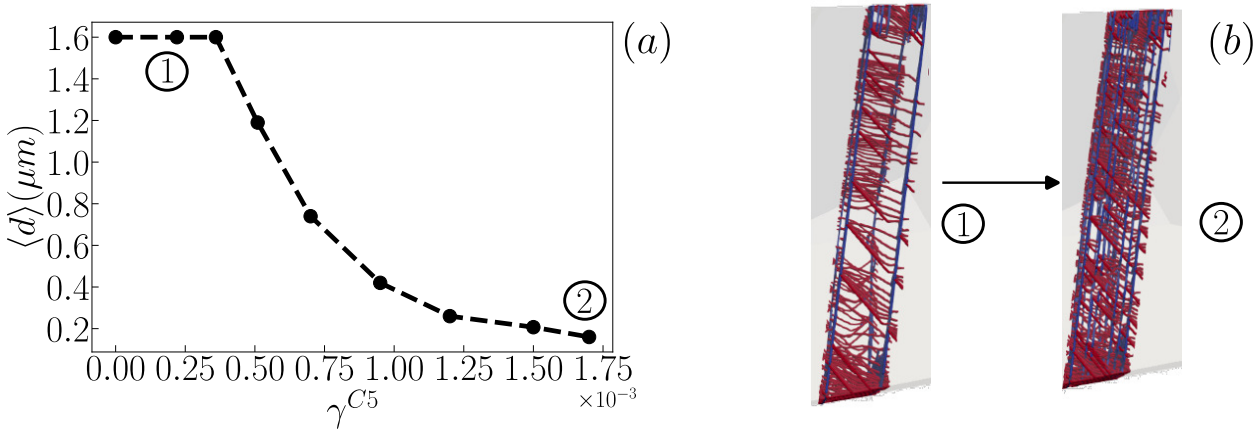

Figure 3.7: *Illustration of the effect of double cross-slip mechanism on the deformation distribution. Evolution of the mean interplanar distance as a function of plastic slip for a particular region inside the grain (b) during loading.*

From these results, we can see how dislocations can arrange themselves, thanks to cross-slip or double cross-slip, to promote the initiation of a slip band in a particular area of the grain close to a stress concentration. These results are coherent with previous observations found in the literature [Gilman and Johnston, 1962; Antolovich and Armstrong, 2014; Hussein et al., 2015] about the slip band thickening mechanism linked to cross-slip activity.

3.4.2 Collinear annihilation contribution

In this section, we describe the contribution of collinear annihilation reactions on the initiation of a slip band. These reactions occur when two dislocations of opposite signs and with the same Burgers vector glide on two different and collinear planes. Once they meet, the sections of the two dislocations annihilate at the intersection between the two slip planes. This results in the formation of a particular configuration illustrated in Fig 3.8. The two initial dislocation lines are separated into two parts, these two parts forming two new independent dislocation sources but shorter than before the collinear reaction. It has been shown through DDD simulations that this mechanism is of major importance for the work hardening of FCC single crystals in [Madec et al., 2003]. Moreover, other simulations have shown that these reactions enable the formation of a particular microstructure during the localization of plastic deformation in the form of PSB during cyclic loading [Déprés et al., 2006]. In this work, collinear annihilations have been proved to participate in some reorganizations of the dislocation microstructure, in particular by the creation of pinning points allowing the apparition of new Frank-Read sources.

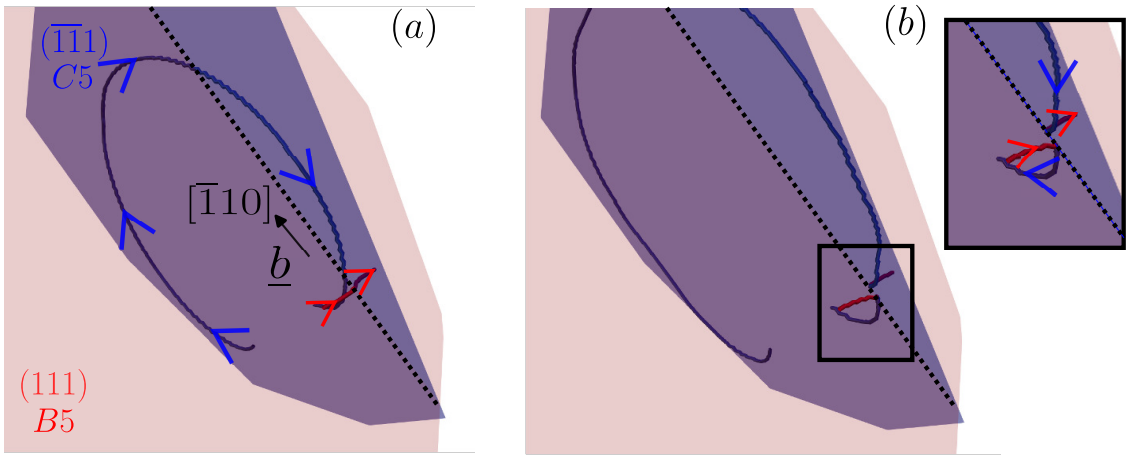

Figure 3.8: *The collinear annihilation mechanism. The blue plane is associated with the primary slip system,* $(\overline{1}11)$ *plane and the red plane is associated with the collinear slip system,* (111) *plane. Configuration before annihilation in (a) and after annihilation in (b). On both graphs, the dashed line is the intersection line of the two slip planes.*

Examples of dislocation microstructure reorganization due to collinear annihilations are illustrated in Fig. 3.9 and Fig. 3.10 for two slip planes extracted from the dislocation mi-

crostructure made with the simulation procedure presented in § 3.2.1. These simulations follow "set 2" simulation conditions with inactive cross-slip. The screenshots in Fig. 3.9(a)-(c) illustrate dislocation dynamics on one given slip plane including initially one dislocation source for two simulation conditions. Screenshots with the blue line consider the mobility of C5 dislocations while there is no density on the collinear slip system B5 (blue line, $\rho^{B5} = 0$). In comparison, screenshots with the orange line illustrate dislocation mobility for the same dislocation source while considering a nonzero dislocation density on the collinear slip system B5 (orange line, $\rho^{B5} \neq 0$). These screenshots are taken at different levels of plastic deformation as illustrated in Fig. 3.9-(d). Screenshot 1 shows the initial state of the dislocation microstructure on the extracted slip plane. Looking at the second screenshot, at a higher level of plastic deformation, it is clear that plastic slip is different between the two simulations. For the simulation considering no dislocations on the slip system B5, the Frank-Read source emitted only two dislocations loops. These loops are visible as they pile up at the grain boundaries. In comparison, the simulation considering the presence of dislocations on the collinear slip system ($\rho^{B5} \neq 0$) shows a much larger number of dislocations at certain grain boundaries. In addition, one can note that the Frank-Read source has been relocated to a new position on the slip plane. The re-localization process is provided by the mechanism of collinear annihilation by the creation of a new "pinning" point. This point at the intersection of two slip planes is located on the left arm of the initial dislocation source. It is interesting to note that this new location of the source is more favourable to plastic slip. Looking at Fig. 3.14-(b) we can see that the new dislocation source is located in the vicinity of the stress concentration region providing greater mobility. As a consequence, the number of dislocations piling up at the grain boundaries in this simulation is much higher than in the other one. For higher levels of plastic deformation as illustrated in Fig. 3.14-(c), plastic slip persists in the simulation with dislocations on the collinear slip system, whereas in the other simulation dislocation dynamics are prevented by the backstress.

Here, collinear reactions do not lead to an increase in the flow stress as observed in some simulations dedicated to strain hardening in single crystals. This is shown in Fig. 3.9-(d) illustrating the stress versus plastic slip curves. Such computation is made thanks to a voxel discretization (see § 1.6.1.4) in the vicinity of the slip plane. On the contrary, the collinear reaction results in the present simulation in a ductility gain. Indeed, at an equivalent stress level ($\tau^{C5} = 90$ MPa), the plastic slip calculated on the simulation with $\rho^{B5} \neq 0$ is much higher than the one with $\rho^{B5} = 0$.

In Fig. 3.10, another slip plane from the same dislocation microstructure is investigated during plastic deformation. Here too, there is a significant difference between the simulation considering the absence of dislocations on the B5 slip system and that considering the presence of dislocations on the B5 slip system. In this particular case, the Frank-Read source initially deposited in the grain volume is located very close to a grain boundary, preventing it

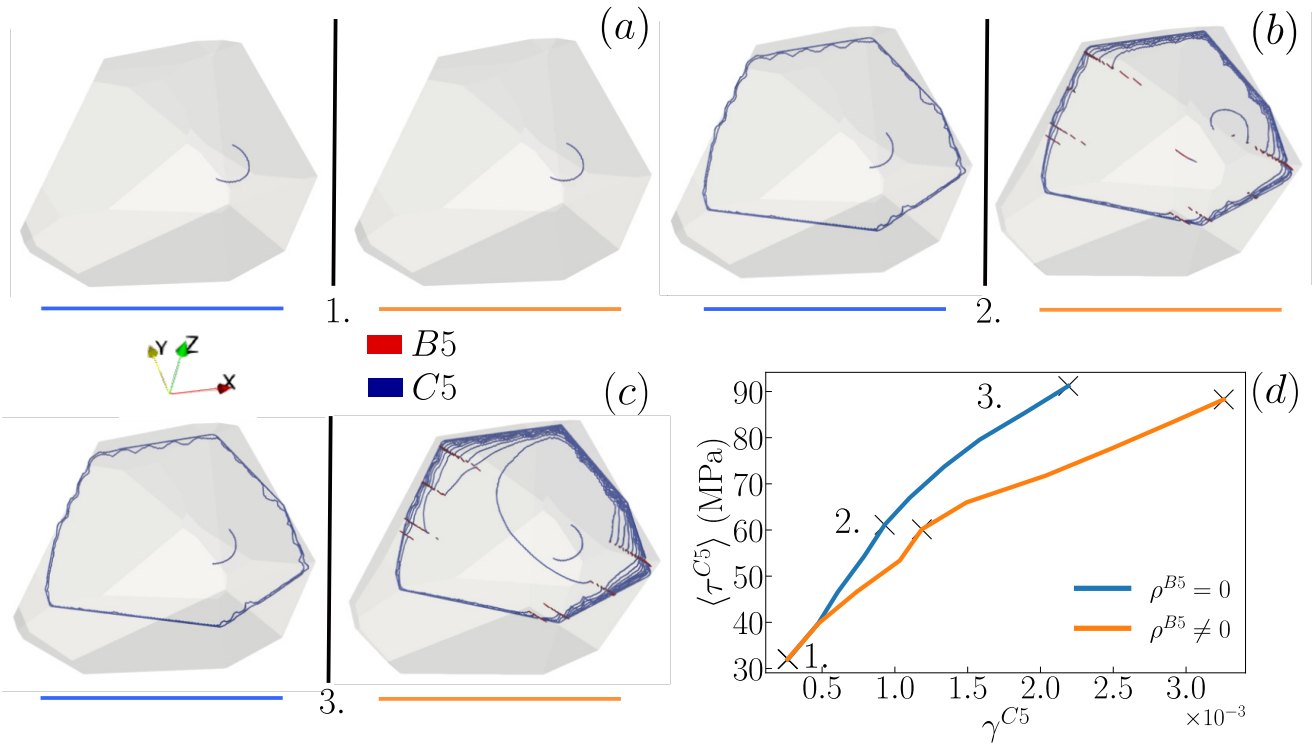

Figure 3.9: *Illustration of how the mechanism of collinear annihilation can help to produce plastic slip on a given slip plane. Comparison is made between a simulation without and with the collinear slip system B5 at three different times during loading (a), (b) and (c). The evolution of the applied stress as a function of the average plastic slip computed in a region around the slip plane (based on the voxel tessellation) is given in (d) for both simulations.*

from producing permanent plastic deformation, as shown in the screenshots Fig. 3.10(a)-(c). However, in the case where we consider density on the slip system B5, the collinear annihilations taking place during the plastic deformation once again allow a dislocation loop made by the initial Frank-Read source to form a new dislocation source with two new pinning points and located in a zone that is more favourable to slip. This is particularly visible in Fig. 3.10-(b). Thus, as shown in Fig. 3.10-(c) the number of dislocation loops piled up at the grain boundaries between the two simulations is very different. The ductility gain provided by this process is illustrated in Fig. 3.10-(d).

With the help of these two results, the role of collinear annihilations on the intragranular plastic behaviour has now been demonstrated. By relocating dislocation sources or forming new dislocation sources in regions favourable to plastic slip through the creation of pinning points, collinear annihilations increase the density of mobile dislocations on the slip planes. In this way, a gain in plastic slip is observed, enabling the initiation of plastic deformation in particular regions.

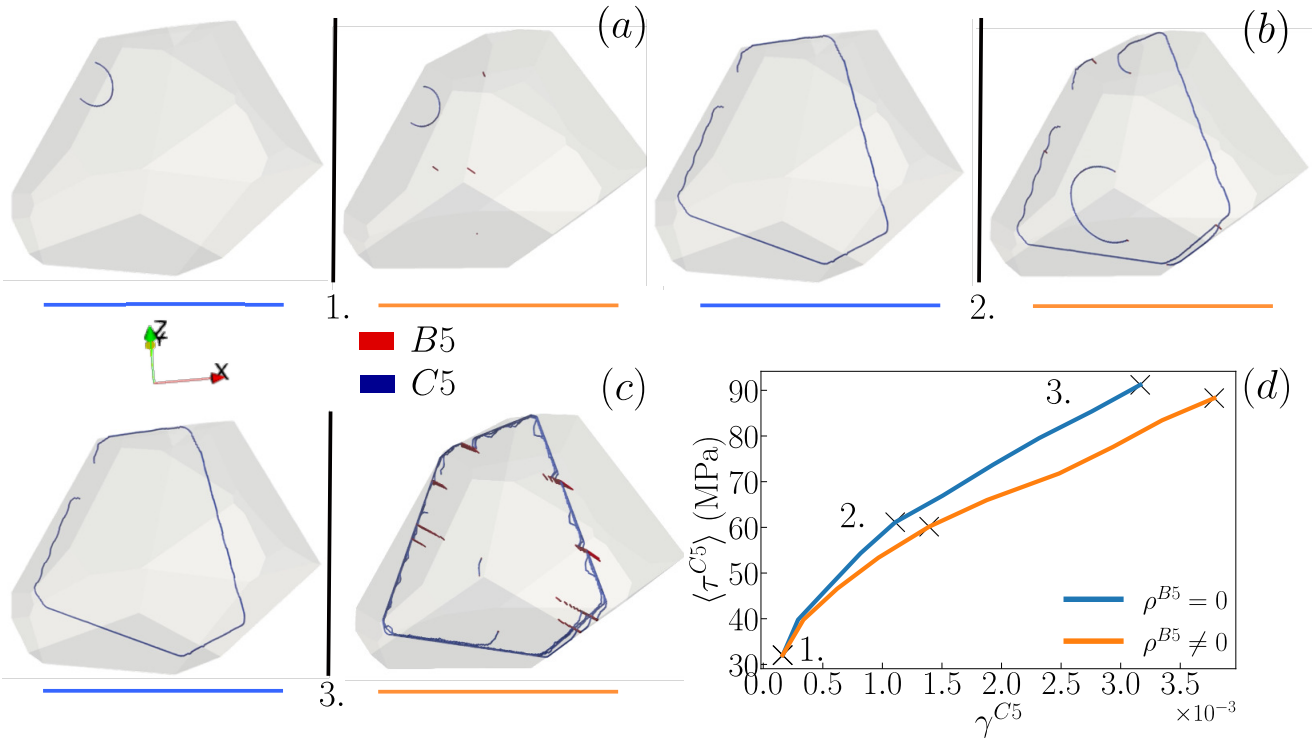

Figure 3.10: *Illustration of how the mechanism of collinear annihilation can help to produce plastic slip on a given slip plane with the formation of a new dislocation source. Comparison is made between a simulation without and with the collinear slip system B5 at three different times during loading (a), (b) and (c). The evolution of the applied stress as a function of the average plastic slip computed in a region around the slip plane (based on the voxel tessellation) is given in (d) for both simulations.*

3.5 Mechanisms involved in slip band persistence

The results of the previous section (§ 3.4) showed how, by certain mechanisms, plastic deformation can be initiated in particular regions of the grain. On the one hand, cross-slip is the mechanism by which a plastic deformation can be initiated in particular regions initially free of dislocations. This is the so-called thickening process described in § 3.4.1. On the other hand, the role of collinear annihilations is restricted to the slip plane level and permits the formation of new dislocation sources. We have demonstrated that collinear annihilation is a strong mechanism in order to relocate dislocation sources in favourable regions for the plastic slip, with the formation of strong "pinning" points.

The presence of intense and persistent intragranular slip bands is directly linked to the existence of flow stress softening mechanisms in these regions. These softening mechanisms can be the result of different contributions, linked to the type of solicitation or to the presence of obstacle-free zones, as in alloys and irradiated metals. These points are discussed in the literature review in § 1.2.2. For pure metals, as these mechanisms have not yet been identified, we propose here to study the role of cross-slip and collinear annihilations on the

persistence of a slip band. To do so, the role of cross-slip and collinear annihilations on the reduction of the kinematic and isotropic hardening is studied through model simulations as described in § 3.2.

3.5.1 Cross-slip contribution

Results presented in Fig. 3.7 showed that by cross-slip, the dislocation density on a particular slip system can be distributed in very close parallel slip planes during plastic deformation. Hence, plastic slip is distributed on a higher number of slip planes. It is reasonable to think that, by this mechanism, a diminution of the backstress (kinematic hardening) on the emitting dislocation sources can be observed. As a consequence, the role of the cross-slip on the kinematic hardening is first studied in this section. Results of the model simulations we made to investigate that point are illustrated in Fig. 3.11-(a). This figure represents the evolution of the applied resolved shear stress as a function of plastic slip for six simulation conditions on slip system C5 (see Tab. 3.1, "set a" simulations). The reference simulation (set a Sim. 1) shows the evolution of the stress as a function of plastic slip for a single dislocation source. In doing so, the hardening rate calculated is that of kinematic hardening only. The other simulations also represent stress evolution as a function of plastic slip but for two dislocation sources disposed on two parallel slip planes. For every simulation, the separation distance varies, from 50b to 2000b. By this process, the cross-slip distribution mechanism in a thin region is mimicked. The results of the calculations show that all the curves are superimposed regardless of the separation distance, and the kinematic hardening rate is essentially unchanged. This result strongly suggests that the backstress due to dislocations piling up at grain boundaries exerts its influence (out-of-plane long-range contribution) on slip planes close to each other. This point will be further discussed in the next paragraphs.

Further calculations were performed to see the influence of cross-slip on isotropic strain hardening (see Fig. 3.11-(b)) in four simulations described in Tab. 3.1, "set b". This figure shows very close average threshold stresses for all the simulations we made. The evolution of the plastic flow, in this case, is very jerky, but computing the apparent flow stress imposed by forest reactions is possible by drawing a line in between the oscillations of the applied stress. As a consequence, distributing plastic deformation on close parallel slip planes is not observed to impact the forest yield stress. This result may seem a bit surprising as we can imagine that the density of dislocations on close planes allows for a reduction of the critical stress of the forest by changing local junction configurations. For instance, by reducing the stiffness of the junctions as a result of the simultaneous passage of dislocations on the same junction, thus limiting the junction length. In fact, our simulations show that in agreement with the forest model, the key parameter for forest strengthening is the number

of forest obstacles and not the details of junction configurations. Hence, the computed flow stress is not really impacted by a distribution of slip on parallel close slip planes that may result from cross-slip activity. One can conclude from the above model simulations that the distribution of plastic slip on close parallel slip planes has a very weak influence on kinematic and isotropic hardening.

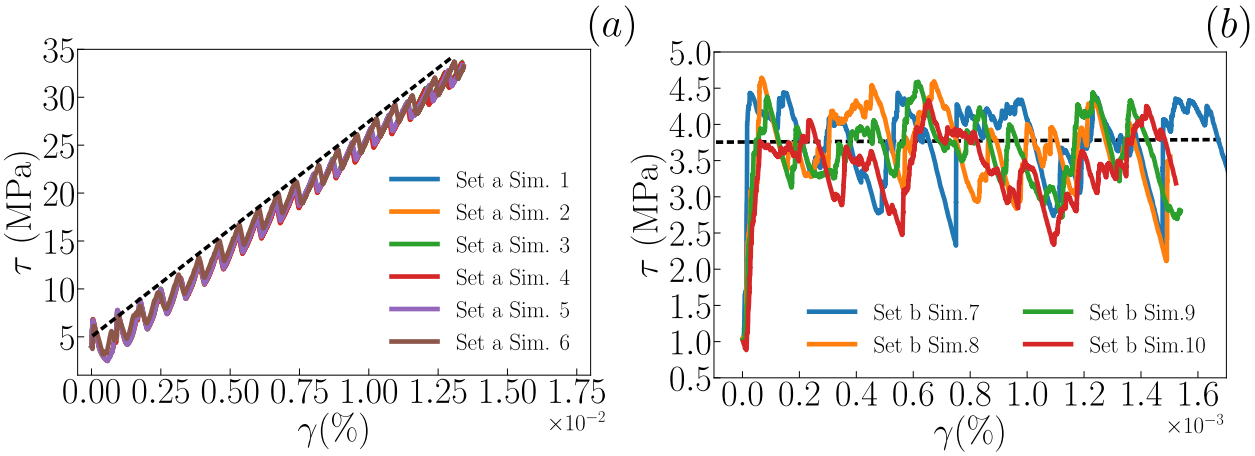

Figure 3.11: *Stress versus plastic slip curves for several simulations. Direct observation of the kinematic hardening (a) and isotropic hardening (b).*

Particularly surprising is the almost total absence of any influence of the distribution of dislocation sources allowed by cross-slip on kinematic hardening. It would have been reasonable for plastic deformation distributed over a larger number of planes to reduce the number of dislocation loops piled up at grain boundaries per slip plane, thereby influencing the backstress. However, by the calculation presented in Fig. 3.12, we show that the backstress does not just affect the slip plane but also has an influence in the out-of-plane direction. Taking two model simulations supposing the plastic deformation on one slip plane as illustrated in Fig. 3.12-(a) and on two slip planes as illustrated in Fig. 3.12-(b) with an interplanar distance of 2000b = 0.5µm we plot the evolution of the backstress [Hirth et al., 1983] as a function of the out-of-plane distance Y in Fig. 3.12-(c). In this figure, those evolutions are calculated at various numbers of dislocations piling up at the grain boundaries N_d (4, 6 and 8). It can be easily seen that the intensity of the backstress is pretty constant until long distances, a decrease of the stress intensity begins between 2 µm and 3 µm. In addition, a comparison between stress evolution for both simulation conditions shows no differences. No matter whether the deformation is distributed on two slip planes or not, the backstress calculated at the same point inside the grain is equivalent. This result explains why in the previous simulations all the curves were superimposed seeing no effect on the kinematic hardening rate. The distances for which the backstress decreases are greater than the classic slip band thicknesses and therefore could not contribute as a softening mechanism contributing to slip band persistence.

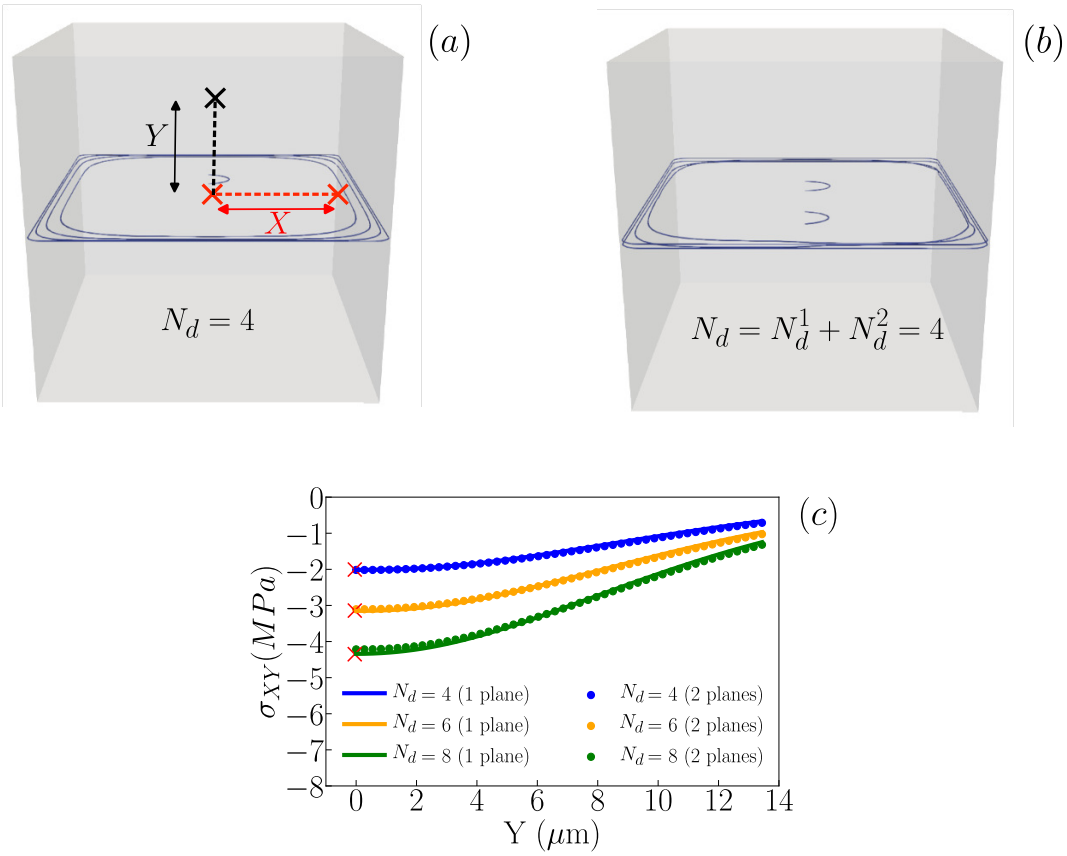

Figure 3.12: *In-plane internal stress component as a function of Y, the slip plane normal. Computation is realised for two simulations, one with only one Frank-Read source and the other one with two Frank-Read sources on two // slip planes. Interplanar distance is fixed to* 0.5 µ*m. The stress is computed from the centre of the grain and following Y direction (black dotted line).*

3.5.2 Collinear annihilation contribution

In this part of the manuscript, investigations on softening mechanisms are extended to the particular case of collinear annihilations. It is now clear that the role of collinear annihilations in the arrangement of dislocations within a slip plane is considerable. Collinear annihilations increase the density of mobile dislocations on a slip plane, thereby allowing significant plastic deformation. Hence, we wish to verify the role that increasing the mobile dislocation density on a slip plane could have on kinematic and isotropic strain hardening. To do so, we performed the same model simulations as in § 3.5.1. Results of the model simulations in the case of kinematic (a) and isotropic (b) hardening are illustrated in Fig. 3.13. As in the simulations of the role of cross-slip, the forest strength and the kinematic strain hardening slope are both constant across various simulations. Dislocations located on the same slip plane annihilate or interfere with others, leading to no change in the hardening behaviour.

However, looking at the distribution of dislocation loops along the grain boundaries in Fig. 3.9-(c) it is possible to notice a very strong heterogeneity. Indeed, on the upper part of

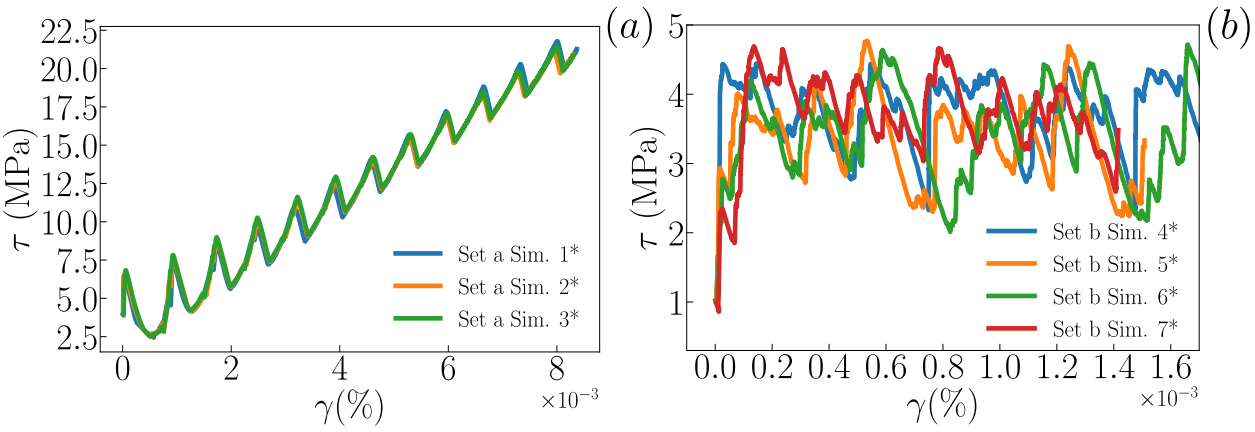

Figure 3.13: *Illustration of the role of mobile density on both kinematic (a) and isotropic (b) hardening.*

the slip plane about fifteen dislocation loops have piled up, while on the lower part, there are only four. This difference is explained by the successive annihilation of the lines due to the passage of dislocations of the collinear system during the plastic deformation. What Fig. 3.14 shows is that due to this heterogeneity of the plastic slip, the internal stress field in the case where $\rho^{B5} \neq 0$ becomes heterogeneous, whereas it is quasi-homogeneous in the case where $\rho^{B5} = 0$. By comparing this distribution with that of the applied stress, one can notice a phenomenon which tends to homogenize the total stress ($\tau_{tot}^{C5} = \tau_{int}^{C5} + \tau_{app}^{C5}$) on the slip plane. In the figure, internal resolved shear stresses are given in absolute value, and the internal stress distribution is in on all voxels opposite to the applied resolved shear stresses as dislocations are polarized at the grain boundary. Further calculations of this internal stress homogenization process were carried out. We conclude from this study that this homogenization process does not significantly modify strain-hardening for the strain amplitudes we can simulate.

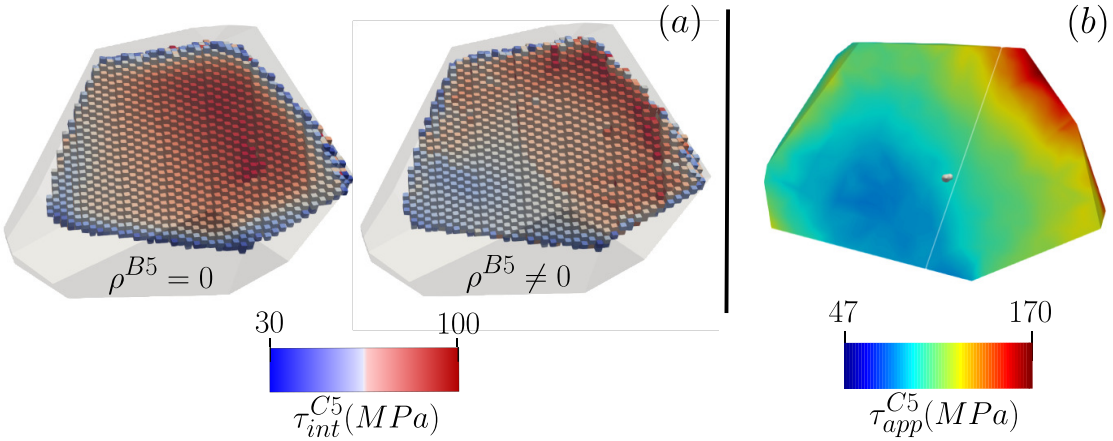

Figure 3.14: *Stress state on a particular slip plane during plastic deformation at* $\langle \tau_{app}^{C5} \rangle = 90$ *MPa. Illustration of the internal stress mapping for both simulations, without and with dislocation density on the collinear slip system (a). Corresponding applied stress mapping on the same slip plane (b).*

These results clearly show the importance of cross-slip and collinear annihilation on the potential initiation of a slip band but do not explain how it could persist. We'll see in Chapter IV how, by integrating other behaviours such as reactions between dislocations and grain boundaries, we can introduce the idea of persistence.

3.6 Original microstructural behaviours

In this part, a description of some original microstructural behaviours we observed with the help of DDD simulations is given. This description is purely qualitative and is intended to give the reader a more precise view of the various mechanisms that take place in a discrete manner in DDD simulations. For each behaviour described, the dislocation microstructure is shown with some explanations and schematic illustrations when necessary.

Some of these reactions are related to slip systems interactions in-between the primary and collinear slip system (§ 3.6.1). These microstructural behaviours confirm the role of collinear annihilations on slip band initiation. The strong line tension due to the particular configurations created during collinear annihilations is the reason for some of these original behaviours. It is important to note that the line tension is directly dependent on the curvature of the dislocation line [Foreman, 1967; Gomez-Garcia et al., 1999] and stress values can be very high.

Other mechanisms related to dislocation contact reactions (§ 3.6.2) and line recombination are described in the following. These mechanisms are particularly of interest to explain cross-slip activity monitored in the vicinity of grain boundaries not necessarily oriented along the screw direction. In addition, it is also shown that some dislocations, by a line recombination process, can bypass obstacles such as dislocation pileups.

3.6.1 Collinear annihilation reactions

3.6.1.1 Piled up dislocations backward movement

The first original behaviour presented in this section of the manuscript is the motion of some dislocation lines close to grain boundaries. In simulations, it is often found that some dislocations can move away from the grain boundary regions once they are stacked in a pileup. This behaviour is illustrated in Fig. 3.15 by the six screenshots, (a) to (f) describing the kinematics of the reactions. For these illustrations, the dislocation microstructure of one particular slip plane taken from the complete microstructure is extracted. The kinematics is here detailed point by point:

- Step 1, Fig. 3.15-(a): This step illustrates the dislocation microstructure on the slip

plane (belonging to slip system C5) before any dislocations from slip system B5 crosses it. Two dislocation loops are piled up at the grain boundaries.

- Step 2 Fig. 3.15-(b): A dislocation from the slip system B5 crosses the slip plane leading to a collinear annihilation with one of the dislocations piled up at the grain boundaries. The dislocation Burgers vector is illustrated to show the collinear annihilation direction. As a result, the same configuration as illustrated in Fig. 3.8 is created.
- Step 3 Fig. 3.15-(c): Once again, a dislocation line from the slip system B5 crosses the slip plane reacting with the other dislocation piled up at the grain boundaries resulting in a second collinear annihilation. One of the parts of the dislocation line formed during the first collinear annihilation starts to translate slightly to the right. It's clear that the two dislocation lines formed by collinear annihilations have a very important curvature, resulting in increased line tension.
- Step 4 Fig. 3.15-(d): The dislocation line is further translated to the right. This is the effect of the line tension applied to this part of the dislocation line. As a result, it pushes the dislocation backward from the grain boundaries to reduce the line curvature and reduce the tension applied to the dislocations.
- Step 5 and 6 Fig. 3.15-(e) and (f): The dislocation line starts to bow out from the configuration shown in (e). From this process, a new dislocation can be emitted on the slip plane, as shown in (f) leading to the creation of a novel dislocation source. The same process is repeated for every collinear annihilation reaction on the top of the slip plane allowing plastic slip to be more permanent on this particular slip plane.

The observation and description given by these screenshots demonstrate the potential of collinear annihilation to initiate or maintain plastic slip on a given slip plane. It also demonstrates the importance of line tension in pushing the dislocation lines out from the grain boundary region and thus in opposition to the applied stress field on the slip system. To the author's knowledge, this relaxation mechanism close to grain boundaries has never been described in the literature and it was therefore important to illustrate the process step by step.

A schematic presentation of such a re-emission process, induced by a collinear annihilations process and line tension, is illustrated in Fig. 3.16. This figure pictures the reaction taking place during the mechanism presented just before, with the sign of the dislocation segments highlighted. The fact that the line circuit is shown makes it easier to understand how a dislocation line can bow out in the direction opposite to the pile-up packing. As shown in Fig. 3.15, the line tension associated with the collinear annihilation pushes a section of the dislocation line out of the grain boundaries (to the right side of the schematic). In doing

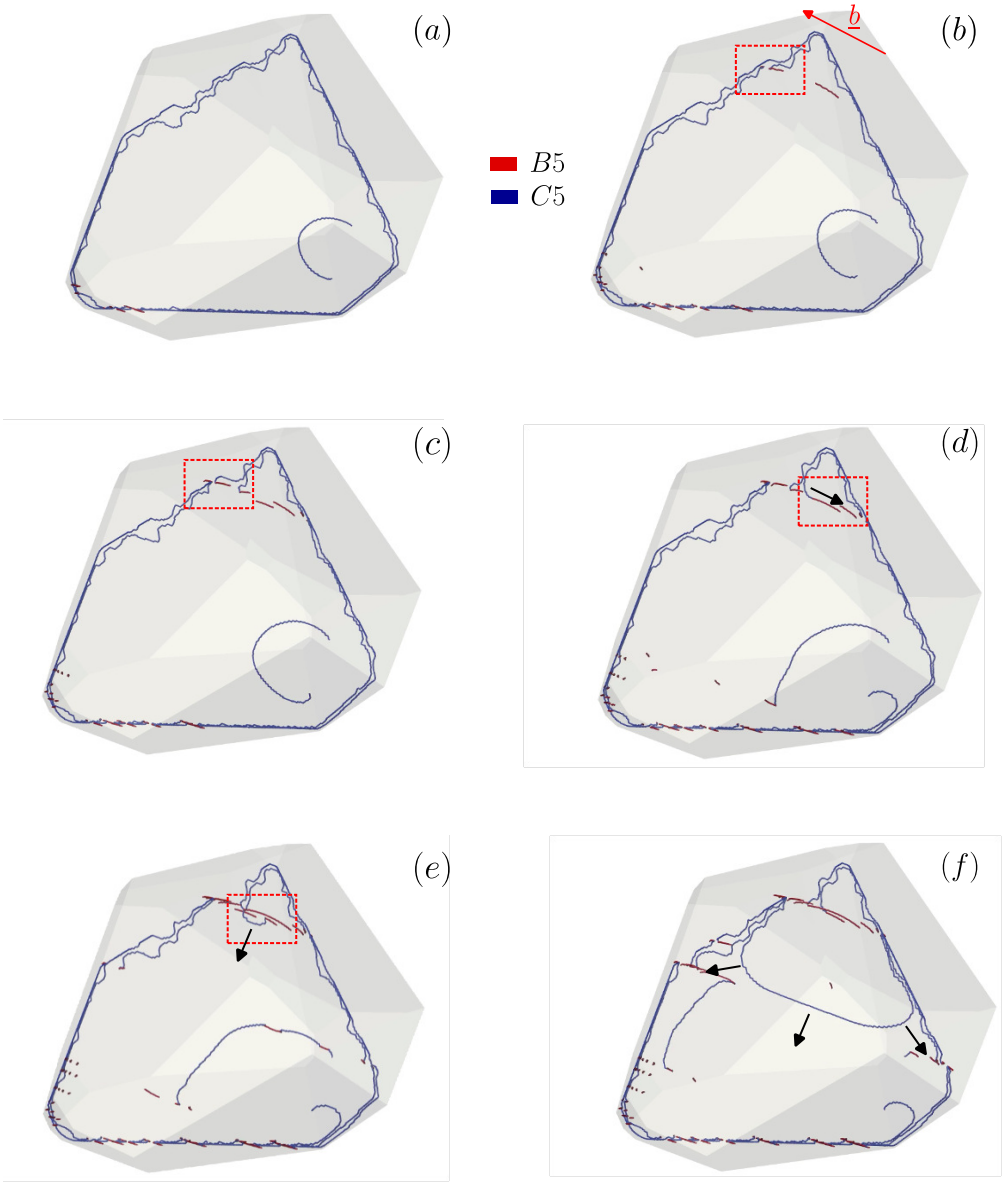

Figure 3.15: *Screenshots highlighting the role of the line tension in dislocation re-emission on one particular slip plane during plastic deformation. (a) dislocations piled up at the grain boundary, (b)-(d) collinear annihilation reactions at grain boundary and (e)-(f) re-emission of a dislocation loop from the top of the slip plane.*

so, a straight line portion is made with a sign opposed to the dislocation segments part of the pile-up. This new segment has the same sign as the dislocations piled up on the lower part of the slip plane and glide in a direction opposed to the segments stacked in the pile-up. If such a segment is long enough, it can act as a dislocation source in this region with very high internal stress.

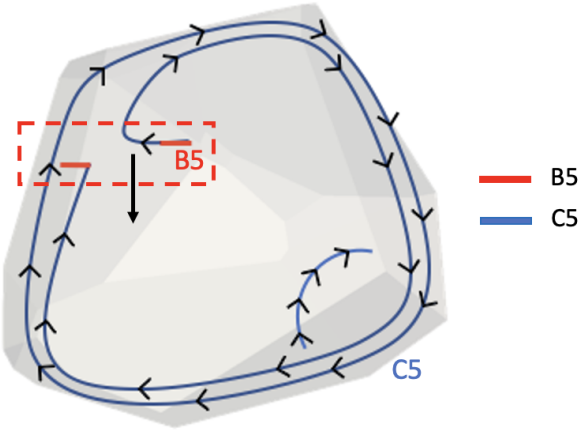

Figure 3.16: *Schematic representation of the re-emission process with the sign of each dislocation segment.*

3.6.1.2 Lengthening or shortening of Frank-Read sources

Another behaviour that we observed many times in DDD simulations is particularly intense plastic activity on collinear slip systems (like B5 in the simulation following "set 2" conditions) as illustrated in Fig. 3.7-(b) while its Schmid factor remains very low. One reason explaining intense plastic activity on such systems is the role played by collinear annihilations. In collinear annihilation reactions, the portion of the dislocation line belonging to the collinear slip system B5 can either be elongated or shortened. In the case of elongation, the critical stress for dislocation emission [Foreman, 1967] is rapidly reduced. This process is often monitored during simulations as illustrated in Fig. 3.17. In this figure, three screenshots taken from a particular region inside the grain are illustrated. For visualization purposes, only two slip planes belonging to C5 and one slip plane to B5 are represented. Fig. 3.17-(a) illustrates the result of one collinear annihilation with a very short line portion of B5 as highlighted by the black dotted square. With this length, is it impossible for the new dislocation source to emit dislocation loops. Nevertheless, during the simulation, due to a dragging effect provided by the motion of the dislocation part on slip system C5 the dislocation on B5 is elongated as illustrated in Fig. 3.17-(b). At a higher level of plastic deformation (later in the simulation), the dislocation segment is even more elongated as illustrated in Fig. 3.17-(c). As a result, the dislocation source bends for a lower stress and this allows plastic slip to be initiated on a slip system with a low Schmid factor. The evolution of the critical stress for a Frank-Read source as a function of its length is given by the following equation and is illustrated in Fig. 3.17-(d) for the edge and screw dislocation character:

$$\sigma_c = A \times \frac{\mu b}{2\pi} \times \frac{1}{L} \times \left[log(\frac{L}{r}) + B \right] \tag{3.6}$$

with L the dislocation length, r the dislocation core radius (close to b) and $A = 1$ for edge character and $A = 1.5$ for screw character. Such phenomena are frequently observed in the

simulations and appear to be very efficient in promoting plastic slip on a collinear slip system with a very low Schmid factor.

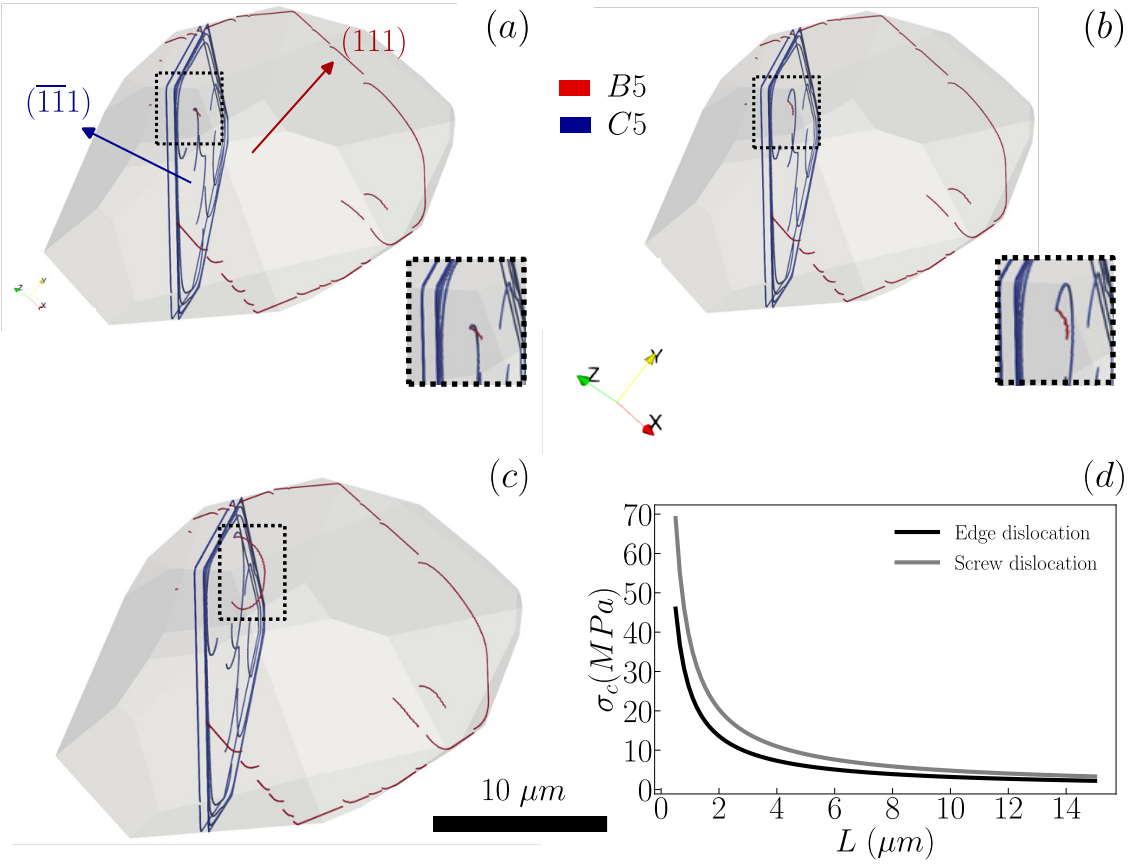

Figure 3.17: *Illustration of one elongation mechanism observed during the simulation due to dislocation dragging on the collinear slip system B5 by dislocations on the primary slip system C5. By this process, the length of the line is increased to a certain value lowering the critical stress for dislocation emission.*

Note that the opposite mechanism can be attributed to dislocation line shortening, raising the critical stress for the Frank-Read sources and limiting plastic slip.

3.6.2 Line recombination reactions

3.6.2.1 Cross-slip near non-screw GB direction

Cross-slip allows the screw character dislocations to change slip system, moving from the so-called primary slip system to the collinear (deviate) slip system of the same Burgers vector. In the simulations presented in this manuscript, cross-slip is modelled following the Friedel-Escaig model [Bilby, 1957; Escaig, 1968a]. From this model, cross-slip is decomposed in distinct states. First, to allow cross-slip it is necessary that dissociate dislocations form a perfect screw dislocation. This is called the constriction step. Secondly, the perfect screw

dislocation must dissociate in a stable configuration with two partial dislocations on the deviated slip system. This transition is controlled by a critical nucleation length for which it is energetically favourable to spread the stacking fault ribbon on the deviated slip system. In DDD simulations, this transition step which is a function of the temperature and local stress state is numerically tested by an algorithm described in § 1.6.1.3. In addition, in DDD simulations, the cross-slip length (l) can increase during the process in accordance with the theory. This is illustrated in Fig. 3.18 for dislocations piling up at a grain boundary oriented in the screw direction.

This drawing shows, in an ideal setting, a cross-slip event resulting from a dislocation in the primary slip system piled up against a grain boundary oriented along the screw direction as illustrated in step 1. The calculation of the cross-slip probability gives rise to the possibility of deviation (step 2), and part of the dislocation loop is emitted onto the deviated slip system (step 3). Calculating the stress expressed on each arm of this dislocation results in a more or less significant elongation of the cross-slip length (l_j) and therefore of the dislocation line. By the lengthening of the deviated dislocation, the bow out is facilitated and allows dislocations to multiply on the deviated slip system.

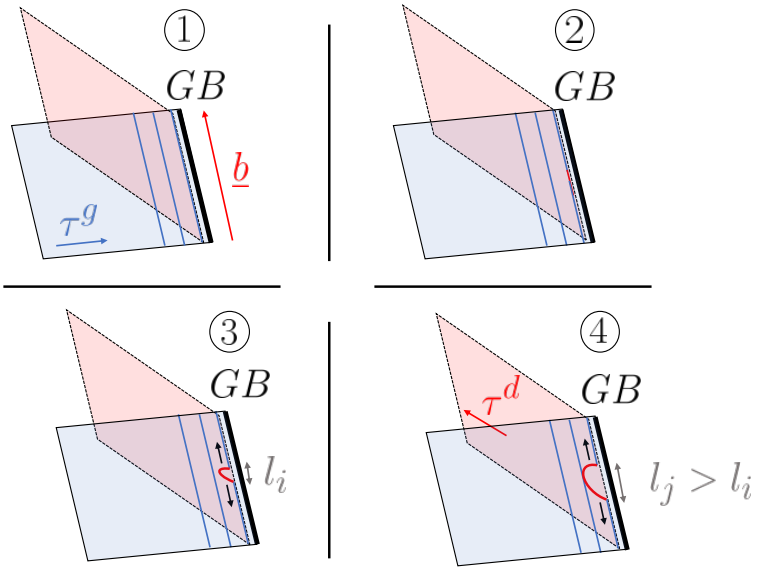

Figure 3.18: *Schematic illustration of the cross-slip close to a grain boundary oriented along the screw direction, modelling the ideal case of the Friedel-Escaig theoretical model.*

This kind of representation is perfectly valid in ideal cases. However, consideration of more realistic simulation conditions, such as the modelling of grains with a Voronoi-type geometry, involves grain boundaries whose planes are not necessarily oriented in the screw direction. However, even for this type of configuration, many cross-slip events are counted close to the grain boundaries. This is made possible by dislocation line recombination mechanisms, which we will describe in the specific case of a cross-slip event occurring close to a grain boundary that is not oriented in the screw direction. In the case shown schematically in

Fig. 3.19 and derived from the dislocation microstructure simulated in Fig. 3.20, the disorientation of the grain boundary with respect to the screw direction remains low. Thus, for this type of configuration, it is quite possible to obtain the type of mechanisms that we describe below. However, this seems less and less likely as the disorientation increases. Indeed, the initial length of screw dislocations would become smaller and smaller and the stress applied to each of the arms of the source should no longer be sufficient to allow elongation of the cross-slip length. It is reasonable to think that in this type of configuration, the cross-slip events observed close to the grain boundaries are linked to the drag of debris up to the grain boundary. This debris may also have originated from previous cross-slip events in the grain or be the result of previous collinear annihilation. In the case of collinear annihilation, this leads to an important notion, namely independence from thermal activation. In fact, this type of reaction is not directly controlled by thermal activation and therefore allows us to better understand how the cross-slip can be so active in our simulations and for the levels of plastic deformation reached. Note that, the description of the mechanisms we give below applies to a cross-slip event arising from the dislocation pileup, but the mechanisms would be perfectly identical in the case of the presence of debris at the grain boundaries.

A description of Fig. 3.19 is given step by step:

- Step 1: Dislocations are piling up against a grain boundary which is not oriented along the screw direction. The dislocation line length belonging to the screw character is considerably reduced compared with the previous ideal case.
- Step 2: A cross-slip event is observed for one very small portion of the line which is oriented along the screw direction.
- Step 3: Small lengthening of the dislocation line due to stress expressed on both arms. Due to this process, dislocation III moves toward dislocation II.
- Step 4: The distance between dislocation III and II becomes very low, so a reaction is necessary. The only possibility that follows Frank's rule is to perform line recombination. In this particular case, no junctions can take place between III and II dislocations as they have the same Burgers vector, the only possible reaction is a line recombination between these two dislocations to reduce the energy of the system. By doing so, deviated dislocation on the left-hand side becomes connected with dislocation II while the right-hand side is still connected to dislocation III. By doing so, the cross-slip length can continue to grow in order to allow dislocation to bow out.
- Step 5 and 6: Lengthening of the deviated dislocation continues by the same procedure with the other dislocation piled up against the grain boundary, dislocation I.

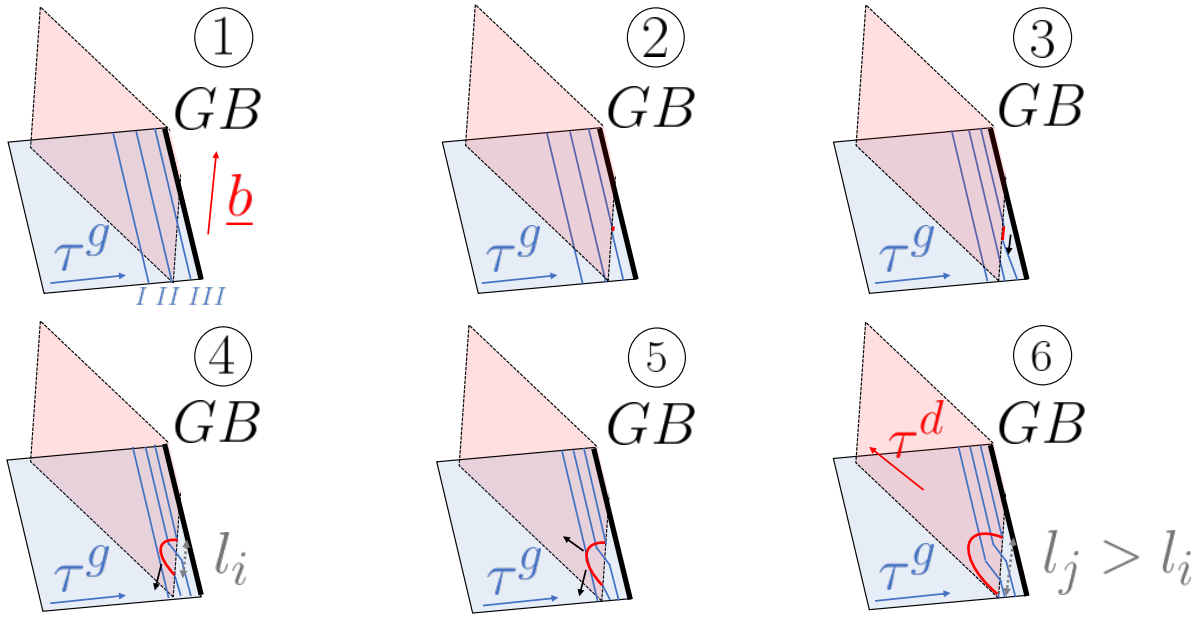

Figure 3.19: *Schematic illustration of the cross-slip close to grain boundary not orientated along the screw direction. Lengthening of the deviated dislocation is realised by systematic line recombination in the pileup started from a tiny collinear dislocation line at the beginning.*

This mechanism is often recorded during the simulations in the dislocation microstructure as illustrated in Fig. 3.20. The lengthening of the deviated dislocation line is particularly visible in this figure. By this process, cross-slip can be activated everywhere in the grain volume, no matter the grain boundary orientation. Due to a lack of time, we did not have the time to investigate the most favourable grain boundary orientation to promote such a mechanism.

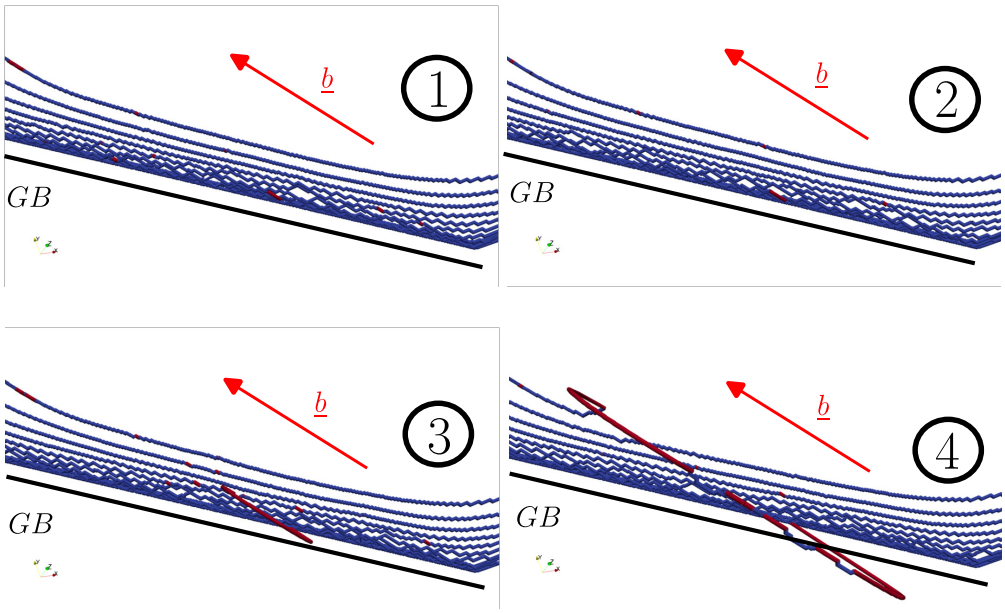

Figure 3.20: *Direct observation on the process of dislocation line recombination favouring cross-slip emission on the deviate slip system.*

3.6.2.2 Line recombination to by-pass obstacles

The equivalent mechanism of line recombination as the one depicted in § 3.6.2.1 is observed for the by-pass of collinear reactions obstacles generated during plastic deformation. As observed in Fig. 3.9, reactions between collinear slip systems produce many obstacles in particular regions close to the GBs where the dislocation density is high. The obstacles generated with collinear reaction being mobile in the screw direction, they can move, after a few deformation steps, far away from the grain boundaries. Once again, one can think that the accumulation of such obstacles may highly reduce the mobility of the primary slip system dislocations. The reality suggested by simulations is different and dislocation line recombination allows an easy bypass of these obstacles as illustrated in Fig. 3.21. This additional reaction mechanism is here divided into three steps: step 1, a dislocation loop on the primary slip system is approaching the result of a collinear reaction. Step 2, a reaction is necessary as dislocations are now very close and the dislocations on the primary slip system have the same sign. Hence, a line recombination is possible to reduce the elastic energy as in previous illustrations. Step 3, a part of the mobile dislocations on the primary slip system is made free to glide further and to produce more plastic slip. With this process the stacking of dislocation in the pile-up is made possible even with the existence of many collinear obstacles and the dislocation microstructure close to GBs is well organized (relaxed).

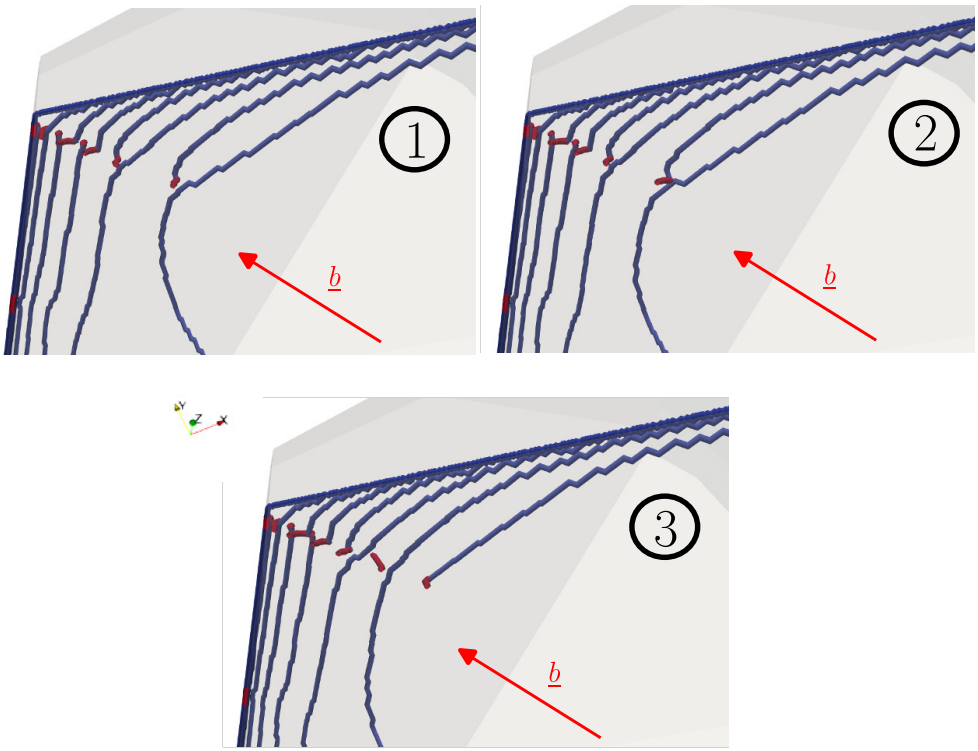

Figure 3.21: *Direct observation on the process of line recombination leading to the by-pass of collinear interactions obstacles. By this process, dislocations are still able to pileup close to GBs and produce more permanent plastic slip on the slip plane.*

3.7 Conclusion

In the course of this chapter, we have been able to demonstrate the dominant role of contact reactions between all dislocations and thermally-activated mechanisms such as cross-slip. These mechanisms strongly influence the local plastic slip.

In particular, we have shown that for the model material system considered (pure nickel), cross-slip homogenizes slip within the grain during plastic deformation. Indeed, we have shown that in the primary system, i.e. the most active, the number of dislocation sources increased considerably when cross-slip is active. We have also shown that cross-slip homogenization leads to a temporary change in the distribution of regions within the grain with the most intense plastic slip. However, this effect appears to be transient and our results show that plastic slip always appears to be more favourable in zone II, close to the region of stress concentration. Thus, the results obtained by considering the influence of cross-slip in the simulations do not call into question the conclusions reached in Chapter II.

We then turned our attention to identifying the mechanisms directly linked to the dislocation microstructure that explain the initiation of plastic strain localization in particular regions. To this end, cross-slip and collinear annihilation were identified as key mechanisms. We have shown that cross-slip allows the thickening of plastic deformation from one slip plane to several parallel slip planes, leading to the transition from a slip trace structure to a slip band structure. Secondly, it was shown that collinear annihilations are essential mechanisms for the formation of pinning points in regions of larger stress and more favourable to plastic slip. Through this mechanism, sources of dislocations are created in many regions but they are more active in the regions where the stress is high. However, this mechanism is limited to the scale of the slip plane, which is not the case for cross-slip which can form new sources everywhere in the grain. These two mechanisms are not independent since, as we have shown, the cross-slip considerably increases the density of dislocations on the deviated slip system and thus increases the probability of collinear annihilation.

In addition, these two mechanisms do not lead to a very effective change in isotropic and kinematic strain hardening, as might reasonably be expected in the small range of plastic deformation that was simulated. Through a series of model simulations, we have shown through different case studies that the backstress stress as well as the critical stress of the forest is not altered by the activation of these two mechanisms. However, the dislocation microstructures illustrated in this chapter reveal a high degree of heterogeneity in plastic slip at the scale of the slip planes, the consequences of which will be discussed in Chapter IV.

Finally, we have illustrated in this chapter a series of mechanisms related to reactions between dislocations and microstructure organizations during plastic deformation. Through these observations, we demonstrate once again the predominant role of collinear annihilations

as well as certain line recombination mechanisms associated with a decrease in the elastic energy, i.e., elastic relaxation. These mechanisms were illustrated with a qualitative analysis of their effect on the dislocation microstructure organization during plastic deformation.

Chapter IV

Modelling grain boundary resistance in the DDD framework

Résumé :

Au cours de ce chapitre, nous nous intéressons à développer et intégrer une règle locale permettant de prendre en considération les réactions entre dislocations et joints de grains au cours de la déformation plastique. Les résultats présentés au chapitre précédent ont notamment permis de montrer que les contraintes en tête d'empilement étaient d'un niveau très important pour des taux de déformation plastique pourtant relativement faible. En considérant le cas limite où la transmission/absorption des dislocations au niveau des joints de grains entraîne l'annulation du backstress, nous montrons l'influence de telles réactions sur la présence d'un glissement plastique local et intense. Par ailleurs, l'influence d'une activité du cross-slip plus ou moins forte ainsi que le rôle joué par les systèmes de glissement non colinéaires sont discutés à travers une série de simulations DDD. Pour finir, plusieurs simulations sont réalisées en considérant différents chargement élastiques intragranulaire et montrant une fois de plus le rôle joué par la région de concentration de contrainte sur l'apparition d'un glissement plastique intense et localisé. A travers ces résultats, les réactions entre dislocations et joints de grains apparaissent comme des mécanismes prépondérants pour permettre d'expliquer la persistance d'une bande de glissement au cours de la déformation plastique.

Contents

4.1 Introduction

The literature review in § 1.4 underscores the complexity inherent in the mechanisms governing contact reactions between dislocations and grain boundaries. This topic has been extensively studied over many years and yet a comprehensive understanding still remains elusive. The range of contact mechanisms is diverse and intricately linked to features at the atomic scale. Consequently, incorporating such mechanisms into a DDD code requires meticulous attention. Insights gleaned from the literature review in § 1.4 highlight that the various reaction mechanisms, whether involving transfer to adjacent grains or integration into the grain boundary, are driven by energy-related considerations. A reaction can only occur if it tends to minimise energy, which means reducing the total energy of the system. Consequently, these reactions frequently coincide with a substantial reduction in the long-range stresses affecting the dislocation source, commonly referred to the backstress, as discussed in [Georgieva, 1996].

Based on this last statement, we believe that the effect of dislocation/GB interactions on the localization of plastic deformation is of great importance. Indeed, long-range stress reduction could be the mechanism to explain the persistence of intense plastic deformation in very local regions. As an example, it has been shown that stress reduction mechanisms, such as in the case of elastic screening, play an important role in plastic behaviour, by considerably reducing the backstress. For more information we refer the reader to [Korzeczek, 2017] or to the simulations presented in [Quek et al., 2014].

In this chapter, we first present the work carried out to develop and integrate dislocation/GB interactions into the "microMegas" DDD code through the implementation of a new local rule (§ 4.3). Secondly, through a series of calculations and simulations, we investigate the contributions of dislocation/GB interactions to the problem of plastic strain localization. The importance of these mechanisms on the plastic behaviour of a grain is demonstrated in different case studies (§ 4.4). Finally, calculations are carried out using simulation configurations that are as realistic as possible and for different elastic loadings in order to discuss the role of elastic strain incompatibilities (§ 4.6).

4.2 Motivations

The calculations presented in Chapter III showed the difficulty of simulating localized plastic deformation in the context of monotonic loading and for pure polycrystalline materials. Despite the identification of mechanisms linked to cross-slip and collinear annihilation promoting strain localization, the calculated strain hardening rates, and in particular the backstress, remain very high and this prevents permanent localization phenomena (see the

calculations reported in § 3.5.1 and § 3.5.2). Consequently, the calculations performed in the previous chapters highlight no major plastic slip gradients over the grain volume, even for a high level of elastic loading heterogeneity. Although the influence of the stress concentration region is visible in our results with and without cross-slip (see for example Fig. 2.12 and Fig. 3.6), the plastic deformation remains rather homogeneous with a large number of slip traces of the same intensity.

The simulation result shown in Fig. 3.9-(c) highlights a weakness in the calculations made in the preceding chapters. Indeed, a strong heterogeneity in the number of dislocations stacked at grain boundaries is observed in this image. Near the stress concentration zone, the number of dislocation loops piled-up against grain boundaries reaches significant values, as discussed in § 3.5.2. Since these dislocations have the same sign, this dislocation pattern results in high stresses at the head of the pileup. In ideal cases, such as single (Eq. 4.1) and double pileups (Eq. 4.2), theoretical models allow this stress to be calculated [Hirth et al., 1983]. The double pileup model is simply an extension of the simple pileup model, considering two walls located at an equal distance from the dislocation source. Consideration of a second dislocation obstacle thus leads to the apparition of a second pileup whose dislocations are of opposite signs to the first one, resulting in the correction of the value at the head of the pileup by $\frac{\pi}{4}$ due to the attraction in between dislocations. Returning to Fig. 3.9-(c), we can determine the value of the stress at the head of the pileup in the case of the theoretical single and double pileup model. Let's apply such calculations close to the region of stress concentration on the slip plane in Fig. 3.9-(c). The number of dislocations (N) calculated in this region is 15, while the average resolved shear stress calculated on the slip plane is 90 MPa. Therefore:

$$\tau^s_{head} = N \times \tau^s_{app} = 15 \times 90 = 1.3 \text{ GPa} \tag{4.1}$$

or,

$$\tau^s_{head} = N \times \tau^s_{app} \times \frac{\pi}{4} = 15 \times 90 \times \frac{\pi}{4} = 1.06 \text{ GPa} \tag{4.2}$$

Those computed stress values are high and much larger than the applied stress. In the literature, studies have shown through for instance molecular dynamics simulations that the critical stress for dislocation transmission is typically between 400 MPa and 1 GPa for FCC materials [Pan et al., 2021]. Therefore, this calculation of the stress concentration associated with the dislocation pile-up close to a GB is questioning the initial simplification we made in the previous chapters, i.e. the assumption of impenetrable grain boundaries for the deformation amplitude explored in DDD simulations.

The above observation motivates the additional work carried out in this chapter to consider grain boundary penetrability in our DDD simulation code.

4.3 Dislocation-grain boundary short distance interaction

4.3.1 Implementation

Local rules are usually used in DDD codes to model dislocation core properties, which rely on atomistic scale consideration at the mesoscopic scale. Such rules are for example used to model cross-slip as explained in § 1.6.1.3, dislocation climb or dislocation-dislocation reaction. Following the way local rules have been implemented in the past in DDD simulation codes, the strategy we adopted is to select a physical variable of interest (e.g. stress or dislocation density) and define from that variable whether or not a dislocation-grain boundary reaction is expected.

Here, it must be noted that what we defined as dislocation-GB reaction can either be transmission or incorporation into the grain boundary. We are not interested in modelling the atomic details of the reactions, but rather in defining for each dislocation segment touching a grain boundary the outcome of a possible grain boundary reaction.

A simple and efficient way of defining the penetrability of grain boundaries, using a predefined variable of the DDD code, is to calculate the stress that acts on the dislocations near the grain boundaries. Indeed, the calculation of the stress at the head of pileups or generated by any dislocation pattern in the DDD code does not require specific computations, as the stress on each dislocation segment is calculated at all the simulation time steps. One can therefore define a threshold stress above which a grain boundary is considered penetrable by dislocations. We name this stress τ_{GB}, the grain boundary penetrability stress.

For a better overview of the simulation rule we developed, we provide an example. Fig. 4.1 shows the calculation of the resolved shear stress at the head of the pileup (τ^s_{tot}) during plastic deformation for a given configuration, i.e. a Frank-Read source embedded in a cubic grain. As shown in Fig. 4.1-(a), the simulation is carried out until five dislocation loops pile up at the grain boundaries. The total resolved shear stress (τ^s_{tot}) is calculated following Eq. 4.3 by the summation of the applied loading (τ^s_{app}), the dislocation interactions (τ^s_{int}) and the local line tension (τ^s_{LT}) contributions.

$$\tau^s_{tot} = \tau^s_{app} + \tau^s_{int} + \tau^s_{LT} \tag{4.3}$$

Fig. 4.1-(b) shows a comparison between the applied resolved shear stress and the average resolved shear stress at the head of the pileup. The average resolved shear stress at the head of the pileup $\langle \tau^s_{tot} \rangle$ is calculated here by calculating the mean value of τ^s_{tot} for each of the segments in contact with the grain boundaries (segments represented in Fig. 4.1-(c)). This

figure shows that $\langle \tau^s_{tot} \rangle$ increases rapidly as a function of the number of dislocations piling up at the grain boundaries and the value of the applied stress.

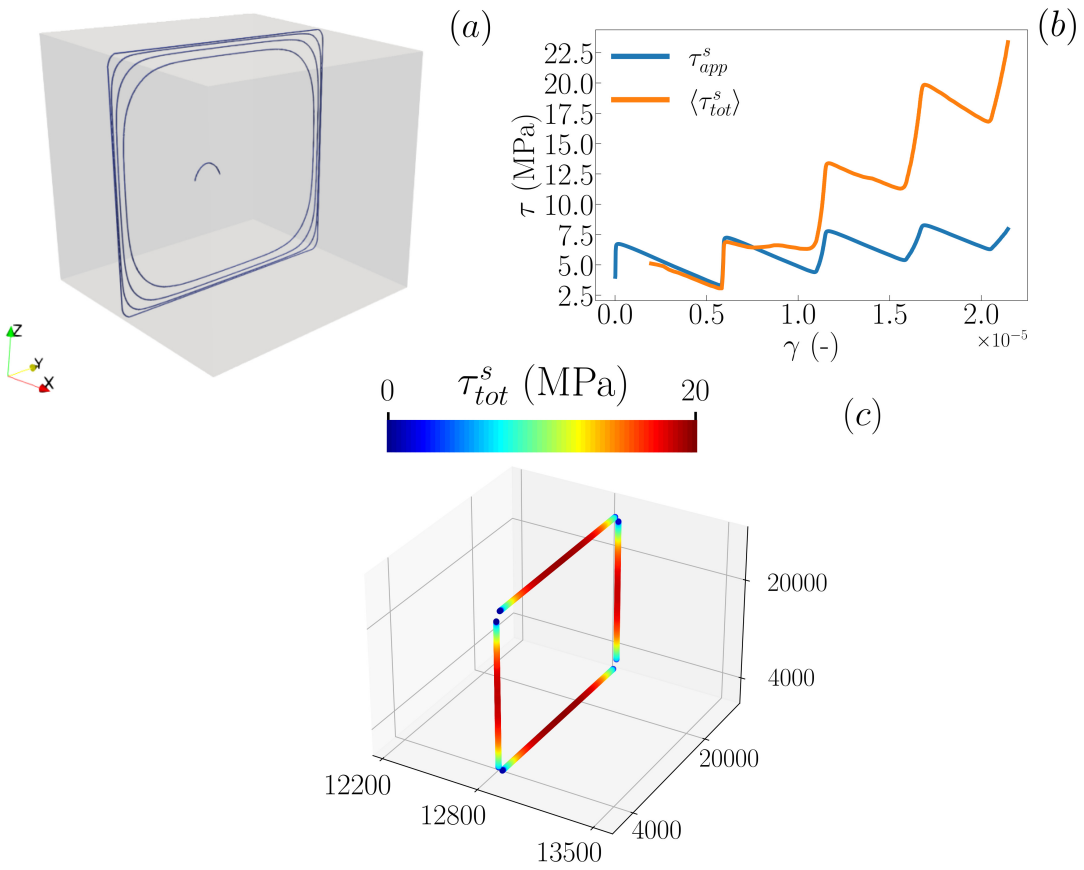

Figure 4.1: *Illustration of the stress field distribution inside a cubic grain after four dislocation loops emission from a FR source: (a) the four dislocations piled up at grain boundaries, (b) evolution of the average applied resolved shear stress field versus the average total resolved shear stress on dislocation segments at the head of pileups as a function plastic slip and (c) the local resolved shear stress field computation at the head of the pileup for the segments touching grain boundaries.*

Computation of τ^s_{tot} can then be compared to the grain boundary penetrability stress τ_{GB} for each segment, in order to define the penetrability of the grain boundaries as :

$$\begin{aligned} \tau^i_{reac} = \tau^i_{app} + \tau^i_{int} < \tau^{GB} &\implies P^{GB}_i = 0 \\ \tau^i_{reac} = \tau^i_{app} + \tau^i_{int} \geq \tau^{GB} &\implies P^{GB}_i = 1 \end{aligned} \tag{4.4}$$

With P^{GB}_i denoting the penetrability of the grain boundary for the segment i, zero refers to impenetrable and 1 refers to full penetrability. If the penetrability is set to one, then the segment should either be transmitted or at least be absorbed in the grain boundary.

As we did not wish to simulate the details of dislocation absorption or transmission in a grain boundary in this work, the effect shared by these two reactions is described here as a simple penetration of the dislocation into the grain boundary, which induces a cancellation

of the elastic stress field associated with the absorbed dislocation segments. This solution is mechanically equivalent to making penetrated dislocation segments disappear, but without having to deal with the topological issues associated with the reconstruction of the dislocation lines at the frontier between the grain and the grain boundary.

$$\underset{\sim}{\boldsymbol{\sigma}}^{i}_{int} = O_{kl} \tag{4.5}$$

With $O_{kl} = 0$ for all k and l (Einstein notation). By this process, a segment under penetrability condition no longer interacts with other dislocations and thus no more backstress coming from this segment is exerted on all other dislocations. This solution can be considered as the limit case where dislocations reacting with the GB are perfectly transmitted or absorbed without creating any defects in the GB. This implementation is extremely simple in comparison with some of the methods presented in § 1.4.3 but is perfectly suited to our study and will enable us to identify strong trends related to the reactions between grain boundaries and dislocations.

It is important to note that this implementation can be used to describe any mechanism that may cause a reduction in the backstress. As we shall see in Chapter V, this can also be linked to the plastic activity of neighbouring grains which, by elastic screening, leads to a reduction of the backstress.

4.3.2 Validation

Independently of the implementation details of the local rule presented above, which I have implemented in the DDD code, verification tests must be carried out to better assess the influence of this rule on the simulated plastic behaviours. Two basic verification tests have been carried out and are presented in what follows. The first one considers a grain with a cubic geometry and the second one a grain with a Voronoi geometry of 30 µm size. For these two simulations, the applied stress field is considered to be homogeneous for simplification purposes and the grain boundary penetrability stress is set at a low stress value, $\tau_{GB} = 38$ MPa, to initiate the mechanism at low strain. The imposed τ_{GB} is found to correspond (for both grains) to five dislocations piling up at the grain boundary. This observation is in good agreement with the solution predicted with the double pileup theoretical model as illustrated by Fig 4.2-(a). In both cases, a Frank-Read source is positioned at the centre of the grain, allowing a more homogeneous distribution of internal stresses at the grain boundaries. In Fig 4.2 we can see that the stress at the head of the pileup (for each N dislocations) is lower in the simulations than in the two theoretical models. For the DDD simulations, the stress at the head of the pileup τ^{s}_{head} is the average stress computed on every segment touching the grain boundaries facets (equivalent to $\langle \tau^{s}_{tot} \rangle$ defined in § 4.3.1).

This difference can be explained by the non-equivalent representation of dislocations. In the two theoretical models, dislocations are seen as infinite straight lines of edge character, whereas in the simulations they are finite loops. Considering loops of dislocations instead of infinite straight lines leads to the appearance of smaller pre-factors in the expression of τ^s_{head}, thus reducing the resolved shear stress at the head of the pileup at an equivalent number of dislocations N. These calculations are detailed in the work of [Déprés, 2004] for various configurations of dislocation pileups.

Fig 4.2-(b) shows, in the case of the Voronoi grain, the evolution of the stress as a function of plastic slip. The observed strong stress oscillations are due to the systematic emission of new dislocation loops by the Frank-Read multiplication mechanism. When the stress exerted on the source reaches a critical value, the latter bends more and more easily as the line tension decreases. Afterwards, the next dislocation to be emitted needs higher stress (τ^s_c) due to the backstress (τ_b) associated with the previous dislocation loop, now blocked against grain boundaries :

$$\tau^s_c = \tau^s + \tau_b \tag{4.6}$$

This operation is repeated for each new dislocation nucleated. After a certain period of time, more precisely after the fifth dislocation loop nucleation, a plateau in stress values is observed. This means that the maximum resistance (impenetrability) value of the grain boundaries has been exceeded, a dislocation is absorbed/transmitted, and the backstress is now constant in accordance with Eq. 4.5. Each time a new dislocation reaches the grain boundary region, the self-stress field of the dislocation at the head of the pileup is eliminated, if the critical condition is satisfied, and the number of effective dislocations in the pileup is constant. Locally an equilibrium state is reached and the dislocation close to the grain boundary is organized permanently to form a pileup of 5 dislocations.

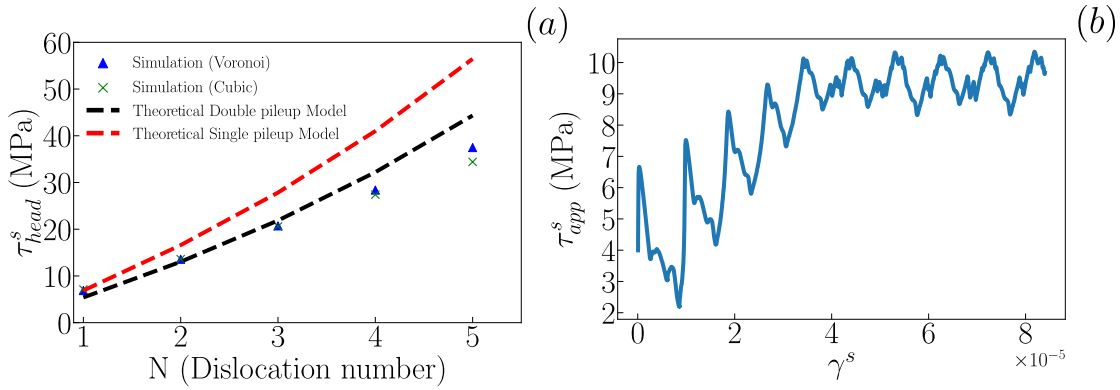

Figure 4.2: *Application of the local rule for a cubic and a Voronoi grain: (a) the evolution of the stress at the head of the pileup is compared to single and double pileup model [Hirth et al., 1983], (b) evolution of the applied resolved shear stress as a function of plastic slip for the Voronoi grain with local rule being activated at* $\tau_{GB} = 38$ *MPa.*

These two validation tests made it possible to verify, for different grain sizes and critical

stresses that the local rule implemented in the DDD code accurately reproduces the expected phenomenology. Here it must be noted that, as no explicit modifications are introduced to compute the resolved shear stress on dislocation segments at the head of the pileup, the new local rule can be applied to very complex configurations with higher dislocation density and heterogeneous applied stress field. For instance, in the case of a heterogeneous stress field, the proposed local rule allows penetrability in a particular region of the grain boundaries if a strongly heterogeneous stress takes place at the GB. In addition, one must realize that the same procedure could be used to define different values of τ_{GB} as a function of the GB facet orientation. Due to a lack of time, we did not investigate such a possibility in the present work. In the next section, we will discuss the role of dislocation/GB contact reaction on plastic strain localization.

4.4 Role on the persistence of plastic slip

The whole point of developing a local rule allowing the penetrability of grain boundaries to be taken into account is to investigate the role that this can have on plastic behaviour and, in particular, on the localization of plastic deformation. For all the simulations presented in this chapter, the grain boundary penetrability stress τ_{GB} is considered to be identical and constant during the loading for every grain boundary, no matter its orientation. This is a simplified assumption to begin with, providing a good starting point for the investigations. However, a more complex situation taking into account a variation of the grain penetrability stress as a function of the number of reactions (τ_{GB} could increase or decrease as a function of the number of dislocations entering the GB) or the orientation of the grain with respect to the slip systems is ready for use. the influence of such interesting and important properties should be studied in the future.

As a starting point, we propose to study the effect of grain boundaries penetrability on the average behaviour of the grain and then on its local behaviour, particularly with regard to the persistence of plastic deformation. By average behaviour, we refer to the calculation of physical quantities integrated over the volume of the grain. In contrast, we define local behaviour as the study of discrete physical quantities, calculated at material points in the grain. A good example of local quantities is the calculation of plastic slip values inside voxels as described in § 1.6.1.4. As the main objective is to study the role of grain boundaries penetrability on the plastic behaviour, we solve dislocation dynamics for various values of τ_{GB}. These values are listed in Tab. 4.1 and lie within the range defined in § 1.4.2.

In this chapter, we present results from several categories of simulations. As described in Chapter III, some simulations solve the dislocation dynamics by considering all the slip

Simulation	**1**	**2**	**3**	**4**
τ_{GB} **(MPa)**	500	650	800	1000

Table 4.1: *Grain boundary penetrability stresses for the various computations carried out in this chapter.*

systems of the FCC structure, simulations that we have called "set 1" in § 3.2.1, and others solve the dislocation dynamics by considering only the most active slip system C5 and its collinear system B5 in the reference grain, simulations that we have called "set 2". Simulations carried out in Chapter III can be used to compare with the simulations presented in this chapter. We will consider the results of Chapter III simulations as that of perfectly impenetrable grain boundaries whose penetrability stress is therefore infinite, i.e. $\tau_{GB} = \infty$. As stated in the previous paragraph, dislocation dynamics is also solved for other elastic loadings with various characteristics (see Tab. 4.2). These elastic loading belongs to the same crystallographic orientation, only the orientation of neighbouring grains is modified as stated in Chapter II (series 1 protocol). The elastic loading named BCs 1 is the one identified in § 2.3.3 and used for the simulations presented in Chapter II and Chapter III.

	Slip System	**max(τ^s) (MPa)**	$\sqrt{V_a^s}$ **(MPa)**
BCs 1	C5	170	12.4
	C3	146	9.8
	C1	48	10.9
BCs 2	C5	152	10.9
	C3	126	9.1
	C1	61	9.3
BCs 3	C5	162	11.78
	C3	139	10.3
	C1	46	7.6
BCs 4	C5	124	5.9
	C3	118	6.6
	C1	29	6.1

Table 4.2: *Elastic loading characteristics of the three coplanar slip systems C5, C3 and C1 for BCs 1, BCs 2, BCs 3 and BCs 4 (values are averaged over the grain volume).*

To consider only the most active slip system C5 and its level of heterogeneity, we have limited the calculation of the criterion defined in § 2.3.3 for the identification of the configurations BCs 2, BCs 3 and BCs 4. This last statement ensure that Eq. 2.6 and Eq. 2.7 can

be rewritten as:

$$\langle \max(\tau^s) \rangle = \frac{\sum_{s=10}^{10} \max(\tau^s)}{1} \tag{4.7}$$

$$\Lambda = \frac{\sum_{s=10}^{10} \sqrt{V_a^s} \times m^s}{1} \times \frac{1}{\langle m^s \rangle} \tag{4.8}$$

BCs 2 and BCs 3 elastic loadings are defined by a high level of heterogeneity as illustrated by Tab. 4.2 and Fig 4.3 illustrating the point cloud calculated with Eq. 4.7 and Eq. 4.8, while BCs 4 is a configuration for which the stress state is much less heterogeneous and with lower stress values. A mapping of the resolved shear stresses on slip system C5 for BCs 1, BCs2, BCs 3 and BCs 4 is given in Appendix B for two visualization viewpoints.

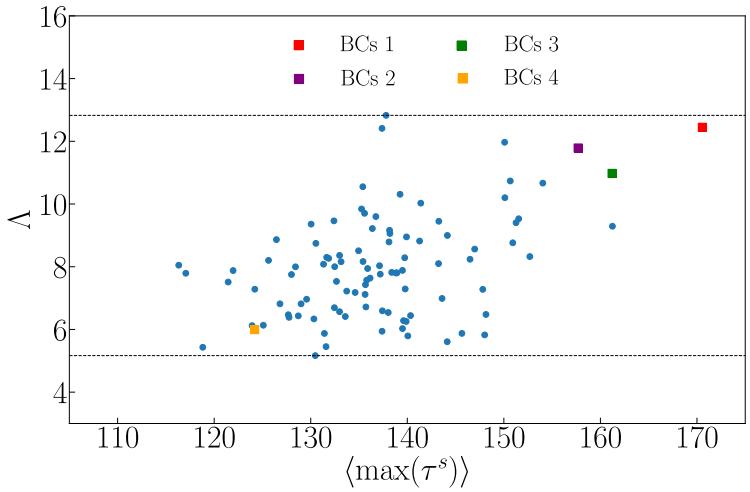

Figure 4.3: *Classification of the configurations of interest in the series 1 simulations database and illustration of the four configurations selected for this chapter. Here, the criterion is only applied to the most active slip system C5 following Eq. 4.7 and Eq. 4.8.*

4.4.1 Effect of grain boundaries penetrability on the average grain behaviour

As previously mentioned, we propose to initially investigate the impact of grain boundary penetrability on the average plastic behaviour of the grain, within the framework of "Set 2" simulation conditions allowing to reach higher deformation levels. By considering the various grain boundary penetrability stresses presented in Table 4.1, we plot the evolution of stress-plastic slip curves (see Figure 4.4). Most of the simulations reach plastic slip values higher than 2.8×10^{-3} on slip system C5 as illustrated in the figure. A quick look at these curves reveals a clear trend: the plastic behaviour of the grain becomes stiffer as the grain boundary penetrability stress increases. For instance, considering the two extreme cases of

500 and 1000 MPa, these two curves exhibit markedly different plastic regimes. With a grain boundary penetrability stress set at 500 MPa, the plastic behaviour appears nearly perfectly plastic ($\frac{\Delta\tau^s}{\Delta\gamma^s} = 5.3$ GPa). This implies that the strain hardening rate is very low, and plastic deformation occurs at nearly constant stress. Conversely, for a grain boundary penetrability stress set at 1000 MPa, the curve indicates a much stiffer plastic behaviour. The computed strain hardening rate is almost equivalent to the configurations in which grain boundaries are treated as impenetrable ($\frac{\Delta\tau^s}{\Delta\gamma^s} = 21.4$ GPa).

Within these curves, distinct stages of plastic deformation can be identified, which we have classified into three distinct intervals. The initial stage (interval 1, for $\gamma^{C5} \in [0.0; 0.0003]$) is characterized by overlapping curves. During this phase, none of the simulations activate the penetrability of grain boundaries ($P^{GB} = 0$). The second stage (interval 2, for $\gamma^{C5} \in [0.0003; 0.001]$) is where grain boundaries start to become penetrable to particular dislocation segments, resulting in a gradual shift in plastic behaviour. The stress required for grain boundary penetrability acts as a yield point, marking the transition from a rigid regime to a less rigid one, with the extent of change depending on the value of τ_{GB}. Finally, the third stage (interval 3, for $\gamma^{C5} \in [0.001; 0.0015]$) is marked by a constant hardening rate. As we stated in the previous paragraph, however, the strain hardening rate varies according to the value of the grain boundary penetrability stress (τ_{GB}). The higher τ_{GB}, the higher the strain hardening rate.

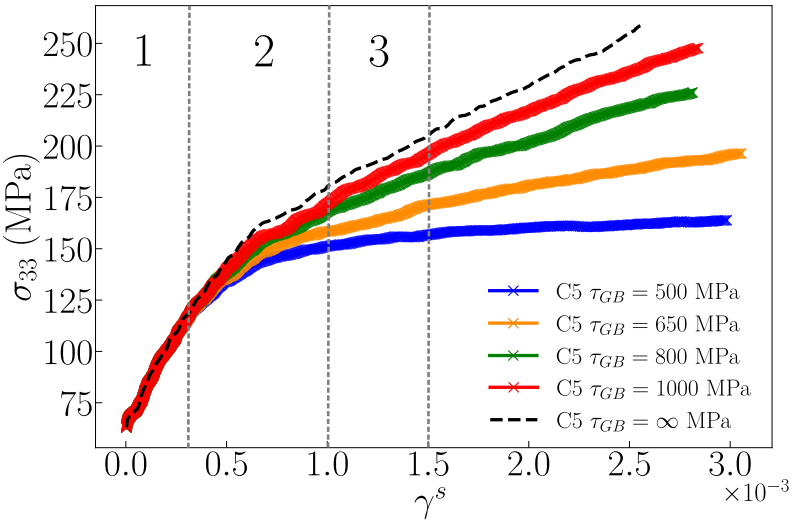

Figure 4.4: *Simulated stress-plastic slip curves for various values of the grain boundaries penetrability stress. The dark dashed curve refers to the impenetrable grain boundaries condition. The three stages are separated by vertical dashed lines (see text for details).*

The variations observed in the plastic behaviour across these different configurations can be attributed to various rates of dislocation storage. The higher the dislocation storage rate within a grain, the more pronounced the strain hardening will be. Dislocation

microstructures in these types of simulations (considering only active and collinear slip systems) significantly restrict the accumulation of dislocations at the core of the grain while encouraging the build-up of polarized dislocations along the grain boundaries. This is simply explained by the very low density of forest dislocations. To be convinced of this statement, one can look at the dislocation microstructure illustrated in Fig 3.9 and Fig 3.10. On the two graphs, it is clear that most of the density is located in the vicinity of grain boundaries. The assumption that the total dislocation density is roughly equivalent to the GND density and that the density of statistically stored dislocations in the grain's central region is negligible is thus quite reasonable. To compute the density associated with polarized dislocations we can write:

$$\rho^s_{GND} \approx \rho^s_{tot} \tag{4.9}$$

Then, by the computation of the total density (ρ^s_{tot}) and the transmitted density (ρ^s_{trans}), it is possible to compare dislocation storage rates for the four simulation conditions. The transmitted density refers to the density of segments where the penetrability condition is verified ($P^{GB} = 1$).

In Fig 4.5-(a) corresponding to interval 1, all the curves overlap, indicating equivalent dislocation storage within the grain across the four configurations. This uniformity arises because the penetrability condition isn't satisfied for any of the dislocation segments, leading to a transmitted density of zero. Moving to the second interval (see Fig 4.5-(b)), discernible differences begin to emerge. Here, the penetrability condition becomes activated in accordance with the predefined values, effectively serving as a yield point. Fig 4.5-(c) corresponding to interval 3 highlights substantially distinct density trends across the four configurations. Taking the example of the grain boundary penetrability stress set at 500 MPa, the dislocation storage rate is nearly negligible, thereby explaining the nearly perfect plastic behaviour observed in Fig 4.4. For this particular configuration, a near-equilibrium exists between the creation of dislocations and those transmitted. For the other configurations, the increase in the grain boundary penetrability stress leads to an increase in the dislocation storage rate and plastic rigidity.

Based on these initial results, the influence of penetrability conditions on the average response of the grain is now easier to understand. A concise overview of the diverse plastic behaviours observed during interval 3, depending on the grain boundary penetrability stress, is detailed in Table 4.3 by the computation of the strain hardening and dislocation density storage rates. We can notice that the strain hardening rate is multiplied by four from $\tau_{GB} = 500$ MPa to $\tau_{GB} = 1000$ MPa which corresponds to the difference in dislocation storage rates.

The results of the simulations in this section are not unexpected. Indeed, the observation of a decrease in the strain-hardening rate comes directly from the programmed local rule,

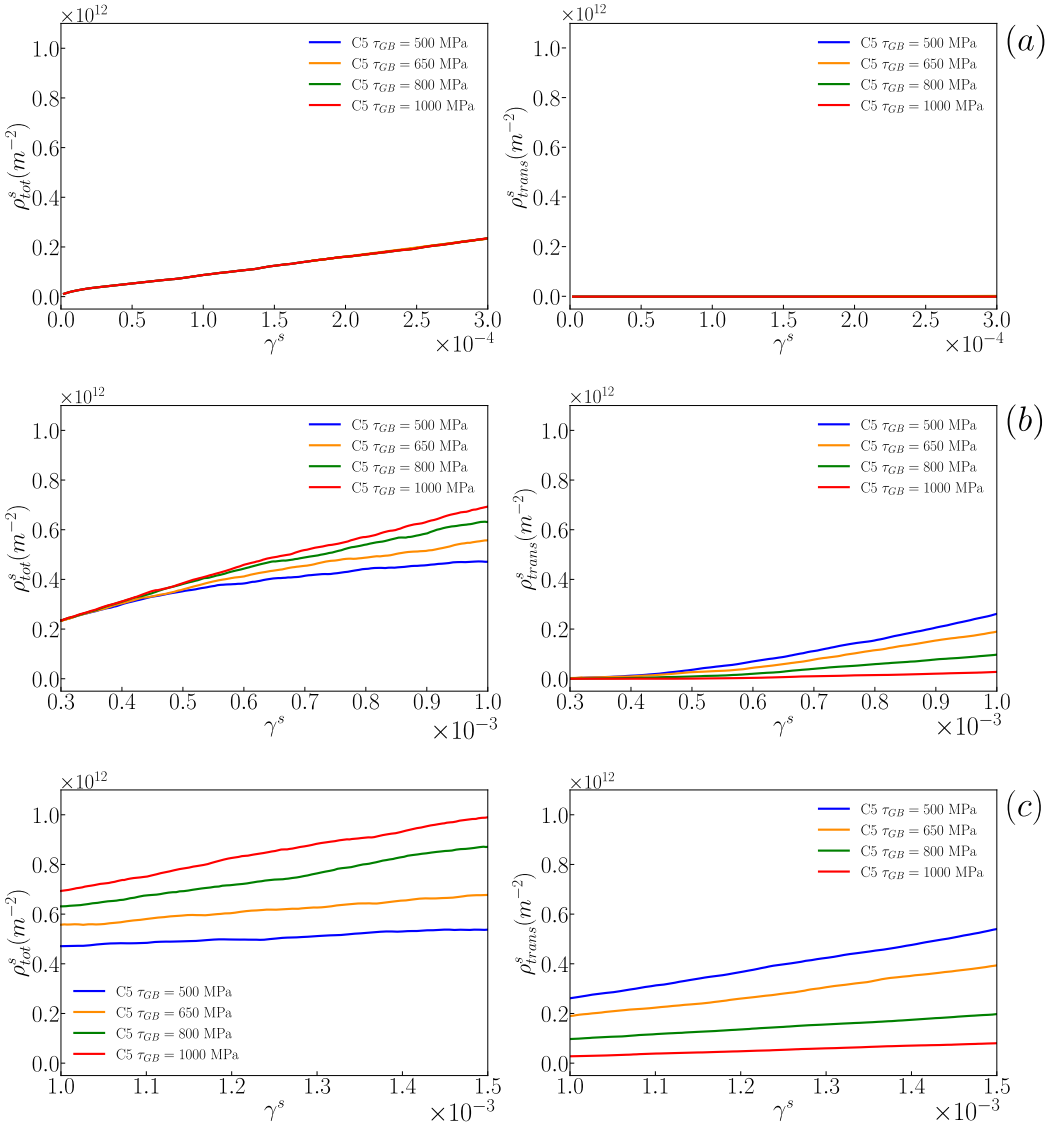

Figure 4.5: *Evolution of the total dislocation density ρ^s_{tot} and the transmitted dislocation density ρ^s_{trans} for interval 1 (a), interval 2 (b) and interval 3 (c).*

τ_{GB} (MPa)	500	650	800	1000
$\frac{\Delta\tau^s}{\Delta\gamma^s}$ (GPa)	5.3	8.9	16.5	21.4
$\frac{\Delta\rho^s_{tot}}{\Delta\gamma^s}$ (m^{-2})	1.34×10^{14}	2.39×10^{14}	4.78×10^{14}	5.93×10^{14}

Table 4.3: *Summary of the strain hardening and dislocation density storage rate in the interval 3 for the various grain boundary penetrability stresses.*

which has a direct effect on the GND dislocation density accumulated at the GB. However, it is interesting to note that the linear relation between kinematic hardening and GND density as demonstrated in the work of [Jiang et al., 2021] is still valid and that we can control directly the strain hardening rate in simulations by changing the grain boundary

penetrability stress. On the basis of these results, we expect to simulate significant effects on a more local scale, this will be detailed in the next section § 4.4.2.

4.4.2 Effect of grain boundaries penetrability on the local grain behaviour

The calculations presented in § 4.4.1 regarding the impact of penetrability conditions on the average plastic behaviour of the grain have revealed important trends. For all the presented results, enabling grain boundaries to be penetrable consistently leads to a significant reduction in the hardening rate. In this section, the influence of the grain boundary penetrability condition is examined at a local level, employing the same simulations as detailed in § 4.4.1. We begin by exploring the two extreme scenarios within our previous simulations. This involves considering the case where grain boundary penetrability becomes feasible from a stress threshold of 500 MPa, juxtaposed against the scenario where grain boundaries are assumed impenetrable. By calculating average plastic slip values across N slices of 1 µm length oriented along $(\overline{1}\overline{1}1)$ planes on the voxel tessellation (see Fig 4.6-(a)) for these two configurations it is then possible to make a quantitative comparison of the impact of grain boundary penetrability on intragranular plastic slip:

$$\gamma^s_{slices} = \frac{1}{nb_{vox}} \times \sum \gamma^s_{vox} \tag{4.10}$$

With nb_{vox} the number of voxels in the slice. The computed local plastic slip is compared for these two configurations at an equivalent plastic slip level of $\gamma^{C5} = 2.5 \times 10^{-3}$ in Fig 4.6-(b). This figure clearly demonstrates that the spatial arrangement of plastic slip experiences significant evolution due to the penetrability property. More specifically, when grain boundaries are treated as impenetrable ($\tau_{GB} = \infty$), the distribution of plastic slip within the grain is relatively uniform, lacking pronounced intensity gradients. Conversely, in scenarios where grain boundaries are penetrable ($\tau_{GB} = 500$ MPa), plastic slip becomes distinctly localized, particularly evident within zones II and III. This localization is characterized by sharp and visible pics in the plastic slip distribution, from the 0 slice to the 30 slice.

The local average plastic slip values for $\tau_{GB} = 500$ MPa are notably higher, often reaching up to threefold compared to the $\tau_{GB} = \infty$ scenario. This distinction is particularly evident in zone III (slice 23), where an intensely marked slip trace is calculated. Values in this slice are computed for both simulations:

- $\gamma^{C5}_{slices} = 0.0095$ ($\tau_{GB} = 500$ MPa)
- $\gamma^{C5}_{slices} = 0.003$, impenetrable grain boundaries ($\tau_{GB} = \infty$)

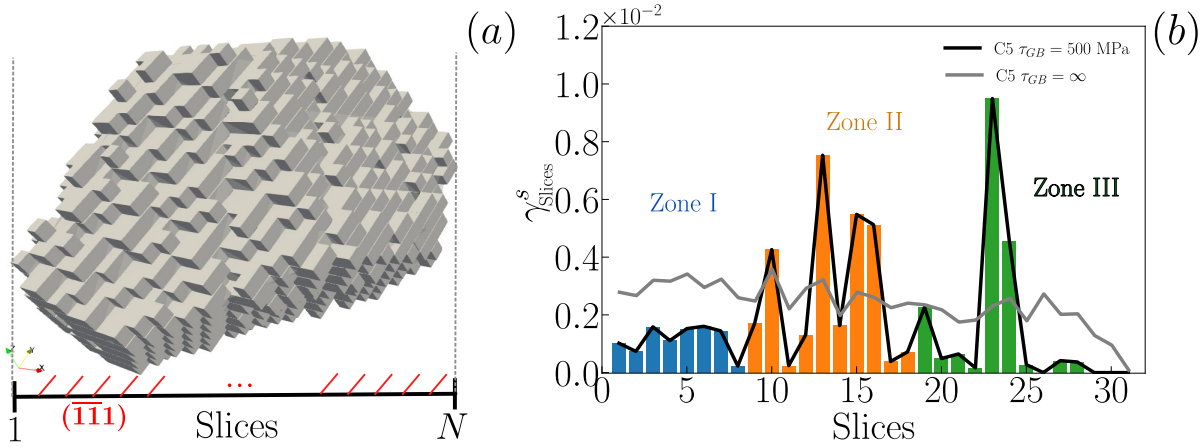

Figure 4.6: *Comparison of the average local plastic slip values for N slices oriented along* $(\bar{1}11)$ *planes. Illustration of slice distribution from the grain geometry and voxel discretization (a). Plastic slip values for two grain boundaries configurations are illustrated in (b). The comparison is made at equivalent plastic slip on the slip system C5,* $\gamma^{C5} = 2.5 \times 10^{-3}$.

This comparison highlights a clear shift from relatively uniform plastic slip distribution to distinctly heterogeneous slip patterns, signifying the strong influence of grain boundaries penetrability. To facilitate a consistent and quantitative comparison of plastic slip localization across various simulations, we propose the use of a localization index. This index serves as a method to assess the degree of localization. Its computation involves counting the number of voxels (nb_{loc}) where the calculated plastic slip value surpasses a predetermined threshold given by a multiple of the average plastic slip $\eta \times \langle \gamma^s \rangle$, with $\langle \gamma^s \rangle$ the average plastic slip values computed on every voxel. This count is subsequently divided by the total number of voxels (nb_{vox}) to derive a localization index percentage:

$$f = \frac{nb_{loc}}{nb_{vox}} \times 100 \tag{4.11}$$

The localization index (f) is computed for all grain boundary penetrability stresses configurations outlined in Tab. 4.1, considering various values of η (3, 4 and 5). The results are depicted in Fig. 4.7. The calculations highlight a decline in the occurrence of intense slip events as the stress for the grain boundary penetrability increases. This trend is notably pronounced in the illustration of the most intense slip traces, calculated for $\eta = 3$ in the figure. This notion is further corroborated by the values of the localization index. The degree of localization quantified by the localization index is quite important in the case where $\tau_{GB} = 500$ MPa. Even for $\eta = 5$, the calculated percentage (5.96 %) in zone III is high and typically refers to the presence of one intense slip trace. Intriguingly, the values of the localization index exhibit a rapid reduction with the elevation of the stress for the grain boundary penetrability. The plastic slip computed within slip traces also experiences a rapid decrease. This trend is mostly apparent in the case of $\tau_{GB} = 1000$ MPa, where no

slip traces are calculated for $\eta = 3$ so that the localization index is equal to zero in every region. Hence, it is evident that the degree of localization (heterogeneity and intensity of plastic slip) is profoundly influenced by the value of the grain boundary penetrability stress.

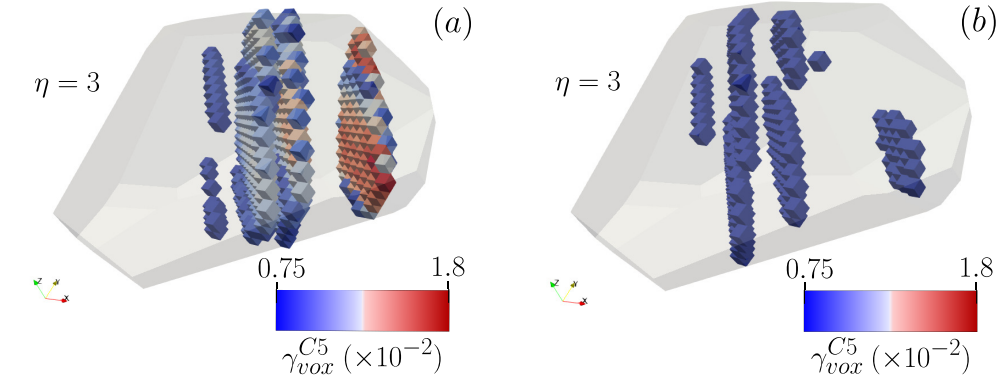

Region	Zone I	Zone II	Zone III
$\eta = 3$	$f = 0.0$ %	$f = 12.8$ %	$f = 8.9$ %
$\eta = 4$	$f = 0.0$ %	$f = 6.6$ %	$f = 7.09$ %
$\eta = 5$	$f = 0.0$ %	$f = 1.27$ %	$f = 5.96$ %

Region	Zone I	Zone II	Zone III
$\eta = 3$	$f = 1.75$ %	$f = 7.1$ %	$f = 0.57$ %
$\eta = 4$	$f = 0.0$ %	$f = 0.38$ %	$f = 0.0$ %
$\eta = 5$	$f = 0.0$ %	$f = 0.0$ %	$f = 0.0$ %

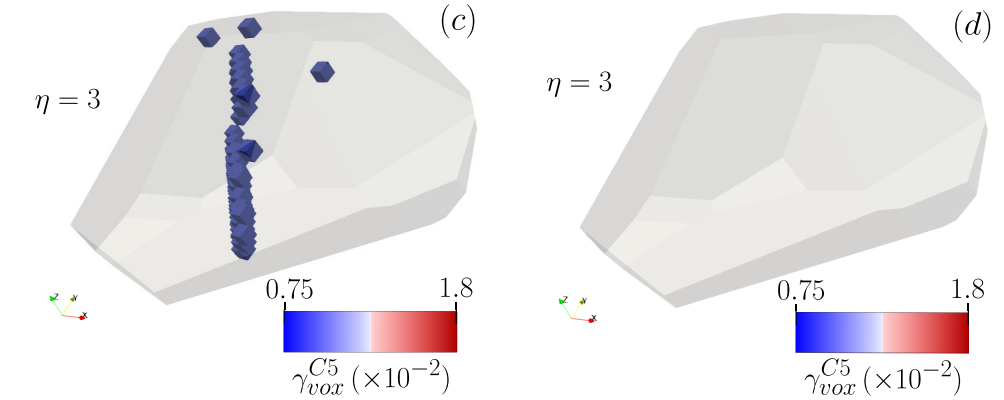

Region	Zone I	Zone II	Zone III
$\eta = 3$	$f = 0.0$ %	$f = 0.78$ %	$f = 0.0$ %
$\eta = 4$	$f = 0.0$ %	$f = 0.0$ %	$f = 0.0$ %
$\eta = 5$	$f = 0.0$ %	$f = 0.0$ %	$f = 0.0$ %

Region	Zone I	Zone II	Zone III
$\eta = 3$	$f = 0.0$ %	$f = 0.0$ %	$f = 0.0$ %
$\eta = 4$	$f = 0.0$ %	$f = 0.0$ %	$f = 0.0$ %
$\eta = 5$	$f = 0.0$ %	$f = 0.0$ %	$f = 0.0$ %

Figure 4.7: *Illustration of the most intense slip traces for* $\gamma_{vox}^{C5} \in [0.0075; 0.018]$ *and for grain boundary penetrability stresses* 500 *MPa (a),* 650 *MPa (b),* 800 *MPa (c) and* 1000 *MPa (d). In the tables are given the computation of the localization index for various values of* η*. The corresponding plastic deformation level is* $\gamma^{C5} = 2.5 \times 10^{-3}$*.*

When focusing on the results where the penetrability stress remains fixed at 500 MPa, the reasons behind the localization of plastic deformation in zone III present somewhat puzzling aspects. Observations from the preceding chapters suggested that regions of stress concentration played a pivotal role in inducing intense plastic slip, consequently leading to localized phenomena near these regions. However, the degree of localization observed here is more pronounced in Zone III compared to Zone II. Interestingly, the applied stress conditions in Zone III differ significantly from those in Zone II. Tab. 4.4 provides insight into various quantities that distinctly characterize the applied loading, including the maximum resolved

shear stress on slip systems C5 and B5, as well as the standard deviation on slip system C5, offering a measure of the heterogeneity level. It is clear that the applied stress conditions in zone III are more uniform, given the lower value of $\sqrt{V_a^{C5}}$. Furthermore, in zone III, the applied loading exhibits less intensity, with $\max(\tau^{C5}) = 140$ MPa.

	Zone I	**Zone II**	**Zone III**
$\boldsymbol{\max(\tau^{C5})}$ **(MPa)**	140	162	140
$\boldsymbol{\langle\tau^{C5}\rangle}$ **(MPa)**	98	101	93
$\boldsymbol{\sqrt{V_a^{C5}}}$ **(MPa)**	10.70	16.14	13.5
$\boldsymbol{\max(\tau^{B5})}$ **(MPa)**	70	56	35
$\boldsymbol{\langle\tau^{B5}\rangle}$ **(MPa)**	35	29	16

Table 4.4: *Maximum and average resolved shear stress and standard deviation values computed in each zone of the grain for the current boundary conditions. Maximum and average resolved shear stress values are given on the slip system C5 and B5.*

This implies that stress concentration is not an indispensable prerequisite for the localization of plastic deformation in our simulations, especially when taking into account the penetrability of grain boundaries. To support this affirmation we solved the dislocation dynamics for two other elastic loading conditions BCs 2 and BCs 3 (see Tab. 4.2). These two conditions exhibit various distributions of stresses on the grain volume (see Appendix B for the mapping of the resolved shear stresses on the C5 slip system).

The illustration provided in Fig. 4.8 shows the distribution of K for both elastic loading BCs 2 & BCs 3. This parameter is computed following the given equation:

$$K = \max(\tau^s) \times \sqrt{V_a^s} \tag{4.12}$$

This parameter serves as a tool to delineate the regions where stress concentration zones are located. When multiplied by the standard deviation, it allows the resolved shear stress values to be weighted based on their dispersion, thereby accounting for their statistical significance. Consequently, a high K value signifies a plane on which a considerable number of high stress values emerge. From these calculations, it becomes evident that the elastic loading BCs 3 appears to be more conducive to the generation of intense plastic slip. This is drawn from the fact that the maximum K parameter in BCs 3 is nearly twice as high as that observed in the elastic loading BCs 2. It is interesting to note that in both cases, the zone of interest delimited by K is not located in the same region of the grain. For the BCs 2 elastic loading, the zone of interest is located between zones II and III. For BCs 3, the zone of interest is located in zone I.

The localization index is calculated for the same level of plastic slip as in Fig. 4.7 and

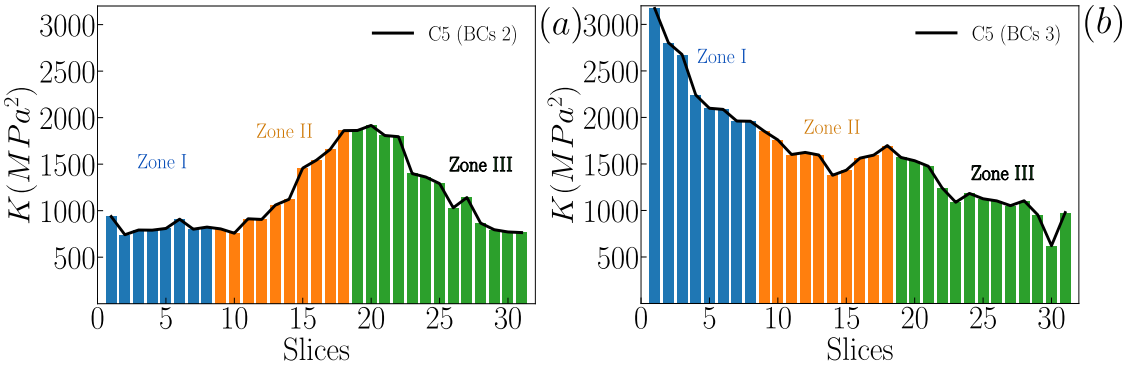

Figure 4.8: *Computation of the K parameter for both elastic loading BCs 2 & BCs 3.*

dislocation dynamics is solved considering the same initial dislocation microstructure and simulation conditions. Results are illustrated in Fig. 4.9. On these plots, both computations lead to various distributions of the most intense slip traces inside the grain.

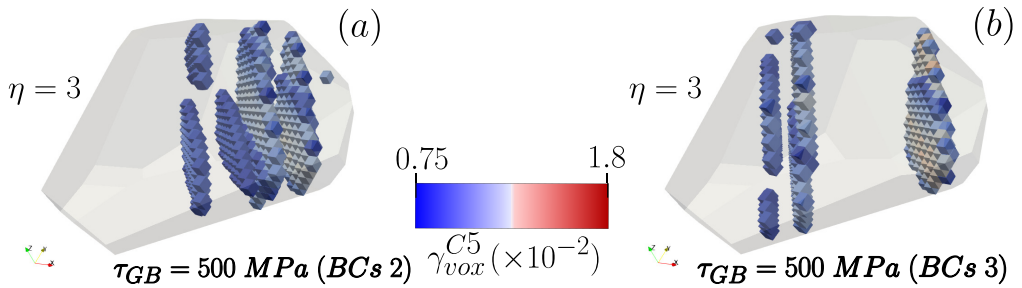

Region	Zone I	Zone II	Zone III
$\eta = 3$	$f = 0.0\ \%$	$f = 5.67\ \%$	$f = 19.1\ \%$
$\eta = 4$	$f = 0.0\ \%$	$f = 0.0\ \%$	$f = 10.1\ \%$
$\eta = 5$	$f = 0.0\ \%$	$f = 0.0\ \%$	$f = 0.34\ \%$

Region	Zone I	Zone II	Zone III
$\eta = 3$	$f = 3.71\ \%$	$f = 5.96\ \%$	$f = 8.79\ \%$
$\eta = 4$	$f = 0.0\ \%$	$f = 2.93\ \%$	$f = 5.95\ \%$
$\eta = 5$	$f = 0.0\ \%$	$f = 0.0\ \%$	$f = 1.8\ \%$

Figure 4.9: *Illustration of the local plastic slip on slip system C5 for BCs 2 (a) and BCs 3 (b) elastic loadings. Local slip events are calculated at an equivalent plastic slip of* $\gamma^{C5} = 2.5 \times 10^{-3}$.

This result strongly suggests an effect of the applied loading conditions. For both simulations, intense slip traces respectively appear in regions of stress concentration. Nevertheless, these events are not necessarily the most intense. This is particularly visible for BCs 3. Indeed, for this elastic loading, the calculation of the localization index clearly shows the presence of an intense plastic slip in zone III. However, as shown in Fig. 4.8, this region is in no way (according to our criteria) favourable to this type of event. In the case of BCs 2, intense plastic activity is also computed in zone III but this is more coherent with the applied loading conditions. It is surprising to see that for the three different loading conditions (BCs 1, BCs 2 and BCs 3), an intense slip trace is systematically obtained in zone III.

A more detailed study carried out with different initial dislocation microstructures and for BCs 1 elastic loading also showed that the plastic slip activity in zone III did not depend

on the initial dislocation microstructure, thus removing the latter from the list of potential explanations for such results. However, the calculation of the cross-slip activity zone by zone and for different initial microstructures shows that zone III is systematically a region of low cross-slip activity. This is explained by the low value of resolved shear stresses on the collinear slip system compared with the other two zones (see Tab. 4.4). As cross-slip is less active in zone III, plastic deformation appears to be very laminar and very intense in this region. This observation provides a possible explanation for the localization observed in that region. Moreover, the plastic activity in this region only appears after intense activity in zone II linked to the presence of the stress concentration. However, the latter quickly becomes more intense and the plastic slip thus exceeds that calculated in zone II (plastic slip per slip trace). It is important to note that most of the plastic deformation in zone III takes place in a single slip plane due to the very low cross-slip activity. Zone I and II, on the other hand, have a greater number of occupied slip planes.

For the other elastic loading (BCs 3), the reasons for intense plastic activity in zone III are more enigmatic as cross-slip activity is not as low as for BCs 1 in zone III. Nevertheless, the resolved shear stress distribution is quite different and could explain the obtained result. It is easy to imagine that the distribution of the resolved shear stress with respect to the grain geometry or the crystallographic orientation may play a decisive role in the initiation of intense localized plastic deformation. The influence of the elastic loading and resolved shear stress distribution will be further discussed in § 4.6.

These results prompt us to extend our research into the role of cross-slip in relation to the localization of plastic deformation. This point will be presented in § 4.5. Furthermore, with these results, we are convinced that very intense plastic slip activity is not always intrinsically linked to the presence of a stress concentration. For example, we can easily be convinced that a region in which grain boundaries are more penetrable than other regions, for whatever reason, could be the direct site of intense and permanent plastic slip.

4.5 On the role of cross-slip under the condition of grain boundaries penetrability

Cross-slip is a mechanism that greatly impacts the arrangement of dislocation microstructures during deformation. In particular, cross-slip allows for rapid dislocation multiplication within the crystal [Gutmanas and Nadgorny, 1970; Tang and El-Awady, 2014], leading to a gain in ductility as discussed in Chapter III and in line with the observations of [Koehler et al., 1954; Gilman and Johnston, 1957]. Additionally, cross-slip control certain dynamic recovery mechanisms. Cross-slip is the mechanism whereby dislocations can bypass obstacles such as forest dislocations [Escaig, 1968a; Humphreys and Hirsch, 1970] or precipitates, as

illustrated in [Huang et al., 2021]. Additionally, through the multiplication of dislocations within the crystal, cross-slip is supposed to facilitate the formation of an intragranular slip band, as noted in Chapter III and consistent with the observations of [Gilman and Johnston, 1962]. The implications of cross-slip are therefore numerous and justify further work on it with our simulations.

Since the late 90s and early 2000s, experimental methods such as AFM have made it possible to study the precise nature of slip marks on the surface of many single crystals after deformation. Some of these works [Brinck et al., 1998; Kramer et al., 2005; Kahloun et al., 2016] put forward the idea that cross-slip would lead to a thickening of the observed slip bands, but at the same time to a reduction in the height of these same bands, symbolizing less localized slip. These results, based on the study of single crystals, do not allow us to draw direct conclusions about the role of cross-slip in the initiation of an intragranular slip band but show particular trends. Considering polycrystalline behaviour, such conclusions are not straightforward.

Until now, particular attention has been paid to the role of stress concentration regions and contact reactions between dislocations and grain boundaries. In this part of the manuscript, we will look in more detail at the role that cross-slip could play in the initiation of a localization of plastic deformation and, in particular, in the distribution of plastic slip within the grain. As a starting point, we describe the effect of cross-slip activity considering activation parameters defined in § 3.2.1 on the plastic behaviour and in particular on dislocation storage. We then carry out a sensitivity study to see how cross-slip activity influences intragranular plastic deformation. Finally, the role of considering all the slip systems during the plastic deformation on the cross-slip activity is further discussed.

4.5.1 Dislocation density storage rate

From the results presented in § 4.4.1 and § 4.4.2, we have shown that the strain hardening rate varies significantly as a function of the grain boundary penetrability properties. Furthermore, we have shown that this is directly linked to the storage of dislocations. In fact, the less penetrable the grain boundaries, the greater the density of stored dislocations. In addition, as most of this density is stored at the grain boundaries, the strain hardening rates are considerably modified [Daveau, 2012; Jiang et al., 2019]. On a more local level, plastic slip appears to be less and less heterogeneous as the grain boundary penetrability stress increases, thus reducing the number of events where plastic slip is considered to be intense.

The physical reasons for such behaviour are directly linked to cross-slip activity during plastic deformation. Indeed, for the same material, geometry and crystalline orientation, it would have been perfectly reasonable to think that the activation of the penetrability

of the grain boundaries for different stress values would be manifested by a simple shift in the stress-plastic slip curves. In this way, the four different configurations would display identical strain hardening rates. The results presented in Fig. 4.10 support this idea. In this illustration, a comparison of the stress-plastic slip curves is shown for two series of simulations, one series with active cross-slip and the other series without active cross-slip. Looking at the simulations without cross-slip it is clear that the strain hardening rates are equivalent.

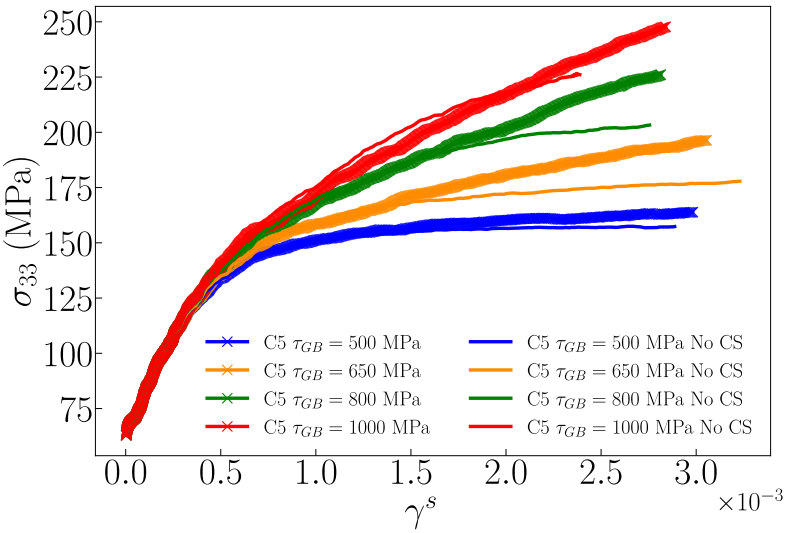

Figure 4.10: *Simulated stress-plastic slip curves for various grain boundaries resistance with and without cross-slip activity.*

It is important to note that for the particular case of $\tau_{GB} = 1000$ MPa, the quasi-constant strain-hardening rate has not yet been reached. Nevertheless, from the shape of the curve, we suppose that this is just a delay due to the high imposed grain boundary penetrability stress. The same simulations with cross-slip, however, show a systematic drop-out of these previous curves towards higher strain-hardening levels. In these simulations, the activity of the cross-slip is thus necessarily linked to the storage of GND density as illustrated in Fig 4.5.

In addition, as the strain hardening rates are not equivalent for the four simulations with cross-slip, it means that cross-slip activity is necessarily different. This idea is supported by the results illustrated in Fig. 4.11. This figure shows the significant variation in cross-slip activity as a function of the grain boundary penetrability stress: the higher the stress, the more active the cross-slip. For $\gamma^{C5} = 2.5 \times 10^{-3}$, the number of slip planes on the primary slip system C5 is 400 for $\tau_{GB} = 500$ MPa, 600 for $\tau_{GB} = 650$ MPa, 800 for $\tau_{GB} = 800$ MPa and 900 for $\tau_{GB} = 1000$ MPa. Such variations in cross-slip activity may be explained by a lower average number of dislocations in the pileups when the grain boundary penetrability stress is low. We paid close attention to the manifestation of cross-slip events

in our simulations and observed their first appearance in the pileups. This assertion is well-founded, as the dislocations in equilibrium in a pileup (apart from the head dislocation) experience zero effective stress. This suggests that the driving force for cross-slip activation is highly potent, facilitating deviation events. However, if the stress required for penetration is low, then the number of dislocations that pile up before they react with the grain boundaries will be relatively small, thereby reducing the probability of deviation. Furthermore, as the grain boundary penetrability stress does not vary during plastic deformation, the maximum number of dislocations that pile up at the grain boundaries cannot change, thus limiting cross-slip events. In addition, we know that cross-slip activity is also dependent on the stress level as expressed in Eq. 1.27 and Eq. 1.28, which indicates that a zone with higher strain hardening exhibits more intense cross-slip activity.

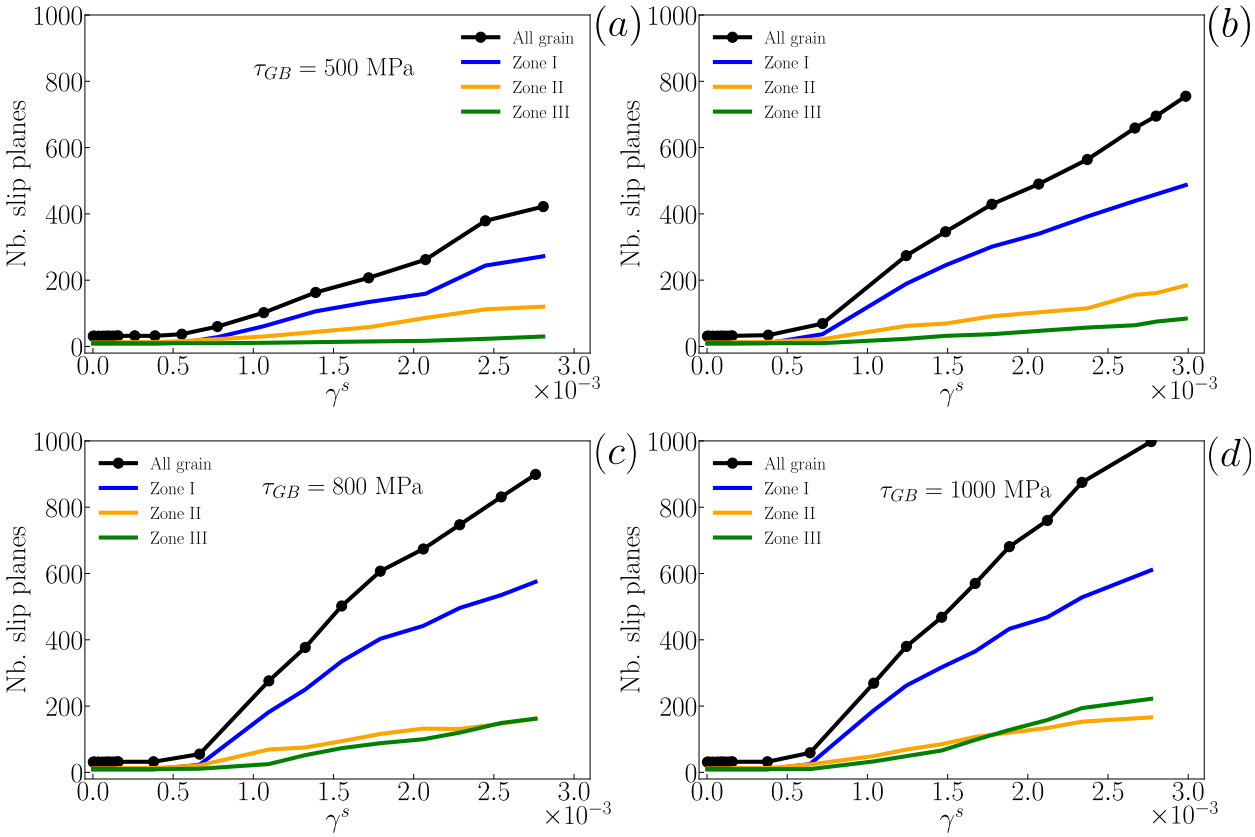

Figure 4.11: *Cross-slip activity for the four grain boundary penetrability stresses :* 500 *MPa (a),* 650 *MPa (b),* 800 *MPa and* 1000 *MPa (d) denoted by the number of* $(\overline{1}\overline{1}1)$ *plane.*

From these results, it becomes evident that higher cross-slip activity leads to more uniform plastic deformation because it creates more slip planes and dislocation sources in the grain volume. As a result, the degree of localization decreases at equivalent plastic deformation levels between these different simulations, as shown in Fig. 4.7. The increased density of stored GND dislocations contributes to this effect. The trends calculated here align with the observations outlined in the review of AFM experimental observations presented in the

previous section. In the upcoming sections, § 4.5.2 and § 4.5.3, we will try to gain comprehension of the parameters that influence cross-slip activity, resulting in greater or lesser homogeneous plastic behaviour at the plastic deformation levels simulated.

4.5.2 Material parameters and crystalline orientation dependency

Cross-slip is known to be a thermally activated mechanism whose activity depends on the stacking-fault energy of the material. Indeed, for materials with a high stacking fault energy, it will be more difficult for dislocations to dissociate into partials, leading to a higher probability for screw dislocations to cross-slip. This consideration can modify the way the material deforms. As an example, in the case of cyclic loading, materials with low stacking fault energy tend to produce planar slip bands, while materials with high stacking fault energy produce wavy slip bands [Feltner and Laird, 1968; Lukáš and Klesnil, 1971; Krejčí and Lukáš, 1971; Li et al., 2011].

In this part of the manuscript, we propose to study the variation of some parameters that are known to influence the cross-slip activity in order to predict and verify the way the grain will deform and how it will impact the distribution of plastic slip. Referring to the presentation of the cross-slip probability law (Eq. 1.26) and activation energy for a mobile (Eq. 1.27) and immobile (Eq. 1.28) dislocation, we can play on the value of τ_{III} (see § 1.6.1.3) to modify cross-slip activity. As stated in § 3.2.1, the value we were previously imposing was calculated in relation to the data of copper, giving $\tau_{III} = 45$ MPa. Decreasing this value should have the effect of activating the cross-slip for lower stress levels which would in turn lead to higher activity for the same level of plastic deformation. Another parameter that can be tuned to trigger cross-slip activity is the α parameter described in § 3.2.1. Increasing the value of this parameter reduces the stress value to be reached on the collinear slip system in order to trigger screw dislocations deviation. This should result in the rise of the cross-slip activity. The list of tested values is given below (results are reported in Fig 4.12) :

- $\alpha = 0.6$ and $\tau_{III} = 45$ MPa;
- $\alpha = 0.9$ and $\tau_{III} = 45$ MPa;
- $\alpha = 0.9$ and $\tau_{III} = 20$ MPa;
- $\alpha = 1$ and $\tau_{III} = 20$ MPa;
- $\alpha = 1$ and $\tau_{III} = 45$ MPa.

For the limit cases, $\alpha = 0.6$ and $\tau_{III} = 45$ MPa and $\alpha = 1$ and $\tau_{III} = 20$ MPa we also perform a comparison between the stress field solved by FEM computation (BCs 3 configuration, by

definition heterogeneous) and a homogeneous stress field imposed by the DDD code with the same crystal orientation (see Fig 4.13). The goal of such comparison is to check the role of the stress heterogeneity on the cross-slip activity. In addition, we investigated with the limit cases the influence of the crystalline orientation on cross-slip. Modifying the crystalline orientation, we can change the cross-slip activity by changing the Schmid factor ratio r between collinear slip systems.

$$r = \frac{m^{C5}}{m^{B5}} \tag{4.13}$$

The two different crystal orientations we compared are finally defined with the parameters :

- $\alpha = 0.6$ and $\tau_{III} = 45MPa$ with $r = 14.9$;
- $\alpha = 0.6$ and $\tau_{III} = 45MPa$ with $r = 1$.

The value of $r = 14.9$ corresponds to the crystalline orientation defined in Tab. 2.2. For this orientation, the difference between the Schmid factors on the primary and deviate slip system is very high. The value of $r = 1$ corresponds to a so-called high-symmetry orientation, namely [001] giving identical Schmid factor on the primary and deviate slip system. For these simulations, plastic deformation is initially limited to two Frank-Read sources (on slip system C5) on two close parallel slip planes and also limited to a thin region in the grain of about 4 µm thick. Cross-slip events are counted in this region to appreciate the variation of the number of slip planes as a function of previously listed parameters. Imposing such conditions for the simulations allows to reach rapidly high dislocation densities in a thin region (slip band-like structure) and to observe cross-slip events at low plastic deformation.

A comparison of cross-slip activity as a function of τ_{III} and α parameters is illustrated in Fig 4.12. In this figure, the number of cross-slip events on C5 and B5 is plotted as a function of plastic slip on slip system C5. Two primary trends emerge from these calculations. First, the quantity of cross-slip events on the deviated system B5 exceeds that of the primary system C5. For plastic slip values around 2.5×10^{-3}, the number of cross-slip events on C5 accounts for approximately 10 % of that on B5.

Second, as previously mentioned, decreased τ_{III} values result in active cross-slip at lower stress levels. This is particularly apparent in Fig 4.12 and for both slip systems. As a consequence, at an equivalent level of plastic slip, simulations where dislocation dynamics is solved considering $\tau_{III} = 20$ MPa instead of $\tau_{III} = 45$ MPa produce more cross-slip events. In the same way, but with a more relative intensity, rising the α parameter allows for more important cross-slip activity. The role of α is particularly evident on C5 and for the two values of τ_{III}. Nevertheless, we do not observe the same effect on the deviated slip system B5, where the role of α does not seem to contribute to intensify the cross-slip activity. This statement can be clarified by looking at the process by which the initial microstructure

is generated for these simulations. As previously mentioned, two Frank-Read sources are introduced into the grain on two slip planes belonging to the C5 slip system. In the early stages of plastic deformation, dislocations accumulate at the grain boundaries without cross-slip events occurring. This is mainly because we impose a threshold stress, τ_{III}, above which cross-slip becomes more prevalent. Therefore, we assume that the first observed events depend on τ_{III} rather than α. This is supported by both graphs in Fig 4.12, the value of α does not modify the moment at which the cross-slip appears. Once dislocations have cross-slipped for the first time, they can swiftly revert back to the primary system due to the significantly increased value of α in these simulations. This phenomenon accounts for the increase in slip planes and dislocation sources on the C5 system, thus explaining the imbalanced role of this parameter between the two systems in these simulations and for the plastic deformation reached.

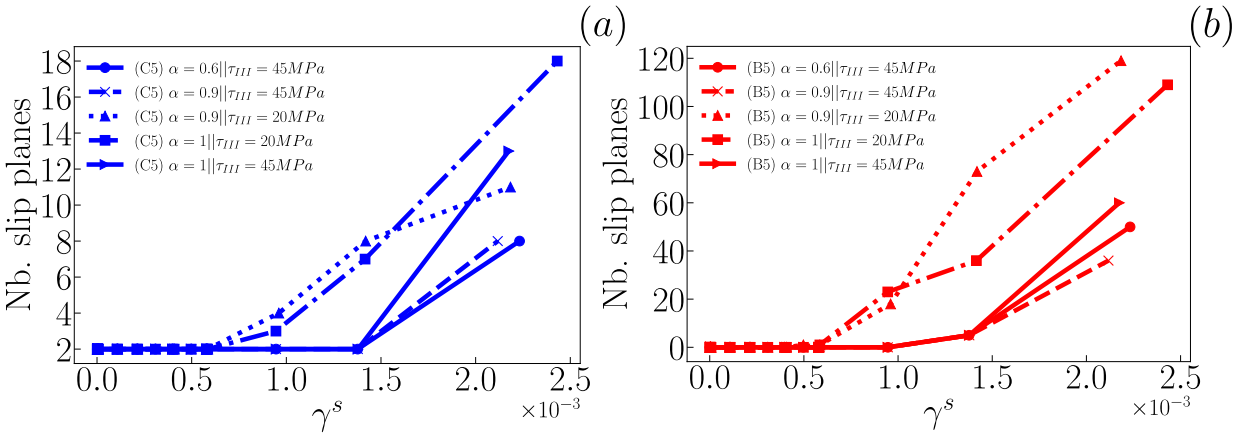

Figure 4.12: *Computation of cross-slip activity for slip system C5 (a) and slip system B5 (b) for various values of α and τ_{III}.*

From the results presented in Figure 4.13, it is evident that the degree of heterogeneity significantly influences cross-slip activity. The selected two extreme scenarios clearly demonstrate that assuming perfect homogeneity in loading results in a significant rise in cross-slip activity. This is particularly evident in Fig 4.13-(a) where the quantity of new planes and dislocation sources on C5 is six times greater in the homogeneous case than in the heterogeneous case. However, Fig 4.13-(b) indicates that this has not yet directly affected the plastic deformation. This graphic depiction highlights the accumulation of dislocations at grain boundaries for identical plastic slip values at $\gamma^{C5} = 2.25 \times 10^{-3}$. For every simulation, five "visible" slip planes are identified. The divergence between the results demonstrated in Fig 4.13-(a) is due to a very high number of tiny segments or debris that have undergone deviation. It should be emphasized that all of these debris items could potentially generate new sources of dislocations and consequently new "observable" planes. These are potential dislocation sources that can create plastic deformation. We can make similar statements regarding Fig 4.13-(c) and Fig 4.13-(d), illustrating the cross-slip activity on slip system B5.

Once again, supposing the loading to be perfectly uniform, significantly boosts cross-slip activity. Furthermore, the effects are more pronounced on the dislocation microstructures as displayed in Fig 4.13-(d). The number of "visible" slip planes is drastically modified by the loading state.

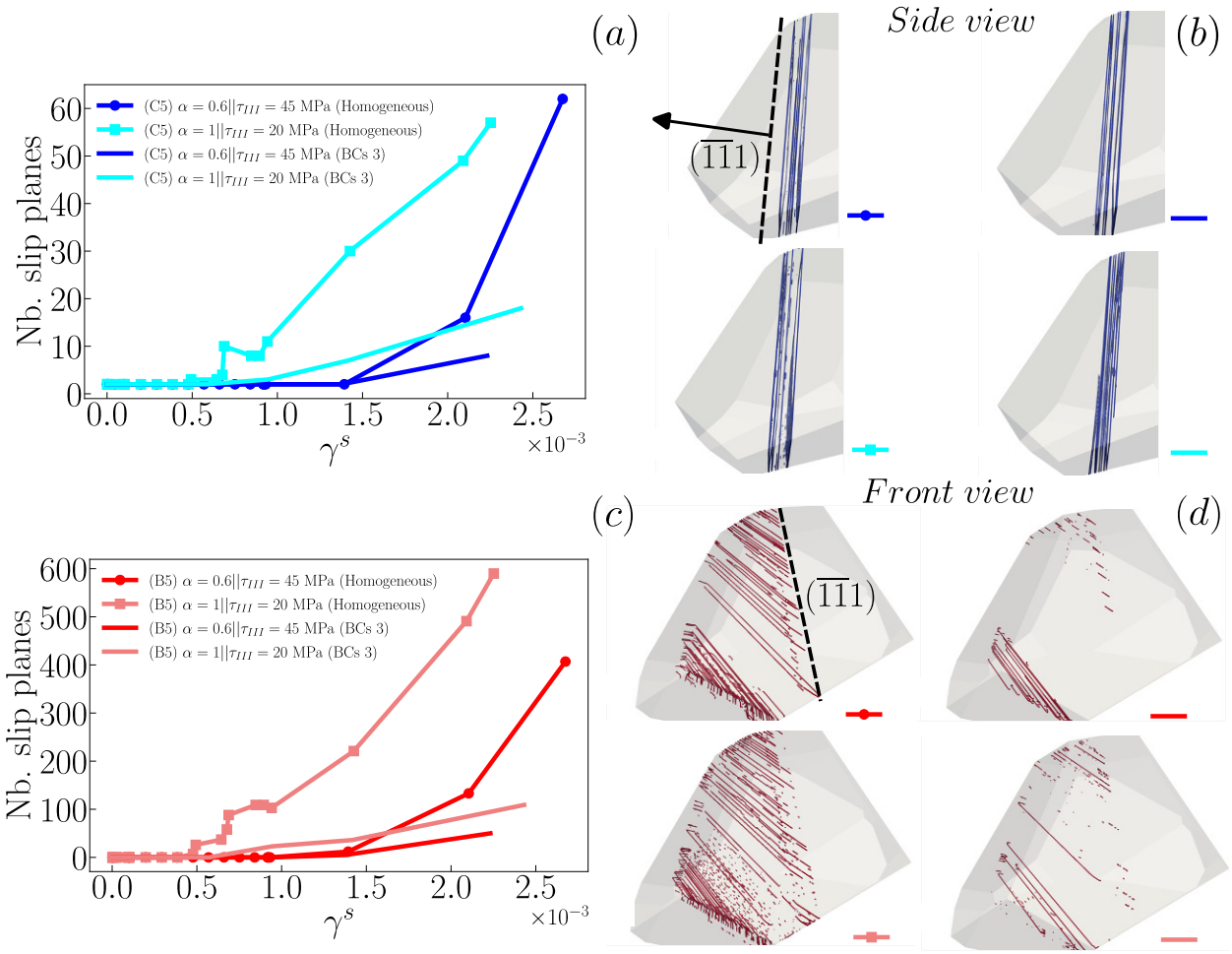

Figure 4.13: *Illustration of the cross-slip activity while considering a perfectly homogeneous and heterogeneous loading. The number of cross-slip events are counted for slip system C5 (a) and for slip system B5 (c). Visualization of the dislocation microstructure at* $\gamma^{C5} = 2.25 \times 10^{-3}$ *for slip system C5 is given in (b) and B5 in (d).*

Finally, Fig 4.14 illustrates the impact of crystal orientation on cross-slip activity. Calculations undertaken for the two different orientations, defined by the r ratio between the Schmid factors, exhibit a significant difference in cross-slip activity. As expected, for r=1, the cross-slip activity is significantly stronger on the two slip systems C5 and B5, as both slip systems have the same predicted plastic activity (Schmid factors) which is high for this orientation.

The calculations conducted in this section demonstrate the influence of specific material parameters, notably τ_{III} and α, on cross-slip activity. Our findings indicate that decreasing τ_{III} and increasing α promote cross-slip activity, as expected. Additionally, we observed that

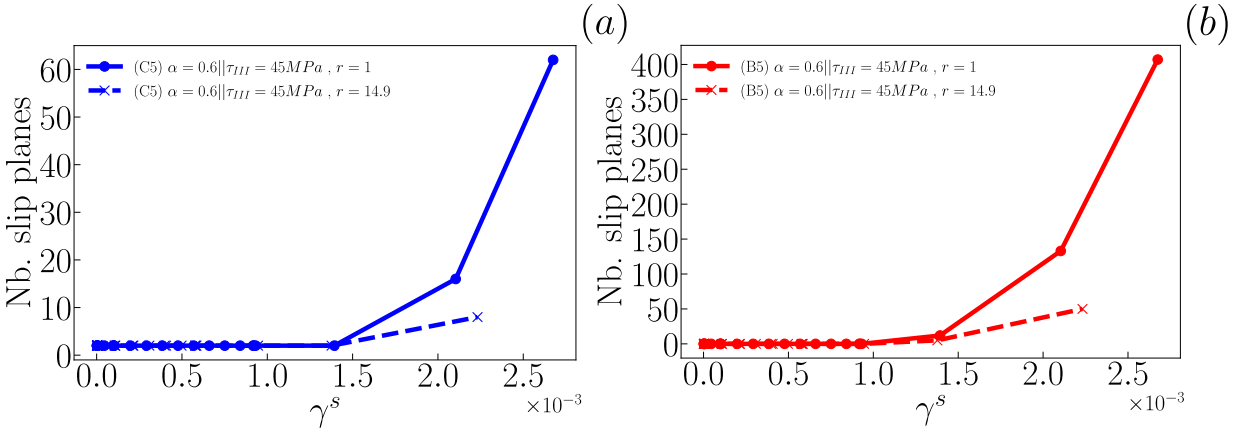

Figure 4.14: *Computation of cross-slip activity for slip system C5 (a) and slip system B5 (b) for various values of r.*

loading heterogeneity levels and crystalline orientation can also impact this activity. These results should be considered in relation to prior calculations (see § 4.4.2) which demonstrated that the plastic deformation within the grain becomes more uniform as cross-slip become more prevalent. Consequently, this reduced the gradient of slip trace intensity at the deformation levels we simulated. These results allow for the observation of strong trends and a better understanding of potential fluctuations in the distribution of plastic slip within the grain during plastic deformation.

4.5.3 On the cross-slip activity under "set 1" condition

The research conducted on identifying parameters that modify cross-slip activity also aimed to include all slip systems ("set 1") within the FCC structure in our simulations. Until now, we have assumed that taking into account only the most active slip system and its collinear system ("set 2") did not change the essence of our statements and therefore, the mechanism leading to plastic strain localization. In other words, we assumed that forest interactions are not essential to understand the localization process. However, our focus on the activity of cross-slip in the previous section has prompted us to take into account additional slip systems. Indeed, cross-slip is a means by which dislocations can bypass obstacles like forest dislocations. These forest dislocations, as well as others (coplanar slip systems), may markedly alter the stress field experienced by a dislocation at short distances. Hence, dislocation-dislocation forest interaction may have some influence on the cross-slip activity and multiplication processes.

In Fig 4.15 the calculation of the cross-slip activity for both configurations "set 1" (see Fig 4.15-(a)) and "set 2" (see Fig 4.15-(b)) is compared for $\tau_{GB} = 500$ MPa. At equivalent plastic slip level ($\gamma^{C5} = 1.1 \times 10^{-3}$), the number of cross-slip events monitored in the grain is significantly different from one configuration to another. In the case of "series 1", we see

a four-fold increase in the number of planes brought by the cross-slip activity in comparison with the "set 2" results. In addition, a cross-slip activity is monitored much earlier in the "set 1" configuration. In this case, we see cross-slip activity appearing from the very beginning of plastic deformation, whereas for the "set 2" configuration, cross-slip activity is observed at deformation larger than $\gamma^{C5} = 0.5 \times 10^{-3}$.

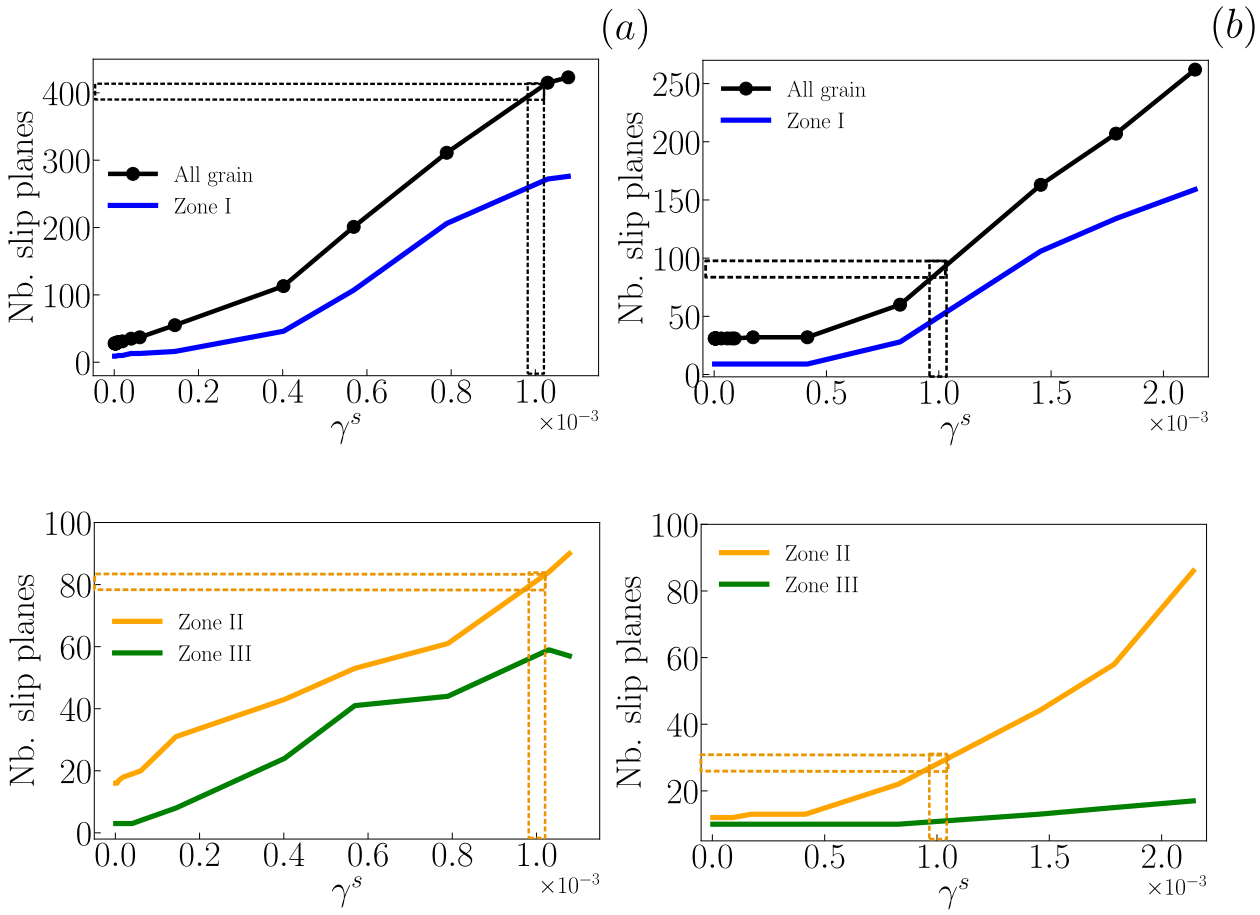

Figure 4.15: *Computation of cross-slip activity on slip system C5 for $\tau_{GB} = 500$ MPa in the case where all slip systems are considered in the simulations (a) and in the case where only C5 and B5 slip systems are considered (b).*

These results lead to the conclusion that, for quantitative simulations, the entire dislocation microstructure must be taken into account, at least as far as cross-slip activity is concerned. Consequently, in the next section (§ 4.6), we take a closer look at how plastic localization manifests itself in simulations with 12 slip system

4.6 Early stages of plastic strain localization under "set 1" condition

Taking all slip systems into account, because of their influence on cross-slip activity (see § 4.5.3), now appears to be an important point. Another reason to consider all the slip systems is that for the crystalline orientation, we studied (see Tab. 2.2), the studied grains are never oriented for single slip conditions. In fact, for the reference grain orientation, we have two coplanar active slip systems. Such simultaneous activity in parallel slip planes could modify the distribution of plastic slip within the grain and therefore the plastic strain localization processes.

It is important to note that the simulations presented in this section with 12 slip systems can hardly reproduce the same levels of plastic slip as those obtained under the "set 2" conditions. In the former case, dislocations are spread across all of the slip systems, leading to a significant increase in the number of segments within the simulations and therefore increasing rapidly the computation cost. For reference, the simulations presented in the following two sections (§ 4.6.1 and § 4.6.2) reached 1,500,000 segments and took approximately one week to calculate. The initial and final state of the microstructure, obtained from this type of simulation, is shown in Fig 4.16 below to give an overview of the number of dislocations simulated.

We first look at the role of stress concentration on the initiation and persistence of intense plastic slip within the grain during plastic deformation following "set 1" simulation conditions and BCs 1 elastic loading (§ 4.6.1). Thereafter, dislocation dynamics is also solved for other elastic loadings as in § 4.4.2. All the simulations presented in this section supposed the grain boundary to be penetrable with $\tau_{GB} = 500$ MPa and cross-slip is active following parameters presented in § 3.2.1.

4.6.1 On the role of stress concentrations

As stated above, we first solved dislocation dynamics considering BCs 1 elastic loading. Results of this simulation are illustrated in Fig 4.17 highlighting the most intense slip traces on slip system C5 ($\gamma_{vox}^{C5} \in [0.0025, 0.0067]$) in Fig 4.17-(a) and the calculation of the average plastic slip slice by slice on slip systems C5 and C3 in Fig 4.17-(b). Slip system C1 is not represented here as its activity is very low. The first statement we can make from these calculations is that plastic slip on slip system C5 is more intense than that on slip system C3. As detailed in Appendix C, slip system C5 is in fact more active than the slip system C3, at equivalent plastic deformation ($\varepsilon^p = 0.1$ %), $\gamma^{C5} = 0.11 \times 10^{-2}$ and $\gamma^{C3} = 0.085 \times 10^{-2}$. Another conclusion we can draw from this simulation is that plastic

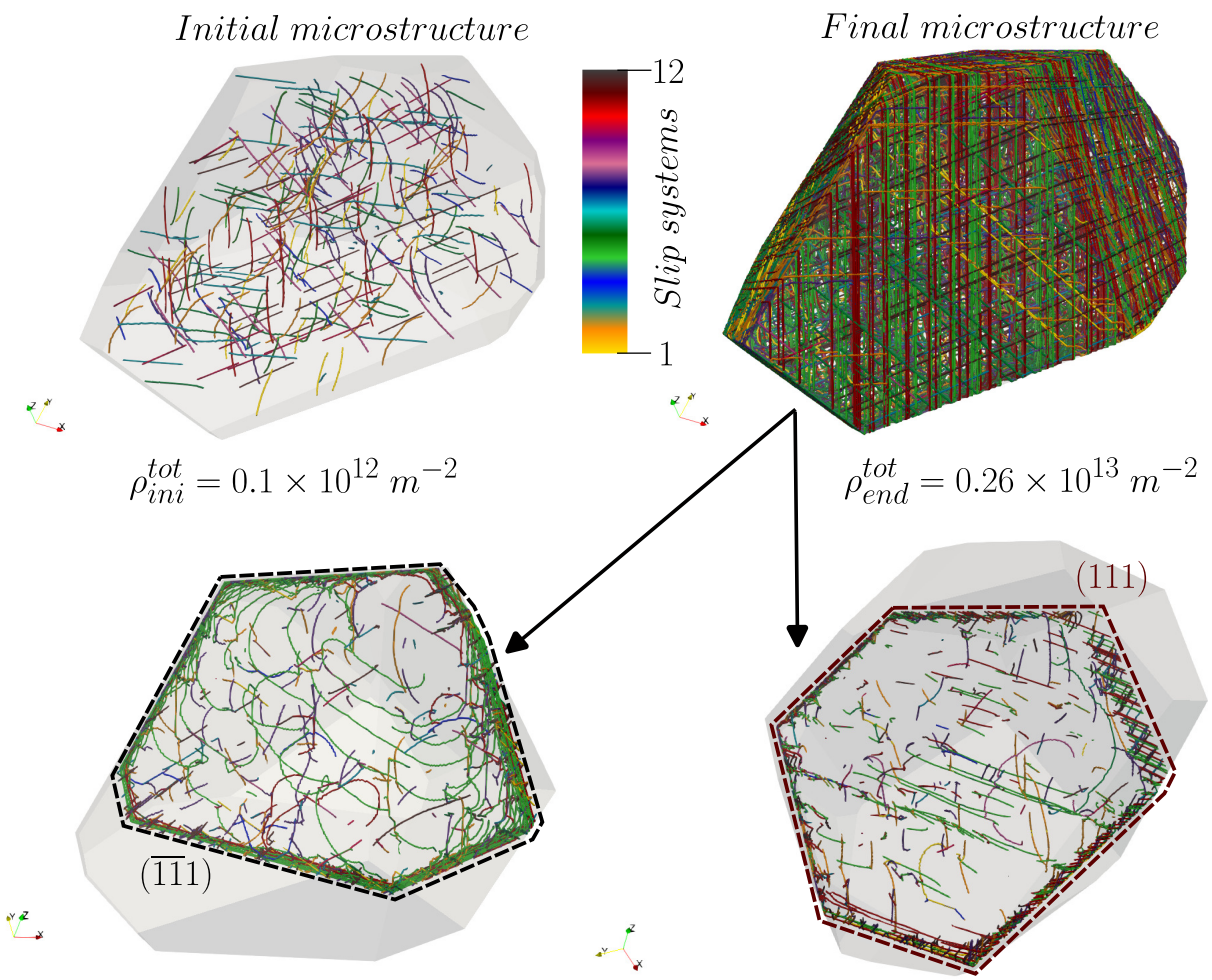

Figure 4.16: *Initial and final dislocation microstructure following "set 1" simulation conditions. Two slices are illustrated, one over* $(\overline{111})$ *plane and the second over* (111) *plane at* $\varepsilon^p = 0.1$ %.

slip is distributed differently between the two active slip systems. On C5, the distribution of plastic slip within the grain is more heterogeneous than on C3. Consequently, regions with intense local plastic activity stand out. This is notably the case for zone II close to the stress concentration, which is undoubtedly the region where plastic slip is the most intense on C5. As an example, the calculation performed in slice 18 shows very significant plastic activity. In comparison, plastic slip on C3 is relatively homogeneous and does not reveal any particularly preferential regions for intense plastic slip. By summing the contributions of the two slip systems (C5 + C3) for each of the slices, plastic deformation becomes somewhat more homogeneous but still reveals areas of more intense plastic activity (zone II). Referring to Tab. 4.2, it is evident that the level of heterogeneity of the elastic loading on C3 is lower, as well as its intensity. This partly explains the results obtained for the distribution of plastic slip. In agreement with this observation, we note that the transmitted density is much higher on C5 than on C3. Those values have been calculated at the end of the simulation ($\varepsilon^p = 0.1\%$) for both slip systems :

- $\rho_{trans}^{C5} = 0.12 \times 10^{12}\ m^{-2} \Leftrightarrow 0.15 \times \rho_{tot}^{C5}$;
- $\rho_{trans}^{C3} = 0.38 \times 10^{11}\ m^{-2} \Leftrightarrow 0.05 \times \rho_{tot}^{C3}$.

Here it must be noted that the transmitted density on C5 reached the value of the total initial dislocation density ρ_{ini}^{tot} (see Fig 4.16). In addition, the proportion of density transmitted on the C5 slip system is three times greater than on C3.

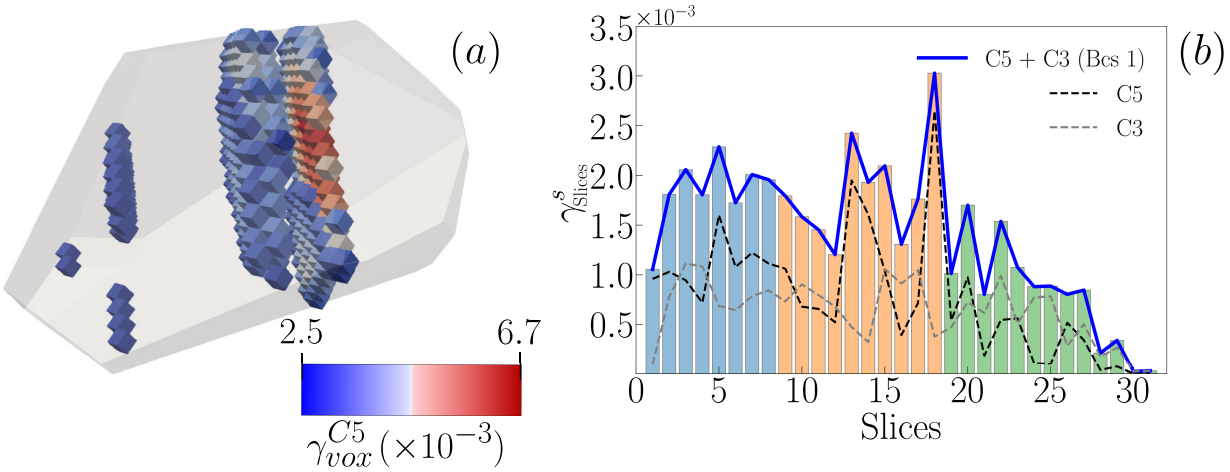

Figure 4.17: *Intragranular plastic strain deformation for BCs 1 at $\varepsilon^p = 0.1$ %. Plastic slip on slip system C5 for $\gamma_{vox}^{C5} \in [0.0025, 0.0067]$ (a) and average plastic slip values inside N slices made along $(\overline{1}11)$ planes (b) for both coplanar slip system C5 and C3.*

In comparison with the "set 2" simulation conditions, plastic slip values are lower. The maximum plastic slip simulated on C5 under the "set 1" simulation conditions is $\gamma^{C5} = 0.11 \times 10^{-2}$ while it is $\gamma^{C5} = 0.3 \times 10^{-2}$ for the "set 2" simulation conditions. Based on this statement, we propose to calculate the plastic slip activity as presented in § 3.3.3. As a consequence, four particular time intervals of equivalent amplitude are selected and illustrated in Fig 4.18-(a). Plastic slip activity is then calculated by plotting the most intense slip traces as illustrated in Fig 4.18-(b) and the average values, slice by slice are illustrated in Fig 4.18-(c). The various states of plastic deformation are listed below for each of the four intervals and for slip system C5 only :

- Interval 1: Plastic slip activity before grain boundaries penetrability is active. The deformation is quite homogeneous without strong gradients. Only zone III exhibits a lower level of plastic activity compared to the two others. The values of $\Delta\gamma_{vox}^{C5}$ illustrated on the graph belong to the interval $[0.3, 0.9] \times 10^{-3}$;
- Interval 2: Plastic deformation after activation of grain boundaries penetrability. Plastic slip activity is highly localized in zone II. The plastic slip distribution on the observed slip traces appears to be heterogeneous as high values are located on the top of

the traces, near the stress concentration region. The values of $\Delta\gamma^{C5}_{vox}$ illustrated on the graph belong to the interval $[0.6, 1.1] \times 10^{-3}$;

- Interval 3: A new slip trace of highly intense plastic slip emerges within zone II. The values of $\Delta\gamma^{C5}_{vox}$ illustrated in the graph belong to the interval $[0.8, 3.1] \times 10^{-3}$. Once again, plastic slip is heterogeneous at the slip trace level;

- Interval 4: Plastic slip activity reappears in the active region observed during interval 2. The values of $\Delta\gamma^{C5}_{vox}$ illustrated in the graph belong to the interval $[0.8, 2.3] \times 10^{-3}$. For this interval, the most intense activity is still localized in zone II.

This analysis first demonstrates that plastic activity varies in intensity and regions during plastic deformation. Indeed, the lowest plastic activity is calculated during interval 1 when the penetrability of grain boundaries is not yet active. Secondly, the spatial distribution and position of the most intense plastic activity zones also vary during plastic deformation. However, once the penetrability of grain boundaries is activated, intense plastic activity is confined to zone II denoting the influence of the stress concentration. The same affirmations can be drawn for the results illustrated in Fig 4.18-(c). In this figure, it is particularly interesting to focus on slices 13, 14 and 18 all belonging to zone II. In comparison, plastic activity on slip system C3 (not represented here) is much more homogeneous. On this system, the maximum value of $\Delta\gamma^{s}_{slices}$ is of 0.2×10^{-3}.

As discussed, this analysis also shows that plastic slip is more or less heterogeneous at the level of the slip traces themselves, particularly for the most intense slip trace (slice 18) on slip system C5. A more detailed analysis of the dislocation microstructure state at the location of the slip trace uncovers several mechanisms. Of particular importance is the collinear annihilation mechanism discussed in § 3.4.2. The results of this detailed analysis are illustrated in Fig 4.19 where a computation of the local plastic slip is performed in Fig 4.19-(a) on slice 18. In addition, for the same slice the resolved shear stress state is also calculated in Fig 4.19-(b). These illustrations show that the heterogeneity in plastic slip distribution at the slice level is directly correlated with the presence of stress concentration on the slip plane. The role of the collinear annihilations on the apparition of plastic slip heterogeneity is illustrated by the time-lapse depicted in Fig 4.19-(c). In these three screenshots, the initial microstructure as well as the microstructure at $\varepsilon^p = 0.064$ % and $\varepsilon^p = 0.1$ % are illustrated. This shows the creation of a very active dislocation source by means of the collinear reactions. This is particularly evident in the second screenshot for $\varepsilon^p = 0.064$ % where we highlight by a red square a region where a new dislocation source is created. Shortly after this event, the stress exerted by the dislocations piled up at the grain boundary activates penetrability in a region very close to the dislocation source, making plastic deformation easy and permanent in this region. This can be seen in the third screenshot in the green square. These observations confirmed a mechanism we already discussed in Chapter III. Nevertheless,

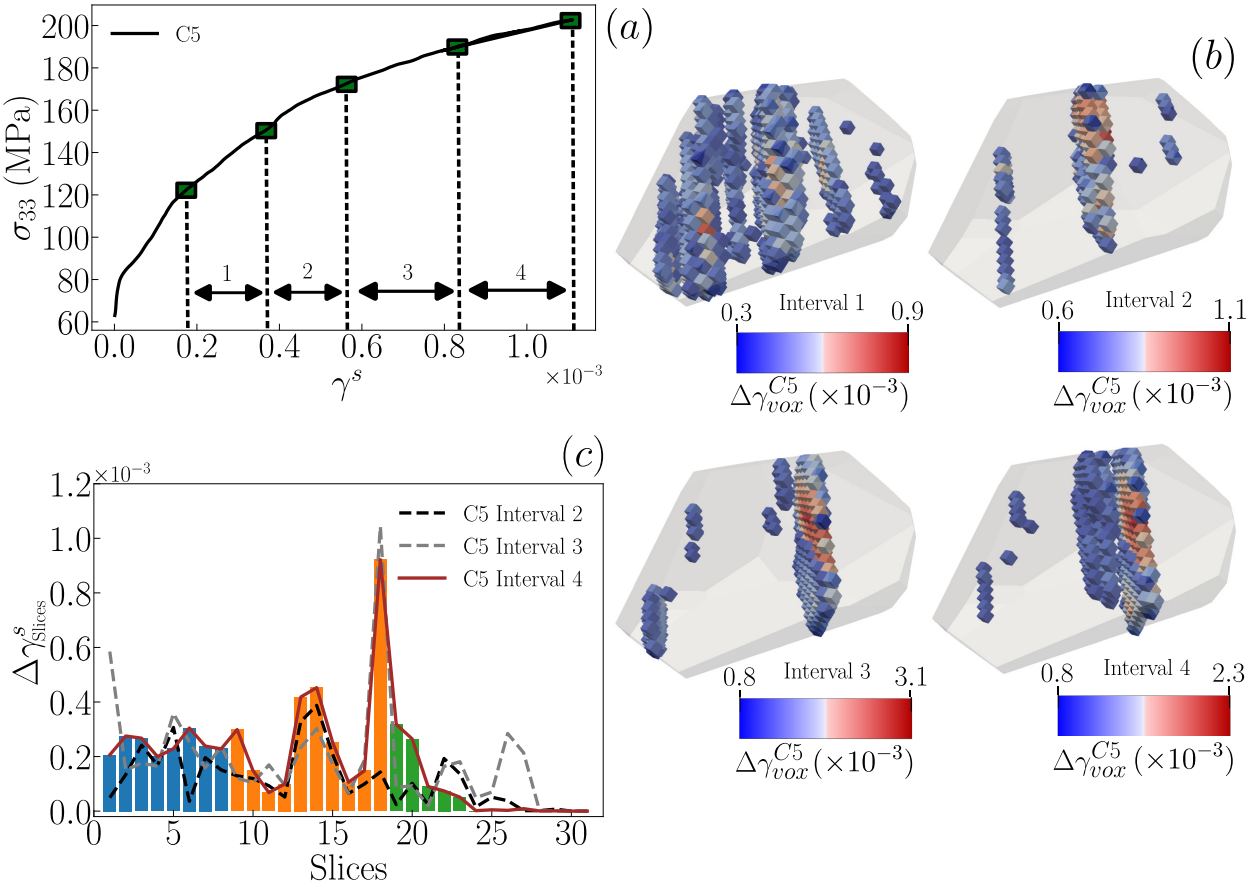

Figure 4.18: *Illustration of plastic activity for various time intervals and for BCs 1 elastic loading condition. The stress-plastic slip curves with four intervals (a), the slip system activity on C5 for different strain intervals (b). A threshold is systematically applied and given by the colormap. The average slip system activity for intervals 2, 3 and 4 on the N slices.*

it is possible to note some differences with our previous observations. In this particular case, the dislocations outside the stress concentration region pile up in a particular way. This mechanism was not observed in previous simulations, as most of these dislocations were annihilated by collinear reactions. The nature of this pileup is original in that the dislocations are particularly numerous and widely spaced. One of the explanations for such behaviour can be linked to the presence of forest dislocations that slow down dislocation mobility. A second explanation would be linked to the number of collinear reactions taking place on the slip plane. By comparing the state of the microstructure with the results shown in Fig 3.9 and Fig 3.10, we can see that the density of dislocations on slip system B5 is much lower in the simulation under the "set 1" conditions than in the "set 2" conditions. The "set 2" simulation conditions certainly favoured plastic deformation on slip system B5 as only two slip systems could accommodate plastic deformation. Here, all the systems are present and justify this significant difference. Nevertheless, apart from this point, the

collinear annihilation mechanism remains essentially unchanged. Collinear annihilations do make it possible to relocate sources of dislocations in regions of high stress that are more favourable to slip. One should note that the same observation was made on the other slip traces observed in zone II (slices 13 and 14) but they are not represented here.

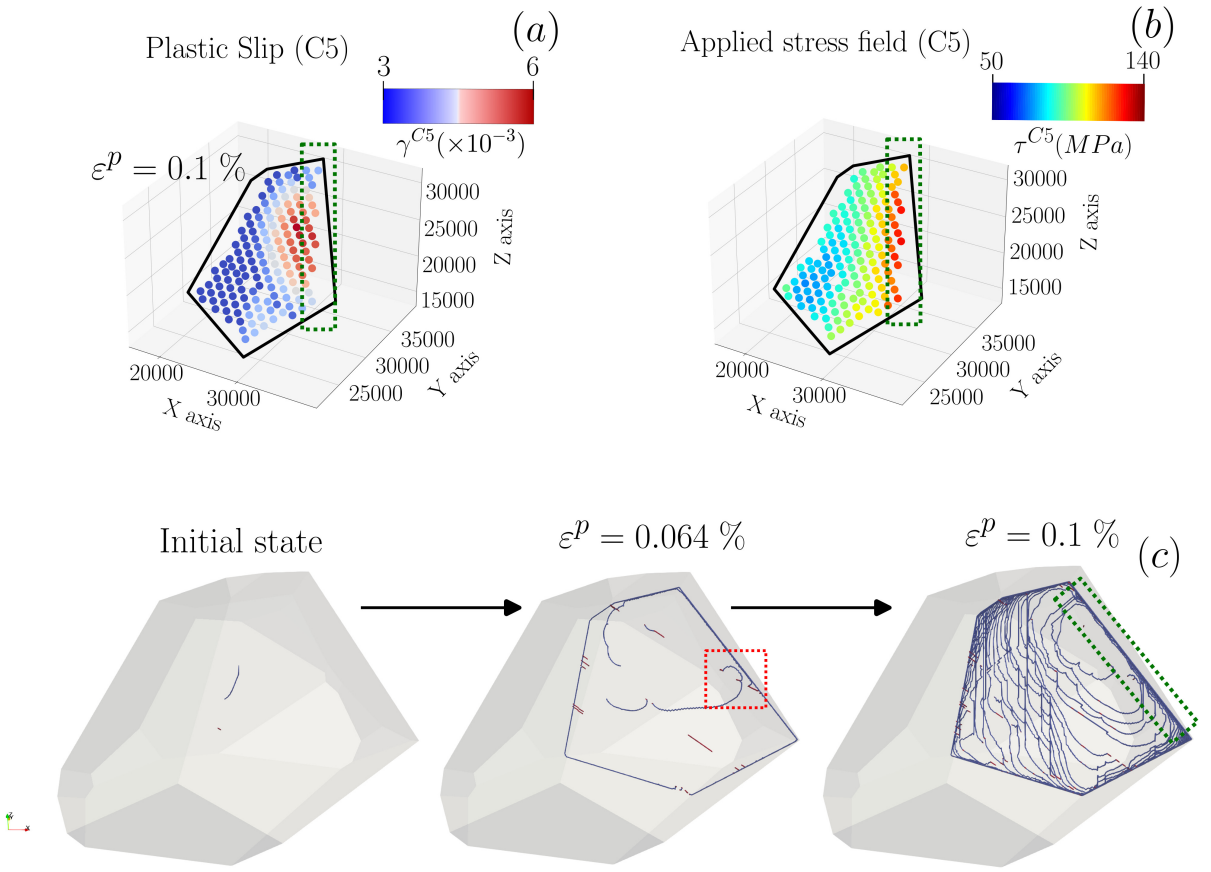

Figure 4.19: *Illustration of the role of stress concentrations on the apparition of intense plastic slip. Plastic slip values on C5 for slice number 18 (a) and the corresponding applied stress (b). Evolution of the dislocation microstructure on the slip plane from initial microstructure to microstructure at* $\varepsilon^p = 0.1$ % *(c), a threshold is applied to only visualize collinear slip systems C5 and B5.*

One can conclude from this section that stress concentrations trigger intense plastic deformation well localized in the grain. This process is amplified by the mechanism of dislocation penetrability in grain boundaries close to the high-stress region. It is interesting to note that the localization computed in zone III for the previous simulations (see Fig 4.7) has completely disappeared. In the next section (§ 4.6.2) we will try to make the same observations for various elastic loading.

4.6.2 Simulations with different elastic loading

In accordance with the calculations carried out in § 4.4.2, we first extend our simulations to two other elastic loading (BCs 2 & BCs 3) for which a high level of heterogeneity as well as a high stress intensity level is obtained. For both configurations, plastic slip as well as plastic activity are computed slice by slice and illustrated in Fig 4.20. In comparison with the results obtained for the BCs 1 elastic loading, the calculation of plastic slip illustrated in Fig 4.20-(a) and Fig 4.20-(c) is characterised by a more homogeneous spatial distribution and a relatively lower intensity on slip systems C5 and C3. For these two simulations and for both slip systems, it is difficult to say whether a region is plastically deformed in a preferential way. The calculation of plastic slip activity shown in Fig 4.20-(b) and Fig 4.20-(d) for slip system C5 only, which is the most active, does however reveal some trends.

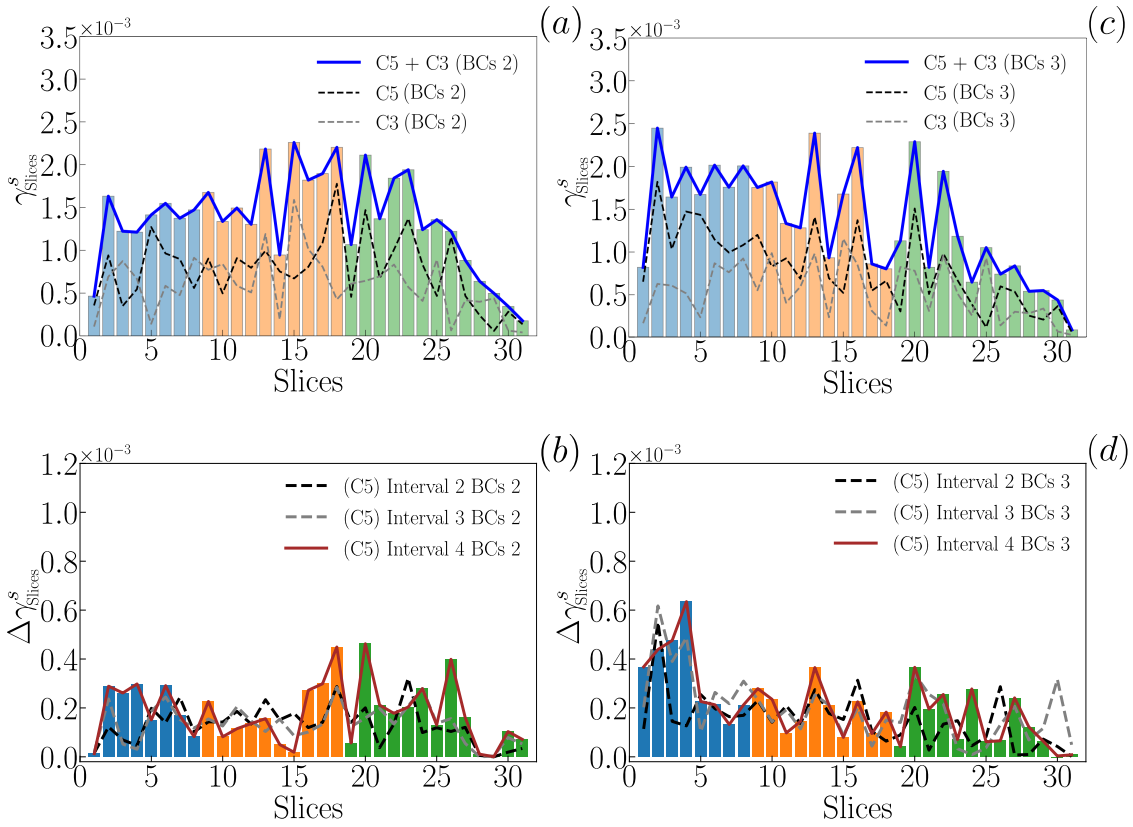

Figure 4.20: *Illustration of average plastic slip values for $\varepsilon^p = 0.1$ % on every N slices along $(\overline{1}11)$ planes for both elastic loading BCs 2 and BCs 3 (a)-(c) and average plastic activity (b)-(d).*

During the last interval (interval 4), and more particularly for BCs 3, it is possible to distinguish the apparition of a preferential region for plastic slip activity. This is particularly visible in slice 4. In comparison, BCs 2 during interval 4 shows weaker but nonetheless significant trends. For this simulation, it is possible to see the beginnings of preferential plastic activity between zone II and zone III (slices 18 and 20). For both simulations, the

regions of activity identified are correlated with the presence of stress concentration, as shown in Fig 4.8.

The above results and those obtained in the previous section show that the microstructure of the dislocations and the interaction between all the slip systems play a role in the onset of intense, localized plastic slip. The fact that plastic slip is less localized with the BCs 2 and BCs 3 conditions, in comparison to that in BCs 1, can be attributed to various factors. It is reasonable to imagine that for these two simulations, there is initially no dislocation source favourably positioned in regions of high stress concentration. As the maximum stress resolved on the most active slip system C5 has a lower intensity for these simulations, cross-slip and collinear annihilation are less efficient, which will delay the nucleation of new dislocation sources in the regions of interest. As the levels of plastic deformation reached are relatively low, some mechanisms may not have emerged yet.

The same type of simulation was done considering BCs 4 elastic loading whose main characteristic is to be the lowest ranked configuration from the developed criterion in Chapter II. BCs 4 is thus characterized by a low heterogeneity level and resolved shear stress intensity (see Tab. 4.2). The calculation of plastic slip illustrated in Fig 4.21-(a) for that simulation highlights a well distributed plastic deformation inside the grain on both slip systems C5 and C3.

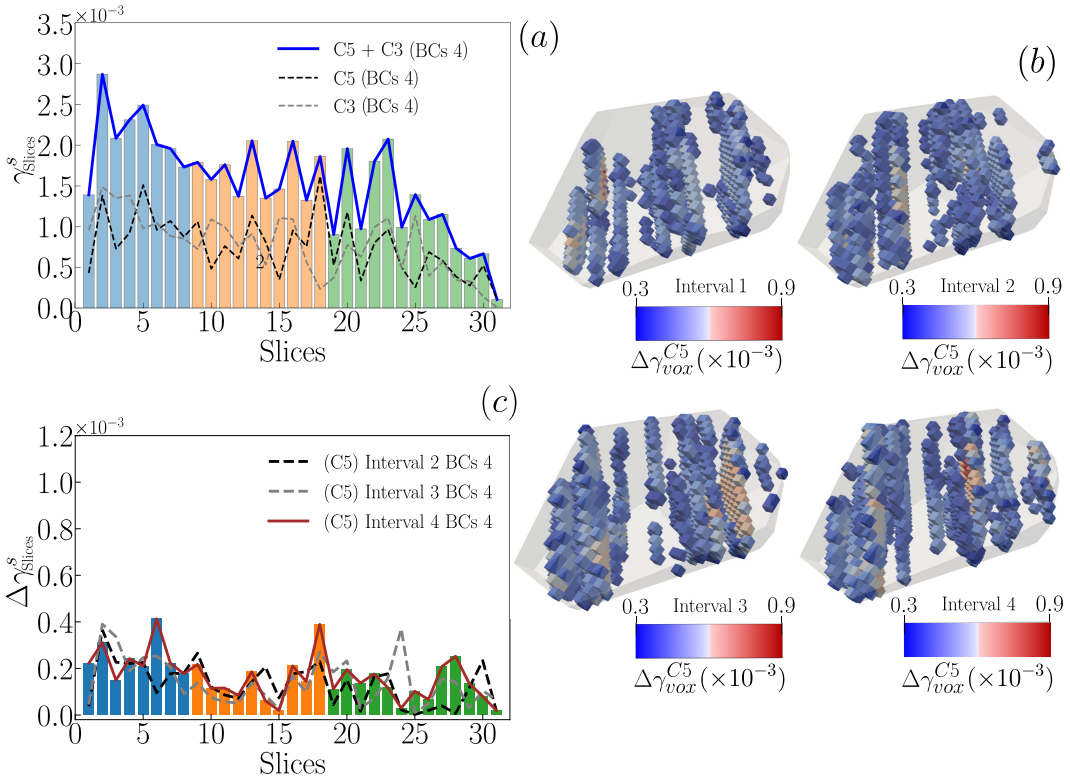

Figure 4.21: *Illustration of the computed average plastic slip values slice per slice for* $\varepsilon^p = 0.1$ % *(a), plastic activity computed for four constant time intervals (b) and average plastic activity slice per slice (c).*

It can be noted that an intense plastic slip peak is calculated in zone I when the contribution of both systems (C5 + C3) is added. Plastic slip activity on slip system C5 illustrated in Fig 4.21-(b) and Fig 4.21-(c) confirms the well distributed plastic deformation state. In comparison with results obtained on BCs 1 simulation (see Fig 4.18), calculations show that plastic activity during intervals 1 to 4 does not vary in position. The intensity of plastic slip varies minimally and is lower than for BCs 1 simulation. Activation of the penetrability of the grain boundaries does not greatly influence plastic slip at the level of deformation reached during the simulation as the transmitted density is sensibly lower.

A more comprehensible comparison of plastic slip distribution for BCs 1 and BCs 4 is given in Fig 4.22 at $\varepsilon^p = 0.1$ %. This graph illustrates the variation in plastic slip distribution and intensity among these two calculations. The effect of the stress concentration region on the plastic slip is here particularly noticeable as depicted by the two red arrows.

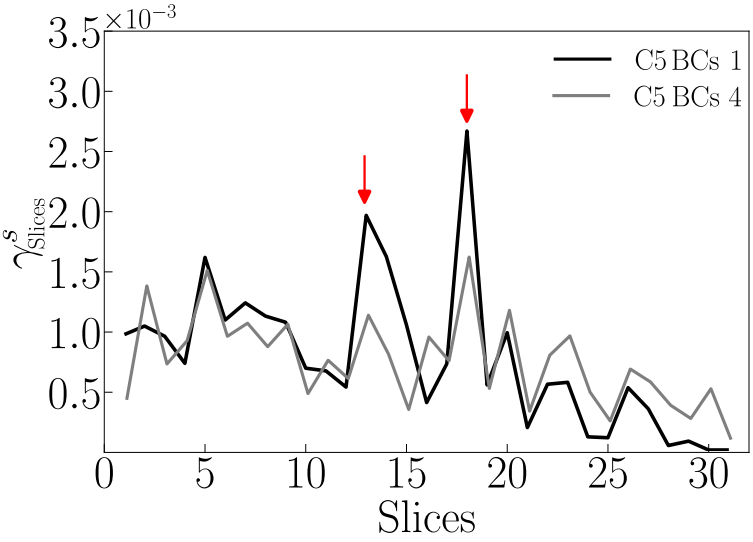

Figure 4.22: *Illustration of the average plastic slip values slice by slice for the simulation with BCs 1 and BCs 4 on slip system C5 at* $\varepsilon^p = 0.1$ %.

The results of this section indicate that plastic deformation at the deformation level attained with DDD simulations is rather uniform within the grain over many slip traces. This is especially evident in three of the four elastic loading configurations (BCs 2, BCs 3 and BCs 4). However, in certain instances, such as the scenario depicted in Fig 4.17 and Fig 4.18-(c), the dislocation microstructure reorganises to generate Frank-Read sources close to areas of stress concentration that are favourable to the production of significant plastic slip. In this case, plastic deformation is preferentially localized in these zones, resulting in a strong gradient of plastic deformation between the different slip traces in the grain. These outcomes of DDD simulations are entirely consistent with the experimental observations found in the literature on pure FCC metals, such as copper and aluminium, where globally uniform deformation patterns are seen (see § 1.2.3), with only a few grains exhibiting more intense slip bands. The experimental observations carried out in the ANR project on pure

nickel samples follow similar conclusions (see Fig 4.23). As can be seen in this figure, for this level of macroscopic plastic deformation (0.5 %), the distribution of intragranular slip bands within the aggregate is homogeneous. The majority of grains have a large number of slip bands very close together and it is therefore difficult to observe a significant plastic slip gradient. However, in some grains, the localization of very intense slip bands is more obvious as depicted in the red squares. More details about that kind of result will be given in the work of my colleague Muhammad Fakhry HATTA.

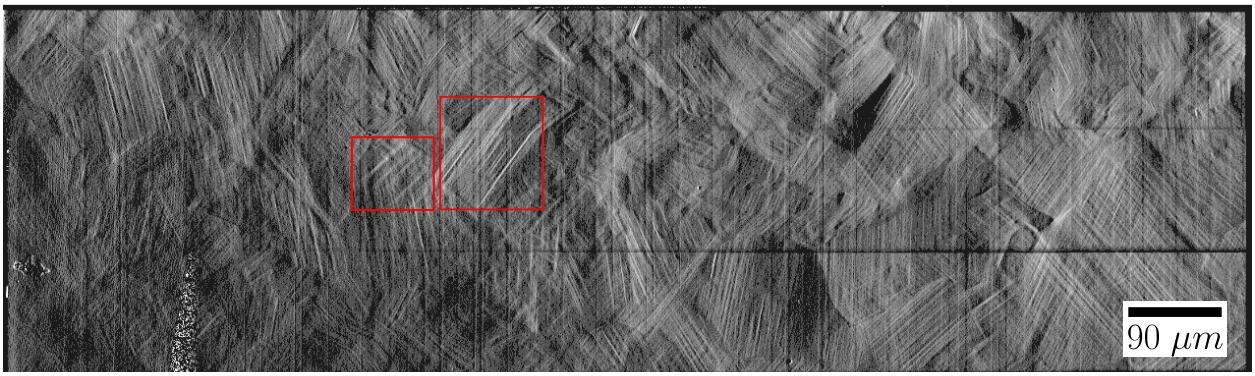

Figure 4.23: *Plastic strain field events at the surface of a pure Nickel sample by DIC measurements at* 0.5 % *macroscopic plastic strain. The Nickel sample was prepared by Muhammad Fakhry HATTA and strained by Jean-Charles STINVILLE in the scope of the ANR project 3DiPolyPlast.*

4.7 Conclusion

This chapter demonstrates the possibility of considering dislocation-grain boundary reaction mechanisms during plastic deformation using an additional local rule. This local GB penetrability rule is used to model a limiting case in which dislocations reacting with a GB no longer interact elastically with dislocations inside the emitting grain. This is achieved by eliminating the self-stress field of dislocation segments close to a GB when a critical stress pushes them against the GB. With this relatively simple criterion, which requires no complex integration in the DDD code, we were able to perform simulations on complex configurations.

In particular, it was shown that taking into account the penetrability of grain boundaries led to significant changes in the intragranular plastic behaviour. Indeed, in the presence of grain boundary penetrability, plastic deformation becomes more localized and persistent, as demonstrated by simulations following "set 2" conditions. In this chapter, we also show the role of the grain boundary penetrability stress that defines the grain boundaries strength and whose effect on slip persistence is of importance, in particular when considering cross-slip to be active. The persistence of plastic slip appears to be initiated close to stress concentration regions if it is permitted by the dislocation microstructure, otherwise, persistence

mechanisms are also observed in other regions without stress concentrations.

From these computations, the GB penetrability stress appears to be a key material parameter in order to get localized and persistent plastic slip. Throughout this chapter, the grain boundary penetrability stress has been considered to be identical for each of the grain boundaries. The introduction of a variation in this stress as a function of the type of grain boundary (depending on the disorientation of the two adjacent crystalline lattices for example) would be a more realistic representation and could also have a strong influence on the development of intragranular plastic slip, of the same order as the stress concentration.

Complementary calculations provide a better understanding of the role of cross-slip on intragranular plastic deformation, particularly with regard to the appearance of more or less intense slip bands and the distribution of these bands within the grain. In our simulations, cross-slip appears to be a mechanism for homogenizing plastic deformation, thereby reducing the effect of grain boundary penetrability at the deformation levels we can reproduce. In addition, the cross-slip also appears to be a mechanism for initiating plastic deformation in particular regions by bringing plastic deformation to favourable regions and also by increasing the number of collinear interactions. The role of the collinear interactions has been demonstrated in the initiation of intense plastic slip via the formation of new dislocation sources.

Subsequently, simulations carried out by considering all the slip systems of the FCC structure showed that the localization of plastic deformation was indeed influenced by the presence of stress concentrations provided that sources were deposited close to the latter. Comparisons were carried out on different elastic loading configurations, considered favourable or unfavourable for the localization of plastic deformation according to the criterion defined in Chapter II. These comparisons showed that in the absence of the mechanisms allowing the sources to be deposited close to a favourable region, plastic deformation is distributed more or less homogeneously in the grain. These observations are fully consistent with the experimental observations made on pure FCC metals, where intense localization events are observed only in a few grains.

Chapter V

Multi-scale simulations of the intragranular plastic behaviour

Résumé :

Au cours de ce chapitre, nous nous proposons d'étudier les potentialités d'une modélisation par un couplage fort entre FEM et DDD via le modèle discret-continu. Comme nous le montrons dans la première partie de ce chapitre, le modèle discret-continu constitue une source d'informations non négligeable quant à la description physique du contraste de diffraction observé lors des expérimentations de topo-tomographie. Par ailleurs, nous montrons dans un cas simplifié, la simulation de ce contraste de diffraction lié à la présence d'une bande glissement. Le contraste simulé montre d'importante variation de l'intensité du faisceau diffracté en accord avec les observations expérimentales. Dans un autre registre, nous montrons que le modèle discret-continu permet aussi d'étudier de manière justifiée les interactions entre grains au cours de la déformation plastique. Les résultats obtenus au cours de ce chapitre montrent par ailleurs que ces interactions donnent lieu à des mécanismes d'écrantages élastiques importants et permettent ainsi de donner une explication quant à l'apparition d'une réduction de l'écrouissage local et donc l'apparition d'une région où la déformation plastique devient plus favorable. La comparaison entre le comportement plastique intragranulaire du grain central dans le cas d'interactions purement élastique et dans le cas d'interactions pouvant devenir plastique montre bien des évolutions des courbes contraintes-déformations très différentes.

Contents

5.1 Introduction

The aim of this final chapter is to present the potential and preliminary results from a set of multi-scale simulations. These simulations are based on a coupling between the DDD and the FEM via the DCM, a description of which is given in § 1.7. This type of modelling provides an even more accurate description of the mechanisms involved in the plastic deformation of a polycrystalline aggregate by considering both elastic and plastic strain incompatibility between grains. The simulations presented in this chapter are idealized, incorporating simplified geometries and particular dislocation microstructures. Beyond the idealized nature of these simulations, the results obtained and the trends observed are important and merit further examination in the context of future research.

In particular, DCM simulations enable the precise calculation of the intragranular elastic rotation and distortion fields due to the presence of dislocation microstructures. This information is of particular interest in the context of the experiments carried out at the synchrotron as part of the ANR project 3DiPolyPlast. Using this type of simulation to explain the diffraction contrast observed during the topo-tomography experiments is also a major objective of the ANR project. The in situ bulk X-ray observations of polycrystalline materials reveal the presence of intragranular diffraction bands-like contrasts. This contrast is observed along crystallographic planes and belongs to active slip systems as reported by the pioneer work of [Tanner, 2013] and more recently by [Proudhon et al., 2020; Stinville et al., 2022b]. The question of nature of this contrast is still an open question, but the most likely reasons are linked to the presence of dislocations piling up at grain boundaries (GND) and dislocation microstructure within the slip band. A detailed presentation of the first simulated diffraction images using the results of a DCM simulation is given in § 5.2 and demonstrates the full potential of this type of comparison.

Using the DCM, it is also possible to study more precisely the role of interactions between grains during plastic deformation and, in particular, the effects of plastic relaxation on a reference grain. These effects appear when plastic deformation is observed in the vicinity of a grain and could play a major role in the appearance of local and persistent plastic slip, as detailed in § 5.3.

5.2 Contribution of dislocation microstructure to diffraction image contrast

In this section, a model case study is presented, using the results of a DCM simulation to simulate the appearance of diffraction spots on the detector during topo-tomography

acquisition. These results obtained jointly with the members of the ANR project, show the direct influence of plastic deformation in the form of a localization band on local diffraction conditions. A detailed description of the calculation of elastic rotation fields is given in this section under the small perturbation assumption.

5.2.1 Coupled simulation (DCM)

To explore the modelling X-ray diffraction image contrasts associated with a slip band-like structure, a simple DCM simulation is used. A polycrystal is defined, as composed of 27 cubic grains with one unique crystalline orientation and with identical edge size of 29 µm. The choice of equivalent crystalline orientations between the grains is based on the desire not to give rise to elastic strain incompatibilities and therefore to only calculate the effect of the presence of plastic deformation in a slip band-like structure. To do so, all the grains in the aggregate are supposed to be elastic except the central grain whose plastic deformation is produced by one Frank-Read source on the slip system A3 and set at a pre-defined position in the grain as illustrated in Fig. 5.1. The crystalline orientation is near simple glide orientation defined by the Schmid factors given in Tab. 5.1. Grain boundaries

(ϕ_1,Φ,ϕ_2) = (-26.56, -35.43, -153.43)

Slip System	**1-B4**	**2-B2**	**3-B5**	**4-D4**	**5- D1**	**6-D6**
Schmid factor	0.36	0.19	0.16	0.126	0.3	0.176
Slip System	**7-A2**	**8-A6**	**9-A3**	**10-C5**	**11-C3**	**12-C1**
Schmid factor	0.129	0.34	0.47	0.0039	0.016	0.02

Table 5.1: *Solution of the calculation of the theoretical unidirectional Schmid factors for the 12 FCC slip systems. The orientation is given (in degrees) according to the Euler angle convention* (ϕ_1,Φ,ϕ_2).

are supposed to be impenetrable to dislocations and the mesh is defined by quad elements with linear interpolation (c3d8). The mesh discretization is defined as a uniform grid of $20 \times 20 \times 20$ elements (per grain). Periodic boundary conditions are used and the imposed strain rate is of 8 s^{-1} along the Z axis. The simulation was run up to $\varepsilon^p = 0.02$ %, all the deformation being made on a single slip plane. In accordance with the calculations carried out in § 3.5.1, we have shown that the long-range elastic field emitted by dislocations on a single or on several slip planes is equivalent. This justifies our decision here, to carry out the deformation on a single slip plane in order to model a slip band-like structure.

5.2.2 Calculation of the elastic rotation and strain fields

The equations for calculating the elastic rotation and strain fields under the small perturbation assumption are given. We are interested here only in the elastic fields because these

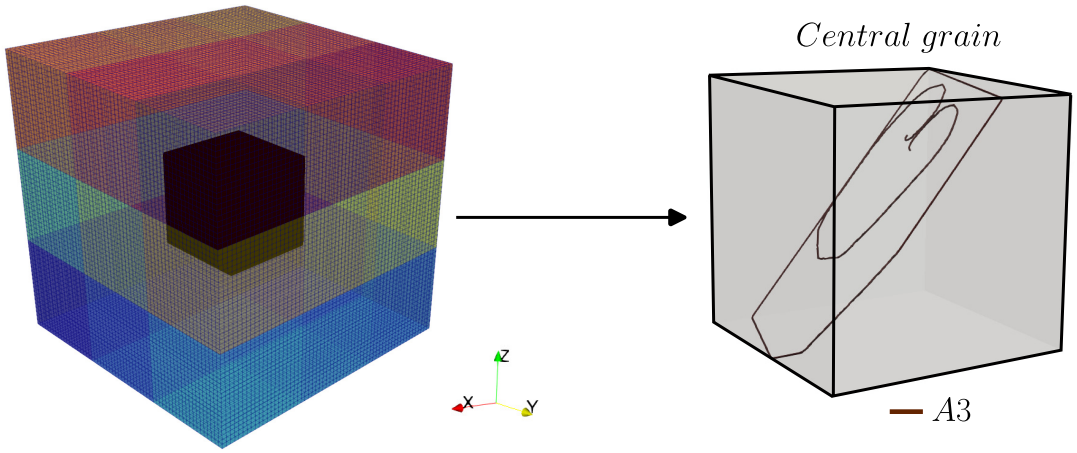

Figure 5.1: *Illustration of the polycrystalline aggregate composed of 27 cubic grains with central grain highlighted in black. The imposed Frank-Read source position is illustrated inside the central grain.*

are the ones that directly impact the orientation and distortion of the crystal (see § 1.5.1) and therefore the diffraction conditions. Under the assumption of small perturbations, one can express the total strain and rotation fields as a linear decomposition of the displacement gradient:

$$\underset{\sim}{\varepsilon}^{tot} = \frac{1}{2}(\mathrm{grad}(\underline{U}) + \mathrm{grad}(\underline{U})^T) \tag{5.1}$$

$$\underset{\sim}{\omega}^{tot} = \frac{1}{2}(\mathrm{grad}(\underline{U}) - \mathrm{grad}(\underline{U})^T) \tag{5.2}$$

Following Eq. 1.9 and Eq. 1.10 one can rewrite:

$$\underset{\sim}{\varepsilon}^{e} = \underset{\sim}{\varepsilon}^{tot} - \underset{\sim}{\varepsilon}^{p} \tag{5.3}$$

$$\underset{\sim}{\omega}^{e} = \underset{\sim}{\omega}^{tot} - \underset{\sim}{\omega}^{p} \tag{5.4}$$

With $\underset{\sim}{\varepsilon}^{p}$ and $\underset{\sim}{\omega}^{p}$ the plastic strain and rotation fields expressed as:

$$\underset{\sim}{\varepsilon}^{p} = \frac{1}{2}\sum_{s=1}^{N}\gamma^{s}(\underline{l}^{s} \otimes \underline{n}^{s} + \underline{n}^{s} \otimes \underline{l}^{s}) \tag{5.5}$$

$$\underset{\sim}{\omega}^{p} = \frac{1}{2}\sum_{s=1}^{N}\gamma^{s}(\underline{l}^{s} \otimes \underline{n}^{s} - \underline{n}^{s} \otimes \underline{l}^{s}) \tag{5.6}$$

With $\underline{l}^{s}$ the slip direction and $\underline{n}^{s}$ the normal to the slip plane. Here, it must be noted that DCM simulation does not intrinsically provide the plastic slip γ^{s} solution at the integration point of the FE mesh, only the plastic strain tensor $\underset{\sim}{\varepsilon}^{p}$, but under the case of simple glide condition on the slip system A3 (see § 5.2.1) one can write:

$$\underset{\sim}{\varepsilon}^{p} = \frac{1}{2}\gamma^{A3}(\underline{l}^{A3} \otimes \underline{n}^{A3} + \underline{n}^{A3} \otimes \underline{l}^{A3}) \tag{5.7}$$

By a simple identification, we can express γ^{A3} from $\underset{\sim}{\boldsymbol{\varepsilon}}^p$ solution and compute $\underset{\sim}{\boldsymbol{\omega}}^p$ to finally get $\underset{\sim}{\boldsymbol{\omega}}^e$. For the needs of the diffraction spots simulation, the solution fields need to be defined on a more refined grid, like a $80 \times 80 \times 80$ grid. As the use of such a grid would be too demanding in computational costs, the solution we used is to linearly interpolate from the initial grid of $20 \times 20 \times 20$ to a refined one. The solution for such interpolation in the case of the DCM simulation of one slip plane inside a cubic grain is given in Fig 5.2. This result shows how the dislocation piled up at grain boundaries, as illustrated in Fig 5.2-(c), influences the crystalline orientation via the rotation and elastic deformation components illustrated in the figure. As expected, the presence of the dislocation stack is noticeable throughout the grain due to its long-range contribution.

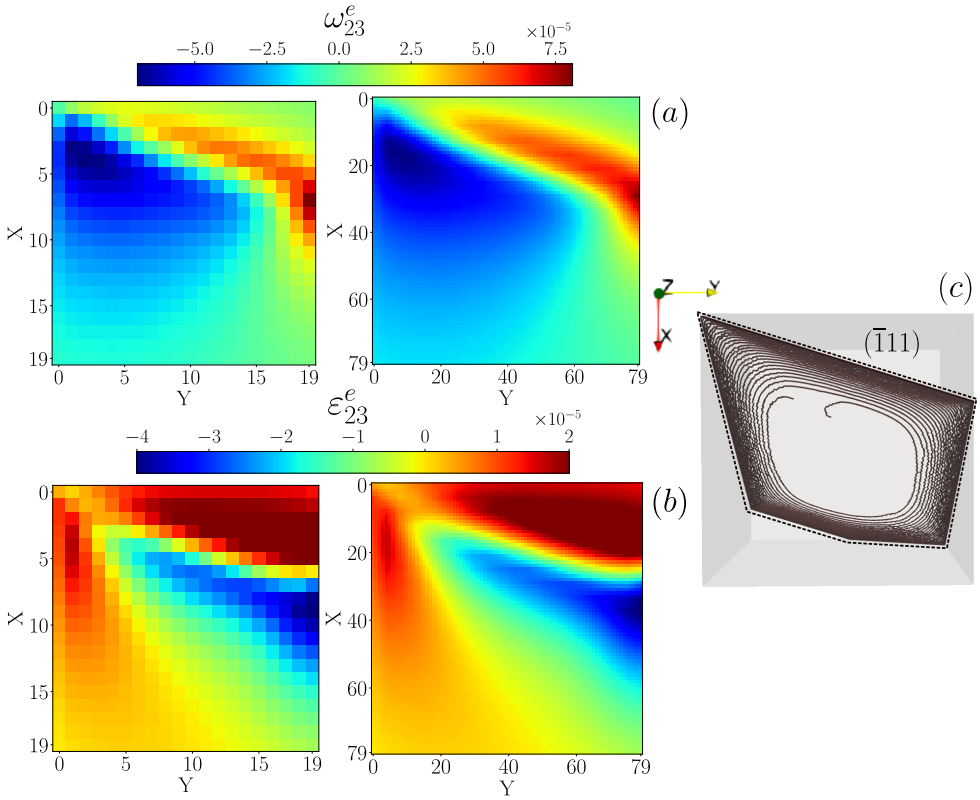

Figure 5.2: *Illustration of the elastic rotation field component ω^e_{23} in (a) and elastic strain component ε^e_{23} in (b) on the initial $20 \times 20 \times 20$ grid and the redefined $80 \times 80 \times 80$ grid. The results are given for one particular slice made in the grain $[x, y, z] = [:, :, 19/79]$ and the dislocation microstructure is depicted in (c).*

5.2.3 Calculation of the local crystal rotation

Applying the rotation field to the crystalline orientation in order to compute the updated crystalline orientation needs careful attention as formulations and expressions of rotation and orientation matrices vary as a function of their convention. In this manuscript, we describe the convention used in *Z-set* where orientation matrices are represented following the Bunge

crystallographic passive convention where the relation between sample and crystal reference frames is expressed as:

$$\underline{V}_c = \underset{\sim}{\boldsymbol{g}}.\underline{V}_s \tag{5.8}$$

With $\underset{\sim}{\boldsymbol{g}}$, the orientation matrix and $\underline{V}_c$ a vector expressed in the crystal reference frame and $\underline{V}_s$ expressed in the sample reference frame. Thus, the orientation matrix is defined as:

$$\underset{\sim}{\boldsymbol{g}} = \begin{pmatrix} X_1 & Y_1 & Z_1 \\ X_2 & Y_2 & Z_2 \\ X_3 & Y_3 & Z_3 \end{pmatrix}$$

With $\underline{X}$, $\underline{Y}$ and $\underline{Z}$ defining the crystal reference frame. The solution of the rotation field as expressed in Eq. 1.7 is a rotation matrix, meaning that $\det(\underset{\sim}{\boldsymbol{R}}) = 1$. This field can be applied to the crystalline orientation as described in the following decomposition of the rotations illustrated in Fig 5.3 in order to compute the new orientation field in the presence of dislocations. Crystal orientation in *Z-set* is defined as a rotation from the sample reference frame to the crystal reference frame, this rotation is expressed as the initial rotation $\underset{\sim}{\boldsymbol{g}}_0^T$ (A to B). Rotation of the crystal lattice is then expressed as a function of the initial crystal reference frame by the rotation $\underset{\sim}{\boldsymbol{R}}$ (B to C), the solution of the computation. Following the

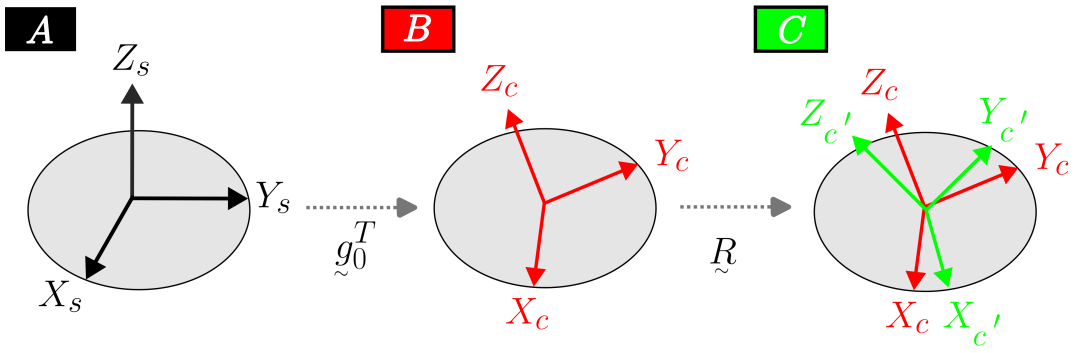

Figure 5.3: *The decomposition of the rotations as implemented in* Z-set.

composition law for rotations, the global rotation $\underset{\sim}{\boldsymbol{g}'}^T$ can be expressed as:

$$\underset{\sim}{\boldsymbol{g}'}^T = \underset{\sim}{\boldsymbol{R}}.\underset{\sim}{\boldsymbol{g}}_0^T \tag{5.9}$$

With $\underset{\sim}{\boldsymbol{g}'}$ the final orientation after application of the rotation field. Then, to compute the updated crystalline orientation one can write:

$$\underset{\sim}{\boldsymbol{g}'} = (\underset{\sim}{\boldsymbol{R}}.\underset{\sim}{\boldsymbol{g}}_0^T)^T = \underset{\sim}{\boldsymbol{g}}_0.\underset{\sim}{\boldsymbol{R}}^T \tag{5.10}$$

In this case, $\underset{\sim}{\boldsymbol{R}}$ is expressed in the sample reference frame which is convenient with DCM computations. The CPFEM (see § 5.2.5) computation made in this chapter expressed $\underset{\sim}{\boldsymbol{R}}$ in the crystal reference frame. Following this assumption, Eq. 5.10 should be modified as (necessary for the comparison made in § 5.2.5):

$$\underset{\sim}{\boldsymbol{R}} = \underset{\sim}{\boldsymbol{R}}_s = \underset{\sim}{\boldsymbol{g}}_0^T . \underset{\sim}{\boldsymbol{R}}_c . \underset{\sim}{\boldsymbol{g}}_0 \tag{5.11}$$

$$\underset{\sim}{\boldsymbol{g}}' = \underset{\sim}{\boldsymbol{R}}_c^T . \underset{\sim}{\boldsymbol{g}}_0 \tag{5.12}$$

Under the small perturbation hypothesis, the disorientation angle of the crystal with respect to its reference crystalline orientation can be calculated as follows. The series expansion of a rotation tensor with respect to its infinitesimal angle theta is (expression is given following Einstein notation) [Forest, 2022]:

$$R_{ij} = \delta_{ij} - \Theta \epsilon_{ijk} n_i \tag{5.13}$$

This expression is equivalent to:

$$\omega_{ij} = -\Theta \epsilon_{ijk} n_i \tag{5.14}$$

With ϵ_{ijk} the third order permutation tensor, n_i the rotation axis and Θ its rotation angle in radians. The angle Θ is defined as:

$$|\Theta| = \sqrt{\omega_{12}^{e2} + \omega_{23}^{e2} + \omega_{31}^{e2}} \tag{5.15}$$

Calculation of the disorientation angle Θ is illustrated in Fig 5.4-(a) for the same slice as in Fig 5.2 and for the entire grain in Fig 5.4-(b). Given the limited level of plastic deformation reached here, the rotation of the crystalline lattice due to the presence of one dislocation pileup is not very high. The maximum disorientation angle in the grain is 0.011° while the average disorientation angle is 0.0036°.

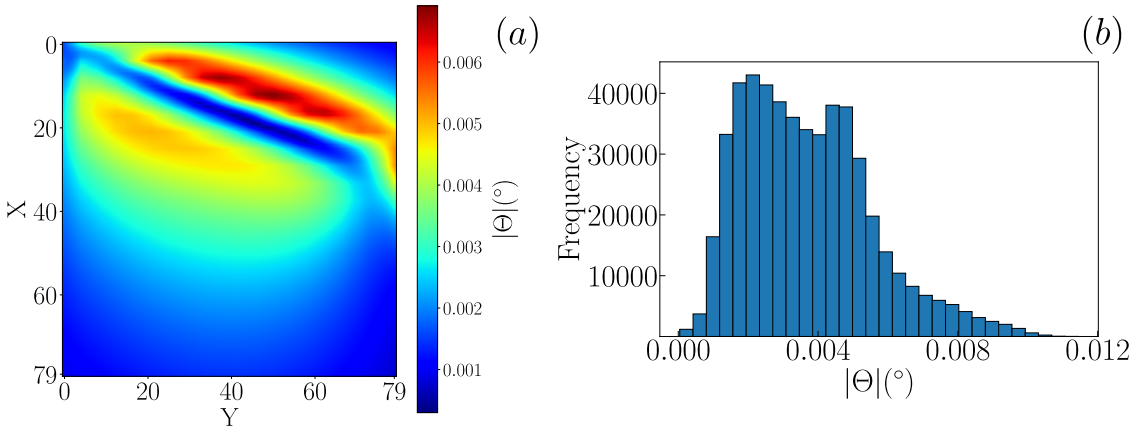

Figure 5.4: *Calculation of the disorientation angle Θ for slice $[x, y, z] = [:, :, 19/79]$ in (a) and for the entire grain in (b).*

5.2.4 Simulation of topo-tomography diffraction spots

As stated in the introduction, DCM simulations can help to provide a number of explanations for the nature of the diffraction contrasts observed in topo-tomography. The simulation we present here allows to simulate diffraction events calculated from an illuminated volume whose orientation is defined on a grid of voxels and derived from the calculation presented in § 5.2.2. The major interest here is not in directly answering the question of the nature of the contrast, but in showing that this type of simulation can be used to obtain information directly related to the dislocation microstructure. To obtain more visible trends in the simulation of the diffraction spots, the disorientation linked to the presence of the plastic deformation imposed in the DCM simulation was multiplied by a factor of ten.

In a topo-tomography experiment, the rotation axis is set parallel to the normal of a given family of (hkl) planes as illustrated in Fig 5.5, designated by the scattering vector $\underline{G}$. The whole setup is then tilted by the Bragg angle so that the Bragg condition is verified:

$$2d\sin(\theta) = n\lambda \tag{5.16}$$

With d the inter-reticular distance, θ the Bragg angle and λ the wavelength. The sample is illuminated by a monochromatic X-ray beam, the incident beam $\underline{k}_i$ and images are acquired on the detector by the intersection with the diffracted beam $\underline{k}_d$. A complete turn around the rotation axis ω (from 0° to 360°) is realised during the acquisition procedure. Through this particular setup, topo-tomography focuses on a selected grain and allows for the reconstruction of a 3D map of the defects within the grain [Ludwig et al., 2007].

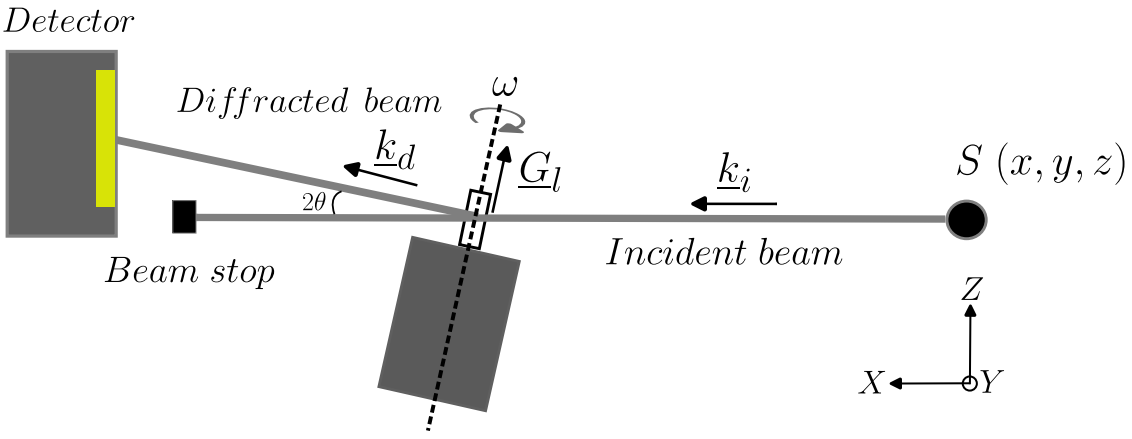

Figure 5.5: *Experimental setup for topo-tomographic experiments. The rotation axis is parallel to the scattering vector $\underline{G}_l$ in the laboratory reference frame and $S\ (x, y, z)$ the X-ray beam source.*

Knowing the incident beam vector $(\underline{k}_i)$ and the scattering vector $(\underline{G}_l)$, one can calculate the diffracted beam vector.

$$\underline{k}_d = \underline{G}_l + \underline{k}_i \tag{5.17}$$

Assuming kinematical diffraction, knowing the detector position it is possible to define the position of the diffraction event from the diffracted vector (geometrical considerations) and to simulate the diffraction spots. The results of the simulation of the diffraction spots are shown in Fig 5.6 for two different reflections, $(0\bar{2}2)$ and $(11\bar{1})$ and for different values of the rotation angle ω.

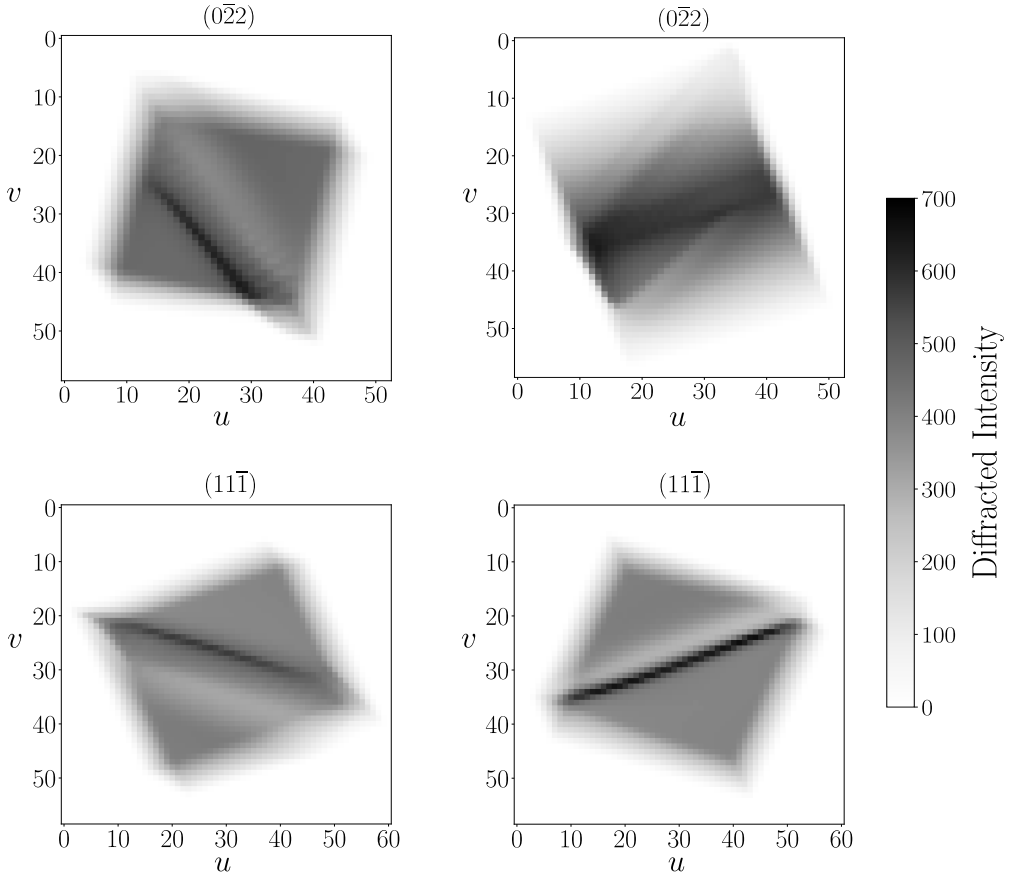

Figure 5.6: *Illustration of the simulation of diffraction spots on a detector for two different reflections* $(0\bar{2}2)$ *and* $(11\bar{1})$ *and for various values of* ω*, (uv) is the detector plane.*

In these results, the intensity of the diffraction events is given in shades of grey to distinguish between high and low intensity events. For this simulation, each voxel in the illuminated volume is considered to have a fixed and equal intensity at every point in the volume. The differences calculated in the diffracted intensity are therefore linked to a greater or lesser number of events intercepting the same pixel on the detector. In these four images, the presence of a contrast linked to the presence of a plastic deformation band is obvious. This is particularly visible in the lower right-hand figure, where the plastic deformation region is delimited by a region of low and high diffraction intensity. The appearance of this type of contrast is directly linked to local rotations of the crystalline lattice and therefore to the presence of a certain number of dislocations which are piled up here. It is worth noting that this contrast is not always visible when varying the rotation angle. Indeed rotating ω has a strong effect on the band contrast visibility in some sort of edge-on configuration when

the slip band is aligned with the diffraction vector $\underline{k}_d$.

These results are a proof of concept that these types of simulations constitute a very interesting tool for gaining a better understanding of the diffraction contrasts observed experimentally, for which an example is given in Fig 5.7. From this figure, we can see that the contrast simulated above with our model case corresponds qualitatively to the contrast observed experimentally.

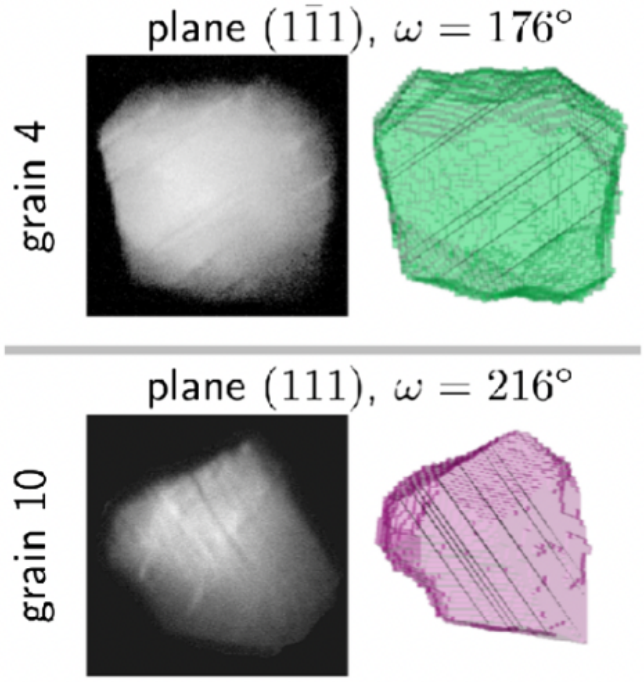

Figure 5.7: *Slip band contrast observed on TT experiment correlated to active slip systems [Proudhon et al., 2020]. Observations are made on an AlLi sample at* 0.38 % *total strain and for two grains (4 and 10) taken from the aggregate microstructure.*

Applied to more realistic configurations, by using digital twins or by defining dislocation microstructures that are more representative of reality, these simulations could provide key information, in particular through the precise and justified description of plastic deformation mechanisms via DDD. Indeed, the information that can be derived from DDD simulations is rich and gives a better understanding of the mechanisms of reactions between dislocations or arrangements during plastic deformation.

5.2.5 Comparison between CPFEM and DCM simulations

The work reported in § 1.5.4 has shown that modelling a crystallographic slip band like structure is not an easy task in the FEM framework whereas it is naturally reproduced in DDD simulations. In this section, we propose to make a comparative and purely qualitative study of the modelling of a slip band-like structure between a DCM simulation and a CPFEM

simulation. The aim is to compare the rotation and deformation fields associated with the presence of a slip band in order to determine the ability of a continuous model to describe this type of phenomenon. It is important to note that CPFEM calculations are much less costly in terms of time and computing resources than DCM calculations. The calculation performed with the DCM is the one presented in the previous sections.

For the CPFEM calculation, the slip band like structure is deliberately introduced in the grain by dividing the grain into two distinct regions, a region where plastic deformation is achievable and a region where it is not. This distinction is illustrated in Fig 5.8 for the central grain. The plastic region is defined so that it follows a slip plane of normal $(\bar{1}11)$ belonging to the A3 slip system. The simulation parameters are identical to those of the DCM simulation.

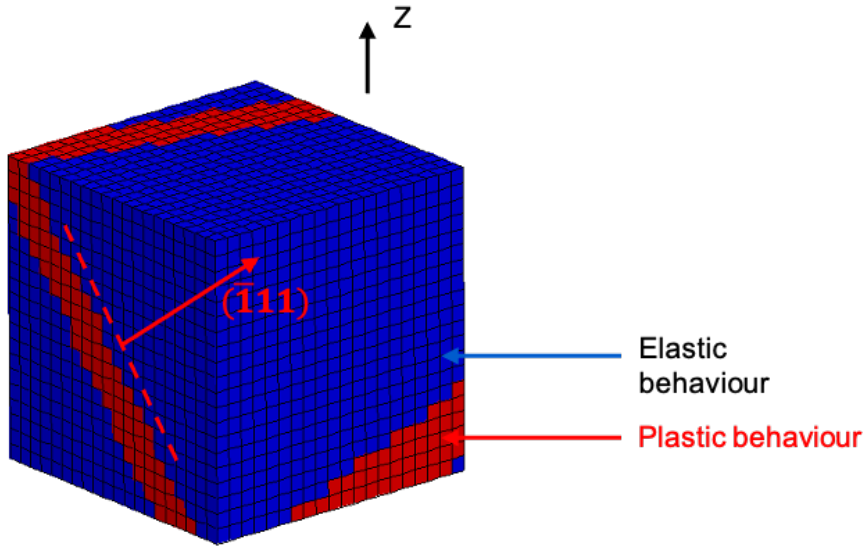

Figure 5.8: *Definition of the slip band like region imposing elastic and plastic behaviours in sub-domains of the central aggregate grain.*

The CP laws to model the plastic behaviour in the plastic region follow density-based hardening equations (Eq. 1.15 and Eq. 1.16) with a Norton plastic flow rule (power law) expressed as:

$$\dot{\gamma}^s = \dot{\gamma}_{ref} \left\langle \frac{|\tau^s| - \tau_c^s}{\tau_{ref}} \right\rangle^n = \left\langle \frac{|\tau^s| - \tau_c^s}{K} \right\rangle^n \tag{5.18}$$

With,

$$K = \tau_{ref} \times \dot{\gamma}_{ref}^{\frac{-1}{n}} \tag{5.19}$$

Such CP laws have already been used and introduced in *'Zset'* by [Han, 2012; Ling et al., 2017]. The CP laws parameters list is given in Tab. 5.2, values are directly taken or slightly modified from [Fivel et al., 1998; Dumoulin, 2001; Devincre et al., 2008]:

At equivalent plastic deformation level ($\varepsilon^p = 0.02$ %), the results of the calculation of

n	K	μ (GPa)	g_c	κ	b_D (Å)
50	10	76.336	$10b$	50	2.489
a_1	a_2	a_3	a_4	a_5	a_6
0.124	0.124	0.07	0.625	0.137	0.122
b_1	b_2	b_3	b_4	b_5	b_6
0	1	1	1	1	1

Table 5.2: *The CP laws parameters for the model CPFEM simulation.*

the extra-diagonal components of the elastic rotation field are illustrated in Fig 5.9 from the DCM and CPFEM simulations. A rapid comparison of these two types of results reveals a number of differences. In the CPFEM simulation, the computed rotation field appears more discontinuous as it is well illustrated for the component 13. These discontinuities are monitored at the boundary between the plastic and the elastic domains. Indeed, the staircase formed by the definition of the plastic domain and the mesh definition lead to strong incompatibility constraints between the two regions. Getting rid of these regions, the fields appear to be more comparable and underline the ability of a CPFEM simulation to well reproduce the elastic fields associated with a dislocation slip band like structure. The shape of the fields between the two simulations is consistent and the values obtained are of the same order of magnitude.

The issues encountered in the CPFEM simulation are mainly caused by the slip band definition and the domain distribution inside the grain. One way to solve this issue in the case of one slip band deformation could be to rotate the mesh to the direction of the slip plane normal in order to reduce the incompatibilities due to the plastic domain shearing. We could also think of using other mesh elements like tetrahedrons to soften the boundary between both deformation domains. Finally, other possibilities are to use smoothing functions at the boundary or to be able to define deformation domain at the level of the Gauss points.

However, it is important to bear in mind that this type of comparison is carried out on a particular configuration for which we define a single plastic deformation region. This shows how, with a few modifications, we could achieve convergence of the results between DCM and CPFEM. Nevertheless, these solutions for performing CPFEM calculations are obviously not feasible for describing these same phenomena but for more realistic configurations. DCM therefore remains the most justified solution in comparison with classical CPFEM modelling.

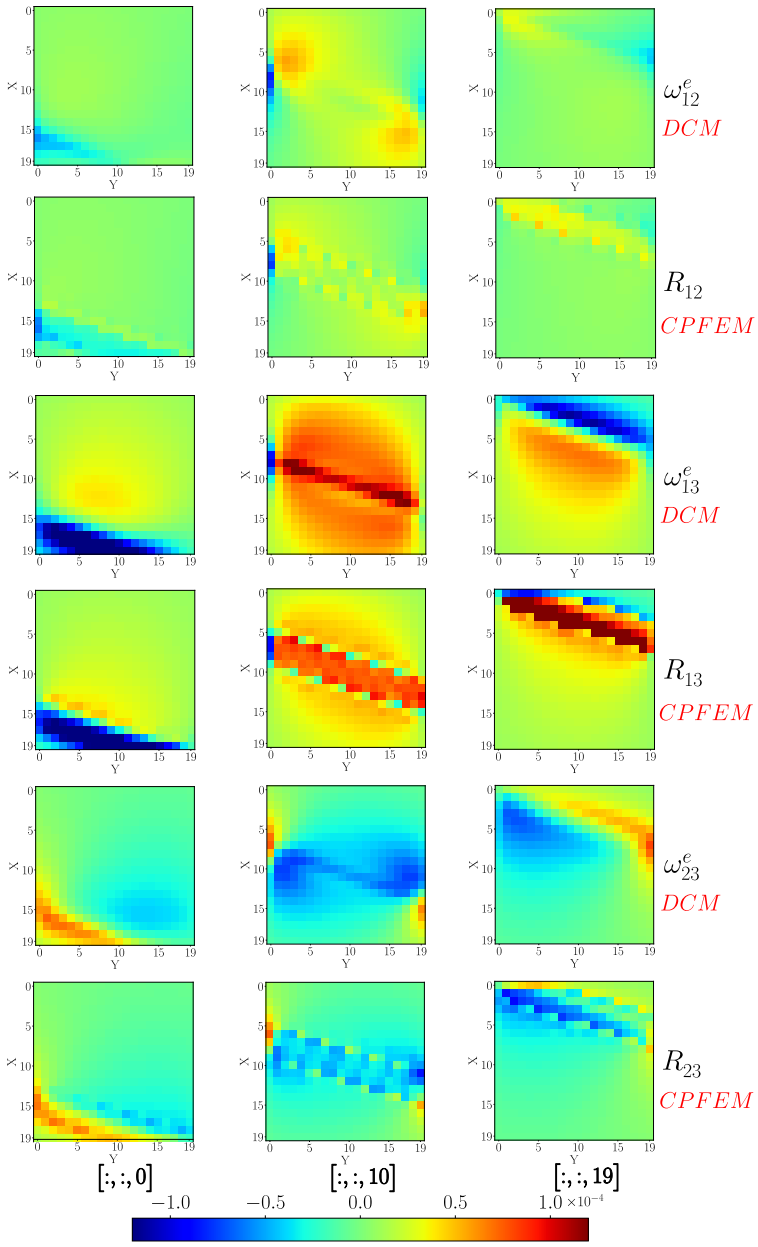

Figure 5.9: *Elastic rotation field computed with the DCM simulation and the CPFEM simulation for the three independent components and for three slices made in the volume in the Z direction. Comparison is made at equivalent plastic deformation* $\varepsilon^p = 0.02$ %.

5.3 Neighbouring grains effect on the intragranular plastic behaviour

The results presented in the previous chapters were carried out by considering only the elastic interactions between the grain simulated in DDD and the other grains in the aggregate. This first assumption allowed us to systematically study the role of the loading on the occurrence of intense and localized plastic slip and according to the hypothesis that slip bands appear in the first grain showing plastic activity. For these simulations, a pre-

factor was applied to the initial stress field, obtained from FEM elastic simulations (see § 2.2.2). In § 5.3.1, we compare this simulation hypothesis with a DCM simulation carried out under the same loading conditions and for the same initial dislocation microstructure. It is important to note that with the DCM, the elastic loading is re-calculated at every time step, considering strain incompatibility effects.

Using DCM, it is possible to study the role of interactions with the other grains in the aggregate that have reached their yield stress. During plastic deformation, the stiffness of the domain changes and decreases considerably. The material deforms more easily than before and at lower stress rates than in the elastic domain. As a result, the interactions between two initially plastic-elastic grains are necessarily modified by considering plastic-plastic interactions. Using DCM, we will demonstrate the role that these interactions can play and the importance that this can have on intragranular plastic strain localization in § 5.3.2.

5.3.1 Embedded grain in an elastic matrix

As stated in the introduction, we will here compare the results of two simulations, one assuming dislocation dynamics solved by a simple DDD scheme and the other by DCM. In order to carry out this comparison, we use the same loading conditions and an identical initial dislocation microstructure for both types of simulation. The simulation parameters are slightly modified compared with those in § 5.2.1. Here, we consider an active cross-slip and an initial dislocation density equal to $\rho^s_{ini} = 1 \times 10^{11}\ m^{-2}$. In addition, the crystalline orientations of the grains adjacent to the reference grain (central grain) are modified so as to allow the appearance of elastic strain incompatibilities and other effects that we will discuss in § 5.3.2.

A comparison of the obtained results is given in Fig 5.10 for the two resolution methods. Fig 5.10-(a) shows the evolution of the density on the primary slip system (A3) as a function of the plastic slip on the same system. This graph shows that the two curves are perfectly superimposed. Thus, in terms of average grain behaviour, the DDD and DCM resolution give the same results. Another comparison is illustrated in Fig 5.10-(b), this time on a more local scale. In this figure, the internal resolved shear stresses on slip system A3 are calculated on a grid of voxels discretising the central grain. This comparison reveals a number of differences, in particular a slight leftward shift in the histogram of stress values calculated for the DCM resolution compared with the DDD resolution. Obtaining such a difference at this scale is not surprising. During plastic deformation, cross-slip events or the formation of junctions can take place at different locations within the grain, resulting in slight differences in the distribution and intensity of internal stress values. Moreover, this slight discrepancy can also arise from the explicit treatment of strain incompatibilities in the DCM (typically the

elastic interaction between dislocations and grain boundaries), which can affect the applied stress and backstress distribution in the studied grain.

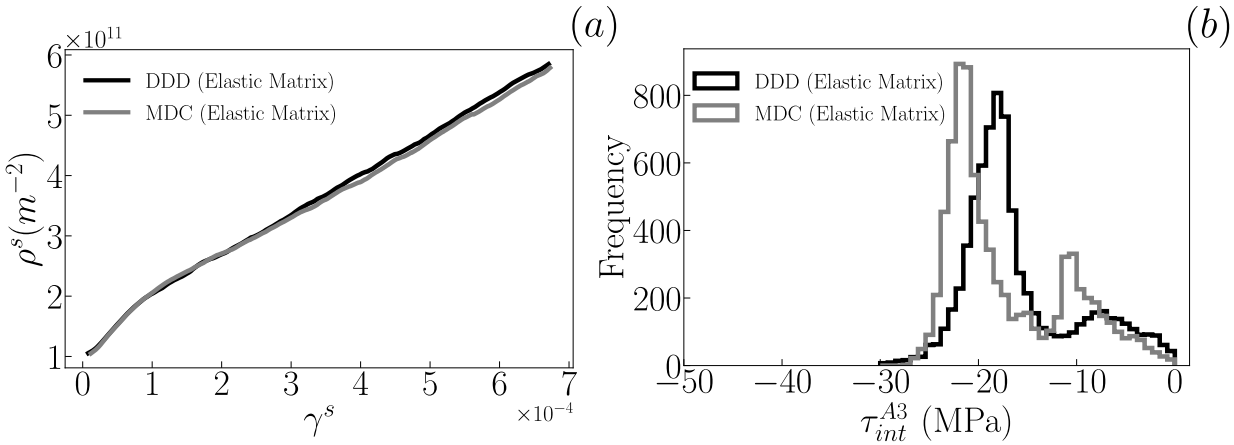

Figure 5.10: *Comparison of the results from DDD and DCM simulations with identical simulation conditions. Evolution of the dislocation density as a function of plastic slip (a) and histograms of the internal resolved shear stresses on the A3 slip system inside the grain (b), values are computed on a* $20 \times 20 \times 20$ *voxel grid.*

These results nevertheless demonstrate a very good consistency between the two methods of resolution, particularly in terms of the mean behaviour of the grain. In order to describe as precisely as possible the mechanisms associated with plastic deformation and the evolution of dislocation microstructures, it is clear that DCM is better suited. In particular, the expression of the long-range internal stresses generated by the dislocations is more justified in this case, as it takes into account the anisotropy of the material. However, as these results show, the resolution with the DDD scheme provides a very good approximation of DCM simulations for the simulation performed in the present study. This comparison between the two simulation methods validates the initial strategy adopted in this thesis as well as the results obtained in the previous chapters.

5.3.2 Embedded grain in a perfect plastic matrix

A proof of concept of what we asserted at the beginning of the section can be given by comparing the evolution of the intragranular plastic behaviour for the same grain whose neighbourhood is different. By considering the same simulation parameters as in section § 5.3.1 it is possible to compare the intragranular plastic behaviour between a grain embedded in an elastic matrix and a grain embedded in a plastic matrix. In the plastic matrix, each of the grains of the aggregate (apart from the central grain) has perfect plastic behaviour solved by CPFEM. Thus, once the yield stress is exceeded, the grains deform plastically without strain-hardening, which corresponds to the most extreme case in terms of change in material rigidity. For the simulation presented here, the critical resolved shear stress is set

to $\tau_c^s = 20$ MPa.

The results of these two simulations are illustrated in Fig 5.11. The description of the mechanical behaviour of the central grain for the two matrix configurations is illustrated in Fig 5.11-(a) via the stress-plastic strain curves. This figure illustrates the fact that the plastic behaviour of the grain is strongly modified according to the type of matrix and therefore the type of interactions between grains in the aggregate. When the matrix is plastic, the strain hardening rate is lower than when the matrix is elastic. For the same level of stress ($\sigma_{33} = 52$ MPa), the plastic deformation achieved by the central grain in the case where the matrix is plastic is much larger (almost twice as much). The mapping of plastic strain values at Gauss points is illustrated in Fig 5.11-(b) and (c) for both simulation conditions. Fig 5.11-(b) illustrates the state of plastic deformation at the surface of the central grain. The calculated values at the surface are very low, which can be explained by the fact that the dislocations pile up at the grain boundaries. By making a series of thin cuts along the $\underline{X}$, $\underline{Y}$ and $\underline{Z}$ normal faces, it is possible to show larger plastic deformation values, as illustrated in Fig 5.11-(c). At first sight, the plastic deformation appears much less intense in the case where the matrix is elastic, which was demonstrated by the stress-plastic deformation curves. In the case where the matrix is plastic, the plastic deformation is in fact larger and we can notice the appearance of a region of more intense plastic deformation located on the face of normal $\underline{Y}$. In this region, plastic deformation seems to be favoured.

These results show that plastic-plastic interactions between grains have a significant effect on the plastic behaviour of the central grain. The difference in the strain hardening rates is significant, as shown by the following values:

- $\dfrac{\Delta\sigma_{33}}{\Delta\varepsilon_{33}^p} = 141$ GPa (Elastic matrix);
- $\dfrac{\Delta\sigma_{33}}{\Delta\varepsilon_{33}^p} = 43.7$ GPa (Plastic matrix).

However, the role of these interactions on the localization of plastic deformation is difficult to study at present. To carry out such a study, the difference in plastic strain between the two simulations for each of the Gauss points is calculated at the same plastic strain level ($\varepsilon_{33}^p = 0.043$ %):

$$\Delta\varepsilon_{33}^p = (\varepsilon_{33}^p)_{PLASTIC} - (\varepsilon_{33}^p)_{ELASTIC} \tag{5.20}$$

The results of this type of calculation are shown in Fig 5.12. Fig 5.12-(a) shows the calculation of the difference in plastic strain between the two simulations and for two different visualisations. It is easy to see the appearance of a red zone on the $\underline{Y}$ normal face in the first view, where intense plastic deformation was calculated in the previous figure. The appearance of a red zone therefore means that at the same plastic deformation level of the grain, the grain embedded in a plastic matrix experiences larger local plastic deformation. In the

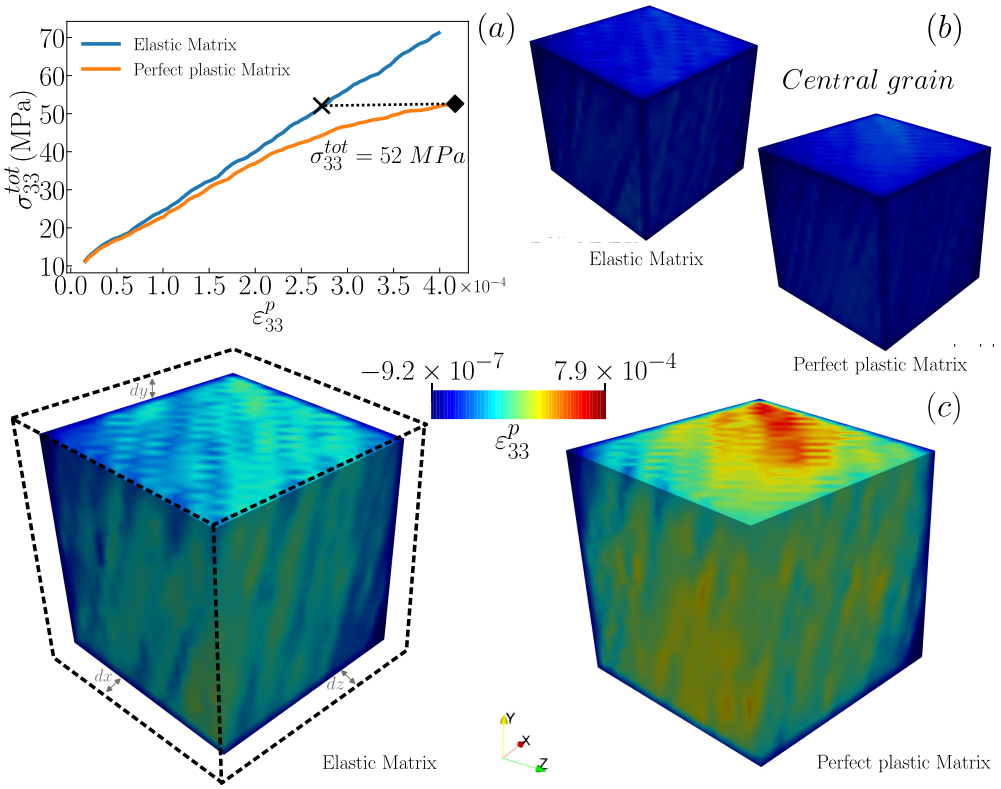

Figure 5.11: *Illustration of the central grain behaviour in both elastic and plastic matrix configuration. Stress-plastic strain curves are illustrated in (a) and the mapping of the plastic strain values at Gauss points is depicted in (b) and (c).*

second view, the presence of the same red zone can also be seen on the other two faces of normal $\underline{X}$ and $\underline{Z}$.

The fact that these zones appear on the surface of the central grain suggests that interactions between grains at these faces play a predominant role. This idea is confirmed by the stress-plastic slip curves shown in Fig 5.12-(b). This figure shows all the stress-plastic slip curves for the grains in the plastic matrix (a total of 26 grains). It can be seen that, depending on the crystalline orientation, the grains begin to plastically deform at different stress values, which can be higher or lower. If we take a closer look at the three faces of the second visualisation showing intense plastic deformation, we can see that the three grains adjacent to the central grain (in direct contact with the faces) are among the grains that plastify first within the matrix. These are grains 5, 15 and 17, whose stress-plastic slip curves are coloured in black in Fig 5.12-(b).

These results show that a zone of intense plastic deformation appears within the framework of the simulation with the plastic matrix in direct correlation with the plastic activity of the neighbouring grains. This effect is also significant since the calculated difference values ($\Delta\varepsilon_{33}^{p}$) are of the order of:

$$\frac{\max(\Delta\varepsilon_{33}^{p})}{\max(\varepsilon_{33}^{p})} = 0.4 \tag{5.21}$$

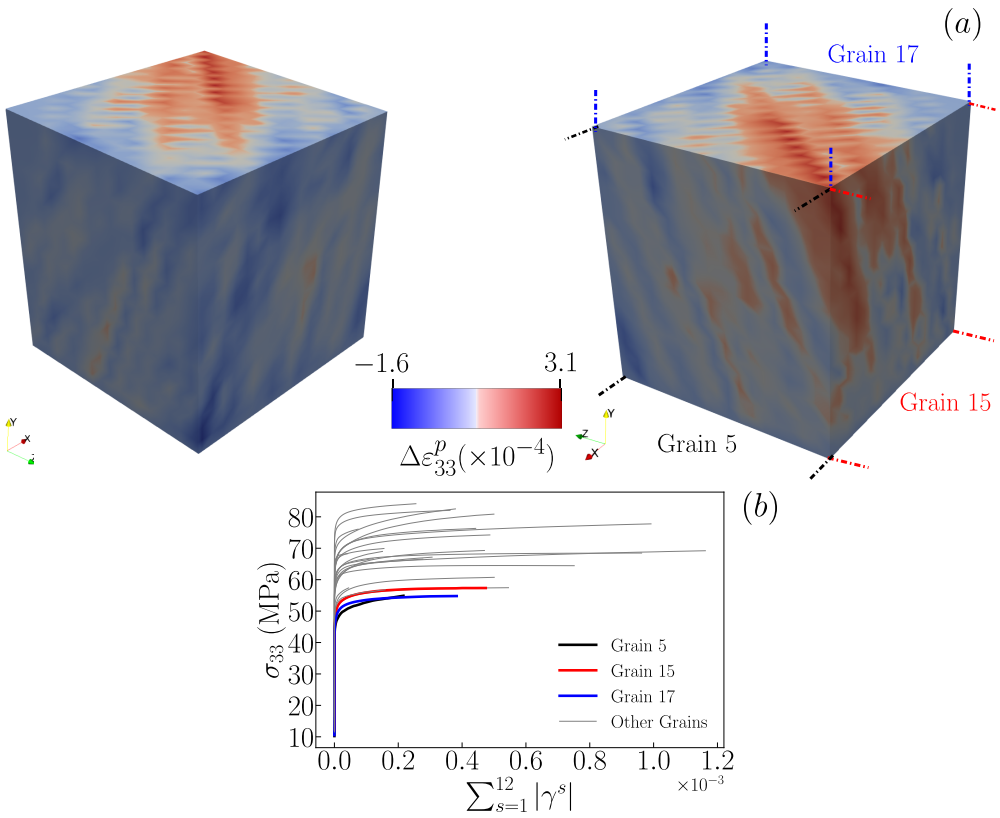

Figure 5.12: *Calculation of $\Delta\varepsilon^p_{33}$ for both elastic and plastic matrix configuration in (a) at $\varepsilon^p_{33} = 0.043$ %. Grains 5, 15 and 17 are the grains in contact with the central grain at the faces shown in the figure. In red are denoted the regions where plastic deformation is higher in the plastic matrix configuration. Stress-plastic slip curves for all the grains of the plastic matrix are illustrated in (b).*

The explanation for such a phenomenon is given by the reduction of plastic strain incompatibilities in these regions through the activation of plastic deformation in the grains neighbouring the central grain. Empirically speaking, we can say that this effect is equivalent to the transmission of plastic deformation from the central grain to neighbouring grains. The reduction in plastic deformation incompatibilities therefore leads to a local reduction in the backstress, which explains the differences in strain hardening rates between the two simulations and local plastic activity.

An illustration of the reduction in plastic strain incompatibilities in the vicinity of the central grain is given in Fig 5.13, which shows the continuity of the plastic deformation of the central grain illustrated in Fig 5.13-(a) with the total deformation (predominantly plastic) of the three neighbouring grains 5, 15 and 17 illustrated in Fig 5.13-(c). Like a mirror effect, the plastic deformation is transmitted from the central grain to neighbouring grains reducing plastic strain incompatibilities and thus leading to a reduction in work hardening linked to a reduction of the backstress in the central grain.

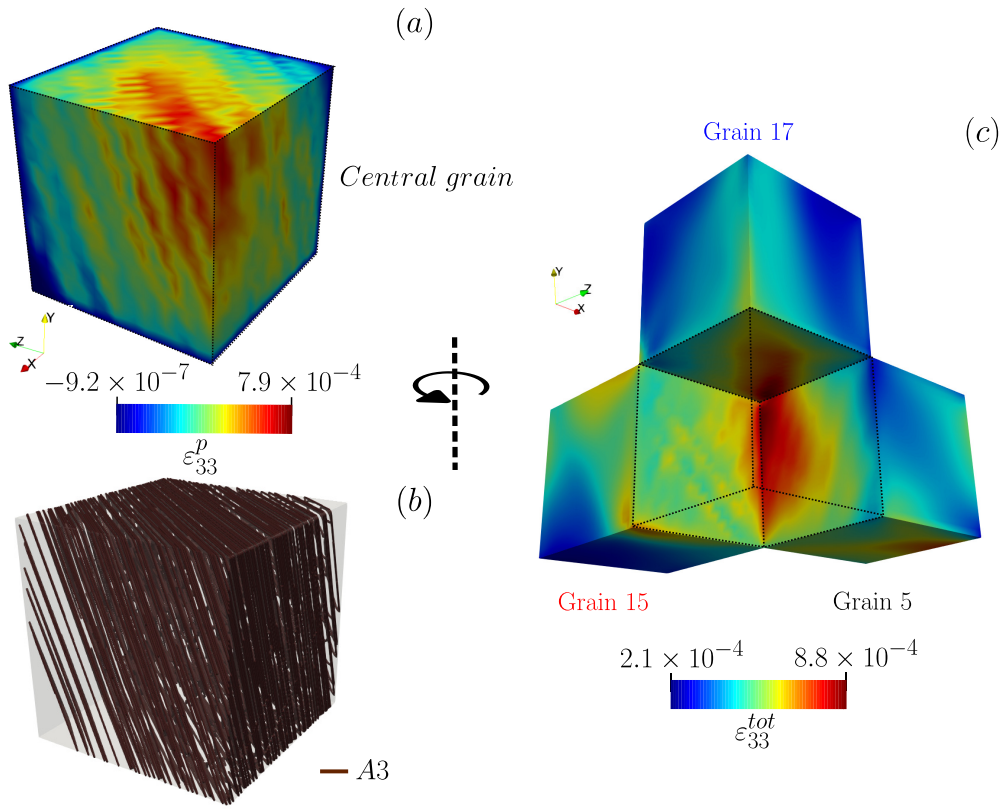

Figure 5.13: *Illustration of the reduction of plastic strain incompatibilities due to plastic activity in the vicinity of the central grain at* $\varepsilon^p_{33} = 0.043$ %. *Mapping of the plastic strain in the central grain (a), corresponding dislocation microstructure (b) and mapping of the total strain in neighbouring grains 5, 15 and 17 (c).*

A similar discussion has already been done by authors through DDD simulations such as [Quek et al., 2014] which we discussed in § 1.4. At the dislocation level, this reduction in backstress can be seen as a screening effect due to the presence of dislocations piled up on the other side of the grain boundary. In an ideal case, this would lead to the complete cancellation of the backstress as illustrated in Fig 5.14, but this is rarely observed due to the varying crystal orientations from one grain to another. Nevertheless, as discussed by [Quek et al., 2014], these screening effects remain of considerable importance and, as we can see from our results, they have a strong impact on the local plastic deformation of a grain and potentially on strain localization persistence.

The plastic activity of the neighbouring grains leading to these elastic screening effects can be the consequence of several events. As we have seen in this chapter, it can be linked directly to the plastic deformation of the neighbouring grain and to its own dislocation microstructure. However, as we stated briefly in Chapter I, the pileups created by one of the two grains (on either side of the grain boundary) can, by creating a stress concentration in the vicinity of the grain boundary, lead to the activation of dislocation sources in the other grain. Under these conditions, the effects observed would be exactly the same as those described in the previous paragraph. A schematic illustration of this process is given in

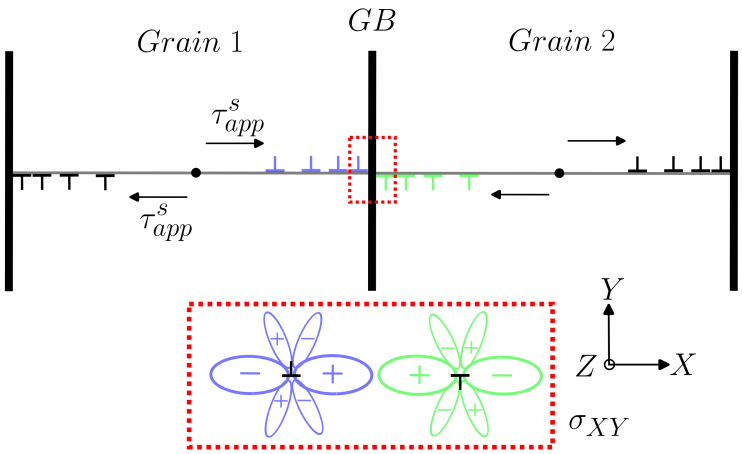

Figure 5.14: *Schematic illustration of the cancellation of the backstress due to dislocations having opposite signs piling up on both sides of the grain boundary. On the bottom of the figure are illustrated the stress lobes for the in-plane stress component σ_{XY} of edge dislocations.*

Fig 5.15. Furthermore, we showed in Chapter IV that the computed stress values at the head of the pileups are very high, eventually leading to dislocation transmission/absorption into grain boundaries. In the case of dislocation transmission, the same elastic screening effects discussed here could be observed.

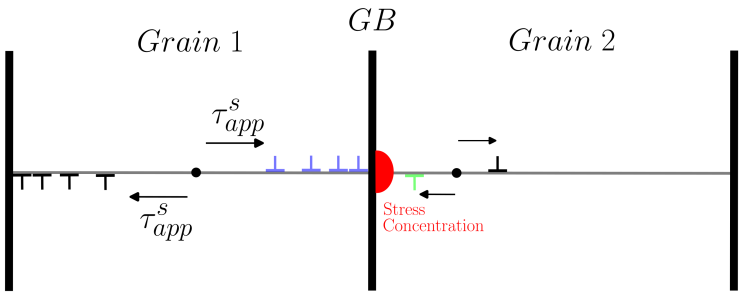

Figure 5.15: *Schematic illustration of dislocation source activation in neighbouring grain (Grain 2) due to plastic activity and dislocation pileup on the other side of the grain boundary (Grain 1). The stress concentration from the dislocation pileup in Grain 1 triggers the activation of the dislocation source in Grain 2.*

On the basis of this discussion and the results of Chapter IV, we can see that there are several mechanisms by which plastic deformation events can occur in preferential regions of the grain. This particularly depends on the grain boundaries penetrability conditions and also on the plastic activity of neighbouring grains. This once again demonstrates the importance of DCM simulations in combining these different mechanisms and obtaining a description of intragranular plastic deformation that is as close as possible to experimental

reality.

5.4 Conclusion

Through the results presented in this chapter, we have demonstrated the major interest in carrying out multi-scale simulations using DCM in order to gain a better understanding of the phenomena associated with intragranular plastic strain localization. These results are mainly proofs of concept in the sense that the simulated study cases are simplified. Nevertheless, the results obtained and the trends observed are quite significant and demonstrate the interest of simulations with a strong coupling between FEM and DDD.

In particular, we have shown in this chapter how exchanges can be made between DCM simulations and X-ray topo-tomography observations. The simulation of diffraction spots based on the results of a DCM calculation shows how it is possible to reproduce the diffraction contrast observed experimentally. These results are encouraging with regard to the objective of better understanding and explaining the existence of such contrast. To achieve this, it will obviously be necessary to make the study cases more complex by using, for example, digital twins that are as close as possible to the experimental reality.

By comparing the intragranular plastic behaviour computed by DDD and DCM in a specific case (elastic matrix aggregate), we have shown that these two resolution methods give very similar results. The use of DCM is more justified and provides a more accurate description of the plastic deformation mechanisms. However, the use of DDD resolution provides an interesting gain in resolution up to a certain number of segments [Jamond et al., 2016]. We have noticed in our simulations that as soon as a certain number of segments is reached during the simulation, the DCM will solve the dynamics more quickly than the DDD. The results obtained in this chapter validate the simulation hypothesis used for most of the simulations presented in this manuscript.

We have also shown how taking into account plastic-plastic interactions between grains can modify intragranular plastic behaviour. In the simplified case of a perfect plastic matrix solved by CPFEM, we demonstrated the presence of a reduction in strain hardening and, in particular, the backstress in the central grain. In addition, these results revealed a zone of intense plastic deformation directly linked to the plastic activity of neighbouring grains, thus illustrating the role of these interactions on intragranular plastic strain localization.

Conclusion and perspectives

Conclusion :

The aim of this thesis was to better understand the mechanism by which the intragranular localization of plastic strain generates intense slip bands that occur during the deformation of polycrystalline aggregates. Two types of modelling were used to achieve this goal. Firstly, FEM and secondly DDD simulations were performed to describe the different mechanisms involved in two different scales, the macroscopic scale (at the scale of the aggregate) and the mesoscopic scale (at the scale of the dislocation microstructure). Throughout this work, the modelling of the elastic and inelastic properties of dislocations, such as reactions between dislocations and the interactions between dislocations and grain boundaries, has served as a basis for understanding the mechanisms controlling plastic deformation.

In order to address the complex issue of the localization of slip band deformations in polycrystals, systematic studies have been carried out using mainly a "weak" coupling between two numerical models, i.e. FEM and DDD simulations (see Chapter II). In particular, we were able to describe precisely the role of the polycrystalline microstructure on the plastic behaviour of a grain and on the evolution of the dislocation microstructure. The results of FEM simulations, reproducing anisotropic elastic behaviour, were used as initial conditions for DDD simulations in order to transfer into the latter the multi-axial behaviours associated with elastic deformation of a polycrystal. To this end, several series of FEM simulations were carried out to gain a better understanding of the role of elastic strain incompatibility on intragranular elastic loading. The result of these calculations is that, in some cases, elastic strain incompatibility between close grains promotes the appearance of stress concentration zones, leading to significant heterogeneity in the intragranular stress state compared with the behaviour of a single crystal. In line with experimental observations, these stress concentration zones appear favourably in regions at the intersection between several grains. These particular regions of stress concentration are varied and include the intersection between two grains leading to the presence of a grain boundary, the intersection between three grains and the formation of a triple junction, or the intersection between four grains and the formation of a quadruple node. Calculations carried out on numerous configurations have shown that stress concentration is most often observed in the vicinity of quadruple nodes. Based on this

result, a criterion based on the heterogeneity of the elastic loading and the level of stress intensity was proposed. This criterion is used to classify configurations (grain and crystal orientations) according to their ability to develop more localized plastic deformation due to elastic loading. On the basis of this criterion, a highly heterogeneous configuration is selected and simulated in DDD simulations. The first simulations we carried out, considering cross-slip as inactive, showed a close link between the presence of stress concentration zones and the occurrence of intense plastic slip events.

Following these first numerical investigations, a more detailed study of the mechanisms linked to the dislocation microstructure was carried out (see Chapter III). This part of the work highlighted the important role of two mechanisms, cross-slip and collinear annihilation, in initiating localized plastic deformation. It is shown that the cross-slip allows the homogenization of the plastic deformation in the grain in a transitory way by introducing a considerable number of dislocations on new slip planes previously not occupied. By focusing on particular regions of the grain such as in the proximity of the stress concentration zone, it was demonstrated that this mechanism could allow the plastic deformation to thicken, from a slip trace-like structure to a slip band-like structure. Combined with this, it has been proven that collinear annihilation enables significant microstructural reorganization at the scale of the slip plane. By creating pinning points, they enable existing dislocation sources to be relocated or new dislocation sources to form in regions that are more favourable to plastic slip. In addition, due to the existence of numerous collinear annihilations, plastic slip in each slip plane can become heterogeneous. In such cases, we observe a larger number of dislocations piled up at grain boundaries in the stress concentration zones. Hence, the back stress in the glide plane can be very heterogeneous. However, these two mechanisms, cross-slip and collinear annihilation, do not allow kinematic and isotropic strain-hardening to be reduced in the slip plane of the most active dislocation sources and therefore do not allow sustainable deformation localization.

The number of dislocations piled up at grain boundaries and in particular near the stress concentration zone led us to reconsider the simple initial assumption to consider grain boundaries impenetrable to dislocations for the low strain levels simulated with DDD (see Chapter IV). Indeed, by applying theoretical pileup models, we are able to show that the stress at the head of the pileup is of the order of about 1 GPa. For such values, and based on the results of the literature, a certain number of inelastic reactions are expected and observed between the dislocation at the head of pileups and the grain boundaries. For this reason, a new local rule was integrated into the DDD code microMegas. This constitutive rule allows modelling contact reaction between dislocations and grain boundaries on a mesoscopic scale and is based on the definition of a grain boundary penetrability stress. By considering this stress to be fixed during plastic deformation and not dependent on the orientation of the crystal and the grain boundary, it was emphasized that grain boundary

penetrability could play a dominant role in the appearance of intense and highly localized plastic slip, even at low strain. Comparisons made between two grain boundary configurations, one considering the grain boundaries to be impenetrable and the other not, show a completely different spatial distribution of plastic slip. Indeed, when considering grain boundary penetrability, plastic slip appears to be highly heterogeneous and localized in particular regions of the grain. The results of this chapter on the grain boundaries penetrability may also lead us to discuss the effects of crystallographic texture that can be found in certain polycrystalline materials. Crystallographic texture represents the non-random distribution of crystallographic orientations within an aggregate, a good representation of which is given by the macro-zones that are well observed in titanium-based alloys, for example. Within these zones, the crystallographic orientation of the grains is constant and, as a result, the grain boundaries are assumed to be more easily penetrable, enabling plastic deformation to be strongly localized in cases where the crystallographic orientation is favourable to slip. These aspects are discussed in particular in [Xu et al., 2020].

In addition, a more detailed cross-slip sensitivity study was carried out in simulations allowing grain boundary penetrability. In agreement with certain experimental observations, we have observed in this investigation that cross-slip leads to strong homogenization of plastic slip across the grain, for the levels of plastic deformation reached in our simulations. With high cross-slip activity, the number of slip traces observed in our simulations is large and each of these traces has a relatively equivalent intensity, which is not the case when the cross-slip is less active. As we have discussed in this chapter, cross-slip activity depends on certain material parameters such as the stacking fault energy. Let's take the case of two FCC materials with very different stacking fault energies, copper and aluminium. Copper has a much lower stacking fault energy than aluminium. Thus, the cross-slip activity in the case of copper will be expected to be lower and so plastic deformation should appear more heterogeneously in the form of intense slip bands whereas in the case of aluminium, plastic deformation will be expected to be more homogeneous without a strong gradient of plastic slip. Similarly, temperature should play a major role in plastic deformation structures, as it is one of the parameters controlling cross-slip activity. The higher the temperature, the more active the cross-slip. In the same set of computations, several simulations carried out with different elastic loadings demonstrate the role of stress concentration on the appearance of intense plastic slip. However, for the levels of plastic deformation reached, only one configuration out of the three simulated gives rise to intense, persistent and localized plastic slip in a band. We conclude that it is possible for a plastic deformation localization to initiate preferentially near a region of stress concentration (these regions are favourable anyway), but that the existence of a persistent localization in a band depends mainly on the material's ability to organize a large number of dislocation sources and on the penetrability properties (i.e direct or indirect transmission of plastic deformation) of the grain boundaries in this

zone.

In the last part of this work (see Chapter V), we present some simulations we made at the end of the third year. Such additional simulations are based on a strong coupling between the DDD and the FEM thanks to the Discrete Continuous Model (DCM). The obtained results demonstrate the key role that these simulations can play in providing a better understanding of the mechanisms of intragranular plastic deformation. Using DCM simulations, we were able to simulate the impact of a plastic deformation band on the appearance of a diffraction contrast during the acquisition of topo-tomography images. Since the precise origins of this experimentally observed contrast are not yet known, this illustrates the extent to which these simulations can serve as sources of information and explanations, particularly with regard to the arrangement of dislocations near the grain boundaries that lead to a strong rotation of the crystal lattice.

By means of simulations carried out under the same loading and microstructure conditions and in the context of a matrix assumed to be elastic, we have shown that there is a very good correspondence between the DDD simulations that we carried out in the course of our work, assuming weak coupling, and the DCM simulations. In particular, at the macroscopic scale (in this case at the grain scale), the results obtained show a perfect suppression of the curves showing the evolution of the dislocation density as a function of the plastic slip. However, a comparison at a more local scale reveals some slight differences, particularly in the distribution of internal stresses within the grain. These results are not surprising, as plastic deformation is a highly non-linear mechanism and it is normal to obtain this type of result. In the two simulations, junctions or cross-slip events may appear in different places, leading to slightly different local results, but without modifying the average behaviour of the grain on a macroscopic scale. In addition, DCM simulations are more realistic, particularly with regard to the expression of the long-range internal stress gnerated by dislocations. It is therefore preferable to use DCM in order to determine precisely where a plastic deformation localization appears. Nevertheless, DDD simulations provide a very close description of this physics and have been a preferred option in our work, notably for numerical cost reasons.

DCM simulations allowed also us to describe the role of interactions between plastically deformed grains. With the help of crystal plasticity, simulations considering a constitutive plastic law in all the grains of a periodic aggregate, except one central grain simulated with a DDD simulation code have been performed. These simulations highlight that plastic strain compatibility can considerably modify the strain-hardening rate of the reference DDD grain and, moreover, lead to the appearance of intense plastic deformation in predefined regions. To the best of our knowledge, these simulations are the first of their kind, using such precision, and they are made possible by the DCM. These simulations serve as a proof of concept, providing a significant opportunity to better understand how plastic deformation occurs at the dislocation scale.

Perspectives :

A number of short and long-term perspectives can be identified following this work. Firstly, in the context of DDD simulations, it would be very interesting to increase the complexity of the local rule introduced into the code in order to model the reactions between dislocations and grain boundaries. We can imagine adding a certain number of mechanisms such as, for example, taking into account the variability of the resistance of the grain boundaries as a function of the plastic deformation and the number of dislocations that have passed through them. Combined with this, it could be very interesting to introduce different penetrability stress values depending on the type of grain boundary. For this, we can, for example, refer to the different geometric transmission criteria discussed in § 1.4. Adding this type of information to the local rule could make it possible to observe certain trends in local plastic slip and to better understand the reasons for the appearance of localized intragranular plastic deformation. Such modification could also open the door for investigations on a key polycrystalline material property, the crystallographic texture.

Secondly, there are numerous insights for multi-scale simulations using DCM. On the short term, it is important to carry out simulations as close as possible to experimental conditions by modelling Voronoi aggregates or by directly using a digital twin from a DCT geometrical reconstruction [Proudhon et al., 2018]. A presentation of the initial tests carried out on a real microstructure, which we are attempting to reproduce using Voronoi and Laguerre tessellations, is given in Appendix D. This will enable direct comparisons with the experimental X-ray topo-tomography observations, or to study more precisely the role of plastic-plastic interactions in more realistic configurations. With regard to these plastic-plastic interactions, it is also necessary to introduce more realistic crystal plasticity laws than in the calculation presented in this manuscript, where we assumed for reasons of simplicity and efficiency, perfect plastic behaviour.

At this stage, the local rule we developed in the microMegas DDD code for modelling reactions between grain boundaries and dislocations is not formulated for immediate use in the DCM simulations. In the classical DDD code, long-range stresses are suppressed simply by setting the field calculated from the analytical formulations to zero. In the DCM scheme, the long-range stresses are calculated using eigenstrains and it is therefore not possible to remove this contribution as simply as in the DDD code. One of the technical prospects of the work presented in this manuscript therefore lies in the search for a method allowing the suppression of long-distance contributions due to the transmission/absorption of a dislocation in a grain boundary.

Thanks to the work done during my thesis, many important investigations could be carried out quickly without additional technical development in the DCM simulations. For example, it would be interesting to study the influence of the plastic deformation of grains

neighbouring the reference DDD grain on the latter's intragranular stress distribution. In addition, simulations can be performed to reveal how the elastic screening effects discussed in this chapter affect the stress at the head of dislocation pileups and, as a consequence, the penetrability of the grain boundaries. All these questions can be studied within a reasonable timeframe and will allow the results presented in this manuscript to be extended.

Conclusion en français :

Le but de ce travail de thèse était de mieux comprendre le mécanisme par lequel la localisation intragranulaire de la déformation plastique génère des bandes de glissement intenses qui se produisent lors de la déformation d'agrégats polycristallins. Deux types de modélisation ont été utilisés pour atteindre cet objectif. D'une part, des simulations FEM et d'autre part des simulations DDD ont été réalisées pour décrire les différents mécanismes impliqués à deux échelles différentes, l'échelle macroscopique (à l'échelle de l'agrégat) et l'échelle mésoscopique (à l'échelle de la microstructure des dislocations). Tout au long de ce travail, la modélisation des propriétés élastiques et inélastiques des dislocations, telles que les réactions entre les dislocations et les interactions entre les dislocations et les joints de grains, a servi de base à la compréhension des mécanismes contrôlant la déformation plastique.

Afin d'aborder la question complexe de la localisation de la déformation en bandes de glissement dans les polycristaux, des études systématiques ont été menées en utilisant principalement un couplage "faible" entre deux modèles numériques, soit des simulations FEM et DDD (voir Chapitre II). En particulier, nous avons pu décrire précisément le rôle de la microstructure polycristalline sur le comportement plastique d'un grain et sur l'évolution de la microstructure des dislocations. Les résultats des simulations FEM, reproduisant un comportement élastique anisotrope, ont été utilisés comme conditions initiales pour les simulations DDD afin de transférer dans ces dernières les comportements multi-axiaux associés à la déformation élastique d'un polycristal. À cette fin, plusieurs séries de simulations FEM ont été réalisées pour mieux comprendre le rôle de l'incompatibilité des déformations élastiques sur le chargement élastique intragranulaire. Le résultat de ces calculs est que, dans certains cas, l'incompatibilité de déformation élastique entre grains proches favorise l'apparition de zones de concentration de contraintes, conduisant à une hétérogénéité significative de l'état de contrainte intragranulaire par rapport au comportement d'un monocristal. Conformément aux observations expérimentales, ces zones de concentration de contraintes apparaissent favorablement dans les régions situées à l'intersection de plusieurs grains. Ces régions particulières de concentration de contraintes sont variées et comprennent l'intersection entre deux grains conduisant à la présence d'un joint de grain, l'intersection entre trois grains et la formation d'une jonction triple, ou l'intersection entre quatre grains et la formation d'un nœud quadruple. Les calculs effectués sur de nombreuses configurations ont montré que la concentration de contraintes est le plus souvent observée à proximité des nœuds quadruples.

Sur la base de ce résultat, un critère basé sur l'hétérogénéité du chargement élastique et le niveau d'intensité des contraintes a été proposé. Ce critère permet de classer les configurations (orientations des grains et des cristaux) en fonction de leur capacité à développer une déformation plastique plus localisée sous l'effet du chargement élastique. Sur la base de ce critère, une configuration fortement hétérogène est sélectionnée et simulée par le biais de simulations DDD. Les premières simulations que nous avons réalisées, en considérant le cross-slip comme inactif, ont montré un lien étroit entre la présence de zones de concentration de contraintes et l'apparition d'événements de glissement plastique intense.

Suite à ces premières investigations numériques, une étude plus détaillée des mécanismes liés à la microstructure des dislocations a été réalisée (voir Chapitre III). Cette partie du travail a mis en évidence le rôle important de deux mécanismes, le cross-slip et l'annihilation colinéaire, dans l'initiation de la déformation plastique localisée. Il est montré que le cross-slip permet d'homogénéiser la déformation plastique dans le grain de manière transitoire en introduisant un nombre considérable de dislocations sur de nouveaux plans de glissement qui n'étaient pas occupés auparavant. En se concentrant sur des régions particulières du grain, par exemple à proximité de la zone de concentration des contraintes, il a été démontré que ce mécanisme pouvait permettre à la déformation plastique de s'épaissir, en passant d'une structure de type trace de glissement à une structure de type bande de glissement. En outre, il a été prouvé que l'annihilation colinéaire permet une réorganisation significative de la microstructure à l'échelle du plan de glissement. En créant des points d'ancrage, ils permettent de déplacer les sources de dislocations existantes ou d'en former de nouvelles dans des régions plus favorables au glissement plastique. De plus, en raison de l'existence de nombreuses annihilations colinéaires, le glissement plastique dans chaque plan de glissement peut devenir hétérogène. Dans ce cas, on observe un plus grand nombre de dislocations empilées aux joints de grains dans les zones de concentration de contraintes. Ainsi, le backstress dans le plan de glissement peut être très hétérogène. Cependant, ces deux mécanismes, le cross-slip et l'annihilation colinéaire, ne permettent pas de réduire l'écrouissage cinématique et isotrope dans le plan de glissement des sources de dislocations les plus actives et ne permettent donc pas une localisation durable de la déformation plastique.

Le nombre de dislocations empilées aux joints de grains et en particulier près de la zone de concentration des contraintes nous a amenés à reconsidérer l'hypothèse initiale de considérer les joints de grains comme impénétrables aux dislocations pour les faibles niveaux de déformation simulés avec DDD (voir Chapitre IV). En effet, en appliquant des modèles théoriques d'empilement des dislocations, nous sommes en mesure de montrer que la contrainte à la tête de l'empilement est de l'ordre d'environ 1 GPa. Pour de telles valeurs, et sur base des résultats de la littérature, un certain nombre de réactions inélastiques sont attendues et observées entre les dislocations en tête d'empilement et les joints de grains. Pour cette raison, une nouvelle règle locale a été intégrée dans le code DDD microMegas.

Cette règle locale permet de modéliser la réaction de contact entre les dislocations et les joints de grains à une échelle mésoscopique et est basée sur la définition d'une contrainte de pénétrabilité des joints de grains. En considérant que cette contrainte est fixe pendant la déformation plastique et ne dépend pas de l'orientation du cristal et du joint de grain, il a été souligné que la pénétrabilité du joint de grain pouvait jouer un rôle dominant dans l'apparition d'un glissement plastique intense et très localisé, même à faible déformation. Les comparaisons effectuées entre deux configurations de joints de grains, l'une considérant que les joints de grains sont impénétrables et l'autre non, montrent une distribution spatiale du glissement plastique complètement différente. En effet, lorsque l'on considère la pénétrabilité des joints de grains, le glissement plastique semble être très hétérogène et localisé dans des régions particulières du grain. Les résultats de ce chapitre sur la pénétrabilité des joints de grains peuvent également nous amener à discuter des effets de texture cristallographique que l'on peut trouver dans certains matériaux polycristallins. La texture cristallographique représente la distribution non aléatoire des orientations cristallographiques au sein d'un agrégat, dont une bonne représentation est donnée par les macro-zones bien observées dans les alliages à base de titane, par exemple. Dans ces zones, l'orientation cristallographique des grains est constante et, par conséquent, les joints de grains sont supposés être plus facilement pénétrables, ce qui permet de localiser fortement la déformation plastique dans les cas où l'orientation cristallographique est favorable au glissement. Ces aspects sont examinés en particulier dans [Xu et al., 2020].

En outre, une étude plus détaillée de la sensibilité au cross-slip a été réalisée dans des simulations permettant la pénétrabilité des joints de grains. En accord avec certaines observations expérimentales, nous avons observé dans cette étude que le cross-slip conduit à une forte homogénéisation du glissement plastique à travers le grain, pour les niveaux de déformation plastique atteints dans nos simulations. Avec une forte activité du cross-slip, le nombre de traces de glissement observées dans nos simulations est important et chacune de ces traces a une intensité relativement équivalente, ce qui n'est pas le cas lorsque le cross-slip est moins actif. Comme nous l'avons discuté dans ce chapitre, l'activité du cross-slip dépend de certains paramètres du matériau tels que l'énergie de faute d'empilement. Prenons le cas de deux matériaux FCC ayant des énergies de faute d'empilement très différentes, le cuivre et l'aluminium. Le cuivre a une énergie de faute d'empilement beaucoup plus faible que l'aluminium. Par conséquent, l'activité du cross-slip dans le cas du cuivre devrait être plus faible et la déformation plastique devrait apparaître de manière plus hétérogène sous la forme de bandes de glissement intenses, alors que dans le cas de l'aluminium, la déformation plastique devrait être plus homogène sans un fort gradient de glissement plastique. De même, la température devrait jouer un rôle majeur dans les structures de déformation plastique, car c'est l'un des paramètres qui contrôlent l'activité du cross-slip. Plus la température est élevée, plus le cross-slip est actif. Dans la même série de calculs, plusieurs simulations

effectuées avec différents chargements élastiques démontrent le rôle de la concentration de contraintes sur l'apparition d'un glissement plastique intense. Cependant, pour les niveaux de déformation plastique atteints, seule une configuration sur les trois simulées donne lieu à un glissement plastique intense, persistant et localisé dans une bande. Nous concluons qu'il est possible qu'une localisation de la déformation plastique s'initie préférentiellement près d'une région de concentration de contraintes (ces régions sont de toute façon favorables), mais que l'existence d'une localisation persistante dans une bande dépend principalement de la capacité du matériau à organiser un grand nombre de sources de dislocations et des propriétés de pénétrabilité (i.e. transmission directe ou indirecte de la déformation plastique) des joints de grains dans cette zone.

Dans la dernière partie de ce travail (voir Chapitre V), nous présentons quelques simulations que nous avons réalisées avec succès à la fin de la troisième année. Ces simulations supplémentaires sont basées sur un couplage fort entre le DDD et la FEM grâce au modèle discret-continu (DCM). Les résultats obtenus démontrent le rôle clé que ces simulations peuvent jouer pour une meilleure compréhension des mécanismes de déformation plastique intragranulaire. Grâce aux simulations DCM, nous avons pu simuler l'impact d'une bande de déformation plastique sur l'apparition d'un contraste de diffraction lors de l'acquisition d'images en topo-tomographie. Les origines précises de ce contraste observé expérimentalement n'étant pas encore connues, ceci illustre à quel point ces simulations peuvent servir de sources d'informations et d'explications, notamment en ce qui concerne l'arrangement des dislocations près des joints de grains qui conduisent à une forte rotation du réseau cristallin.

Au moyen de simulations effectuées dans les mêmes conditions de chargement et de microstructure et dans le contexte d'une matrice supposée élastique, nous avons montré qu'il existe une très bonne correspondance entre les simulations DDD que nous avons effectuées dans le cadre de nos travaux, en supposant un couplage faible, et les simulations DCM. En particulier, à l'échelle macroscopique (ici à l'échelle du grain), les résultats obtenus montrent une parfaite superposition des courbes montrant l'évolution de la densité de dislocations en fonction du glissement plastique. Cependant, une comparaison à une échelle plus locale révèle quelques légères différences, notamment au niveau de la distribution des contraintes internes au sein du grain. Ces résultats ne sont pas surprenants, car la déformation plastique est un mécanisme hautement non linéaire et il est normal d'obtenir ce type de résultat. Dans les deux simulations, des jonctions ou des glissements croisés peuvent apparaître à des endroits différents, conduisant à des résultats locaux légèrement différents, mais sans modifier le comportement moyen du grain à l'échelle macroscopique. En outre, les simulations DCM sont plus réalistes, notamment en ce qui concerne l'expression de la contrainte interne à longue portée émise par les dislocations. Il est donc préférable d'utiliser le DCM pour déterminer précisément où apparaît une localisation de la déformation plastique. Néanmoins, les simulations DDD fournissent une description très proche de cette physique et ont été une

option privilégiée dans notre travail, notamment pour des raisons de coût numérique.

Les simulations DCM nous ont également permis de décrire le rôle des interactions entre les grains déformés plastiquement. A l'aide de la plasticité cristalline, des simulations considérant une loi plastique constitutive dans tous les grains d'un agrégat périodique, à l'exception d'un grain central simulé avec un code de simulation DDD ont été réalisées. Ces simulations mettent en évidence que la compatibilité des déformations plastiques peut modifier considérablement le taux d'écrouissage du grain DDD de référence et, de plus, conduire à l'apparition d'une déformation plastique intense dans des régions prédéfinies. A notre connaissance, ces simulations sont les premières de ce type, avec une telle précision, et elles sont rendues possibles par le DCM. Ces simulations servent de preuve de concept, offrant une opportunité significative de mieux comprendre comment la déformation plastique se produit à l'échelle des dislocations.

Perspectives en français :

Un certain nombre de perspectives à court et à long terme peuvent être identifiées à la suite de ce travail. Tout d'abord, dans le cadre des simulations DDD, il serait très intéressant de complexifier la règle locale introduite dans le code afin de modéliser les réactions entre dislocations et joints de grains. On peut imaginer l'ajout d'un certain nombre de mécanismes comme, par exemple, la prise en compte de la variabilité de la résistance des joints de grains en fonction de la déformation plastique et du nombre de dislocations qui les ont traversés. Combiné à cela, il pourrait être très intéressant d'introduire des valeurs de contrainte de pénétrabilité différentes en fonction du type de joint de grain. Pour cela, nous pouvons, par exemple, nous référer aux différents critères de transmission géométrique discutés dans § 1.4. L'ajout de ce type d'information à la règle locale pourrait permettre d'observer certaines tendances dans le glissement plastique local et de mieux comprendre les raisons de l'apparition d'une déformation plastique intragranulaire localisée. Une telle modification pourrait également ouvrir la voie à des investigations sur une propriété clé des matériaux polycristallins, la texture cristallographique.

Deuxièmement, les simulations multi-échelles utilisant le DCM offrent de nombreuses perspectives. A court terme, il est important de réaliser des simulations au plus près des conditions expérimentales en modélisant des agrégats de Voronoï ou en utilisant directement un jumeau numérique issu d'une reconstruction géométrique DCT [Proudhon et al., 2018]. Une présentation des premiers tests effectués sur une microstructure réelle, que nous tentons de reproduire à l'aide des tessellations de Voronoï et de Laguerre, est donnée en Annexe D. Ceci permettra des comparaisons directes avec les observations expérimentales de topo-tomographie aux rayons X, ou d'étudier plus précisément le rôle des interactions plastiques-plastiques dans des configurations plus réalistes. En ce qui concerne ces interactions plastiques-plastiques, il est également nécessaire d'introduire des lois de plasticité

cristalline plus réalistes que dans le calcul présenté dans ce manuscrit, où nous avons supposé, pour des raisons de simplicité et d'efficacité, un comportement plastique parfait.

À ce stade, la règle locale que nous avons développée dans le code DDD de microMegas pour modéliser les réactions entre les joints de grains et les dislocations n'est pas formulée pour une utilisation immédiate dans les simulations DCM. Dans le code DDD classique, les contraintes à longue portée sont supprimées simplement en mettant à zéro le champ calculé à partir des formulations analytiques. Dans le schéma DCM, les contraintes à longue portée sont calculées à l'aide des contraintes propres et il n'est donc pas possible de supprimer cette contribution aussi simplement que dans le code DDD. Une des perspectives techniques du travail présenté dans ce manuscrit réside donc dans la recherche d'une méthode permettant de supprimer les contributions à longue distance dues à la transmission/absorption d'une dislocation dans un joint de grain.

Grâce au travail effectué durant ma thèse, de nombreuses investigations importantes pourront être menées rapidement sans développement technique supplémentaire dans les simulations DCM. Par exemple, il serait intéressant d'étudier l'influence de la déformation plastique des grains voisins du grain DDD de référence sur la distribution des contraintes intragranulaires de ce dernier. En outre, des simulations peuvent être effectuées pour révéler comment les effets d'écrantage élastique discutés dans ce chapitre affectent la contrainte à la tête des empilements de dislocations et, par conséquent, la pénétrabilité des joints de grains. Toutes ces questions peuvent être étudiées dans un délai raisonnable et permettront d'étendre les résultats présentés dans ce manuscrit.

Appendices

A Consideration of the exact crystallographic orientation in lattice-based DDD simulations

The DDD code used in this manuscript, *microMegas* (*"mM"*) is lattice-based code, meaning that dislocation segments rely on a homothetic lattice whose points are integers. By default, the lattice reference frame is supposed to be aligned with the sample reference frame, assuming the crystalline orientation to be $(\phi_1, \Phi, \phi_2) = (0, 0, 0)$. One solution to model the approximate crystalline orientation in "mM" is to perform homotheties of the initial simulation lattice to find the closest integers that match the exact crystalline orientation. That kind of solution is used in § 5.2.1 to model the simple glide orientation. Nevertheless, for the other DDD simulations presented in this manuscript, another solution is adopted to model the exact crystalline orientation as illustrated in Fig A.1. This solution consists of performing a rotation of the sample reference frame, i.e. the grain geometry, to get the same configuration as the one illustrated at the left of the figure. In "mM", a grain is defined as

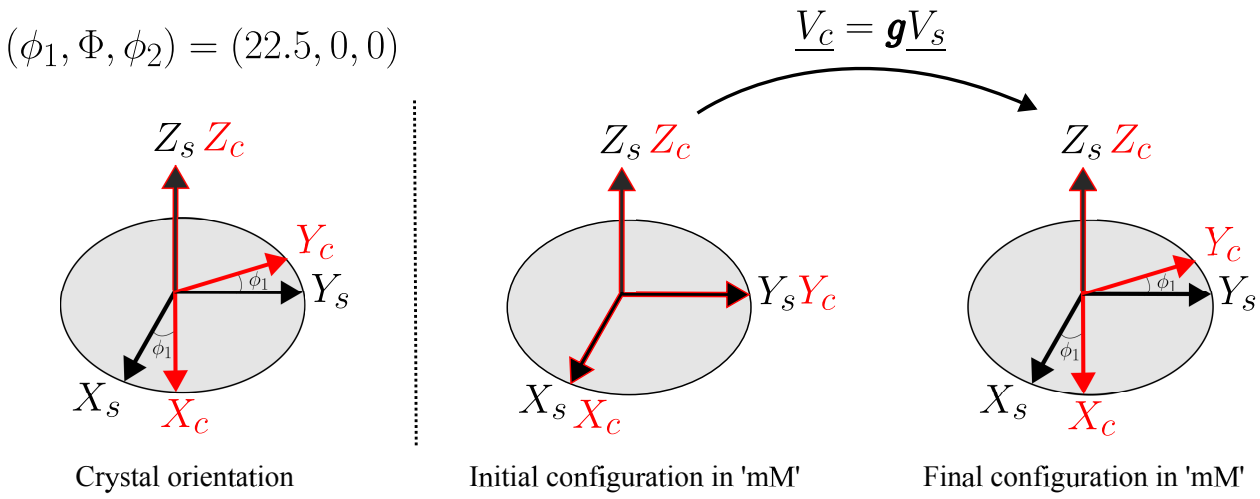

Figure A.1: *Illustration of the necessary calculations to consider the exact crystalline orientation in "mM" in the case where* $(\phi_1, \Phi, \phi_2) = (22.5, 0, 0)$ *for a better understanding. In "microMegas", the crystalline reference frame is by default aligned with the sample reference frame.*

a set of facets (grain boundaries) described by Cartesian plane equations. A plane equation is then defined as:

$$Ax + By + Cz = D \tag{A.1}$$

With $\underline{n}$ the plane normal equal to:

$$\underline{n} = \begin{pmatrix} x \\ y \\ z \end{pmatrix} \tag{A.2}$$

And k a point belonging to the plane:

$$\underline{k} = \begin{pmatrix} A \\ B \\ C \end{pmatrix} \tag{A.3}$$

Thus applying the rotation formula to the plane normal allows us to calculate the equations and to rebuild the grain geometry after rotation. The calculations are performed as follows for one plane equation:

$$\underline{n}' = \underset{\sim}{\boldsymbol{g}}.\underline{n} \tag{A.4}$$

$$\underline{k}' = \underset{\sim}{\boldsymbol{g}}.\underline{k} \tag{A.5}$$

By doing so for every plane equation describing the grain, the final configuration as illustrated in Fig A.1 is reached. Applying the stress field form a FEM computation as explained in § 2.2.2 requires changing the tensor basis as:

$$\underset{\sim}{\boldsymbol{\sigma}}_{FEM} = \underset{\sim}{\boldsymbol{g}}.\underset{\sim}{\boldsymbol{\sigma}}.\underset{\sim}{\boldsymbol{g}}^{-1} \tag{A.6}$$

With $\underset{\sim}{\boldsymbol{\sigma}}$ the solution from the FEM computation is expressed in the sample reference frame.

B BCs 1,2,3 and 4 elastic loading

This appendix illustrates the characteristics of the various elastic loadings on the C5 slip system used for the simulations in Chapter IV. As a reminder, for each of these loadings, the crystalline orientation of the grain is identical, only the crystalline orientations of neighbouring grains change.

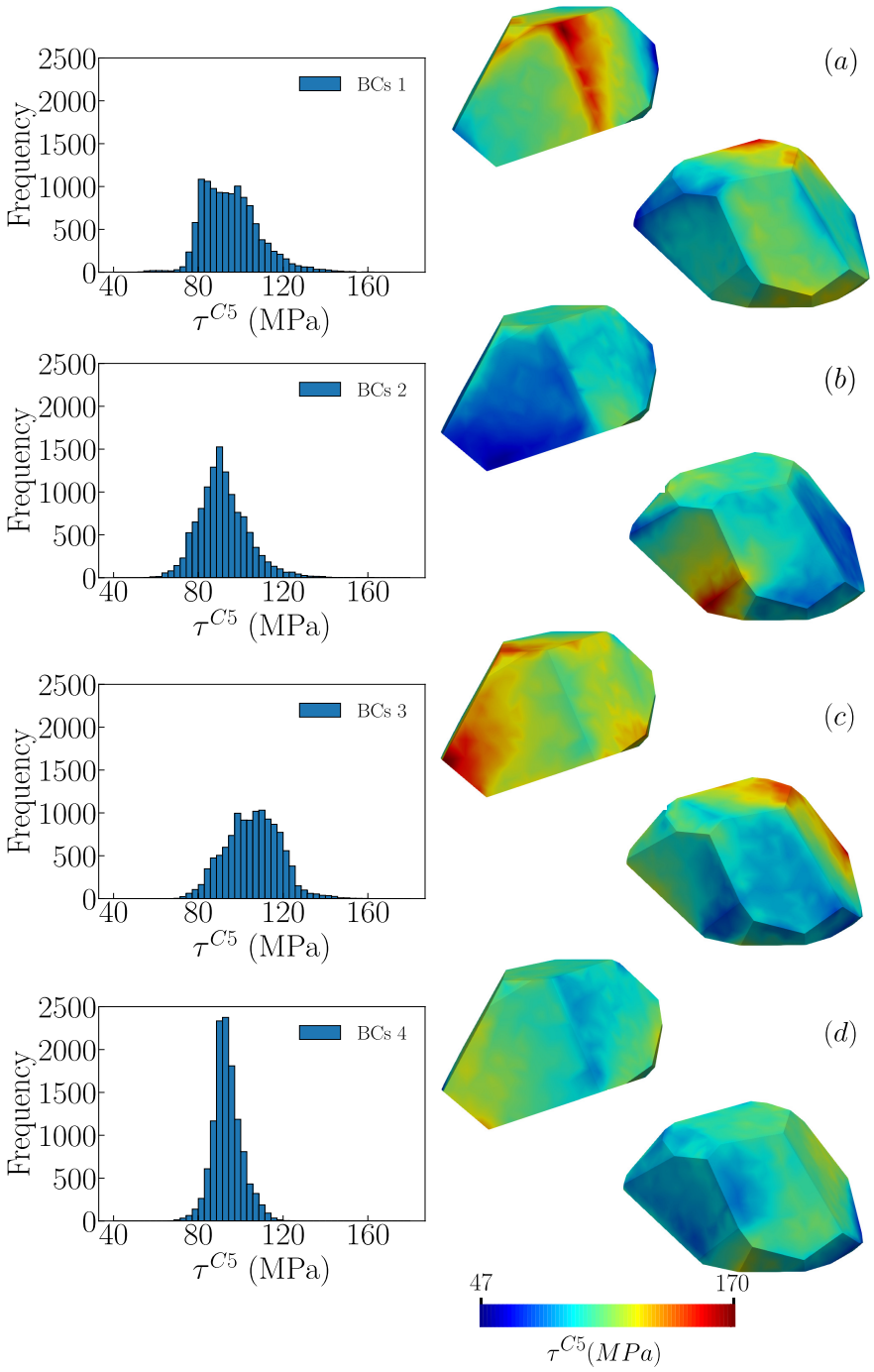

Figure B.1: *Illustration of the elastic loading used in this manuscript: BCs 1 (a), BCs 2 (b), BCs 3 (c) and BCs 4 (d).*

These characteristics are represented by the histogram of the resolved shear stress values and by the mapping of these values on the surface of the grain and for two viewing angles. As the range of values used for the colormap is the same for the different loadings, it is easy to see that the level of heterogeneity has decreased significantly, particularly for the BCs 4 case, which corresponds to a minimal level of heterogeneity and stress intensity. For loadings BCs 2 and BCs 3, heterogeneity is still clearly visible, but the regions of stress concentration are no longer located in the same region as for case BCs 1.

C BCs 1,2,3 and 4 slip system activities

Identical to the previous appendix, we illustrate here the slip systems activities computed for the four elastic loadings used in Chapter IV. It can be seen that for each of the crystalline orientations, the activity hierarchy of the slip systems is preserved. Two slip systems are predominantly active and mostly accommodate plastic deformation, the two collinear slip systems C5 and C3.

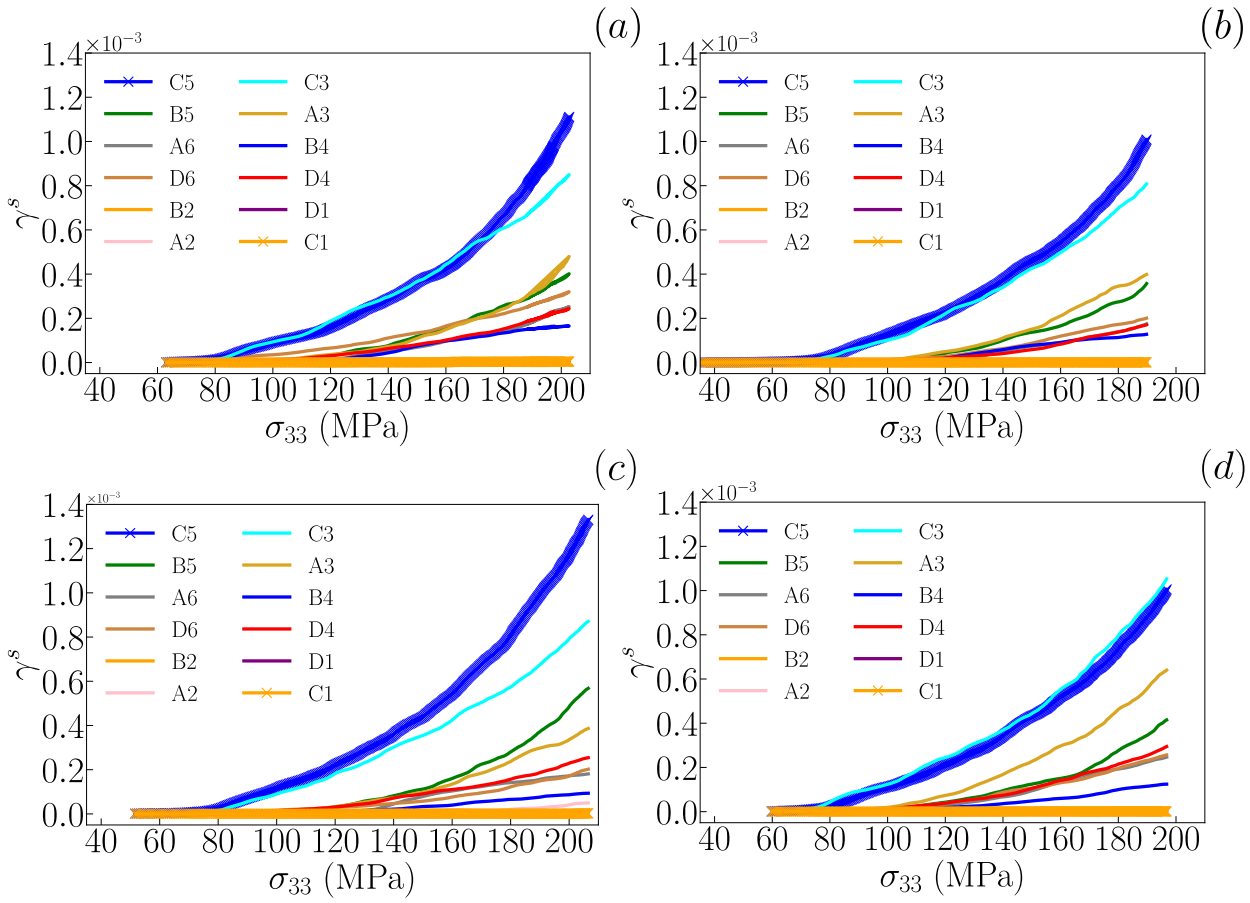

Figure C.1: *Slip system activity of the elastic loading used in this manuscript: BCs 1 (a), BCs 2 (b), BCs 3 (c) and BCs 4 (d).*

D On the simulation of digital twins

As stated in the introduction of this manuscript, different research groups within the ANR project 3DiPolyPlast are working together on the subject of intragranular plastic strain localization in pure polycrystalline materials. In particular, experiments at the Grenoble synchrotron, on ID11, have enabled to carry out volume reconstructions of part of the Nickel samples using DCT by my colleague Zheheng LIU. DCT is a near-field diffraction-based imaging technique that provides high-resolution grain maps of polycrystalline materials, the technique combines the concepts of image reconstruction from projections (tomography) and X-ray diffraction imaging (topography) [Ludwig et al., 2008].

From the reconstruction of the Nickel experimental samples, it is possible to define a mesh and then to simulate the behaviour of the real microstructure during any loading as already done for example in the work of [Proudhon et al., 2018]. In this appendix, we describe attempts to approximate this real microstructure with Voronoi and Laguerre tessellation as the meshing methods are quite complex and require further developments. Such approximations have been proved to well reproduce the real microstructure as shown by [Quey and Renversade, 2018] in the case of an Aluminium polycrystal.

As shown in Fig D.1, it is possible to obtain from the DCT experiment, a representation of the undeformed Nickel sample volume. The domain whose dimensions are illustrated in the figure is paved by voxels, all associated with a specific crystalline orientation.

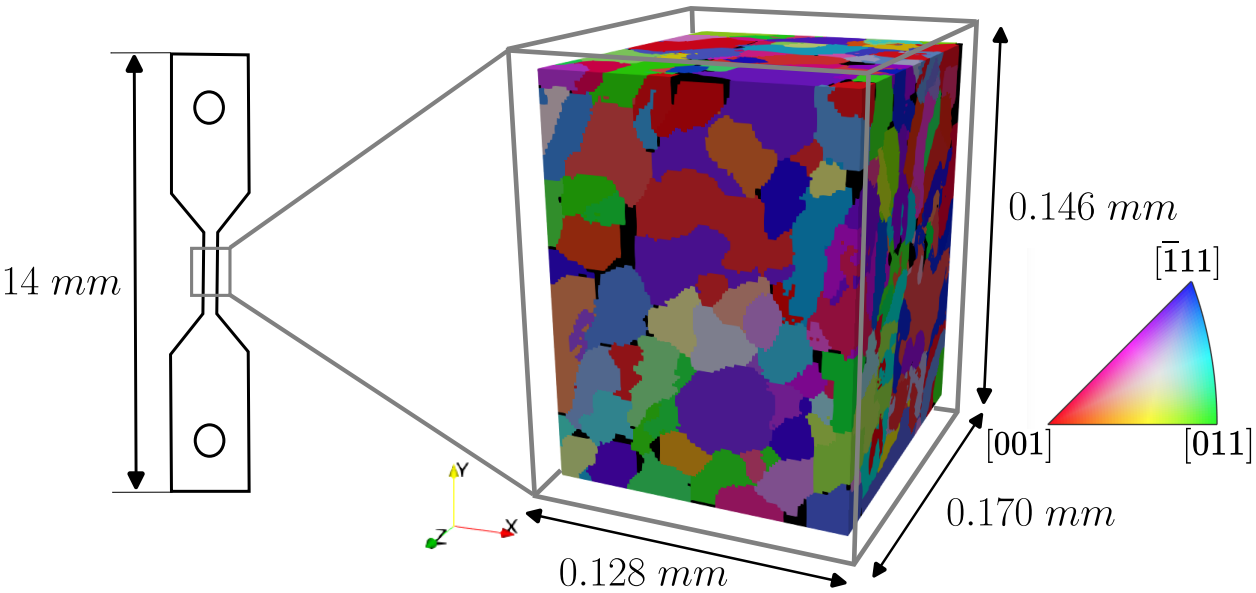

Figure D.1: *DCT reconstruction of the real microstructure from a Nickel sample. Grains are coloured as a function of their crystalline orientation.*

Approximation by Voronoi and Laguerre tessellations:

As previously stated, we will consider here Voronoi and Laguerre tessellations that differ from their definition. Laguerre tessellations allow to introduce size/volume dispersion for the grains contained in the microstructure. Formally, Voronoi cells are defined as follows:

$$C(x_i, \phi) = \{y \in \mathbb{R}^3 : ||y - x_i|| \leq ||y - x_j|| \text{ for all } x_j \in \phi\} \tag{D.1}$$

With ϕ being the set of nuclei points:

$$\phi = \{x_1, x_2, ...\} \tag{D.2}$$

Laguerre tessellations introduced a so-called power function defined as:

$$\text{pow}(y, (x_i, w_i)) = ||y - x_i||^2 - w_i \tag{D.3}$$

With w_i the non-negative weight associated to nuclei x_i. As a consequence, the Laguerre cells are formally defined as:

$$C((x_i, w_i), \phi) = \{y \in \mathbb{R}^3 : \text{pow}(y, (x_i, w_i)) \leq \text{pow}(y, (x_j, w_j)) \text{ for all } (x_j, w_j) \in \phi\} \tag{D.4}$$

With ϕ being the set of weighted nuclei points:

$$\phi = \{(x_1, w_1), (x_2, w_2), ...\} \tag{D.5}$$

Using the DCT reconstruction illustrated in Fig D.1 it is possible to extract the volume and centre of each grain (nuclei). This information can be introduced in the software Neper to generate Voronoi or Laguerre tessellations. Results of these operations are illustrated in Fig D.2 by the volume dispersion and number of neighbours in the synthetic microstructure against the real microstructure. These results reveal significant differences between the two synthetic microstructures and the real microstructure, particularly with regard to the direct neighbour number of a grain within the aggregate. The real microstructure more or less systematically reveals a denser neighbourhood. The use of a Laguerre tessellation allows us to better associate the right volumes with the grains, as shown in the figure, but this does not greatly modify the number of neighbours present. A purely visual comparison of the three microstructures reveals some truly significant differences. In the case of synthetic microstructures, the grain shape corresponds only very slightly to the actual microstructure and is therefore not a convincing result.

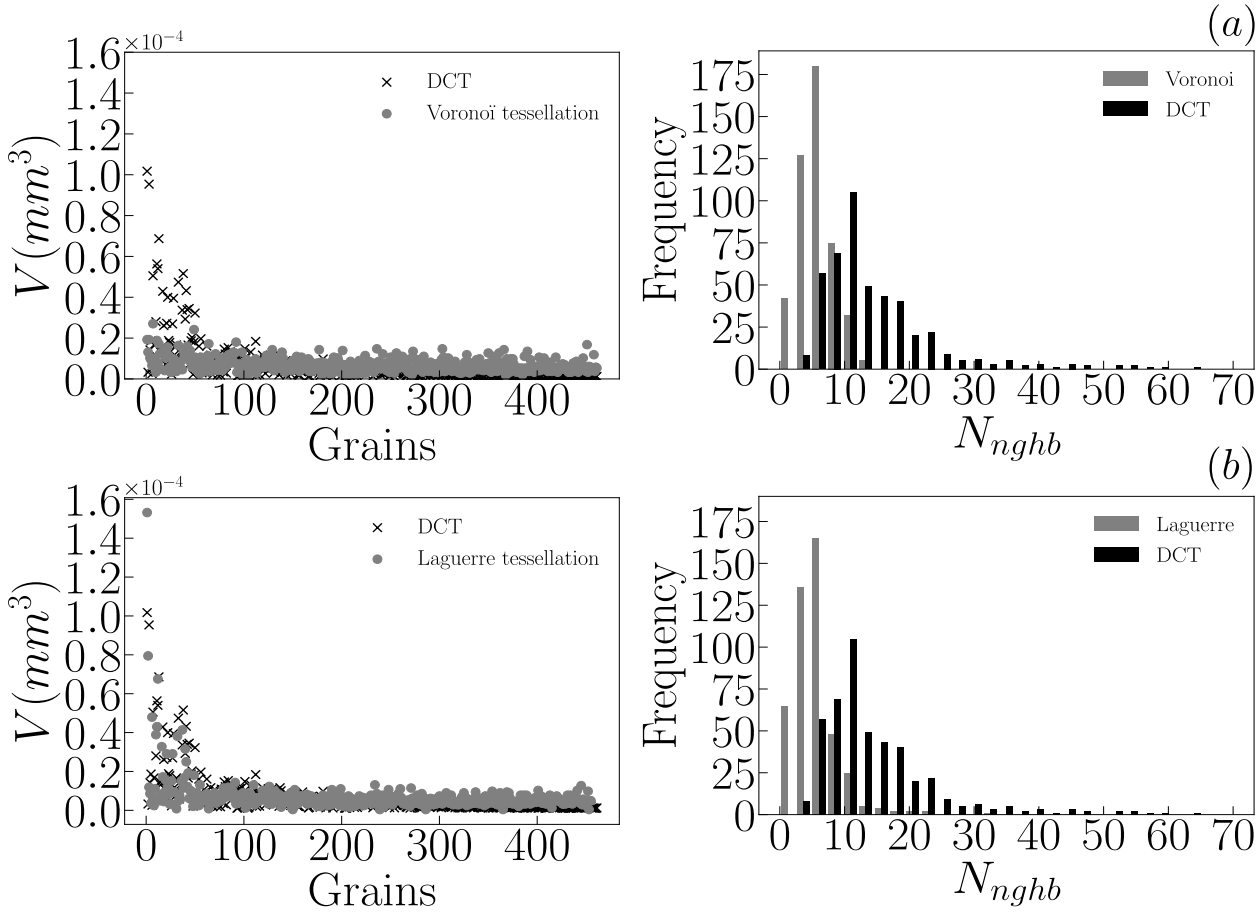

Figure D.2: *Illustration of the grains volumes and number of direct neighbours for Voronoi (a) and Laguerre tessellations (b) compared with the real microstructure issued from a DCT reconstruction.*

The use of an objective function as in [Quey and Renversade, 2018] recently added to the Neper software, could improve results. However, the uneven shape of the grains in the reconstruction of the real microstructure should still result in significant differences.

Bibliography

Abuzaid, W. Z., Sangid, M. D., Carroll, J. D., Sehitoglu, H., and Lambros, J. (2012). Slip transfer and plastic strain accumulation across grain boundaries in hastelloy x. *Journal of the Mechanics and Physics of Solids*, 60(6):1201–1220.

Ahmadikia, B., Kumar, M. A., and Beyerlein, I. J. (2021). Effect of neighboring grain orientation on strain localization in slip bands in hcp materials. *International Journal of Plasticity*, 144:103026.

Ahmed, N. and Hartmaier, A. (2011). Mechanisms of grain boundary softening and strain-rate sensitivity in deformation of ultrafine-grained metals at high temperatures. *Acta materialia*, 59(11):4323–4334.

Antolovich, S. D. and Armstrong, R. W. (2014). Plastic strain localization in metals: origins and consequences. *Progress in Materials Science*, 59:1–160.

Arani, M. M., Ramesh, N., Wang, X., Parson, N., Li, M., and Poole, W. (2022). The localization of plastic deformation in the precipitate free zone of an al-mg-si-mn alloy. *Acta Materialia*, 231:117872.

Arsenlis, A., Cai, W., Tang, M., Rhee, M., Oppelstrup, T., Hommes, G., Pierce, T. G., and Bulatov, V. V. (2007). Enabling strain hardening simulations with dislocation dynamics. *Modelling and Simulation in Materials Science and Engineering*, 15(6):553.

Arsenlis, A., Rhee, M., Hommes, G., Cook, R., and Marian, J. (2012). A dislocation dynamics study of the transition from homogeneous to heterogeneous deformation in irradiated body-centered cubic iron. *Acta Materialia*, 60(9):3748–3757.

Asaro, R. J. and Rice, J. (1977). Strain localization in ductile single crystals. *Journal of the Mechanics and Physics of Solids*, 25(5):309–338.

Ashby, M. (1970). The deformation of plastically non-homogeneous materials. *The Philosophical Magazine: A Journal of Theoretical Experimental and Applied Physics*, 21(170):399–424.

Bamney, D., Reyes, R., Capolungo, L., and Spearot, D. E. (2022). Disclination-dislocation based model for grain boundary stress field evolution due to slip transmission history and influence on subsequent dislocation transmission. *Journal of the Mechanics and Physics of Solids*, 165:104920.

Bargmann, S., Ekh, M., Runesson, K., and Svendsen, B. (2010). Modeling of polycrystals with gradient crystal plasticity: A comparison of strategies. *Philosophical Magazine*, 90(10):1263–1288.

Barton, N. R., Arsenlis, A., and Marian, J. (2013). A polycrystal plasticity model of strain localization in irradiated iron. *Journal of the Mechanics and Physics of Solids*, 61(2):341–351.

Bayerschen, E., McBride, A., Reddy, B., and Böhlke, T. (2016). Review on slip transmission criteria in experiments and crystal plasticity models. *Journal of materials science*, 51:2243–2258.

Besson, J., Cailletaud, G., Chaboche, J.-L., and Forest, S. (2009). *Non-linear mechanics of materials*, volume 167. Springer Science & Business Media.

Bieler, T., Eisenlohr, P., Zhang, C., Phukan, H., and Crimp, M. (2014). Grain boundaries and interfaces in slip transfer. *Current Opinion in Solid State and Materials Science*, 18(4):212–226.

Bilby, B. (1957). Les dislocations by j. friedel. *Acta Crystallographica*, 10(7):488–488.

Boas, W. and Ogilvie, G. (1954). The plastic deformation of a crystal in a polycrystalline aggregate. *Acta Metallurgica*, 2(5):655–659.

Bonneville, J., Escaig, B., and Martin, J. (1988). A study of cross-slip activation parameters in pure copper. *Acta Metallurgica*, 36(8):1989–2002.

Bretin, R., Levesque, M., and Bocher, P. (2019). Neighborhood effect on the strain distribution in linearly elastic polycrystals: Part 1–finite element study of the interaction between grains. *International Journal of Solids and Structures*, 176:36–48.

Brinck, A., Engelke, C., and Neuhauser, H. (1998). Quantitative afm investigation of slip line structure in fe3al single crystals after deformation at various temperatures. *Materials Science and Engineering: A*, 258(1-2):37–41.

Brown, A. (1952). Surface effects in plastic deformation of metals. *Advances in Physics*, 1(4):427–479.

Brown, A. F. (1949). Fine structure of slip-zones. *Nature*, 163(4155):961–962.

Brown, L. (2002). A dipole model for the cross-slip of screw dislocations in fee metals. *Philosophical Magazine A*, 82(9):1691–1711.

Brown, L. M. (2006). Dislocation bowing and passing in persistent slip bands. *Philosophical Magazine*, 86(25-26):4055–4068.

Bulatov, V. V., Reed, B. W., and Kumar, M. (2014). Grain boundary energy function for fcc metals. *Acta Materialia*, 65:161–175.

Cailletaud, G. (1992). A micromechanical approach to inelastic behaviour of metals. *International Journal of Plasticity*, 8(1):55–73.

Chaboche, J.-L. (2008). A review of some plasticity and viscoplasticity constitutive theories. *International journal of plasticity*, 24(10):1642–1693.

Chang, Y. W. and Asaro, R. J. (1981). An experimental study of shear localization in aluminum-copper single crystals. *Acta Metallurgica*, 29(1):241–257.

Charpagne, M., Hestroffer, J., Polonsky, A., Echlin, M., Texier, D., Valle, V., Beyerlein, I., Pollock, T., and Stinville, J. (2021). Slip localization in inconel 718: a three-dimensional and statistical perspective. *Acta Materialia*, 215:117037.

Chassagne, M., Legros, M., and Rodney, D. (2011). Atomic-scale simulation of screw dislocation/coherent twin boundary interaction in al, au, cu and ni. *Acta Materialia*, 59(4):1456–1463.

Chen, N. and Pond, R. (1952). Dynamic formation of slip bands in aluminum. *JOM*, 4:1085–1092.

Chen, Z., Jin, Z., and Gao, H. (2007). Repulsive force between screw dislocation and coherent twin boundary in aluminum and copper. *Physical review B*, 75(21):212104.

Cho, J., Crone, J. C., Arsenlis, A., and Aubry, S. (2020). Dislocation dynamics in polycrystalline materials. *Modelling and Simulation in Materials Science and Engineering*, 28(3):035009.

Choi, Y. S., Groeber, M. A., Shade, P. A., Turner, T. J., Schuren, J. C., Dimiduk, D. M., Uchic, M. D., and Rollett, A. D. (2014). Crystal plasticity finite element method simulations for a polycrystalline ni micro-specimen deformed in tension. *Metallurgical and Materials Transactions A*, 45(13):6352–6359.

Cottrell, A. (1957). The properties of materials at high rates of strain. In *London Conference of Institute of Mechanical Engineers (IME, London, 1957)*, page 18.

Crussard, M. C. (1945). Etude des glissements plastiques dans les cristaux d'aluminium. *Revue de Métallurgie*, 42(9):286–294.

Cui, Y., Po, G., and Ghoniem, N. (2018a). Size-tuned plastic flow localization in irradiated materials at the submicron scale. *Physical review letters*, 120(21):215501.

Cui, Y., Po, G., and Ghoniem, N. (2018b). Suppression of localized plastic flow in irradiated materials. *Scripta Materialia*, 154:34–39.

Cuitino, A. M. and Ortiz, M. (1993). Computational modelling of single crystals. *Modelling and Simulation in Materials Science and Engineering*, 1(3):225.

Daveau, G. (2012). *Interaction dislocations-joints de grains en déformation plastique monotone: étude expérimentale et modélisations numériques*. PhD thesis, Ecole Centrale Paris.

De Koning, M., Kurtz, R. J., Bulatov, V., Henager, C. H., Hoagland, R. G., Cai, W., and Nomura, M. (2003). Modeling of dislocation–grain boundary interactions in fcc metals. *Journal of Nuclear Materials*, 323(2-3):281–289.

De Wit, R. (1967). Some relations for straight dislocations. *physica status solidi (b)*, 20(2):567–573.

Delaire, F., Raphanel, J. L., and Rey, C. (2000). Plastic heterogeneities of a copper multicrystal deformed in uniaxial tension: experimental study and finite element simulations. *Acta Materialia*, 48(5):1075–1087.

Déprés, C. (2004). *Modélisation physique des stades précurseurs de l'endommagement en fatigue dans l'acier inoxydable austénitique 316L*. PhD thesis, Grenoble INPG.

Déprés, C., Robertson*, C., and Fivel, M. (2004). Low-strain fatigue in aisi 316l steel surface grains: a three-dimensional discrete dislocation dynamics modelling of the early cycles i. dislocation microstructures and mechanical behaviour. *Philosophical Magazine*, 84(22):2257–2275.

Déprés, C., Robertson, C., and Fivel, M. (2015). 3d discrete dislocation dynamics investigations of fatigue crack initiation and propagation. *Aerospace Lab*, (9):p–1.

Déprés, C., Robertson, C., and Fivel, M. C. (2006). Low-strain fatigue in 316l steel surface grains: a three dimension discrete dislocation dynamics modelling of the early cycles. part 2: Persistent slip markings and micro-crack nucleation. *Philosophical Magazine*, 86(1):79–97.

Devincre, B. (1995). Three dimensional stress field expressions for straight dislocation segments. *Solid State Communications*, 93(11):875–878.

Devincre, B. (1996). Meso-scale simulation of the dislocation dynamics. *NATO ASI Series E Applied Sciences-Advanced Study Institute*, 308:309–324.

Devincre, B. (2005). Études de la plasticité des solides cristallins par dynamique des dislocations à l'échelle mésoscopique. *Manuscrit hdr, Paris XI-Orsay*, 143:144.

Devincre, B. and Condat, M. (1992). Model validation of a 3d simulation of dislocation dynamics: discretization and line tension effects. *Acta metallurgica et materialia*, 40(10):2629–2637.

Devincre, B., Hoc, T., and Kubin, L. (2008). Dislocation mean free paths and strain hardening of crystals. *Science*, 320(5884):1745–1748.

Devincre, B. and Kubin, L. (2010). Scale transitions in crystal plasticity by dislocation dynamics simulations. *Comptes Rendus Physique*, 11(3-4):274–284.

Devincre, B., Kubin, L., Lemarchand, C., and Madec, R. (2001). Mesoscopic simulations of plastic deformation. *Materials Science and Engineering: A*, 309:211–219.

Devincre, B., Madec, R., Monnet, G., Queyreau, S., Gatti, R., and Kubin, L. (2011). Modeling crystal plasticity with dislocation dynamics simulations: The 'micromegas' code. *Mechanics of Nano-objects*, 1:81–100.

Dewald, M. and Curtin, W. (2006). Multiscale modelling of dislocation/grain-boundary interactions: I. edge dislocations impinging on σ11 (1 1 3) tilt boundary in al. *Modelling and Simulation in Materials Science and Engineering*, 15(1):S193.

Dewald, M. and Curtin, W. (2007). Multiscale modelling of dislocation/grain boundary interactions. ii. screw dislocations impinging on tilt boundaries in al. *Philosophical Magazine*, 87(30):4615–4641.

Dewald, M. and Curtin, W. (2011). Multiscale modeling of dislocation/grain-boundary interactions. *Modelling and Simulation in Materials Science and Engineering*, 19(5):055002.

Di Gioacchino, F. and da Fonseca, J. Q. (2015). An experimental study of the polycrystalline plasticity of austenitic stainless steel. *International Journal of Plasticity*, 74:92–109.

Differt, K. and Essmann, U. (1993). In fundamental aspects of dislocation interactions.

Dimanov, A., El Sabbagh, A., Raphanel, J., Lê, T., Bornert, M., Hallais, S., and Tanguy, A. (2021). Deformation of aluminum in situ sem and full field measurements by digital image correlation: evidence of concomitant crystal slip and grain boundary sliding. *Available at SSRN 3922862*.

Dumoulin, S. (2001). *De l'utilisation d'une loi monocristalline en vue de la caractérisation du comportement plastique du multicristal d'aluminium*. PhD thesis, Chambéry.

Erel, C., Po, G., and Ghoniem, N. (2017). Dependence of hardening and saturation stress in persistent slip bands on strain amplitude during cyclic fatigue loading. *Philosophical Magazine*, 97(32):2947–2970.

Escaig, B. (1968a). Cross-slipping process in the fcc structure.

Escaig, B. (1968b). Sur le glissement dévié des dislocations dans la structure cubique à faces centrées. *Journal de Physique*, 29(2-3):225–239.

Eshelby, J., Frank, F., and Nabarro, F. (1951). Xli. the equilibrium of linear arrays of dislocations. *The London, Edinburgh, and Dublin Philosophical Magazine and Journal of Science*, 42(327):351–364.

Ewing, J. A. and Humfrey, J. (1903). Vi. the fracture of metals under repeated alternations of stress. *Philosophical Transactions of the Royal Society of London. Series A, Containing Papers of a Mathematical or Physical Character*, 200(321-330):241–250.

Feltner, C. and Laird, C. (1968). Factors influencing dislocation structures in fatigued metals. *Transactions of the Metallurgical Society of AIME*, 242(7):1253.

Fivel, M. (2004). *Plasticite Cristalline Et Transition D'echelle Cas Du Monocristal*. Ed. Techniques Ingénieur.

Fivel, M., Gosling, T., and Canova, G. (1996). Implementing image stresses in a 3d dislocation simulation. *Modelling and Simulation in Materials Science and Engineering*, 4(6):581.

Fivel, M., Tabourot, L., Rauch, E., and Canova, G. (1998). Identification through mesoscopic simulations of macroscopic parameters of physically based constitutive equations for the plastic behaviour of fcc single crystats. *Le Journal de Physique IV*, 8(PR8):Pr8–151.

Foreman, A. (1967). The bowing of a dislocation segment. *Philosophical magazine*, 15(137):1011–1021.

Forest, S. (2008). Some links between cosserat, strain gradient crystal plasticity and the statistical theory of dislocations. *Philosophical Magazine*, 88(30-32):3549–3563.

Forest, S. (2022). Mécanique des milieux continus, volume 1: Théorie. *Cours De L'ecole Des Mines. Presses des Mines*.

Franciosi, P. (1985). The concepts of latent hardening and strain hardening in metallic single crystals. *Acta Metallurgica*, 33(9):1601–1612.

Friedel, J. (1957). Regarding seeger's paper on work hardening. *Dislocations and mechanical properties of crystals*, pages 330–332.

Georgieva, E. (1996). Interfaces in crystalline materials, ap sutton, rw balluffi, clarendon press, materials park, oh (1995), isbn 0-198513851-2.

Gerold, V. (1979). Dislocations in solids. *North Holland Amsterdam, The Netherlands*, 4:219.

Ghoniem, N., Tong, S., Huang, J., Singh, B., and Wen, M. (2002). Mechanisms of dislocation-defect interactions in irradiated metals investigated by computer simulations. *Journal of nuclear materials*, 307:843–851.

Ghoniem, N., Tong, S.-H., Singh, B., and Sun, L. (2001). On dislocation interaction with radiation-induced defect clusters and plastic flow localization in fcc metals. *Philosophical Magazine A*, 81(11):2743–2764.

Gilman, J. and Johnston, W. (1957). Dislocations and mechanical properties of crystals, 1957.

Gilman, J. and Johnston, W. (1962). Dislocations in lithium fluoride crystals. *Solid state physics*, 13:147–222.

Gomez-Garcia, D., Devincre, B., and Kubin, L. (1999). Dislocation dynamics in confined geometry. *Journal of computer-aided materials design*, 6(2):157–164.

Goulmy, J., Depriester, D., Guittonneau, F., Barrallier, L., and Jégou, S. (2022). Mechanical behavior of polycrystals: Coupled in situ dic-ebsd analysis of pure copper under tensile test. *Materials Characterization*, 194:112322.

Gruber, B., Weißensteiner, I., Kremmer, T., Grabner, F., Falkinger, G., Schökel, A., Spieckermann, F., Schäublin, R., Uggowitzer, P. J., and Pogatscher, S. (2020). Mechanism of low temperature deformation in aluminium alloys. *Materials Science and Engineering: A*, 795:139935.

Gutmanas, E. and Nadgorny, E. (1970). Dislocation multiplication by multiple cross slip. *SOV PHYS SOLID STATE*, 12(3):733–734.

Hall, E. (1951). The deformation and ageing of mild steel: Iii discussion of results. *Proceedings of the Physical Society. Section B*, 64(9):747.

Han, S., Eisenlohr, P., and Crimp, M. A. (2018). Ecci based characterization of dislocation shear in polycrystalline arrays during heterogeneous deformation of commercially pure titanium. *Materials Characterization*, 142:504–514.

Han, X. (2012). *Modélisation de la fragilisation due au gonflement dans les aciers inoxydables austénitiques irradiés*. PhD thesis, Paris, ENMP.

Hanriot, F., Cailletaud, G., and Rémy, L. (1991). Mechanical behaviour of a nickel-base superalloy single crystal. *A. Freed, K. Walker, Editeurs: High temperature constitutive modelling-Theory and application, ASME, New-York*, pages 139–150.

Haouala, S., Alizadeh, R., Bieler, T., Segurado, J., and LLorca, J. (2020). Effect of slip transmission at grain boundaries in al bicrystals. *International Journal of Plasticity*, 126:102600.

Hasson, G. and Goux, C. (1971). Interfacial energies of tilt boundaries in aluminium. experimental and theoretical determination. *Scripta metallurgica*, 5(10):889–894.

Heidenreich, R. and Shockley, W. (1947). Electron microscope and electron-diffraction study of slip in metal crystals. *Journal of Applied Physics*, 18(11):1029–1031.

Hirsch, P. (1977). Point defect cluster hardening. In *Vacancies' 76. Proceedings of a conference on'point defect behaviour and diffusional processes' organized by the Metals Society and held at The Royal Fort, University of Bristol, on 13-16 September, 1976*.

Hirth, J. P., Lothe, J., and Mura, T. (1983). Theory of dislocations. *Journal of Applied Mechanics*, 50(2):476.

Holm, E. A., Olmsted, D. L., and Foiles, S. M. (2010). Comparing grain boundary energies in face-centered cubic metals: Al, au, cu and ni. *Scripta Materialia*, 63(9):905–908.

Huang, Z., Yang, C., Allison, J. E., Qi, L., and Misra, A. (2021). Dislocation cross-slip in precipitation hardened mg–nd alloys. *Journal of Alloys and Compounds*, 859:157858.

Hull, D. and Bacon, D. J. (2001). *Introduction to dislocations*. Butterworth-Heinemann.

Humphreys, F. and Hirsch, P. B. (1970). The deformation of single crystals of copper and copper-zinc alloys containing alumina particles-ii. microstructure and dislocation-particle interactions. *Proceedings of the Royal Society of London. A. Mathematical and Physical Sciences*, 318(1532):73–92.

Hunter, A., Leu, B., and Beyerlein, I. J. (2018). A review of slip transfer: applications of mesoscale techniques. *Journal of materials science*, 53:5584–5603.

Hussein, A. M. and El-Awady, J. A. (2016). Quantifying dislocation microstructure evolution and cyclic hardening in fatigued face-centered cubic single crystals. *Journal of the Mechanics and Physics of Solids*, 91:126–144.

Hussein, A. M., Rao, S. I., Uchic, M. D., Dimiduk, D. M., and El-Awady, J. A. (2015). Microstructurally based cross-slip mechanisms and their effects on dislocation microstructure evolution in fcc crystals. *Acta Materialia*, 85:180–190.

Hutchinson, J. W. (1976). Bounds and self-consistent estimates for creep of polycrystalline materials. *Proceedings of the Royal Society of London. A. Mathematical and Physical Sciences*, 348(1652):101–127.

Ikeno, S., Abou, S., Tada, S., and Uetani, Y. (1990). Observation of slip bands in polycrystalline aluminum deformed in tension. *Journal of Japan Institute of Light Metals*, 40(12):918–924.

Jamond, O., Gatti, R., Roos, A., and Devincre, B. (2016). Consistent formulation for the discrete-continuous model: Improving complex dislocation dynamics simulations. *International Journal of Plasticity*, 80:19–37.

Jaoul, B. (2008). *Etude de la plasticité et application aux métaux*. Presses des MINES.

Jiang, M. (2019). *Investigation of grain size and shape effects on crystal plasticity by dislocation dynamics simulations*. PhD thesis, Université Paris Saclay (COmUE).

Jiang, M. and Devincre, B. (2022). Uncovering the existence of anti-backstress associated with dislocations accumulated at grain boundaries during plastic deformation. *Computational Materials Science*, 208:111328.

Jiang, M., Devincre, B., and Monnet, G. (2019). Effects of the grain size and shape on the flow stress: A dislocation dynamics study. *International Journal of Plasticity*, 113:111–124.

Jiang, M., Monnet, G., and Devincre, B. (2020). Stress fields of finite-size dislocation walls and prediction of back stress induced by geometrically necessary dislocations at grain boundaries. *Journal of the Mechanics and Physics of Solids*, 143:104071.

Jiang, M., Monnet, G., and Devincre, B. (2021). On the origin of the hall-petch law: A 3d-dislocation dynamics simulation investigation. *Acta Materialia*, 209:116783.

Jin, Y., Bernacki, M., Agnoli, A., Lin, B., Rohrer, G. S., Rollett, A. D., and Bozzolo, N. (2015). Evolution of the annealing twin density during δ-supersolvus grain growth in the nickel-based superalloy inconel™ 718. *Metals*, 6(1):5.

Jin, Z.-H., Gumbsch, P., Albe, K., Ma, E., Lu, K., Gleiter, H., and Hahn, H. (2008). Interactions between non-screw lattice dislocations and coherent twin boundaries in face-centered cubic metals. *Acta Materialia*, 56(5):1126–1135.

Jin, Z.-H., Gumbsch, P., Ma, E., Albe, K., Lu, K., Hahn, H., and Gleiter, H. (2006). The interaction mechanism of screw dislocations with coherent twin boundaries in different face-centred cubic metals. *Scripta Materialia*, 54(6):1163–1168.

Kacher, J. and Robertson, I. (2012). Quasi-four-dimensional analysis of dislocation interactions with grain boundaries in 304 stainless steel. *Acta Materialia*, 60(19):6657–6672.

Kahloun, C., Monnet, G., Queyreau, S., Le, L., and Franciosi, P. (2016). A comparison of collective dislocation motion from single slip quantitative topographic analysis during in-situ afm room temperature tensile tests on cu and feα crystals. *International Journal of Plasticity*, 84:277–298.

Kassner, M., Geantil, P., and Levine, L. E. (2013). Long range internal stresses in single-phase crystalline materials. *International Journal of Plasticity*, 45:44–60.

Kitajima, S. and Ono, N. (1995). Slip mode of polycrystalline pure metals in tensile deformation. *physica status solidi (a)*, 149(1):201–211.

Kobayashi, S., Inomata, T., Kobayashi, H., Tsurekawa, S., and Watanabe, T. (2008). Effects of grain boundary-and triple junction-character on intergranular fatigue crack nucleation in polycrystalline aluminum. *Journal of materials science*, 43:3792–3799.

Kobayashi, S., Tsurekawa, S., and Watanabe, T. (2005). Grain boundary hardening and triple junction hardening in polycrystalline molybdenum. *Acta Materialia*, 53(4):1051–1057.

Koehler, J., Cohen, M., of Mining, A. I., and Engineers, M. (1954). *Dislocations in metals*. Institute of Metals Division, The American Institute of Mining and ....

Koning, M. d., Miller, R., Bulatov, V., and Abraham, F. F. (2002). Modelling grain-boundary resistance in intergranular dislocation slip transmission. *Philosophical Magazine A*, 82(13):2511–2527.

Konuma, M. (1964). Plastic deformation of polycrystalline coppermdash;observations of slip bands and etch pits and considerations on the deformation mechanism. *Journal of the Japan Institute of Metals*, 28(12):781–787.

Korbel, A. and Martin, P. (1986). Microscopic versus macroscopic aspect of shear bands deformation. *Acta Metallurgica*, 34(10):1905–1909.

Korzeczek, L. (2017). *Modélisation mésoscopique en 3D par le modèle Discret-Continu de la stabilité des fissures courtes dans les métaux CFC*. PhD thesis, Université Paris-Saclay.

Kramer, D., Savage, M., and Levine, L. E. (2005). Afm observations of slip band development in al single crystals. *Acta materialia*, 53(17):4655–4664.

Krejčí, J. and Lukáš, P. (1971). Dislocation substructure in the surface layer of fatigued al and ni. *physica status solidi (a)*, 8(1):299–307.

Kubin, L. (2013). *Dislocations, mesoscale simulations and plastic flow*, volume 5. Oxford University Press.

Kubin, L. P., Canova, G., Condat, M., Devincre, B., Pontikis, V., and Bréchet, Y. (1992). Dislocation microstructures and plastic flow: a 3d simulation. In *Solid state phenomena*, volume 23, pages 455–472. Trans Tech Publ.

Latypov, M. I., Stinville, J.-C., Mayeur, J. R., Hestroffer, J. M., Pollock, T. M., and Beyerlein, I. J. (2021). Insight into microstructure-sensitive elastic strain concentrations from integrated computational modeling and digital image correlation. *Scripta Materialia*, 192:78–82.

Lee, T., Robertson, I., and Birnbaum, H. (1989). Prediction of slip transfer mechanisms across grain boundaries. *Scripta metallurgica*, 23(5):799–803.

Lemarchand, C., Devincre, B., and Kubin, L. (2001). Homogenization method for a discrete-continuum simulation of dislocation dynamics. *Journal of the Mechanics and Physics of Solids*, 49(9):1969–1982.

Lepinoux, J. and Kubin, L. (1987). Dynamic organization of dislocation structures: A simulation. *Scr. Metall.;(United States)*, 21(6).

Li, P., Li, S., Wang, Z., and Zhang, Z. (2011). Fundamental factors on formation mechanism of dislocation arrangements in cyclically deformed fcc single crystals. *Progress in Materials Science*, 56(3):328–377.

Li, Y. and Laird, C. (1994). Cyclic response and dislocation structures of aisi 316l stainless steel. part 1: single crystals fatigued at intermediate strain amplitude. *Materials Science and Engineering: A*, 186(1-2):65–86.

Lim, A., Haataja, M., Cai, W., and Srolovitz, D. (2012). Stress-driven migration of simple low-angle mixed grain boundaries. *Acta materialia*, 60(3):1395–1407.

Lim, A., Srolovitz, D., and Haataja, M. (2009). Low-angle grain boundary migration in the presence of extrinsic dislocations. *Acta materialia*, 57(17):5013–5022.

Lim, H., Carroll, J., Battaile, C. C., Buchheit, T., Boyce, B., and Weinberger, C. (2014). Grain-scale experimental validation of crystal plasticity finite element simulations of tantalum oligocrystals. *International Journal of Plasticity*, 60:1–18.

Lim, L. and Raj, R. (1985). Continuity of slip screw and mixed crystal dislocations across bicrystals of nickel at 573 k. *Acta Metallurgica*, 33(8):1577–1583.

Lindholm, U. and Yeakley, L. (1965). Dynamic deformation of single and polycrystalline aluminium. *Journal of the Mechanics and Physics of Solids*, 13(1):41–53.

Ling, C., Tanguy, B., Besson, J., Forest, S., and Latourte, F. (2017). Void growth and coalescence in triaxial stress fields in irradiated fcc single crystals. *Journal of Nuclear Materials*, 492:157–170.

Liu, B., Eisenlohr, P., Roters, F., and Raabe, D. (2012). Simulation of dislocation penetration through a general low-angle grain boundary. *Acta Materialia*, 60(13-14):5380–5390.

Livingston, J. and Chalmers, B. (1957). Multiple slip in bicrystal deformation. *Acta Metallurgica*, 5(6):322–327.

Llanes, L. and Laird, C. (1992). The role of annealing twin boundaries in the cyclic deformation of fcc materials. *Materials Science and Engineering: A*, 157(1):21–27.

Ludwig, W., Lauridsen, E. M., Schmidt, S., Poulsen, H. F., and Baruchel, J. (2007). High-resolution three-dimensional mapping of individual grains in polycrystals by topotomography. *Journal of Applied Crystallography*, 40(5):905–911.

Ludwig, W., Schmidt, S., Lauridsen, E. M., and Poulsen, H. F. (2008). X-ray diffraction contrast tomography: a novel technique for three-dimensional grain mapping of polycrystals. i. direct beam case. *Journal of Applied Crystallography*, 41(2):302–309.

Lukas, P. (1996). Fatigue crack nucleation and microstructure.

Lukáš, P. and Klesnil, M. (1971). Dislocation structures in fatigued single crystals of cu zn system. *physica status solidi (a)*, 5(1):247–258.

Luppo, M., Bailat, C., Schäublin, R., and Victoria, M. (2000). Tensile properties and microstructure of 590 mev proton-irradiated pure fe and a fe–cr alloy. *Journal of nuclear materials*, 283:483–487.

Lütjering, G. and Weissmann, S. (1970). Mechanical properties of age-hardened titanium-aluminum alloys. *Acta Metallurgica*, 18(7):785–795.

Ma, A., Roters, F., and Raabe, D. (2006). A dislocation density based constitutive model for crystal plasticity fem including geometrically necessary dislocations. *Acta Materialia*, 54(8):2169–2179.

Madec, R. (2001). *Des intersections entre dislocations à la plasticité du monocristal CFC: étude par dynamique des dislocations*. PhD thesis, Paris 11.

Madec, R., Devincre, B., Kubin, L., Hoc, T., and Rodney, D. (2003). The role of collinear interaction in dislocation-induced hardening. *Science*, 301(5641):1879–1882.

Madec, R., Devincre, B., and Kubin, L. P. (2002). From dislocation junctions to forest hardening. *Physical review letters*, 89(25):255508.

Mahajan, S. and Williams, D. (1973). Deformation twinning in metals and alloys. *International Metallurgical Reviews*, 18(2):43–61.

Mandel, J. (1965). Généralisation de la théorie de plasticité de wt koiter. *International Journal of Solids and structures*, 1(3):273–295.

Mandel, J. (1973). Equations constitutives et directeurs dans les milieux plastiques et viscoplastiques. *International Journal of Solids and Structures*, 9(6):725–740.

Marano, A., Gélébart, L., and Forest, S. (2019). Intragranular localization induced by softening crystal plasticity: Analysis of slip and kink bands localization modes from high resolution fft-simulations results. *Acta Materialia*, 175:262–275.

Marano, A., Gélébart, L., and Forest, S. (2021). Fft-based simulations of slip and kink bands formation in 3d polycrystals: influence of strain gradient crystal plasticity. *Journal of the Mechanics and Physics of Solids*, 149:104295.

Marian, J., Fitzgerald, S., and Po, G. (2020). Discrete dislocation dynamics simulations of irradiation hardening in nuclear materials. *Handbook of Materials Modeling: Applications: Current and Emerging Materials*, pages 2243–2271.

Martin, J. W. (1980). *Micromechanisms in particle-hardened alloys*. Cambridge university press.

Mecking, H. and Kocks, U. (1981). Kinetics of flow and strain-hardening. *Acta metallurgica*, 29(11):1865–1875.

Meng, F., Ferrié, E., Déprés, C., and Fivel, M. (2021). 3d discrete dislocation dynamic investigations of persistent slip band formation in fcc metals under cyclical deformation. *International Journal of Fatigue*, 149:106234.

Miao, J., Pollock, T. M., and Jones, J. W. (2012). Microstructural extremes and the transition from fatigue crack initiation to small crack growth in a polycrystalline nickel-base superalloy. *Acta Materialia*, 60(6-7):2840–2854.

Miller, B. D. (2009). *The effect of local conditions on deformation processes in low stacking-fault energy FCC alloys*. University of Illinois at Urbana-Champaign.

Miura, T., Fujii, K., Fukuya, K., and Ito, Y. (2009). Characterization of deformation structure in ion-irradiated stainless steels. *Journal of nuclear materials*, 386:210–213.

Mughrabi, H. (1978). The cyclic hardening and saturation behaviour of copper single crystals. *Materials Science and Engineering*, 33(2):207–223.

Mughrabi, H. (1983). Dislocation wall and cell structures and long-range internal stresses in deformed metal crystals. *Acta metallurgica*, 31(9):1367–1379.

Mura, T. and Mura, T. (1987). General theory of eigenstrains. *Micromechanics of defects in solids*, pages 1–73.

Nishioka, H., Fukuya, K., Fujji, K., and Kitsunai, Y. (2008). Deformation structure in highly irradiated stainless steels. *Journal of Nuclear Science and Technology*, 45(4):274–287.

Onimus, F., Béchade, J., and Gilbon, D. (2013). Experimental analysis of slip systems activation in neutron-irradiated zirconium alloys and comparison with polycrystalline model simulations. *Metallurgical and Materials Transactions A*, 44:45–60.

Onimus, F., Dupuy, L., Gaumé, M., Kassem, W., and Mompiou, F. (2021). Deformation mechanisms of zirconium alloys after irradiation studied by dislocation dynamics simulations and in situ straining experiments in tem. In *Zirconium in the Nuclear Industry: 19th International Symposium*, pages 24–p. ASTM International.

Onimus, F., Monnet, I., Béchade, J., Prioul, C., and Pilvin, P. (2004). A statistical tem investigation of dislocation channeling mechanism in neutron irradiated zirconium alloys. *Journal of Nuclear Materials*, 328(2-3):165–179.

Pan, H., He, Y., and Zhang, X. (2021). Interactions between dislocations and boundaries during deformation. *Materials*, 14(4):1012.

Patra, A. and McDowell, D. L. (2016). Crystal plasticity investigation of the microstructural factors influencing dislocation channeling in a model irradiated bcc material. *Acta Materialia*, 110:364–376.

Pearson, K. (1895). Vii. note on regression and inheritance in the case of two parents. *proceedings of the royal society of London*, 58(347-352):240–242.

Peirce, D., Asaro, R., and Needleman, A. (1982). An analysis of nonuniform and localized deformation in ductile single crystals. *Acta metallurgica*, 30(6):1087–1119.

Peirce, D., Asaro, R. J., and Needleman, A. (1983). Material rate dependence and localized deformation in crystalline solids. *Acta metallurgica*, 31(12):1951–1976.

Petch, N. (1953). The cleavage strength of polycrystals. *J. Iron Steel Inst.*, 174:25–28.

Philibert, J. (1979). Dislocations et déformation plastique. *Les éditions de la physique*, 101.

Pilvin, P., Onimus, F., Brenner, R., Pascal, S., Feaugas, X., and Saï, K. (2017). Finite element assessment of an affine self–consistent model for hexagonal polycrystals. *European Journal of Mechanics-A/Solids*, 61:345–356.

Pokharel, R., Lind, J., Kanjarla, A. K., Lebensohn, R. A., Li, S. F., Kenesei, P., Suter, R. M., and Rollett, A. D. (2014). Polycrystal plasticity: comparison between grain-scale observations of deformation and simulations. *Annu. Rev. Condens. Matter Phys.*, 5(1):317–346.

Pokharel, R., Lind, J., Li, S. F., Kenesei, P., Lebensohn, R. A., Suter, R. M., and Rollett, A. D. (2015). In-situ observation of bulk 3d grain evolution during plastic deformation in polycrystalline cu. *International Journal of Plasticity*, 67:217–234.

Polák, J., Helešic, J., and Obrtlík, K. (1990). Cyclic strain localization in copper single crystals and polycrystals. *Scripta Metallurgica et Materialia*, 24(2):415–419.

Pourian, M. H., Pilvin, P., Bridier, F., and Bocher, P. (2014). Heterogeneous elastic behavior of hcp titanium polycrystalline aggregates simulated by cellular automaton and finite element. *Computational materials science*, 92:468–475.

Priester, L. (2020). Les joints de grains: De la théorie à l'ingénierie.

Proudhon, H., Guéninchault, N., Forest, S., and Ludwig, W. (2018). Incipient bulk polycrystal plasticity observed by synchrotron in-situ topotomography. *Materials*, 11(10):2018.

Proudhon, H., Pelerin, M., King, A., and Ludwig, W. (2020). In situ 4d mechanical testing of structural materials: The data challenge. *Current Opinion in Solid State and Materials Science*, 24(4):100834.

Proudhon, H., Poole, W. J., Wang, X., and Brechet, Y. (2008). The role of internal stresses on the plastic deformation of the al–mg–si–cu alloy aa6111. *Philosophical Magazine*, 88(5):621–640.

Quek, S. S., Wu, Z., Zhang, Y. W., and Srolovitz, D. J. (2014). Polycrystal deformation in a discrete dislocation dynamics framework. *Acta materialia*, 75:92–105.

Quey, R. (2019). Neper reference manual. *no. May*.

Quey, R. and Renversade, L. (2018). Optimal polyhedral description of 3d polycrystals: Method and application to statistical and synchrotron x-ray diffraction data. *Computer Methods in Applied Mechanics and Engineering*, 330:308–333.

Rauch, E. (1993). *Etude de l'écrouissage des métaux, aspects microstructuraux et l ois de comportement, Institut National Polytechnique de Grenoble*. PhD thesis, Thèse de HDR.

Raza, S. (1982). Slip bands in nickel polycrystals at a low temperature. *Scripta Metallurgica*, 16(12):1325–1328.

Read, W. T. and Shockley, W. (1950). Dislocation models of crystal grain boundaries. *Physical review*, 78(3):275.

Reppich, B. (1992). Materials science and technology, rw cahn, p. haasen, and ej kramer eds., vol. 6. *Plastic Deformation and Fracture of Materials*, pages 312–57.

Rice, J. R. (1971). Inelastic constitutive relations for solids: an internal-variable theory and its application to metal plasticity. *Journal of the Mechanics and Physics of Solids*, 19(6):433–455.

Rosi, F. D. and Mathewson, C. (1950). A study of the plastic behavior of high-purity aluminum single crystals at various temperatures. *JOM*, 2:1159–1167.

Roters, F., Eisenlohr, P., Hantcherli, L., Tjahjanto, D. D., Bieler, T. R., and Raabe, D. (2010). Overview of constitutive laws, kinematics, homogenization and multiscale methods in crystal plasticity finite-element modeling: Theory, experiments, applications. *Acta materialia*, 58(4):1152–1211.

Roy, S., Gatti, R., Devincre, B., and Mordehai, D. (2019). A multiscale study of the size-effect in nanoindentation of au nanoparticles. *Computational Materials Science*, 162:47–59.

Sangid, M. D., Rotella, J., Naragani, D., Park, J.-S., Kenesei, P., and Shade, P. A. (2020). A complete grain-level assessment of the stress-strain evolution and associated deformation response in polycrystalline alloys. *Acta Materialia*, 201:36–54.

Sansal, C. d. (2007). *Plasticité et effet de taille dans les polycristaux à grains micrométriques: simulations mésoscopiques et modélisation*. PhD thesis, Châtenay-Malabry, Ecole centrale de Paris.

Schmid, E., Boas, W., Schmid, E., and Boas, W. (1935). Kristallelastizität. *Kristallplastizität: Mit Besonderer Berücksichtigung der Metalle*, pages 15–24.

Seal, J. R., Crimp, M. A., Bieler, T. R., and Boehlert, C. J. (2012). Analysis of slip transfer and deformation behavior across the α/β interface in ti–5al–2.5 sn (wt.%) with an equiaxed microstructure. *Materials Science and Engineering: A*, 552:61–68.

Sharp, J. (1974). Deformation of neutron irradiated copper alloys. *Acta Metallurgica*, 22(4):449–457.

Shen, Z., Wagoner, R., and Clark, W. (1986). Dislocation pile-up and grain boundary interactions in 304 stainless steel. *Scripta metallurgica*, 20(6):921–926.

Shen, Z., Wagoner, R., and Clark, W. (1988). Dislocation and grain boundary interactions in metals. *Acta metallurgica*, 36(12):3231–3242.

Shuvalov, L. A. et al. (1988). *Modern crystallography IV: physical properties of crystals*. Springer.

Spearot, D. E. and Sangid, M. D. (2014). Insights on slip transmission at grain boundaries from atomistic simulations. *Current Opinion in Solid State and Materials Science*, 18(4):188–195.

Stein, C. A., Cerrone, A., Ozturk, T., Lee, S., Kenesei, P., Tucker, H., Pokharel, R., Lind, J., Hefferan, C., Suter, R. M., et al. (2014). Fatigue crack initiation, slip localization and twin boundaries in a nickel-based superalloy. *Current Opinion in Solid State and Materials Science*, 18(4):244–252.

Stinville, J., Echlin, M., Texier, D., Bridier, F., Bocher, P., and Pollock, T. (2016). Sub-grain scale digital image correlation by electron microscopy for polycrystalline materials during elastic and plastic deformation. *Experimental mechanics*, 56(2):197–216.

Stinville, J., Ludwig, W., Callahan, P., Echlin, M., Valle, V., Pollock, T., and Proudhon, H. (2022a). Observation of bulk plasticity in a polycrystalline titanium alloy by diffraction contrast tomography and topotomography. *Materials Characterization*, 188:111891.

Stinville, J., Vanderesse, N., Bridier, F., Bocher, P., and Pollock, T. (2015). High resolution mapping of strain localization near twin boundaries in a nickel-based superalloy. *Acta Materialia*, 98:29–42.

Stinville, J. C., Ludwig, W., Callahan, P. G., Echlin, M. P., Valle, V., Pollock, T. M., and Proudhon, H. (2022b). Observation of bulk plasticity in a polycrystalline titanium alloy by diffraction contrast tomography and topotomography. *Material Characterization*, 188:111891.

Suresh, S. (1998). *Fatigue of materials*. Cambridge university press.

Sutton, A. P. (1995). Interfaces in crystalline materials. *Monographs on the Physice and Chemistry of Materials*, pages 414–423.

Tabourot, L. (1992). *Loi de comportement élastoviscoplastique du monocristal en grandes transformations*. PhD thesis, Institut National Polytechnique de Grenoble-INPG.

Tang, Y. and El-Awady, J. A. (2014). Formation and slip of pyramidal dislocations in hexagonal close-packed magnesium single crystals. *Acta Materialia*, 71:319–332.

Tanner, B. K. (2013). *X-ray diffraction topography: international series in the science of the solid state*, volume 10. Elsevier.

Taylor, G. I. (1934). The mechanism of plastic deformation of crystals. part i.—theoretical. *Proceedings of the Royal Society of London. Series A, Containing Papers of a Mathematical and Physical Character*, 145(855):362–387.

Teodosiu, C., Nicolae, V., and Paven, H. (1975). The influence of the core conditions on the linear anisotropic elastic field of a straight dislocation. *physica status solidi (a)*, 27(1):191–204.

Thomas, R., Lunt, D., Atkinson, M., da Fonseca, J. Q., Preuss, M., Barton, F., O'Hanlon, J., and Frankel, P. (2019). Characterisation of irradiation enhanced strain localisation in a zirconium alloy. *Materialia*, 5:100248.

Tran, H., Tummala, H., Péron-Lührs, V., Fivel, M., Habraken, A., et al. (2015). Interaction between dislocation and coherent twin boundary by quasicontinuum model. In *COMPLAS XIII: proceedings of the XIII International Conference on Computational Plasticity: fundamentals and applications*, pages 992–1002. CIMNE.

Tummala, H. (2016). *3D Discrete Dislocation Dynamics simulations of the role of interfaces in confined materials-: application to electronic devices such as LEDs*. PhD thesis, Université catholique de Louvain (1970-....).

Van der Giessen, E. and Needleman, A. (1995). Discrete dislocation plasticity: a simple planar model. *Modelling and Simulation in Materials Science and Engineering*, 3(5):689.

Vattré, A., Devincre, B., Feyel, F., Gatti, R., Groh, S., Jamond, O., and Roos, A. (2014). Modelling crystal plasticity by 3d dislocation dynamics and the finite element method: the discrete-continuous model revisited. *Journal of the Mechanics and Physics of Solids*, 63:491–505.

Volterra, V. (1907). Sur l'équilibre des corps élastiques multiplement connexes. In *Annales scientifiques de l'École normale supérieure*, volume 24, pages 401–517.

Wechsler, M. (1972). Dislocation channeling in irradiated and quenched metals. Technical report, Ames Lab., Ames, IA (United States).

Weygand, D., Friedman, L., Van der Giessen, E., and Needleman, A. (2002). Aspects of boundary-value problem solutions with three-dimensional dislocation dynamics. *Modelling and Simulation in Materials Science and Engineering*, 10(4):437.

Xiong, Y., He, T., Lu, Y., Ren, F., Volinsky, A. A., and Cao, W. (2018). Tensile deformation temperature impact on microstructure and mechanical properties of aisi 316ln austenitic stainless steel. *Journal of Materials Engineering and Performance*, 27:1232–1240.

Xu, Y., Joseph, S., Karamched, P., Fox, K., Rugg, D., Dunne, F. P., and Dye, D. (2020). Predicting dwell fatigue life in titanium alloys using modelling and experiment. *Nature communications*, 11(1):5868.

Yeratapally, S. R., Glavicic, M. G., Hardy, M., and Sangid, M. D. (2016). Microstructure based fatigue life prediction framework for polycrystalline nickel-base superalloys with emphasis on the role played by twin boundaries in crack initiation. *Acta Materialia*, 107:152–167.

Yoshida, S. and Nagata, N. (1966). Deformation of polycrystalline aluminium at high strain rates. *Transactions of the Japan Institute of Metals*, 7(4):273–279.

Zhang, M., Bridier, F., Villechaise, P., Mendez, J., and McDowell, D. (2010). Simulation of slip band evolution in duplex ti–6al–4v. *Acta materialia*, 58(3):1087–1096.

Zhang, M., Zhang, J., and McDowell, D. (2007). Microstructure-based crystal plasticity modeling of cyclic deformation of ti–6al–4v. *International Journal of Plasticity*, 23(8):1328–1348.

Zhou, C. and LeSar, R. (2012). Dislocation dynamics simulations of plasticity in polycrystalline thin films. *International Journal of Plasticity*, 30:185–201.

Zhu, T. and Gao, H. (2012). Plastic deformation mechanism in nanotwinned metals: An insight from molecular dynamics and mechanistic modeling. *Scripta Materialia*, 66(11):843–848.

Zhu, T., Li, J., Samanta, A., Kim, H. G., and Suresh, S. (2007). Interfacial plasticity governs strain rate sensitivity and ductility in nanostructured metals. *Proceedings of the National Academy of Sciences*, 104(9):3031–3036.

Zhuang, Z., Liu, Z., and Cui, Y. (2019). *Dislocation Mechanism-Based Crystal Plasticity: Theory and Computation at the Micron and Submicron Scale*. Academic Press.

Zset (2022). http://zset-software.com/downloads/versions/.

RÉSUMÉ

Comprendre les processus de déformation conduisant à la défaillance des matériaux polycristallins est l'un des principaux défis de la science des matériaux. A ce jour, les mécanismes de localisation de la déformation plastique en bandes de glissement et la propagation de la déformation à travers un agrégat polycristallin ne sont pas entièrement compris. L'investigation de tels phénomènes est l'objectif du projet ANR 3DiPolyPlast. Dans l'approche de simulation multi-échelles proposée, des simulations de Dynamique des Dislocations Discrètes (DDD) seront utilisées afin de mieux modéliser le comportement individuel et collectif des dislocations à l'échelle mésoscopique. La majorité des simulations réalisées sont basées sur un couplage dit faible entre la DDD et la Méthode des Eléments Finis (MEF), dans lequel le champ de contrainte issu d'un calcul MEF en élasticité est utilisé comme condition initiale de chargement intragranulaire. Cette hypothèse permet de réaliser une étude plus systématique et physiquement justifiée des différents mécanismes ayant lieu durant la déformation plastique au sein de la microstructure de dislocation. Les simulations réalisées montrent le rôle joué par la microstructure polycristalline sur la localisation de la déformation plastique, notamment à travers les incompatibilités de déformations élastiques entraînant l'apparition de concentrations de contraintes intragranulaires. A l'aide de ces simulations, nous montrons qu'au cours de la déformation plastique, certains mécanismes comme le cross-slip ou les annihilations colinéaires permettent à la déformation plastique de s'initier dans certaines régions du grain. L'observation méticuleuse de cette microstructure de dislocation nous a permis de reconsidérer une des hypothèses initiales de nos simulations DDD, l'impénétrabilité des joints de grains. De fait, le nombre de dislocations s'empilant aux joints de grains est important et les contraintes calculées en tête de ces empilements sont de l'ordre du GPa. Une partie du travail présenté dans ce manuscrit a donc été dédié à l'implémentation d'une règle locale permettant de modéliser les mécanismes de réactions entre dislocations et joints de grains au cours de la déformation plastique. Par ailleurs, nous avons montré que ces mécanismes de réactions étaient à l'origine d'une forte diminution de l'écrouissage cinématique entraînant dans des régions locales du grain la présence d'un glissement plastique intense. D'autres calculs ont été réalisés dans le cadre du modèle discret-continu (MDC) qui couple les calculs d'éléments finis de plasticité cristalline effectués sur l'agrégat polycristallin complet avec des simulations DDD. Cette modélisation permet une description plus précise des mécanismes de déformation plastique et représente un atout majeur dans l'étude du rôle des interactions entre grains, notamment durant la déformation plastique de ces derniers. Ces simulations se révèlent aussi être une source d'informations afin de mieux comprendre les contrastes de diffraction observés expérimentalement en topo-tomographie rayons X.

MOTS CLÉS

Localisation, Dislocations, Polycristaux, Déformation plastique, Dynamique des dislocations discrètes, Méthode des éléments finis

ABSTRACT

Understanding the deformation processes leading to the failure of polycrystalline materials is one of the major challenges in materials science. To date, the mechanisms of plastic strain localization into slip bands and the propagation of deformation through a polycrystalline aggregate are not fully understood. Investigating such phenomena is the aim of the 3DiPolyPlast ANR project. In the proposed multi-scale simulation approach, Discrete Dislocation Dynamics (DDD) simulations will be used to better model the individual and collective behavior of dislocations at the mesoscopic scale. The majority of the simulations carried out are based on a so-called weak coupling between DDD and the Finite Element Method (FEM), in which the stress field resulting from a FEM calculation in elasticity is used as the initial intragranular loading condition. This assumption enables a more systematic and physically justified study of the various mechanisms taking place during plastic deformation within the dislocation microstructure. The simulations carried out show the role played by the polycrystalline microstructure on the localization of plastic deformation, notably through elastic deformation incompatibilities leading to the appearance of intragranular stress concentrations. Using these simulations, we show that during plastic deformation, certain mechanisms such as cross-slip or collinear annihilation allow plastic deformation to initiate in certain regions of the grain. Meticulous observation of this dislocation microstructure has enabled us to reconsider one of the initial assumptions of our DDD simulations, the impenetrability of grain boundaries. In fact, the number of dislocations stacking up at grain boundaries is significant, and the stresses calculated at the head of these stacks are of the order of the GPa. Part of the work presented in this manuscript has therefore been dedicated to the implementation of a local rule to model the reaction mechanisms between dislocations and grain boundaries during plastic deformation. In addition, we have shown that these reaction mechanisms are responsible for a sharp decrease in kinematic strain hardening, leading to intense plastic slip in local regions of the grain. Further calculations were carried out within the framework of the discrete-continuous model (DCM), which couples crystal plasticity finite element calculations carried out on the complete polycrystalline aggregate with DDD simulations. This modeling provides a more precise description of plastic deformation mechanisms, and represents a major asset in the study of the role of interactions between grains, particularly during their plastic deformation. These simulations are also proving to be a source of information for better understanding the diffraction contrasts observed experimentally in X-ray topo-tomography.

KEYWORDS

Localization, Dislocations, Polycrystals, Plastic deformation, Discrete dislocation dynamics, Finite element method